The Design, Construction and Initial Operation of the Canterbury University ST Radar

A Thesis Submitted in Partial Fulfillment of the
Requirements for the Degree of Doctor of Philosophy

by
Trevor K. Carey-Smith

Department of Physics and Astronomy
University of Canterbury

2003

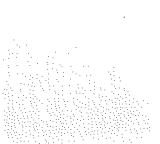

Abstract

This thesis describes the design, construction and initial operation of the Canterbury University Stratosphere-Troposphere Atmospheric Radar (CUSTAR), which is capable of continuous measurement of the vertical wind profile from 3 to 15 km in altitude, with a temporal resolution of 2 minutes and a height resolution of 300 metres.

A novel, cost-effective antenna array has been designed to maximise the effective aperture, while keeping side-lobes at a minimum. The beam pattern of the array has been investigated in great detail using astronomical radio sources. Vela XYZ and Centaurus A both pass directly over the radar site, and using these strong sources, the best estimate of the pointing angle of the beam, in the east-west plane, was found to be $0.01° \pm 0.20°$ from the zenith. The best estimate of the half-power full-width of the antenna beam was found to be $6.51° \pm 0.54°$.

The Canterbury University ST radar has been operating since September, 2002, during which time the tropopause height has been determined hourly. A seasonal variation in tropopause height of approximately 1 km between September/October and November/December was observed, which agrees with climatalogical radiosonde measurements performed in Christchurch. Comparisons were performed between the radar tropopause height and the tropopause height measured by radiosondes in three locations throughout New Zealand. It was found that the correlation between the radar and radiosonde tropopause heights was similar to the correlation between different radiosonde sites, suggesting that the radar is capable of finding the tropopause height with similar accuracy to radiosonde measurements.

The structure of a cold front which passed over Christchurch on September 10, 2002, has been examined in detail using radar signal to noise ratio profiles. Gravity wave oscillations, that were most likely to be caused by orography, were observed underneath the frontal surface, which was found to have a slope of 0.4°. The wave activity was thought to occur due to the strong cross-mountain background wind and also the increase in atmospheric stability associated with the frontal passage.

Contents

Tables

Figures

Chapter 1

Introduction

The atmosphere is vital to life on Earth. To ensure our continued survival we need to protect the environment in which we live. To this end, a comprehensive understanding of the atmosphere, including its structure and dynamics, is very important. Very high frequency (VHF) radars can be used in a wide range of atmospheric research activities and, due to their high temporal and altitude resolution, are ideal for studying small-scale, time-varying phenomena such as frontal regions, waves and turbulence.

In recent years it has been realised that anthropogenic effects can produce significant changes in the Earth's atmosphere, so much so that atmospheric science and research is now involved in international politics. In order to make accurate predictions as to how humanity's current actions are shaping the future atmosphere, sophisticated models, based on the physics and chemistry of both the atmosphere and ocean, are necessary. The accuracy of these models is increased as more is learnt about the atmosphere. Of major import, particularly in the case of "global warming", is the understanding of mechanisms used to transport trace gases, such as carbon dioxide and water vapour, around the Earth's atmosphere and between its well-defined layers.

It is also of great public interest to obtain accurate predictions of the short-term weather conditions. This is particularly true in regions where severe weather phenomena often occur with little warning. In these situations, the ability to have up to the minute information about the atmosphere is invaluable.

VHF radars (often called clear-air or wind-profiling radars) are well suited to the investigation of both small scale dynamics and long-term climatology. This is because they can run continuously, typically with a temporal resolution of less than 5 minutes and height resolution of less than 300 metres. They can produce a vertical profile of the three-dimensional wind vector and also information about the structure of the atmospheric scatterers. The resulting data is useful for long-term

dynamical studies, producing valuable information on mean winds and large scale processes such as planetary waves and atmospheric tides. Smaller scale phenomena, for example, gravity waves and frontogenesis, can also be studied with excellent temporal and spatial precision.

1.1 Atmospheric Measurement Techniques

Atmospheric parameters can be measured at the Earth's surface relatively simply. Temperature, pressure, wind speed and direction, humidity and rainfall can all be measured easily and accurately with meteorological weather stations, which are spread (albeit unevenly) all over the Earth. Upper-air measurements are much more difficult and therefore less common-place.

Measurement of atmospheric parameters above ground level can be divided into two categories, *in situ* techniques and remote-sensing techniques. *In situ*, refers to techniques in which the instrument used is located within the region of the atmosphere under consideration. Remote sensing techniques are those in which the instrument is separate from the measurement region and they generally make use of electromagnetic radiation to probe the region in question.

Kites, balloons, rockets and aircraft have all been used to make *in situ* measurements of the atmosphere. Kites were first used to study the variation of temperature with altitude in 1749 by Alexander Wilson [*Shaw*, 1926], but could only reach heights of several kilometres (Teisserenc de Bort reached a height of 5900 metres in 1903 [*Geddes*, 1939]). Manned balloons were first used to probe the atmosphere in 1783 and during the 19th century, the use of free balloons increased. By 1900 balloons were being fitted with mechanical devices to record temperature, pressure and humidity, which typically operated up to heights of 15-20 km and even up to 37 km [*Shaw*, 1926]. Due to the uncontrolled nature of a balloon flight, these systems were unreliable as the instruments collecting the atmospheric data were not always recoverable. In 1927, the radiosonde, which transmits atmospheric data back to the ground as it is collected, was designed by Pavel Molchanov [*Wallace and Hobbs*, 1977]. This device, which is relatively inexpensive, made recovery of the balloon-borne instrument unnecessary and therefore the technique became much more reliable. These systems are capable of making observations up to 40 km and are now often fitted with GPS receivers or tracked from the ground with radar to

find their horizontal velocity, which arises solely due to their advection by the background wind. Rockets were first used for atmospheric purposes in the late 1940's, but it was not until the late 1950's that they began to be used regularly at a large range of sites [*Craig*, 1965]. Rocketsondes travel up to heights of 80 km and release instrumentation which descends with the aid of a parachute, taking (and transmitting back to the ground) measurements on its journey. Atmospheric sensors fitted to commercial aircraft are also routinely used to make measurements of the upper air.

Remote sensing techniques are usually either satellite based or ground based, but can also be operated from aircraft, balloons and rockets. All remote sensing instruments can be divided into two categories, passive and active. Passive instruments measure radiation provided to them from the atmosphere, such as scattered solar radiation or emitted microwave and infrared radiation. Ground based passive instruments include spectrometers such as the Dobson spectrometer which measures the absorption of ultraviolet radiation by ozone. There are many satellite based passive instruments which operate in the ultraviolet, visible, infrared and microwave regions of the spectrum, providing measurements of temperature, cloud cover, trace gas concentrations, aerosol composition and many other atmospheric quantities [*Houghton et al.*, 1984]. Active instruments transmit their own signal and measure the properties of the reflected signal. Devices in this category include radar and lidar. Lidars (light detection and ranging) operate in a similar manner to radars (which are discussed in detail below) in that a transmitted signal, usually in the visible, reflects off atmospheric molecules and aerosols and is then received by the instrument. Lidars can be used to determine the gaseous composition, density and temperature of the atmosphere and also the line of sight velocity of the scatterers. They are often used to obtain information on aerosols and trace gas concentrations.

1.2 Atmospheric Radar

1.2.1 Radar History

A good overview of the history of atmospheric radar is given by *Probert-Jones* [1990], *Fletcher* [1990] and others in the Battan Memorial Volume edited by *Atlas* [1990]. Radar (radio detection and ranging) was developed by Watson Watt in 1936 before the beginning of World War II. The first radars that were used operated at frequen-

cies no higher than about 300 MHz. However, toward the end of the 1930's, the British invention of the cavity magnetron allowed radars to use frequencies up to 10 GHz. Early on in the use of these microwave radars it was found that some of the echoes were due to Rayleigh scatter from hydrometeors and soon these radars were being used to measure and track rain storms. Radars used for this purpose today are called weather radars.

Studies of the clear air also started at the beginning of radar history. *Colwell and Friend* [1936] detected clear air echoes from the troposphere when they were using 10 to 200 metre wavelength radars to study the ionosphere. In the same year, *Watson Watt et al.* [1936] also detected clear air echoes. *Colwell and Friend* attributed these echoes to temperature inversions in the troposphere, which in turn would cause large gradients in the refractive index of the air. During the late 1940's and 1950's many researchers also recorded isolated echoes which were often termed angels, as people were unsure as to what actually caused them.

From the mid 1960's to the early 1970's, much work was done with 10 to 100 cm radars and it was during this time that many of the methods of reflection were understood. Such things as turbulence and convection were found to increase the power of the returning radar signal. Reflection caused by turbulence came to be known as Bragg scatter (see Section 2.2.3). Two other types of echo processes were proposed and are known as Fresnel reflection and Fresnel scatter (see Section 2.2.2).

Radars used to study the atmosphere in the 80 to 110 km range are either MF (medium frequency), meteor radars or large, high powered VHF radars, also known as MST (mesosphere-stratosphere-troposphere) radars, which are discussed below. MF (or partial reflection wind) radars make wind measurements by analysing the patterns produced on the ground by the reflection of radio waves from the lower ionosphere [*Fraser*, 1965; *Briggs et al.*, 1969]. During the day the lower height limit of these radars can be reduced to 60 km due to the increase in ionisation. Meteor radars normally operate at higher frequencies than MF radars and obtain atmospheric parameters by tracing the movement of meteor ablation trails [*Greenhow*, 1954; *Marsh et al.*, 2000].

1.2.2 VHF Radars

In the 1970's there was a large shift to the use of VHF ($30-300$ MHz) radars for atmospheric research, as these frequencies were found to be very useful for probing the

troposphere and stratosphere. Jicarmarca Radio observatory in Peru was converted to the first atmospheric VHF radar by John Green in 1969. It operated at 50 MHz and Doppler wind velocities were obtained and published by *Woodman and Guillen* [1974]. The first VHF radar built exclusively to probe the lower atmosphere was the Sunset radar in Colorado. It operated at 40 MHz and its first results were published by *Green et al.* [1975]. The 53 MHz SOUSY radar in Germany was completed in 1976 by the Max Plank Institute in Lindau. The Poker Flat radar in Alaska was built in 1979, with its first results published by *Balsley et al.* [1979]. It produced continuous wind measurements in the troposphere, stratosphere and mesosphere for seven years before being shut down in 1986 [*Hardy and Gage*, 1990]

At present, there are many VHF and UHF (ultra high frequency, 300−3000 MHz) radars in operation around the world. They range from very large radars like the Gadanki radar in India [*Rao et al.*, 1995] and the MU radar in Japan [*Fukao et al.*, 1985], to smaller ones like the Canadian VHF atmospheric radar [*Hocking*, 1997b] and the Buckland Park VHF radar near Adelaide, Australia [*Vincent et al.*, 1987]. The MU radar operates at 46.5 MHz, using an antenna array made up of 475 individually phased crossed Yagi-Uda antennas each with its own transmitter. It can operate in the Doppler beam swing mode (see Section 2.4.2) using 1657 different beams directions and it has a peak power of 1 MW. This radar, which can receive atmospheric echoes from as high as 100 km, is also capable of operating in the spaced antenna mode (see Section 2.4.3). The Buckland park radar operates principally in the spaced antenna mode, but can also operate in the Doppler beam swinging mode, having three specific beam directions. It has a peak power output of about 100 kW and is designed to run unattended for long periods of time producing a continuous data set. The Canterbury University radar is a similar size to the Buckland Park radar. Generally, smaller radars are not as versatile as the larger ones, but are easier to operate, can run continuously and are less expensive.

A major application of VHF and UHF radars is in wind profiler networks, where the results from a number of spatially separated radars are centrally collated. There are networks in the United States [e.g. *Strauch et al.*, 1984], Europe and across the equatorial Pacific Ocean region [*Hocking*, 1997a]. These networks are particularly useful for medium range weather forecasting as they give a good spatial resolution, which is needed to obtain accurate initial conditions for use in numerical weather prediction models. Single radars can also assist with weather forecasting, particu-

larly in the short-range as they have good temporal resolution.

1.3 Thesis Overview

This thesis describes the design, construction and initial operation of the Canterbury University Stratosphere-Troposphere Atmospheric Radar (CUSTAR). This chapter has provided a brief justification for the thesis and has discussed the various techniques used to probe the atmosphere.

Chapter 2 covers the necessary atmospheric and radar theory. Included is a discussion of the atmosphere's structure, constituents and dynamics. The focus of this discussion is on the troposphere and stratosphere and their mutual interaction. The physics of VHF radar theory is then described with reference to the various scattering mechanisms and the radar equation which quantifies the radar's performance. The different techniques used to measure wind speed are also discussed briefly. Finally, this chapter introduces an additional project in which the ST radar will be able to record the influx of meteors using the detection of head echoes via radial scatter.

The hardware and operational details of the radar are described in Chapter 3. The majority of this chapter is taken up with a description of the antenna array and its design. The first section covers antenna theory and the following sections explain the design of the array and its construction. The main electronic components are also discussed in this chapter. These include the transmit-receive switch, the transmitter, the receiver and the analogue to digital converter. The complete system and its operational parameters are also fully detailed.

Chapter 4 describes the results from a measurement campaign whose aim was to verify the antenna beam pattern. The theoretical shape of the beam is detailed first. The verification technique, which uses reverse radio astronomy, is explained before a brief description of positional astronomy is given. The verification was first applied to a single row of the antenna and the results from this test are detailed with particular focus on results obtained on April 25, 2001. Results are then shown from the complete array which verify the beam direction using Vela XYZ and Centaurus A.

The atmospheric results obtained from the radar are covered in Chapter 5. Some initial results and the signal processing scheme used to deduce useful atmospheric parameters are presented first. In the next section, comparisons between different

methods of data integration are described. Tropopause height measurements derived from radar signal power profiles make up a large part of the remainder of Chapter 5. The methods for obtaining tropopause height from radar signal to noise ratio and atmospheric temperature profiles are described. Tropopause heights found by the radar are compared with those from radiosonde measurements and model data. A short case-study which shows the effect a frontal passage has on the radar signal power is also detailed.

Chapter 6 summarises the work presented in the preceding chapters and reiterates the main findings. Possible further work with the data already collected and modifications to the existing system are also detailed in this chapter.

Chapter 2

Background and Theory

2.1 The Atmosphere

The atmosphere is made up of layers categorised by their temperature gradients as shown in Figure 2.1. In the troposphere, which stretches from the Earth's surface to around 10 km, the temperature decreases rapidly from 290 K to 220 K. This decrease has a global mean rate of 6.5 $\mathrm{K\,km^{-1}}$ and is linked to heating caused by the Earth's surface. The troposphere is characterised by the large amount of mixing that occurs. The tropopause marks the top of this layer and its height varies from $\simeq$8 km in the polar regions to $\simeq$16 km in the tropics. As shown in Figure 2.2, the

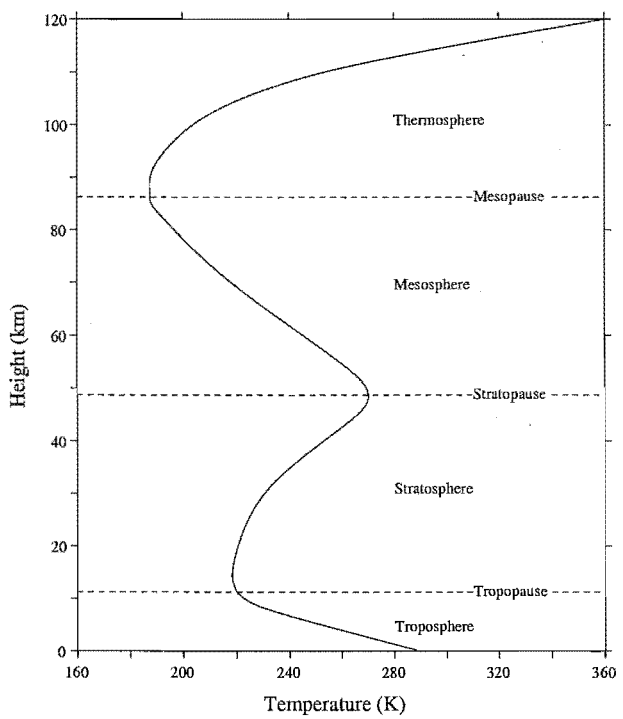

Figure 2.1: Temperature profile of the atmosphere.

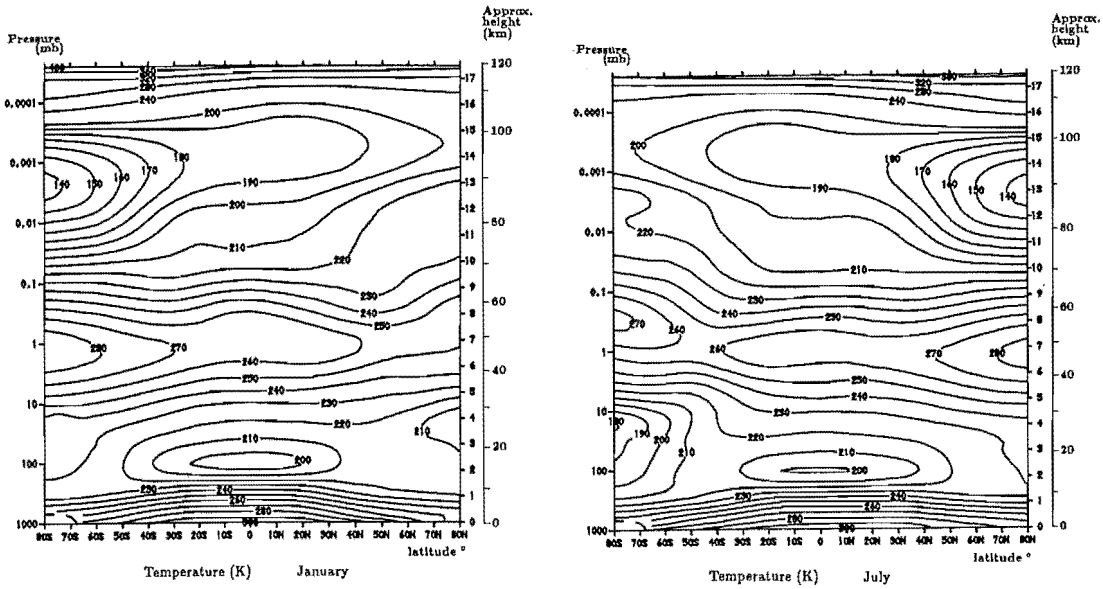

Figure 2.2: Latitude vs. height cross sections of zonal mean temperature for January and July [*Fleming et al.*, 1990].

height of this interface also varies through the year. The data in this figure (and Figure 2.4) is from the zonal mean[1] COSPAR International Reference Atmosphere (CIRA86) presented by *Fleming et al.* [1990].

The stratosphere which is much more stable begins at the tropopause and extends to 50 km in altitude. In this layer, due to the absorption of ultra-violet light by ozone, the temperature increases with height to a maximum of $\simeq$ 270 K at the stratopause. The next layer is the mesosphere, in which the temperature again decreases. At an altitude of 85 km, the temperature is only 190 K. Above 85 km, the temperature increases in the region called the thermosphere [*Salby*, 1996]. All these figures vary with latitude and time as shown in Figure 2.2.

2.1.1 Motion in the Atmosphere

Motion in the atmosphere occurs from the micro-scale (1 – 1 000 m) through meso-scale (1 – 1 000 km) to macro-scale processes (1 000 – 100 000 km). Figure 2.3 summarises these scales.

Motions on the largest scale are planetary waves which occur globally having

[1]The term "zonal mean" refers to the global mean at a particular latitude.

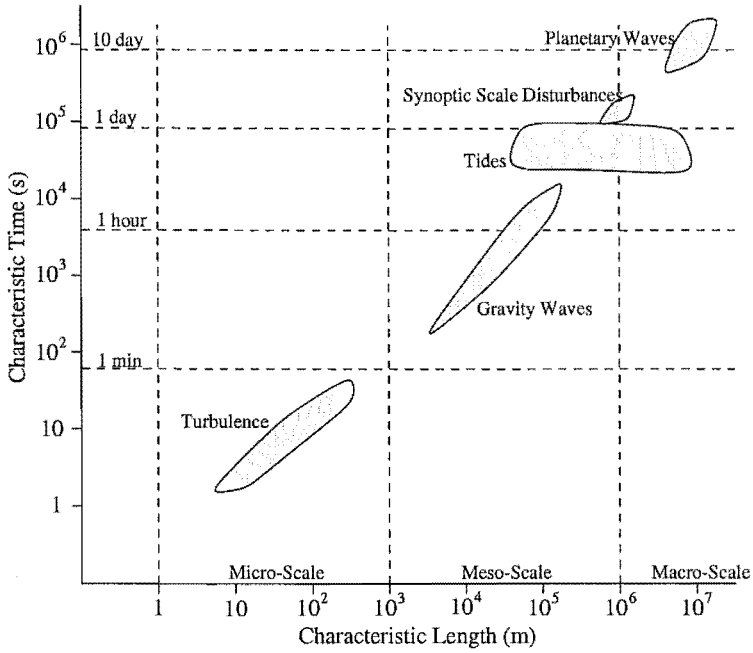

Figure 2.3: Characteristic scales of motion in the atmosphere [*Ruster*, 1984].

horizontal spatial scales of $\sim 10\,000$ km. Synoptic scale motions are those linked with cyclones and anti-cyclones which greatly affect tropospheric weather systems. These have horizontal scales of $\sim 1\,000$ km and typical periods of one day in length. Atmospheric tides include diurnal, semidiurnal and terdiurnal components which span scales anywhere between 30 km to 10 000 km. Gravity waves (or buoyancy waves) have horizontal spatial scales from a few kilometres to ~ 100 km (trapped lee waves can sometimes be observed for several hundreds of kilometres) and periods up to the local inertial period

$$\tau = \frac{\pi}{\Omega \sin \phi}, \tag{2.1}$$

where Ω is the Earth's angular velocity and ϕ is latitude [*Salby*, 1996]. At time-scales of less than a few minutes and lengths less than ~ 100 m turbulence is dominant. The vertical spatial scales associated with these atmospheric motions are usually one or two orders of magnitude smaller than the horizontal scales detailed above.

VHF radars can measure small scale motions such as gravity waves and turbulence. Atmospheric tides and planetary waves can also be investigated by studying data collected over a longer time period. These atmospheric motions are of great importance when trying to understand and model the atmosphere.

The temperature structure described earlier is closely related to the zonal mean

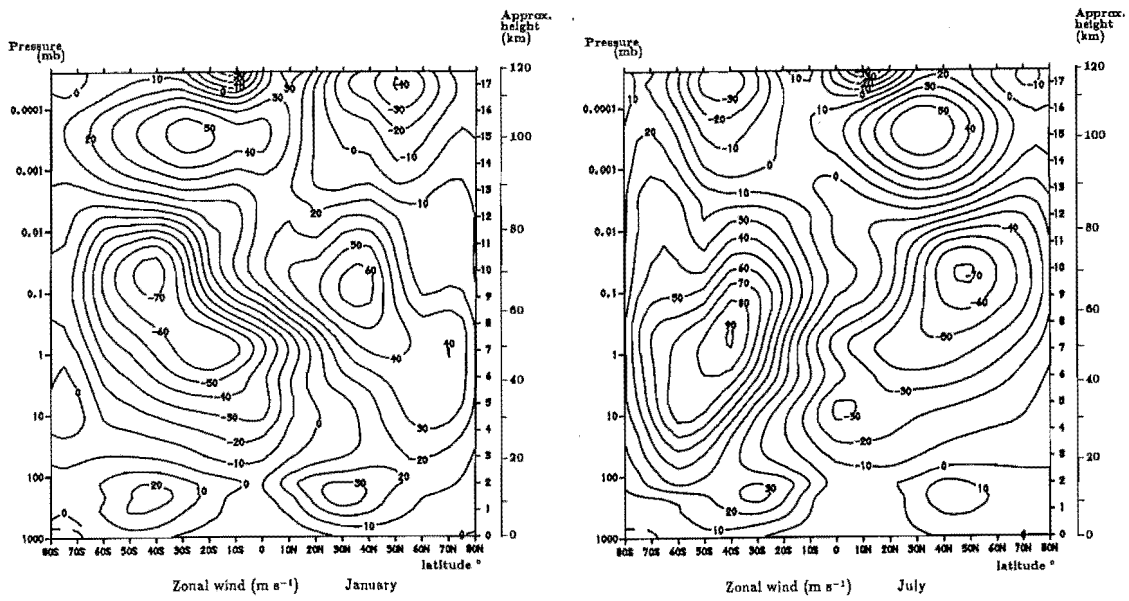

Figure 2.4: Latitude vs. height cross sections of zonal mean wind for January and July [*Fleming et al.*, 1990].

circulation in the atmosphere shown in Figure 2.4. At mid-latitudes there are mean westerly (from the west) flows in the troposphere known as the subtropical jet-streams. These zonal means reach speeds of 20 to 30 $\mathrm{m\,s^{-1}}$. Above the tropopause the mean wind-speed decreases before increasing again to a maximum of 60 to 70 $\mathrm{m\,s^{-1}}$ in the mesosphere (easterly in the summer hemisphere and westerly in the winter hemisphere). The subtropical jet-streams in the troposphere have a large effect on the movement of synoptic scale weather systems around the globe.

2.1.2 Static Stability

The marked difference in the dynamics of the troposphere and stratosphere is due to the differing static stabilities in these regions. Static stability is related to potential temperature, θ, given by Poisson's equation

$$\theta = T\left(\frac{p_s}{p}\right)^{\frac{R}{c_p}}, \tag{2.2}$$

where R is the gas constant for dry air and c_p is the specific heat of air at a constant pressure. θ can be defined as the temperature that a parcel of dry air at pressure p and temperature T would have if it were expanded or compressed adiabatically to

a standard pressure p_s (e.g. 1000 mb).

A relationship between the rate of decrease of temperature with respect to height (the lapse rate, Γ) and the rate of change of potential temperature with respect to height z can be obtained from Equation 2.2 as

$$\frac{T}{\theta}\frac{\partial\theta}{\partial z} = \frac{\partial T}{\partial z} + \frac{g}{c_p}, \tag{2.3}$$

where g is the gravitational acceleration [*Holton*, 1992]. If the potential temperature is constant with height, then

$$-\frac{\partial T}{\partial z} = \frac{g}{c_p} \equiv \Gamma_d, \tag{2.4}$$

where Γ_d is the dry adiabatic lapse rate. If the potential temperature changes with height then the lapse rate will be different from Γ_d and Equation 2.3 becomes

$$\frac{T}{\theta}\frac{\partial\theta}{\partial z} = \Gamma_d - \Gamma. \tag{2.5}$$

If $\Gamma < \Gamma_d$ an air parcel displaced from its equilibrium position will tend to return to its equilibrium position, that is the atmosphere is statically stable.

A parcel that is displaced in a stable atmosphere will oscillate about its equilibrium position. The frequency of this oscillation can be derived and is given by

$$\omega_B^2 = g\frac{1}{\theta}\frac{\partial\theta}{\partial z} \qquad \left(= g\frac{\partial \ln\theta}{\partial z}\right), \tag{2.6}$$

where ω_B is the Brunt-Väisälä frequency. The static stability criteria for dry air are

$$\begin{aligned}
\omega_B^2 > 0 \quad \text{or} \quad \frac{\partial\theta}{\partial z} > 0 \qquad & \text{statically stable} \\
\omega_B^2 = 0 \quad \text{or} \quad \frac{\partial\theta}{\partial z} = 0 \qquad & \text{statically neutral} \\
\omega_B^2 < 0 \quad \text{or} \quad \frac{\partial\theta}{\partial z} < 0 \qquad & \text{statically unstable.}
\end{aligned} \tag{2.7}$$

The atmosphere as a whole is statically stable. Because the temperature in the troposphere decreases with height it can, on small scales, become unstable. This causes overturning and mixing of air which in turn acts to stabilise the region so that on a large scale the troposphere becomes statically stable. The stratosphere has a much larger $\partial\theta/\partial z$ and is much more stable than the troposphere due to its increase in temperature with height. This stability means that there is little vertical movement in the stratosphere and also across the tropopause.

2.1.3 The Tropopause

The existence of the tropopause can be explained in terms of radiation and convection. If the atmosphere is heated from below by infrared radiation from the Earth's surface it will have a strong lapse rate near the ground which, if there is no convection, will decrease smoothly with height. However, as explained previously, the high lapse rate will cause instabilities and convective overturning of the air, adjusting the temperature profile near the Earth's surface away from radiative equilibrium. At greater altitude, where the atmosphere is statically stable, the atmosphere will be in radiative equilibrium and the abrupt change between this layer and the convectively adjusted layer below it has been identified as the tropopause.

While this explanation holds true for some areas, such as the tropics, it cannot explain the observed structure in other regions. The tropopause can be quite complicated, having multiple levels, steps or tropopause folds (see Figure 2.9). Breaks or folds in the tropopause can have a large effect on the interchange of trace gases between the stratosphere and troposphere, processes that must be understood for prediction of climate change [*Price and Vaughan*, 1993; *Holton et al.*, 1995]. The sensitivity of the height of the tropopause to various parameters, including temperature, ozone distribution and rotation rate, has been investigated by *Thuburn and Craig* [1997].

The height of the tropopause can be defined using vertical profiles of temperature (see Section 5.5), ozone concentration [*Bethan et al.*, 1996], Brunt-Väisälä frequency [*Hooper and Arvelius*, 2000] and VHF radar signal to noise ratio (see Section 5.4).

The tropopause has been shown to have a three-fold structure as depicted in Figure 2.5 [*DeFant and Taba*, 1957; *Palmén and Newton*, 1969]. The three regions that produce this structure are the polar, mid-latitude and tropical regions, each of which has a different circulation. The polar and tropical regions undergo circulation in which air rises at low latitudes due to radiative heating and falls at high latitudes due to cooling. Air in the mid-latitude region circulates in the opposite direction.

The polar and mid-latitude regions are separated by what has been called the polar-front (see Figure 2.6 and associated text). The upper region of this front marks the break between the polar tropopause and the mid-latitude tropopause and usually occurs at latitudes of between 50° and 55°. The polar tropopause is typically at a height of 8 km whereas the mid-latitude tropopause occurs at around 10 km. The mid-latitude and tropical air regions are not separated by a front, but there is

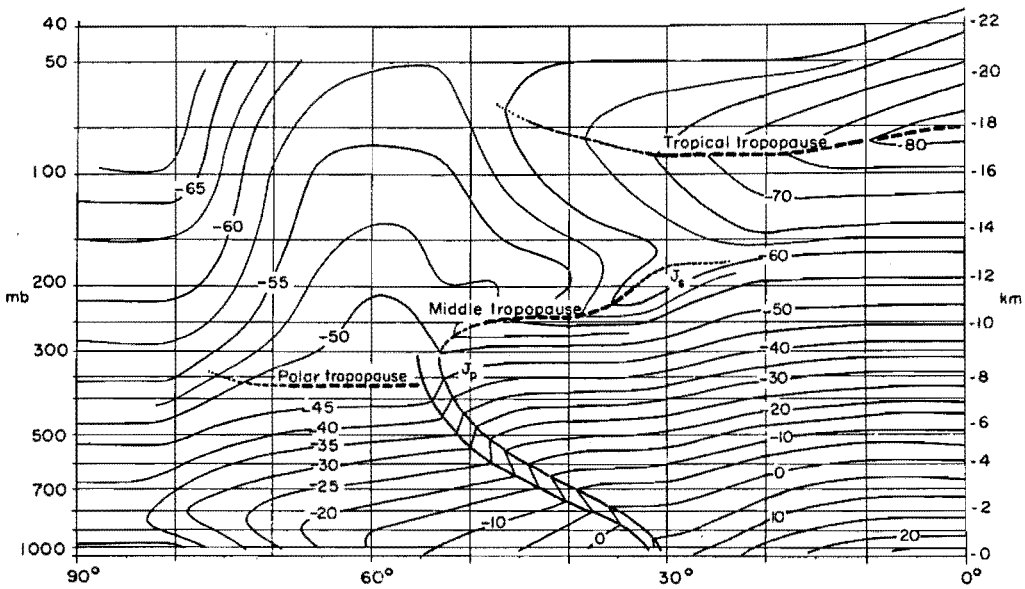

Figure 2.5: Meridional cross-section showing mean temperature (°C) in the Northern Hemisphere on the 1st of January, 1956. J_p and J_s refer to the polar and subtropical jet streams [*DeFant and Taba*, 1957].

a break in the tropopause which occurs at latitudes of between 30° and 35°. The tropical tropopause is at an altitude of approximately 17 km.

This discussion has been made with reference to data from the Northern Hemisphere, but the arguments made can be extended to include the Southern Hemisphere also.

2.1.4 Atmospheric Fronts

When two different air masses, characterised by their temperature, come together, the boundary between them becomes a front, or sloping transition zone. This formation process is called frontogenesis and the reverse process, or frontal decay, is called frontolysis. These processes also occur to air parcels that enter or leave a frontal zone. A front can be defined as an elongated region with a strong temperature gradient and relatively large static stability. Frontal regions are typically 100 km wide and 1000 km long [*Bluestein*, 1986].

Figure 2.6 shows a frontal region in the mid-latitudes between cold air from the polar region and warm air from the tropics. The wind and temperature fields and

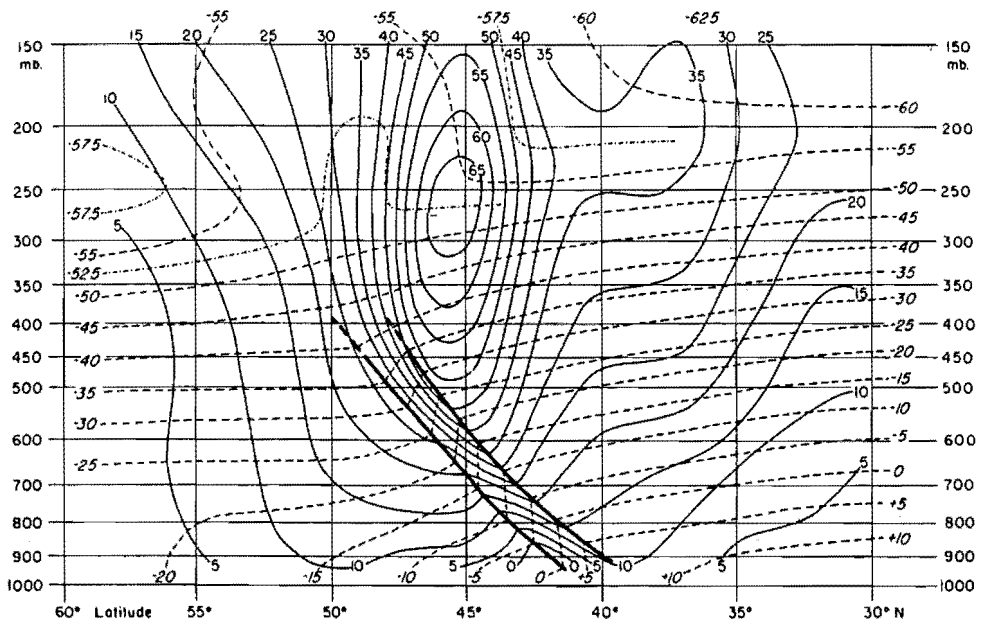

Figure 2.6: Cross section of a polar front along longitude 80°W. Thick lines represent the boundaries of the front. The temperature field in °C (dashed line) and zonal wind field in $\mathrm{m\,s^{-1}}$ (thin solid line) are shown [*Palmén and Newton*, 1948].

the boundaries of the front are shown. On both sides of the front, the temperature decreases with height, as would be expected in the troposphere. However, inside the frontal boundaries the temperature is almost constant with height. This is because the horizontal temperature gradient needs to be large to match the cold air on the left side to the warm air on the right. The very small vertical temperature gradient means that the air inside the front has a large static stability.

Frontal zones are associated with increased rainfall. A schematic view of warm and cold air movement and cloud formation near a cold front is shown in Figure 2.7. The movement shown is relative to the motion of the front. The air on the warm side moves along the front and rearward while it ascends as shown in Figure 2.8. Where the frontal surface is at ground level, there is typically a strong upward motion of around 5 $\mathrm{m\,s^{-1}}$. This reduces to less than 0.5 $\mathrm{m\,s^{-1}}$ as the air moves further up the front. Both of these regions of upward warm air movement produce increased precipitation. A band of heavy rain is associated with the vertical motion at the surface cold front and a large area of light to moderate rainfall spreads back from

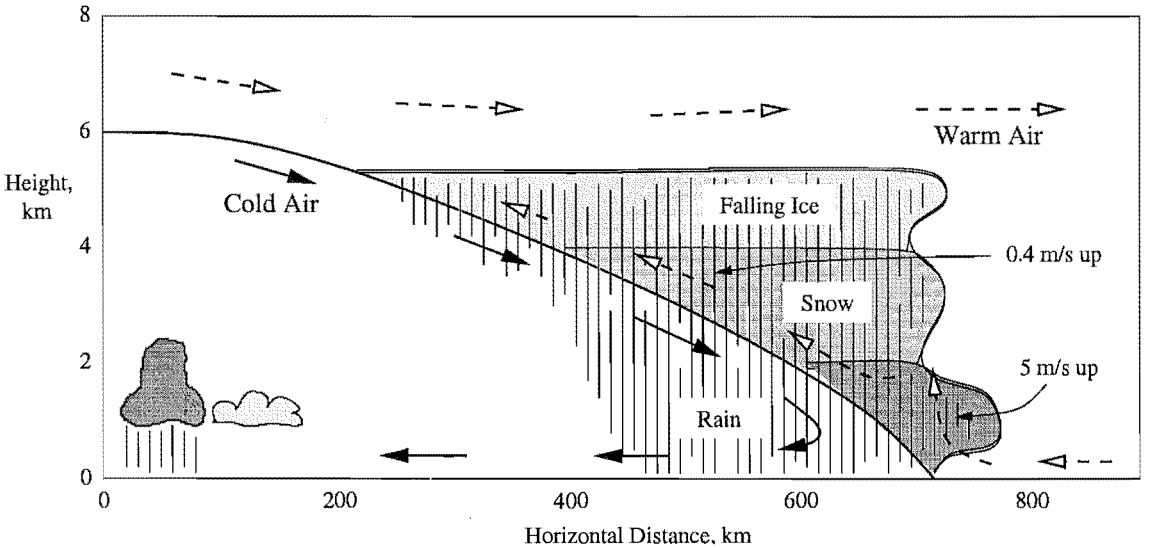

Figure 2.7: A schematic cross-sectional view of a cold front and its associated cloud formation and rainfall pattern [After *Keyser*, 1986].

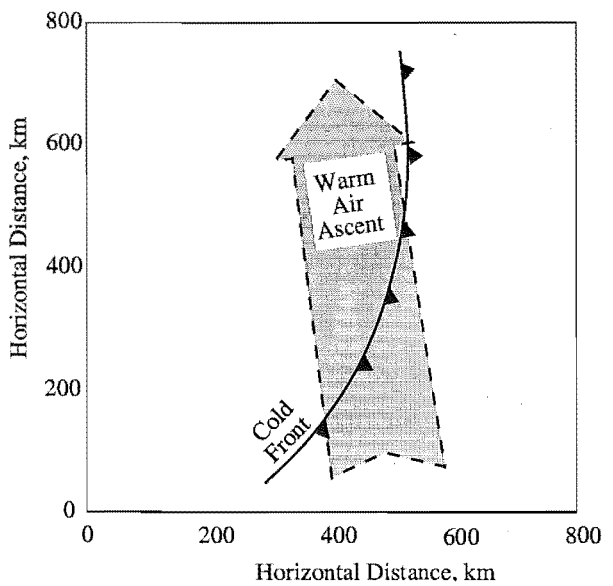

Figure 2.8: A plan view of a cold front showing the rearward warm air movement [*Browning*, 1990].

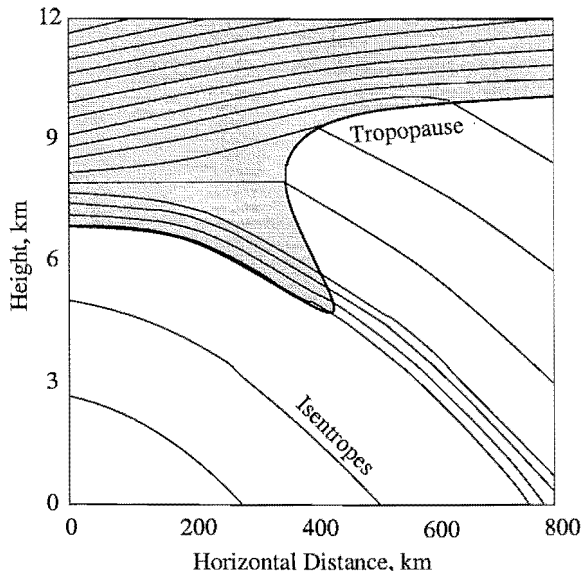

Figure 2.9: A schematic representation of a tropopause fold. The thick line represents the tropopause, the thin lines are isentropes and the shaded area is stratospheric air [After *Keyser*, 1986].

this point [*Browning*, 1990].

The increase in static stability and high precipitation rates associated with frontogenesis occur near the surface, in the lower 5 or 6 km of the troposphere. There are also upper-level effects, such as tropopause folding, that occur as a result of frontogenesis. Tropopause folding is a process in which a thin slice of stratospheric air is extruded into the mid-troposphere as a front strengthens [*Keyser*, 1986]. Figure 2.9 shows a well developed tropopause fold. The thin lines are isentropes, or lines of constant potential temperature, which are normally horizontal. Where the front is passing, the isentropes from the stratosphere extend down into the troposphere, which acts to bring stratospheric air down into the troposphere. This air will have a high static stability, depicted in the diagram by closely spaced isentropes.

2.1.5 Gravity Waves

Atmospheric gravity waves are ubiquitous throughout the atmosphere. They can occur from periods of a few minutes (limited by the Brunt-Väisälä frequency, ω_B; see Equation 2.6) up to several hours (limited by the inertial period; see Equation 2.1). For in-depth discussions on gravity waves, the reader is referred to *Hines* [1974] and

Scorer [1978].

Atmospheric gravity waves can exist only when the atmosphere is stably stratified so that an air parcel displaced vertically will undergo buoyancy oscillations. Of particular interest in the study of gravity waves is whether or not they can propagate vertically, as this is one of the main mechanisms used to transport energy and momentum through the atmosphere. To determine the conditions for vertical propagation, the vertical wavenumber, $m = 2\pi/\lambda_z$, can be used. It can be expressed using

$$m^2 = \frac{\omega_B^2}{(c-\overline{u})^2} - k^2 + \frac{1}{(c-\overline{u})}\frac{d^2\overline{u}}{dz^2}, \tag{2.8}$$

where c is the phase speed of the waves, $\overline{u}$ is the background wind and $k = 2\pi/\lambda_x$ is horizontal wavenumber [*Salby*, 1996]. When $m^2 > 0$, the gravity waves are internal and can propagate vertically, but when $m^2 < 0$, they are external (or evanescent) waves which decay exponentially in the vertical direction.

According to Equation 2.8, the vertical propagation of gravity waves is affected by a number of variables. If the horizontal wavelength is large or ω_B is large (i.e. large static stability) then vertical propagation is likely. This is also true if the horizontal wind speed is large or the wave speed is small. If m^2 approaches zero at a particular height then wave activity at this point will be fully reflected (except for evanescent waves which form along the exterior of the boundary) and this point is sometimes referred to as the *turning point* [e.g. *Salby*, 1996]. Waves below this point can also reflect up from the ground forming trapped waves that can propagate downwind (analagous to behaviour in a waveguide). If $c - \overline{u}$ decreases to zero ($m^2 \to \infty$) then the wave will be absorbed at this height, which is often labelled the *critical level*. *Scorer* [1978], who finds this label unhelpful and unspecific[2], suggests that at this height, the wave activity often breaks down into billow motion, e.g. rotors and "cat's eyes".

Atmospheric gravity waves tend to increase their amplitudes of oscillation with increasing height, compensating for the upward decrease of atmospheric density in order to keep their kinetic energy density constant [*Hines*, 1960]. At some point, due to their large amplitude, the waves become unstable and eventually break. This often leads to the dumping of large amounts of energy and momentum into the

[2]The term "critical level" is slightly misleading because when the "critical angle" is reached in optics, total internal reflection occurs, and this is synonymous to gravity wave reflection from a "turning point".

background flow.

Gravity waves can be generated by a number of mechanisms and orography is perhaps the most obvious source. When a stable air parcel is forced to rise over a barrier, for instance a mountain range, it becomes displaced from its equilibrium point. The restoring force that acts to return the parcel to its original position, causes the parcel to undergo oscillations. The mountain waves that are created contain the energy and momentum that is produced by the air passing over the obstruction [*Durran*, 1990]. Due to the stationary nature of the obstacle, the waves produced tend to be stationary and have zero phase speed. In this situation, because $c = 0$, Equation 2.8 can be rewritten in terms of the Scorer parameter, l, given by

$$l^2 = \frac{\omega_B^2}{\overline{u}^2} - \frac{1}{\overline{u}}\frac{d^2\overline{u}}{dz^2}. \tag{2.9}$$

In this case, the condition for vertical propagation is when $l^2 > k^2$ [*Holton*, 1992].

There are many mechanisms, other than flow over orography, that can produce gravity waves and *Fritts* [1993] gives a good review of these sources. Frontal systems and areas of strong convection can act as obstacles and so produce waves in the same way as orography. Convective cells can initiate wave motions in the planetary boundary layer which can produce gravity waves at larger scales. The dynamical instability of wind shear has also been shown to excite gravity waves.

2.2 Radar Scattering Mechanisms

All clear-air radar backscatter arises from irregularities in the radio refractive index of the air, which can be written as

$$n = 1 + \frac{3.73 \times 10^{-1} e}{T^2} + \frac{7.76 \times 10^{-5} p}{T} - \frac{N_e}{2.48 \times 10^{-2} f^2} \tag{2.10}$$

where e is the partial pressure of water vapour (mb), p is the atmospheric pressure (mb), T is the absolute temperature (K), N_e is the number density of free electrons (m^{-3}) and f is the frequency of the radio waves (Hz) [*Gage*, 1990]. The scattering arises from oscillations induced in the electrons, either bound or free, which are constituents of the medium.

The first term in Equation 2.10 arises from fluctuations in the bound electrons of water vapour. This dominates in the lower troposphere, below 5 km, where high humidity is common. The second term also arises from bound electron fluctuations, but these are in the dry air of the upper troposphere and stratosphere. The

third term, which is usually negligible below 50 km, contains the contribution from free electrons. This term dominates in the mesosphere where the electron density increases rapidly with height [*Woodman and Guillen*, 1974; *Balsley and Gage*, 1980].

The vertical gradient of the refractive index, often labelled M, is given by

$$M = -7.76 \times 10^{-5}(\frac{p}{T})(\frac{\partial \ln \theta}{\partial z})\left[1 + \frac{15,500q}{T}\left(1 - \frac{\frac{\partial \ln q}{\partial z}}{2\frac{\partial \ln \theta}{\partial z}}\right)\right], \qquad (2.11)$$

where p is the atmospheric pressure (mb), T is the absolute temperature, θ is the potential temperature and q is the specific humidity [*Vanzandt et al.*, 1978]. The second term in the square brackets is solely due to humidity and can be ignored above the first few kilometres of the atmosphere. M is a very important parameter when studying turbulence, fronts and regions of high static stability, such as the stratosphere, as it contains the term $\partial \ln \theta / \partial z$ which is directly related to atmospheric stability (see Equations 2.6 and 2.7).

2.2.1 Clear-Air Scattering

Clear-air echoes arise mainly from processes known as Fresnel reflection, Fresnel scatter and turbulent scatter. The relative importance of the different processes that cause clear-air scattering is still not completely understood. One of the major clues to the scattering mechanisms involved is the aspect sensitivity of the scatterers. If the scatterers were horizontally stratified, most of the reflections from a vertically pointing beam would come straight down and reflections from an off-vertical beam would not return to the transmission point (see Figure 2.10a). If the radar beam was incident on an area of what is called isotropic turbulence, then the direction of the beam would make no difference to the amount of backscatter (see Figure 2.10b). The actual radiation received in an off-vertical beam using a real radar is usually somewhat less than that in a vertical beam, but not zero.

There have been a number of mechanisms proposed to explain the aspect sensitivity of backscatter. Two of these, Fresnel reflection/scatter and anisotropic turbulent scatter, will be described here.

2.2.2 Fresnel Reflection/Scatter

Reflection of radio waves by a single stratified layer is called Fresnel reflection. When there are many of these layers in a scattering volume, the process is known as Fresnel scatter.

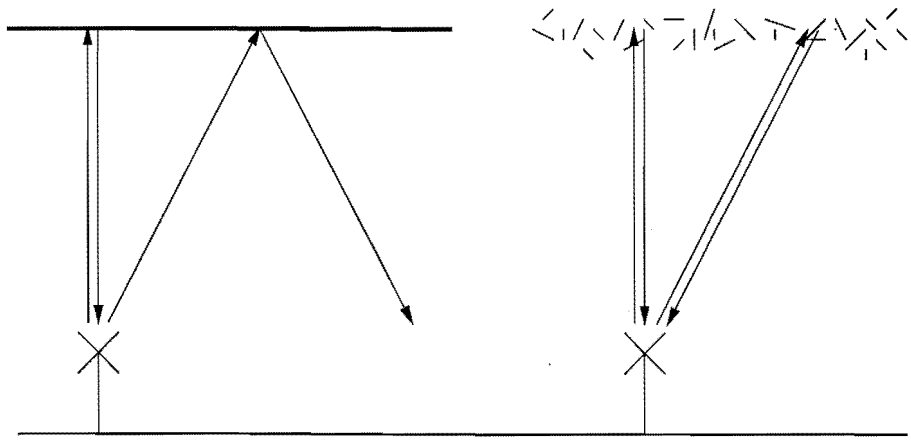

Figure 2.10: Radar scattering mechanisms: **(a)** reflection from a horizontally stratified region and **(b)** scattering from isotropic turbulence. In reality, the scattering is a mixture between these two processes.

Fresnel reflection, or specular reflection, occurs when there is a very steep vertical gradient or discontinuity in the refractive index [*Gage and Green*, 1978; *Röttger and Liu*, 1978]. This can stretch over a large horizontal area causing high aspect sensitivity. In most cases this will provide very strong returns from a vertically pointing beam, but little from off-vertical beams. However, if the gradient or discontinuity is wrinkled or rough, diffuse reflection occurs and this allows greater reflection from off-vertical beams.

Fresnel scatter occurs when there are many layers with steep vertical gradients in the refractive index in the same range resolution cell [*Gage and Balsley*, 1980; *Hocking and Röttger*, 1983; *Gage et al.*, 1985]. The layers are at random separation, so the reflected radio signal looks more like scatter than reflection. *Luce et al.* [1995, 2001] observed temperature sheets that would form steep vertical gradients using high resolution *in situ* temperature measurements.

Fresnel reflection/scatter is very aspect sensitive, and although the layers will on average be horizontal, on short time and length scales, they can be quite variable. By investigating the variation in echo power with azimuth angle, *Tsuda et al.* [1997a] found that a single sheet with a linear tilt could not explain their observations, which showed echo power varying over more than one cycle in 360° of azimuth angle. Their observations could only be explained by assuming a corrugated surface. In a high

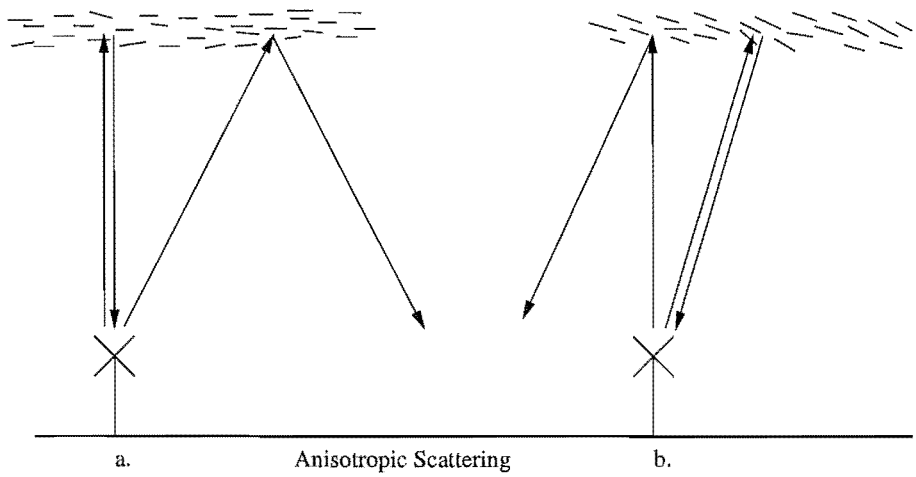

Figure 2.11: Anisotropic scatter: **(a)** scatterers aligned for maximum vertical reflection and **(b)** irregularities aligned off-vertical.

resolution study using 57 antenna pointing directions to measure the echo power distribution from 0° to 7° off zenith, *Worthington et al.* [2000] found that aspect sensitivity caused by specular layers varied on a timescale of minutes. Tilted layers have been studied in some detail and these are discussed along with tilted anisotropic scatters in the next section.

Both Fresnel reflection and scatter need to have layers that are spread over horizontal scales of the order of the Fresnel zone, given by

$$d = \sqrt{z\lambda}$$

where z is the height of the layer and λ is the radar wavelength.

2.2.3 Turbulent Scatter

Turbulent scattering, also known as Bragg scatter, was the first mechanism used to describe clear-air radar backscatter [*Booker and Gordon*, 1950]. Irregularities in the atmospheric refractive index caused by turbulence can reflect radar signals back to their source. There are two types of turbulent scatter; isotropic and anisotropic.

Turbulent scatter is isotropic when the refractive index irregularities are randomly orientated and statistically similar in all directions. This type of scatter has no aspect sensitivity, see Figure 2.10b.

Anisotropic scatter is aspect sensitive as shown in Figure 2.11. Instead of randomly orientated irregularities, they are aligned in one particular way more than

any other [*Doviak and Zrnić*, 1984; *Waterman et al.*, 1985]. Normally the scatterers are aligned so that radio waves are reflected predominantly in the vertical direction. *Hocking et al.* [1986] made aspect sensitivity measurements using the accurately calibrated SOUSY radar. They found that in the troposphere and lower stratosphere the scatterers were more aspect sensitive, and in the upper stratosphere the scatter became more isotropic.

It has also been shown that anisotropic scatterers and Fresnel layers can be tilted thereby destroying the specularity of echoes observed at vertical incidence. While on average the echo power is strongest for a vertically pointing beam, there are times when the maximum is at angles away from the zenith. This has been attributed by *Gage et al.* [1981a] and *Tsuda et al.* [1997b] to laminae (or Fresnel layers) following the motion of gravity waves, so that at times the laminae are tilted. *Worthington et al.* [1999] showed that a skewed power distribution pattern was often related to wind shear caused by gravity waves or jet streams and *Worthington* [2001] found that this asymmetry could be observed throughout the troposphere and lower stratosphere and may also extend over horizontal scales of thousands of kilometres. Tilted aspect-sensitive layers have been used by *Worthington* [1999] to calculate the orientation of mountain waves.

Understanding the extent of tilted aspect sensitivity is necessary when using radar to make wind measurements. It is thought that, by having an off-vertical incidence angle, the horizontal wind will contaminate the vertical wind velocity measurement. *Röttger et al.* [1990] showed that by using spatial interferometry to find absolute phases, the mean incidence angle of the radar beam could be evaluated and used to calculate the tilt angle of any aspect sensitive layers. *Briggs* [1992] used a similar technique to find the zenith angle dependence and azimuth angle dependence of radar backscatter.

Both Fresnel reflection/scatter and turbulent scattering are valid ways of describing radar backscatter and in fact *Hocking* [1987] has shown that specular reflectors and turbulence can coexist in close proximity.

2.2.4 Measuring Turbulence

Turbulence can be investigated using VHF radar, as its presence produces small-scale perturbations in the radio refractive index (see Equation 2.10). The refractive index structure constant C_n^2 is a measure of the variability of the refractive index

field. From C_n^2, the kinetic energy dissipation rate ϵ can be determined, and this gives an excellent measure of the intensity of atmospheric turbulence [*Gage et al.*, 1980; *Hocking*, 1985].

C_n^2 can be calculated from radar backscatter power as it is related to the volume reflectivity, η, by [*Ottersten*, 1969]:

$$\eta = 0.38\ C_n^2 \lambda^{1/3}. \tag{2.12}$$

Section 2.3.2, which derives the radar equation for distributed targets, shows how η is related to backscattered power.

C_n^2 by itself is a rather crude indicator of the intensity of turbulence. A more useful parameter is ϵ, the energy dissipation rate, which can be deduced from the structure constant using the relation

$$\epsilon = \left(\gamma C_n^2 \frac{\omega_B^2}{F^{1/3}} M^{-2}\right)^{3/2}, \tag{2.13}$$

where γ is a constant, ω_B is the Brunt-Väisälä frequency, M is the vertical gradient in the refractive index and F is the filling factor which represents the fraction of the radar volume that consists of turbulence. There have been many suggestions for values for γ and F and *Hocking and Mu* [1997] cover these in some depth.

Another measure of turbulence is the spectral width or Doppler frequency spread of a received radar signal [*Sato and Woodman*, 1982]. In areas of turbulence, the mean square velocity fluctuation, $\overline{v^2}$, of scatterers is increased and this is related to the spectral width, W_t, of backscattered signal by the relation

$$\overline{v^2} = \frac{\lambda^2 W_t^2}{4}. \tag{2.14}$$

$\overline{v^2}$ can then be used to calculate the energy dissipation rate using

$$\epsilon \simeq 0.4\ \overline{v^2} \omega_B, \tag{2.15}$$

where ω_B is the Brunt-Väisälä frequency [*Hocking*, 1985].

There are other processes which also increase the spectral width, e.g. beam-broadening and shear-broadening, which need to be accounted for before accurate energy dissipation rates can be obtained [*Hocking*, 1983; *Nastrom*, 1997].

Beam-broadening occurs due to the finite angular width of the antenna beam. When a vertical beam is in the path of horizontal air movement, there should be no

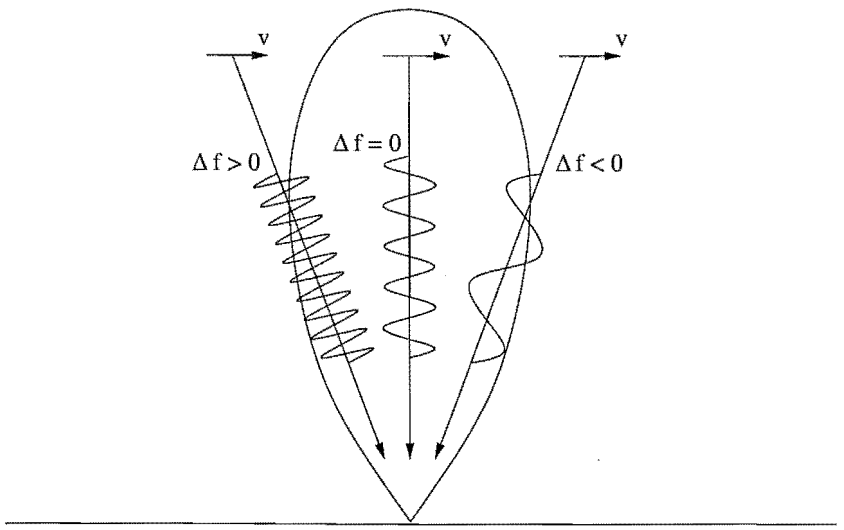

Figure 2.12: Beam broadening and its effect on returned radar signals [*Hocking*, 1983].

Doppler shift in the returned radar signal. However, because the edges of the beam are not vertical, a component of the horizontal wind will be perpendicular to the radio-wave propagation direction and will produce a frequency shifted signal in these regions (see Figure 2.12). Where the air is travelling toward the beam, the frequency will be increased, and where it is moving away, the frequency will be decreased. The outcome of this is an increase in the width of the resulting atmospheric spectral peak.

The increase in spectral width due to beam-broadening is directly proportional to the horizontal velocity, v, of the wind. The one standard deviation width of a spectrum, which is broadened solely by beam-broadening, is given by

$$W_v = 0.30\ \theta_{\mathrm{FW}} v, \tag{2.16}$$

where θ_{FW} is the half-power full-width of the antenna (which is assumed to be used for both transmission and reception) [*Hocking*, 1985].

For antenna beams that point in off-zenith directions, shear-broadening must also be taken into account. This effect is caused by signals in the same range bin reflecting from different altitudes, which due to shear may have different horizontal velocities.

Once these non-turbulent broadening effects have been found and the actual spectral width of the atmospheric signal, W, has been calculated (see Section 5.2.4),

the spectral width due to turbulence, W_t, can be obtained using the relation

$$W_t^2 = W^2 - W_v^2. \tag{2.17}$$

Equations 2.14 and 2.15 can then be used to calculate the energy dissipation rate.

A comparison between the two methods of measuring ϵ outlined in this section was performed by *Furumoto and Tsuda* [2001] using the MU radar and high resolution RASS[3] measurements. They found that calculations of ϵ from echo intensity measurements were less reliable than those from spectral width measurements due to the large effect humidity has on the refractive index gradient. However, their measurements were performed during calm conditions, when non-turbulent effects on the spectral width are less important.

2.3 The Radar Equation

Of prime importance when designing a radar is the amount of power received compared with the power transmitted. This information is contained in the radar equation. *Sato* [1989] gives a good summary of the basic derivation of this equation.

2.3.1 The Radar Equation for a Hard Target

The radar equation is in its simplest form when the scatter arises from a single hard target. During transmission, the power density, S_i, incident on an object perpendicular to the direction of propagation is given as

$$S_i = \frac{P_t G_t L_t}{4\pi r^2}, \tag{2.18}$$

where P_t is the radiated power, G_t is the gain[4] (including ohmic losses) of the antenna array, r is the range from the transmitter array and L_t is a loss factor representing the attenuation in the signal path from the transmitter to the antenna.

The power incident on the hard target is assumed to scatter isotropically. The scattered power density, S_s, at a range r' from the scatterer will be

$$S_s = \frac{S_i \sigma}{4\pi r'^2}, \tag{2.19}$$

[3]RASS (radio acoustic sounding system) is a remote-sensing technique for observing a temperature profile in the troposphere and lower stratosphere with good temporal and height resolutions.

[4]Definitions for gain and effective aperture, A_e, are given in Section 3.1.1.

where σ is the effective area of the scatterer as observed by the radar. The power, P_r, received by the radar, assuming it has an effective collecting area of A_e is given by

$$P_r = S_s A_e L_r, \tag{2.20}$$

where L_r is a loss factor taking into account the attenuation in the signal path from the antenna to the receiver. By combining Equations 2.18, 2.19 and 2.20 the radar equation is obtained.

$$P_r = \frac{P_t G_t A_e L \sigma}{(4\pi r^2)(4\pi r'^2)}, \tag{2.21}$$

where $L = L_t L_r$.

For a monostatic radar, that is one with co-located transmitting and receiving antennas, G_t and A_e are linked by the relation

$$G_t = \frac{4\pi A_e}{\lambda^2}, \tag{2.22}$$

where λ is the radar wavelength. In this case Equation 2.21 becomes

$$P_r = \frac{P_t A_e^2 L \sigma}{4\pi \lambda^2 r^4} \tag{2.23}$$

where $r' = r$ as the transmitting antenna is the same distance from the scatterer as the receiving antenna.

2.3.2 The Radar Equation for Distributed Targets

If there is more than one target in the scattering volume, the electric field received by the radar will be the sum of the fields scattered by the individual targets. In this case σ in Equation 2.23 should be replaced with $\Sigma\sigma$. However, if the number of these scatterers is large and isotropically distributed, it is more convenient to use the volume reflectivity η, which is defined as

$$\eta \equiv \frac{d\sigma}{dV}. \tag{2.24}$$

The process of obtaining an expression for the power scattered from uniformly distributed scatterers is the same as that for power scattered from fluctuations in the refractive index, or turbulence and is described well by *Flood* [1968]. The power backscattered from the region shown in Figure 2.13 is given by

$$P_s = \frac{k_0^4 P_i}{4\pi^2 R_0^2} \left| \int_V \Delta n \exp\left[i2\mathbf{k} \cdot \mathbf{r}\right] dV \right|^2. \tag{2.25}$$

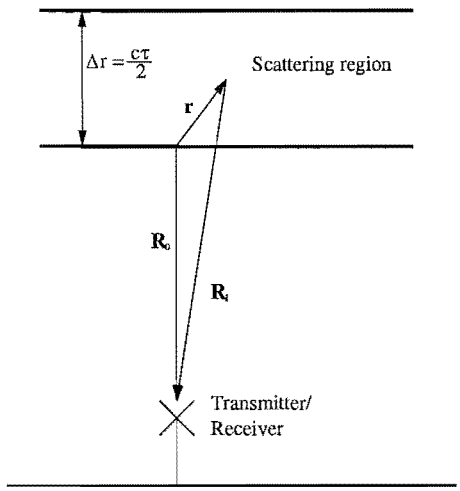

Figure 2.13: The geometry of radar backscatter, showing the scattering volume which is dependent on the radar pulse width, τ.

where $k_0 = \frac{2\pi}{\lambda}$, R_0 is the distance to the scattering region, Δn is the small fluctuations in the refractive index and $\mathbf{k}$ is the propagation vector and can be written as

$$\mathbf{k} = k_0 n \hat{\mathbf{k}}, \tag{2.26}$$

where $\hat{\mathbf{k}}$ is a unit vector in the direction of propagation and n is the complex refractive index.

By comparing Equation 2.25 with Equation 2.19, an expression for σ is obtained

$$\sigma = \frac{k_0^4}{\pi} \left| \int_V \Delta n \exp\left[-i2\mathbf{k_i} \cdot \mathbf{r}\right] dV \right|^2, \tag{2.27}$$

and from Equation 2.24

$$\eta = \frac{k_0^4}{\pi V} \langle \left| \int_V \Delta n \exp\left[-i2\mathbf{k_i} \cdot \mathbf{r}\right] dV \right|^2 \rangle, \tag{2.28}$$

where $\langle\rangle$ denotes an ensemble average.

V in the above equation depends on the half-power full-width θ_{FW} of the antenna beam and the range cell Δr as

$$V = \pi \left(\frac{r\theta_{\mathrm{FW}}}{2} \right)^2 \Delta r. \tag{2.29}$$

The beam width is directly related to the effective aperture of the antenna by the relation

$$\theta_{\mathrm{FW}} \simeq \frac{\lambda}{\sqrt{A_e}} \tag{2.30}$$

(see Section 3.1.1).

Using the above equations in a similar process to that used for the single hard target, the radar equation for distributed targets can now be written as

$$P_r = \frac{P_t A_e \pi \Delta r L}{64 r^2} \eta, \tag{2.31}$$

where L is a loss factor. This equation reveals that the received power falls off as r^2 rather than r^4, as it does for a hard target. However, the Δr term means that if the range resolution of the radar is increased, then received power will decrease, and this has a major effect on the design considerations of the radar (see Section 3.4).

If the radar is properly calibrated, Equation 2.31 can be used along with Equation 2.12 to calculate the structure constant, C_n^2. In homogeneous, isotropic turbulence, the structure constant is given by

$$C_n^2 = a^2 L_0^{\frac{4}{3}} M^2, \tag{2.32}$$

where L_0 is the scale length of the turbulence spectrum, a^2 is a constant, which can be between 1.8 and 2.8 depending on the definition of L_0, and M is the vertical gradient of the refractive index [*Gage and Balsley*, 1980]. It follows from Equations 2.12, 2.31 and 2.32, that for turbulent scatter P_r can be approximated by

$$P_r \propto \frac{M^2}{r^2}, \tag{2.33}$$

which is an important result implying that above the first few kilometres of the atmosphere, received power is closely related to static stability (see Equation 2.11).

2.3.3 Specular Echoes

The radar equation for Fresnel reflection has a much simpler derivation than the previous radar equations. As long as the Fresnel layer is larger than the radar beam width, it acts like a mirror with a small reflectivity, ρ. The receiving antenna will therefore be a mirror image located $2r$ from the transmitting antenna and the received power will be

$$\begin{aligned} P_r &= \frac{P_t G_t}{4\pi(2r)^2} A_e L |\rho|^2 \\ &= \frac{P_t A_e^2 L}{4\lambda^2 r^2} |\rho|^2. \end{aligned} \tag{2.34}$$

$|\rho|^2$ can be thought of as a power loss factor arising from the imperfect reflectivity of the Fresnel layer.

The above equation only holds true if the beam direction is perpendicular to the surface of the layer. As soon as the antenna (or layer) is tilted, the power will decrease, quite dramatically if the beam width is small. This feature makes these layers aspect sensitive.

Gage et al. [1981b] derived an expression for $|\rho|^2$ in regions of Fresnel scatter, showing how it depends on the half-wavelength harmonic component of M, the gradient in the refractive index. By assuming that this component is proportional to the mean value of M, they formed the expression

$$|\rho|^2 = (\Delta r)^2 \frac{F(\lambda)^2}{16} \overline{M}^2, \tag{2.35}$$

where Δr is the range resolution defined by the pulse width and $F(\lambda)^2$ is the proportion of M that makes up the half-wavelength harmonic component. This result shows that P_r is again proportional to M^2/r^2, as it was for turbulent scatter.

The above relation for $|\rho|^2$ means that it is difficult to use signal power as a measure of turbulence, as M is increased by not only turbulent scatter, but also by Fresnel scatter. However, because Fresnel scatter is strongly aspect sensitive, it is possible to severely reduce the amount of Fresnel scatter by using off-vertical beams and thereby reducing the impact on M.

None of the three radar equations detailed in this section represents exactly what happens to a radar pulse in the atmosphere. The real atmosphere is much more complicated than any of these situations and a more accurate radar equation would probably be a mixture of these cases. The equations are also only valid in the far field, where radiation from the antenna appears to be coming from a point source. One definition for the far field is

$$R = 2l^2/\lambda, \tag{2.36}$$

where l is the maximum dimension of the antenna. For the CUSTAR antenna this distance is just under 900 metres.

2.4 Measuring Wind Velocities

Measuring atmospheric winds is a major part of radar use and to achieve this more information than just the received power is required. In this section, some of the techniques used to measure atmospheric motion will be discussed.

2.4.1 The Doppler Method

The Doppler method involves measuring the frequency shift of a returned radar signal and from that deducing the velocity of the air from which it was reflected. A very directional beam is needed so that the backscattered signal is incident from one direction. The Doppler frequency shift, f_d, of echoes from a moving target relative to the radar is

$$f_d = \frac{2}{\lambda} v_d, \tag{2.37}$$

where λ is the radar wavelength and v_d is the velocity component of the target along the radar beam.

For a line-of-sight target velocity of around 3 $\mathrm{m\,s^{-1}}$, a typical f_d for a VHF radar is around 1 Hz. It is very difficult to directly detect such a small frequency shift, but it can be calculated from the phase difference $\Delta\phi$ between two successive pulses. This is given by

$$\Delta\phi = 2\pi f_d T_{\mathrm{IPP}} = \frac{4\pi T_{\mathrm{IPP}}}{\lambda} v_d, \tag{2.38}$$

where T_{IPP} is the inter-pulse period.

When the antenna beam is pointing in the vertical direction, the Doppler method can only be used to find the vertical velocity of the air. This information, however, is very useful and can be used to study atmospheric phenomena such as gravity waves. At this stage the Canterbury University radar operates in only this mode.

2.4.2 Doppler Beam-Swing Method

To obtain a three dimensional wind velocity using Doppler frequency shifts, the beam of the radar must be steerable in at least three directions. In each of these directions, the velocity component is deduced and the final velocity vector can be calculated. This method assumes that the velocity is uniform over the horizontal space spanned by the off-vertical beams. As long as the beams have a small zenith angle (a usual beam angle is around 10° off vertical) this is approximately true.

The need to have a steerable beam makes this method quite difficult to implement. The normal way to steer an antenna is to introduce a progressive phase change across the array. To do this, each antenna element needs to have the option of switching between two or more different lengths of cable.

Often wind-profiling radars have five beam directions, one vertical and one in each of the four cardinal directions. Some large radars such as the MU radar [*Fukao*

et al., 1985] have many more beam directions, allowing for more diverse experiments to be performed.

2.4.3 Spaced Antenna Method

To obtain a full wind velocity vector without a steerable beam, the spaced antenna method can be used. It requires at least three receiving antennas, which are usually separate from the transmitting antenna, and uses a technique called full correlation analysis. The wind velocity can be determined by studying the motion of a diffraction "pattern" as it moves over the separated antennas. The pattern is formed from irregularities and gradients in the atmosphere's radio refractive index and is assumed to be nearly constant during its passage over the radar site. By comparing the three signals received by the antennas it is possible to deduce the speed and direction of the moving pattern and therefore the wind velocity. *Briggs* [1984] gives an excellent summary of this technique.

2.5 Interstellar Meteors

In addition to atmospheric probing, the ST radar can also be used to detect meteoric ionisation.

In the design and construction of the CUSTAR system, work was carried out on the application of the vertically pointing antenna array (see Chapter 3) to measure the meteoric plasma generated by meteoroids incident on the atmosphere with small zenith angles. This additional capability will complement an associated research project (interstellar dust detection by radar) operated by the University of Canterbury, Physics and Astronomy Department [*Baggaley and Galligan*, 2001].

That project employs the transverse geometry technique using AMOR (Advanced Meteor Orbit Radar), which is a phase coherent system operating at 26 MHz [*Baggaley et al.*, 1994]. AMOR uses spaced stations to receive specular echoes from meteoric ionisation trails, which must be orthogonal to the reflecting radar pulse. The condition of orthogonality allows time-of-flight velocity components and a measurement of the plasma elevation to be obtained from the spaced receiving stations. The provision of three components of the atmospheric trajectory of the ablating meteor yields the sun-centred velocity and hence solar system orbits of the meteoroid.

A single station arrangement is able to provide the same dynamical information

by employing radial scattering (rather than transverse scattering). An ablating meteoroid generates a plasma column consisting of electrons and positive atomic ions of meteoric species (Mg, Fe, Ca, Na). The length of the column is about one atmospheric scale height (see Equation 5.19) and its radius is several mean free paths ($\sim$ 1 m). In addition, a spherical distribution of plasma is generated in the immediate vicinity of the meteoroid. Whereas radar reflection from the kilometres-long ionisation column (the body echo) is highly aspect sensitive, scattering from the plasma ball (the head echo) is nearly isotropic, though having a scattering cross-section which is $\sim 10^3$ less than the transverse case [*Baggaley*, 2002].

The plasma ball travelling at the same speed as the meteoroid will produce echoes with a rapid change of phase accompanied by decreasing range. The aspect angle to the antenna beam axis can be estimated by measuring the number of range bin crossings and a good measurement of the meteoroid speed ($\sim$ 0.2% accuracy, which is a factor of 10 better than the AMOR transverse technique) and deceleration can also be obtained. Knowledge of the approximate line-of-sight speed from range changes can be used to "fine tune" the velocity inferred from pulse to pulse phase changes (note that the plasma target will traverse many wavelengths between radar pulses).

The resulting pre-atmospheric speed and celestial coordinates allows for calculation of the heliocentric velocity components and orbit. During the course of a day and also season, the zenith-pointing beam can sample different celestial directions. This technique has been employed by *Elford* [1999], and also by *Mathews et al.* [1999] in attempts to detect meteors of interstellar origin (by the properties of their solar-hyperbolic orbits).

The present contribution is to provide a platform for the detection of interstellar meteoroids as an adjunct to the programme already in operation in the Physics and Astronomy Department. The specific aim is to calibrate the antenna beam (see Chapter 4) and provide the capability of sampling ranges between 80 and 110 km (see Section 3.4.3).

Chapter 3

Design of the Canterbury University ST Radar

This chapter contains the practical design of the Canterbury University Stratosphere-Troposphere Atmospheric Radar (CUSTAR), which is located at the Birdlings Flat Upper Atmosphere Research Station and has geographical coordinates of 43° 49.5′ S, 172° 41.5′ E. The design of the antenna array is covered first, beginning with a discussion of antenna theory. The next section describes the electronic hardware. This includes the transmit-receive switch, the transmitter, the receiver and the analogue to digital converter. The last section covers the typical operational details of the radar.

3.1 Antenna Theory

Before discussing the specific design of the antenna array for the Canterbury University radar, it is advantageous to cover some principles of antenna theory. More detailed discussions can be found in *Kraus* [1988] and *Wolff* [1966]. An antenna is a device that radiates (or receives) energy. Its purpose is to provide a transition between a guided radio-frequency (R.F.) wave and a free-space R.F. wave.

For the moment consider the antenna in circuit terms as a device with a pair of terminals to which a generator is connected. The device presents an impedance Z to the generator where $Z = R + jX$. R may be thought of in two parts,

$$R = R_r + R_d, \tag{3.1}$$

R_r being the radiation resistance and R_d the ohmic loss resistance which is taken to be negligible so that $R \approx R_r$. When a current flows in the antenna, radiation occurs and thus energy is lost to the system, represented in current terms by R_r. The reactance is inevitable in an object large enough to radiate at the frequency concerned, but can usually be made small by adjusting the dimension of the radiator.

In reception, an antenna acts in the reverse way. R.F. waves passing the antenna induce emfs in the antenna and, supposing a "load" impedance has been connected

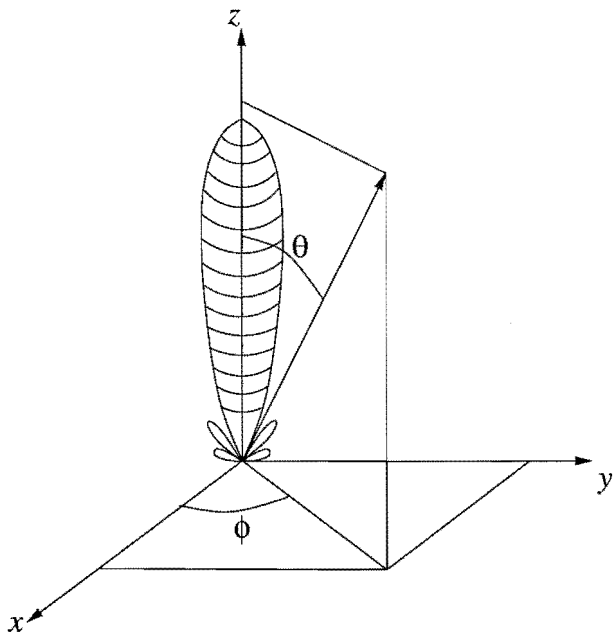

Figure 3.1: Coordinate system used for antenna field pattern calculations.

to its terminals, will deliver power to the load. The antenna behaves as a linear generator with the impedance Z described above. In the absence of some specific signal in the frequency range being considered, the power delivered may be expressed as

$$P = kT_A\Delta f, \tag{3.2}$$

where k is Boltzmann's constant, Δf is the bandwidth and T_A is the antenna temperature. This is the power that would be detected if the antenna was receiving only black body radiation of temperature, T_A. In practice, T_A is usually affected by the presence of radiating bodies such as the sun and stars in the direction of the antenna's beam (see Chapter 4).

An antenna can also be characterised by its radiation pattern which describes how the field intensity varies in different spatial directions around the antenna. The field pattern needs to be observed from a distance and comparisons between field intensities in different directions should be made at the same distance. This distance needs to be in the far field where the radiation appears to be coming from a point source (see Section 2.3.3).

Figure 3.1 shows a field pattern and its coordinate system. To evaluate the strength of the electric field, both its θ and ϕ components, $E_\theta(\theta,\phi)$ and $E_\phi(\theta,\phi)$,

are needed. From these components, the Poynting vector, $S(\theta, \phi)$, or power per unit area, is given by

$$S(\theta, \phi) = \frac{E_\theta^2(\theta, \phi) + E_\phi^2(\theta, \phi)}{Z_0}, \tag{3.3}$$

where Z_0 ($= 376.7\ \Omega$) is the intrinsic impedance of free space. The normalized power pattern with a maximum value of unity is then

$$P_n(\theta, \phi) = \frac{S(\theta, \phi)}{S(\theta, \phi)_{\max}}. \tag{3.4}$$

3.1.1 Field Pattern Parameters

Most antenna patterns are not uniform, having regions of high electric field and regions of no electric field. These are called lobes and nulls, respectively. Usually there is one major lobe, called the main beam, and numerous smaller ones called side-lobes. A measure of the size of the main lobe is its full-width at half-maximum (FWHM), or angle between the half power points of the beam. The beam-width between first nulls (BWFN) is also used.

The size of the main lobe can be most accurately defined by calculating the angular area it covers, that is, its solid angle[1], Ω_A. This quantity is derived by integrating the normalized power pattern (Equation 3.4)

$$\Omega_A = \int_0^{2\pi} \int_0^{\pi} P_n(\theta, \phi)\, d\Omega, \tag{3.5}$$

where $d\Omega = \sin\theta\, d\theta\, d\phi$. A very good approximation can be obtained using the FWHM in the two planes, θ_{FW} and ϕ_{FW},

$$\Omega_A \simeq \theta_{\text{FW}} \phi_{\text{FW}}. \tag{3.6}$$

The beam solid angle is closely related to the directivity, D. This is the ratio of the maximum radiation intensity to the average radiation intensity and is given by

$$D = \frac{4\pi}{\Omega_A}. \tag{3.7}$$

In other words, if the beam is highly directive, it will have a small beam solid angle.

The gain of an antenna is the ratio of its maximum radiation intensity to the maximum radiation intensity of a reference antenna. When an isotropic antenna is used as the reference, the antenna's gain is identical to its directivity except for

[1]A solid angle is measured in steradians (sr) and there are 4π sr in a sphere.

ohmic losses (k) which reduce its efficiency ($G = kD$). Gain is normally measured in decibels (dB), with a third letter to specify what reference antenna is being used; for example, dBi for an isotropic antenna, or dBd for a simple dipole. Unless otherwise noted, gain is usually measured with respect to an isotropic antenna.

The effective aperture, A_e, of an antenna is directly related to its gain by the relation

$$G = \frac{4\pi A_e}{\lambda^2}, \tag{3.8}$$

where λ is the radar wavelength.

3.1.2 Dipole Radiation Pattern

An electric dipole is a linear conductor often with a source connected at its centre. Its geometry is shown in Figure 3.2a. Unlike an isotropic point source which has a field pattern that is the same in all directions (and is only a theoretical abstraction), the dipole has directions of higher radiation and directions of no radiation. This is because from a distant point, p, as in Figure 3.2a, the radiation arriving from different points on the dipole will not necessarily be in phase. When $\beta = 90°$, all the radiation will be in phase and the field strength will be at a maximum. When $\beta = 0°$ and 180°, the field strength is zero.

For a half-wavelength dipole, which has a length of $L = \lambda/2$, the field pattern is given by

$$E_{dipole} = \frac{\cos[(\pi/2)\cos\beta]}{\sin\beta}. \tag{3.9}$$

This gives a "dough-nut" shaped pattern as shown in Figure 3.2b.

3.1.3 Array Theory

This section describes the theory needed to calculate the radiation pattern of a two-dimensional array of sources.

When two or more dipoles, or other types of antenna, are connected together as an array, the radiation pattern alters accordingly. The simplest case of two isotropic point sources separated by a distance, d, is analogous to Young's double slit experiment [*Young*, 1807]. The radiation pattern in this case can be expressed as

$$E = E_0(e^{j\psi/2} + e^{-j\psi/2}) = 2E_0\cos\frac{\psi}{2}, \tag{3.10}$$

where the phase difference, $\psi = \frac{2\pi d}{\lambda}\cos\phi$, is obtained from Figure 3.3. Relative

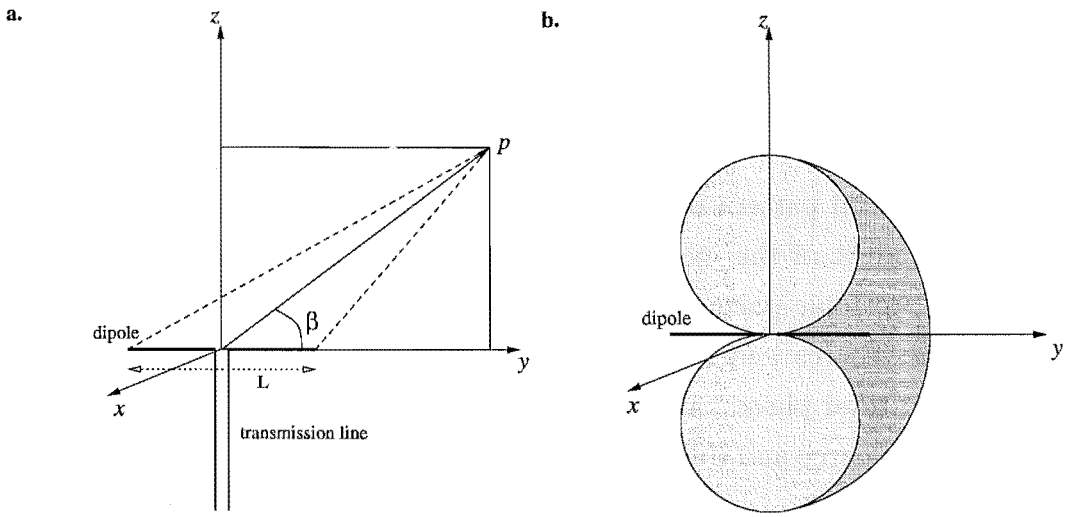

Figure 3.2: **(a)** The coordinate system used for dipole field pattern calculations, showing a dipole and transmission line connected at its centre and **(b)** the doughnut shaped radiation pattern associated with the dipole.

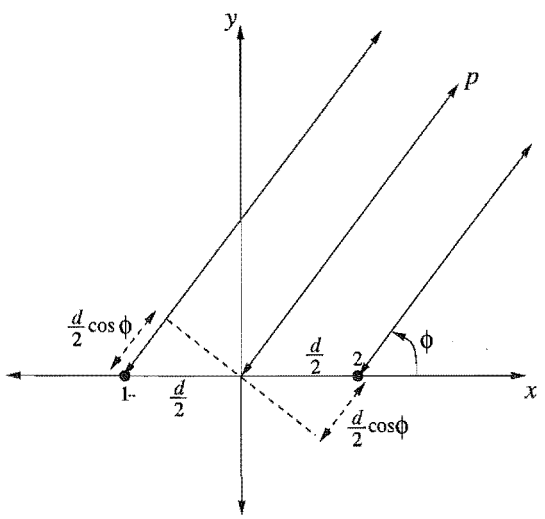

Figure 3.3: At a distant point, p, there may be a phase difference between the radiation from two isotropic point sources dependent on the angle ϕ.

to the origin, radiation from source 1 has traveled an extra $\frac{d}{2}\cos\phi$ (giving a phase difference of $\frac{2\pi}{\lambda}\frac{d}{2}\cos\phi$) and from source 2 it has been retarded by the same amount.

Equation 3.10 can be extended to include any type of source using the following definition known as pattern multiplication:

> The total field pattern of an array of non-isotropic but similar sources is the product of the individual source pattern and the pattern of an array of isotropic point sources each located at the phase centre of the individual source and having the same relative amplitude and phase, while the total phase pattern is the sum of the phase patterns of the individual source and the array of isotropic point sources.

This relation can be used for a one-dimensional array of many sources and also for a two-dimensional array such as that used in this project.

The next step in this process is to find the field pattern of a one-dimensional array of isotropic point sources. If the first source in Figure 3.4 is taken as the origin, or phase reference, then the phase difference of the radiation coming from each source is $\psi = \frac{2\pi}{\lambda}d_1\cos\beta$. The field pattern for N sources then becomes

$$\begin{aligned} E_{1D} &= E_0(1 + e^{jkd_1\cos\beta} + e^{j2kd_1\cos\beta} + \cdots + e^{j(N-1)kd_1\cos\beta}) \\ &= E_0\sum_{n=0}^{N-1} e^{jnkd_1\cos\beta}. \end{aligned} \tag{3.11}$$

where $k = \frac{2\pi}{\lambda}$ and E_0 is the scalar field for one source which for a normalized field pattern can be taken as unity.

Figure 3.5 shows a two-dimensional or planar array. The sources along the y-axis can be described by Equation 3.11 and the rows of sources in the x-direction can be treated as individual sources with radiation patterns also given by Equation 3.11. Therefore

$$E_{2D} = E_{1D}\sum_{m=0}^{M-1} e^{jmkd_2\cos\alpha}, \tag{3.12}$$

for an array with M sources on the x-axis. In spherical coordinates (θ, ϕ),

$$\begin{aligned} \cos\beta &= \sin\theta\sin\phi \\ \text{and}\quad \cos\alpha &= \sin\theta\cos\phi. \end{aligned} \tag{3.13}$$

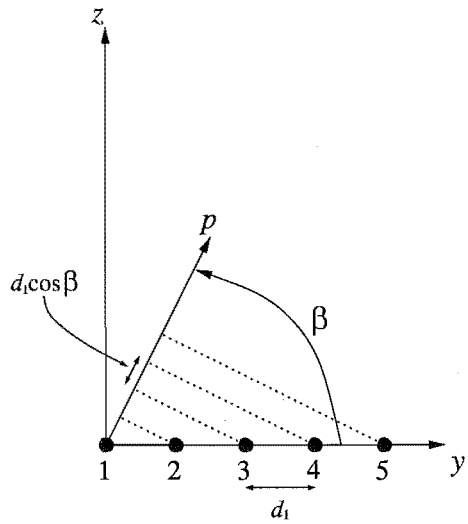

Figure 3.4: A linear array of point sources showing the phase differences observed from point, p.

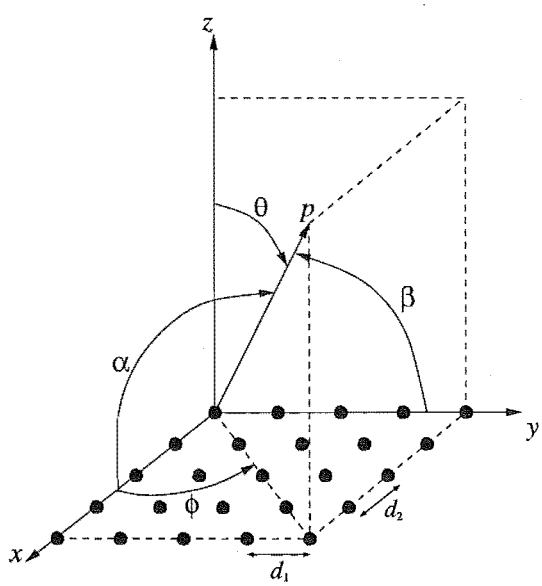

Figure 3.5: A planar array of point sources.

If the sources are spaced equally in both directions ($d_1 = d_2$) and E_0 is taken to be unity, Equation 3.12 becomes

$$E_{2D} = \sum_{n=0}^{N-1} \sum_{m=0}^{M-1} e^{jkd(n \sin\theta \sin\phi + m \sin\theta \cos\phi)}. \tag{3.14}$$

For an array with non-isotropic sources, the field pattern can be found by multiplying Equation 3.14 by the field pattern of the individual non-isotropic sources.

3.1.4 Yagi-Uda Antennas

A common way of increasing the gain of an antenna without using more than one source (as discussed in the previous sections) is to use a Yagi-Uda, or Yagi, antenna. This is an antenna with one driven element, or dipole, and one or more parasitic elements which obtain their power through coupling with the driven element. The length of the parasitic elements and their spacing from the driven element affect the field pattern of the antenna.

Yagi-Uda antennas can be used as the individual elements of an array to lessen the interaction between the antenna and the ground. This is very important, especially when the ground plane is sloped or uneven. However, when the array is large, the increase in directivity obtained when using Yagi-Uda antennas is limited as the total field pattern is dominated by the array factor rather than the pattern of the individual sources.

3.2 The Antenna Array

To achieve accurate wind measurements, a wind-profiling radar needs to transmit a very narrow and precisely directed beam. At frequencies in the VHF range, a frequently used basis for this is a large array of aerials all transmitting in phase. All the aerials, either single dipoles or Yagi-Uda antennas, add together to form a thin beam pointing vertically. This design used for the CUSTAR antenna array was orginally put forward by *Bennett* [1992] and has been developed by *Dunford* [1998].

3.2.1 Antenna Design Philosophy

The CUSTAR antenna array has been designed to maximize gain and directivity while minimizing side-lobes and the overall cost. It was decided that it would be

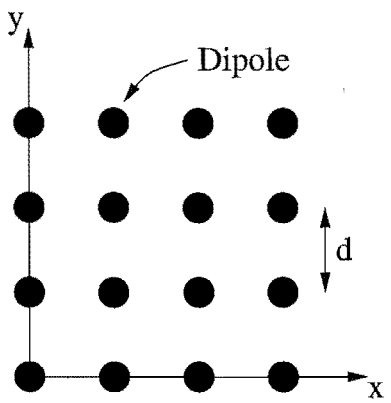

Figure 3.6: The layout of a typical antenna array.

easiest and most economical to make the individual elements and feed lines out of copper wire. This means that the elements need to be separated by exactly half or one wavelength to keep the open wire feed lines taut and the feed points all in phase. An excellent way to achieve a high directivity with the above constraint, is to space the individual sources by 0.707 λ, but arrange the feed lines so that they are diagonal to this spacing.

To achieve maximum directivity, the sources of an array need to cover a large area. The optimum design for this array would be to cover the area with elements all spaced by half a wavelength. However, by using fewer elements, the array will be less expensive to build. Therefore it would be advantageous to space the sources further apart, reducing the number, but still covering the same large area.

Figure 3.7 is a diagram of the antenna pattern of a square array (see Figure 3.6) showing the power of the antenna against zenith angle in a plane perpendicular (or parallel) to the rows of elements. The pattern is calculated using Equation 3.14 setting both N and M to 8. Figure 3.7a shows the antenna pattern for an antenna with an element spacing of half a wavelength. Here the maximum power is directed vertically with the side-lobes tapering off so that there are minimal ground-lobes. Figure 3.7b shows the antenna pattern obtained using an element spacing of one wavelength. Here the power comes to a maximum not only in the vertical direction, but also in the ground plane. This is very disadvantageous for an ST radar as a large proportion of noise comes from ground clutter, i.e. radar signal reflecting off nearby orography. Figure 3.7c is for an element spacing of 0.707 λ, showing a small increase in radar power at right angles to the zenith, but still significantly less than

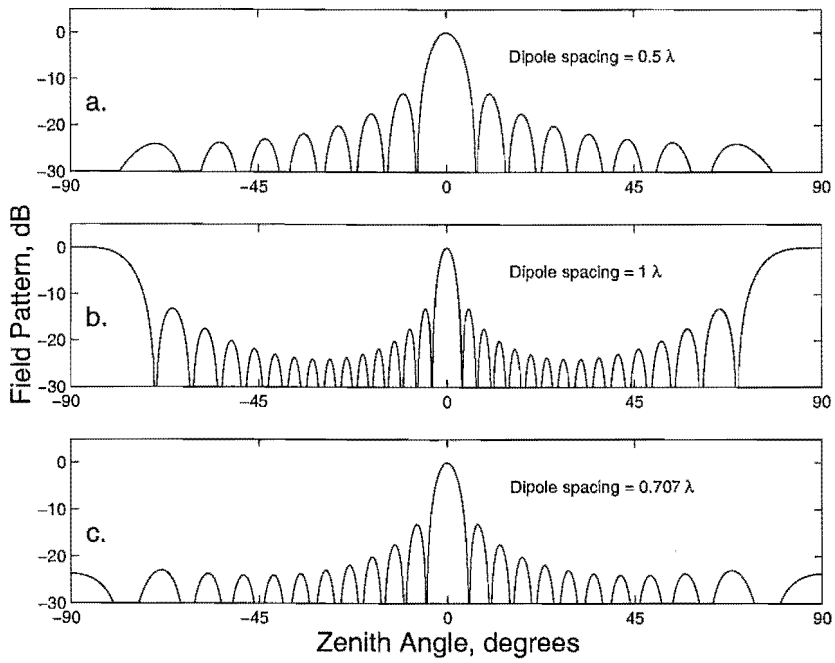

Figure 3.7: The power pattern in the y-direction of an antenna with the same shape (but larger) as that in Figure 3.6 with three different dipole spacings.

the peak power.

From Figure 3.7 it is clear that an element spacing of 0.707 λ could be used successfully. However, each element needs to be in phase and therefore they need to be joined together with feed lines of length $\lambda/2$, or multiples thereof. When using coaxial cable as the feed line, the actual physical distance between the elements is irrelevant as the line can be folded without difficulty. This is not the case when using open wire feed lines, as folding the wires becomes impractical. The elements therefore need a physical spacing of one wavelength. This is achieved by spacing the elements by 0.707 λ in the x and y-direction and then feeding each element in lines that are diagonal to x-y, this layout being shown in Figure 3.8.

The antenna polar diagram for the array in Figure 3.8 is not the same as those displayed in Figure 3.7 because they do not take into account the difference in the shape of the array. The triangular (or diamond) shape significantly reduces the side-lobes of the power pattern, as shown in Figure 3.9. Figure 3.9a is the same as Figure 3.7c, except for the change in y-axis scale. Figures 3.9b and 3.9c are sections along the y and x-axes of Figure 3.8 where the element spacing is 0.707 λ. All of these patterns contain ground-lobes, as would be expected from a spacing not

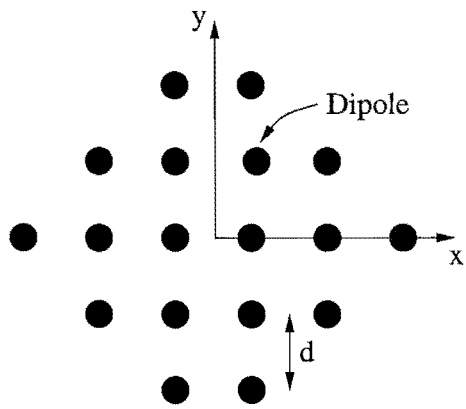

Figure 3.8: The design pattern of the Canterbury antenna array.

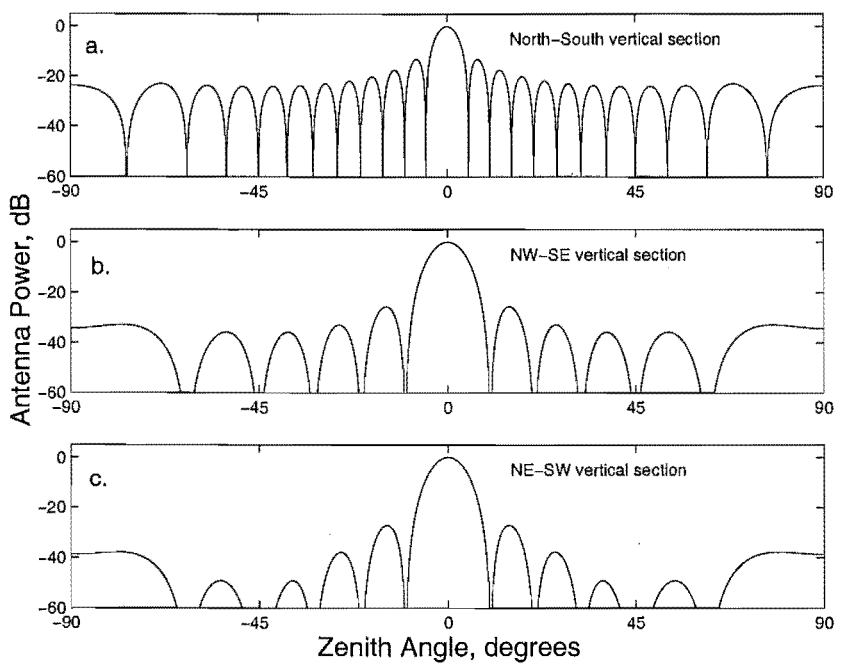

Figure 3.9: The power pattern of an antenna with a dipole spacing of 0.707 λ. The top diagram is from an array like that in Figure 3.6 and the lower two diagrams are from an array like that in Figure 3.8.

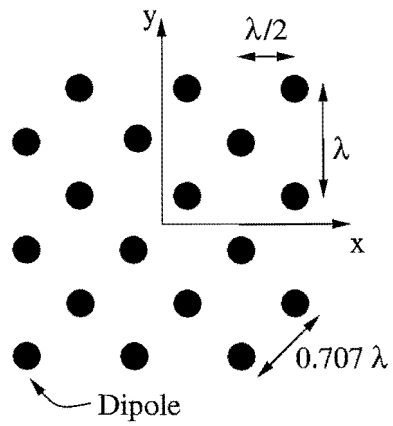

Figure 3.10: The design pattern of the Canterbury antenna array rotated by 45°.

equal to half a wavelength, but as a result of the triangular shape, the second two orientations have much smaller side-lobes.

The array shown in Figure 3.10 is the same as that in Figure 3.9, but has been rotated by 45°. It has an element spacing of 0.707 λ in the diagonal direction, but a spacing of one wavelength in the x (or y) direction. Ordinarily a spacing of one wavelength would give an array pattern with large ground-lobes as shown in Figure 3.7b. However, even though the individual sources are one wavelength apart, each row of sources has half that spacing. From a distant point all the sources in a row are approximately the same distance away (Figure 3.11a), thus they are in phase and appear as a single source. Each row, however, is at a different distance (Figure 3.11b) and therefore at a different phase. Thus when looking in either the x or y-direction in Figure 3.10, the antenna polar diagram resembles Figure 3.7a and when looking along either of the diagonals, it resembles Figures 3.9b and 3.9c.

The three-dimensional beam pattern for an array of this shape is best calculated using the coordinate system of Figure 3.5, but with the x and y-axes positioned as in Figure 3.10. For this array Equation 3.14 can be rewritten as

$$E_{2D} = \sum_{n=1}^{N}\sum_{m=1}^{M}\left(e^{jkd((2n-1)\sin\theta\sin\phi+(-1)^{(n+m)}(2m-1)\sin\theta\cos\phi)} + e^{-jkd((2n-1)\sin\theta\sin\phi+(-1)^{n+m}(2m-1)\sin\theta\cos\phi)}\right), \quad (3.15)$$

where the first exponential term is for the points above the x-axis and the second is for the points below the x-axis. In this equation, d is set to one quarter of a

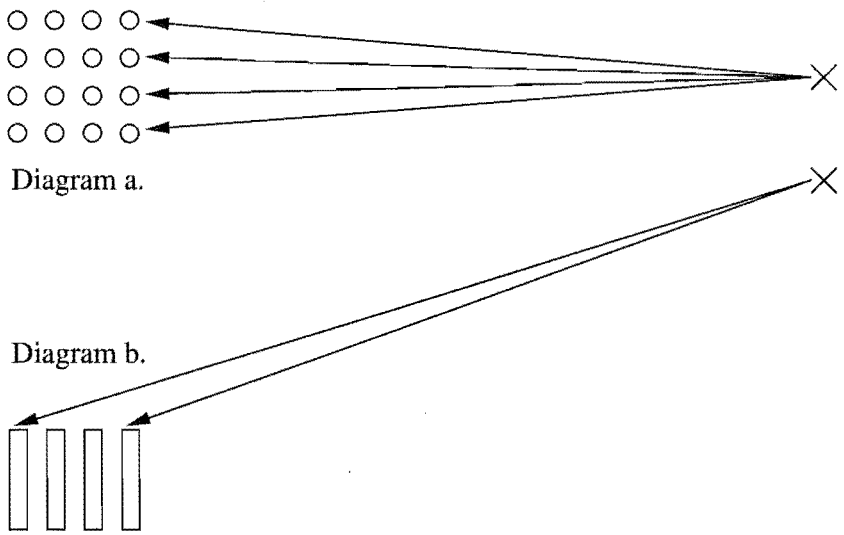

Figure 3.11: From a distant point, **(a)** dipoles perpendicular to the point will be in phase and **(b)** those in line with the point may not be in phase.

wavelength. This can be rewritten as

$$E_{2D} = \sum_{n=1}^{N}\sum_{m=1}^{M} \cos((2n-1)kd\sin\theta\sin\phi + (-1)^{(n+m)}(2m-1)kd\sin\theta\cos\phi). \quad (3.16)$$

For the array shown in Figure 3.10, N and M would be set to 3, but for the Canterbury University antenna array (see Figure 3.12) and for the patterns shown in Figures 3.9b and 3.9c they would be set to 8.

The above equation is true only if each element in the array is an isotropic point source. For an array of dipoles or Yagi-Uda elements, the equation needs to be multiplied by the field pattern of the individual element. For the CUSTAR antenna array, the point sources are replaced with two element Yagi-Uda antennas, as is described in the next section. However, the field pattern of an individual dipole, E_{dipole}, can be used as an approximation of the Yagi-Uda, because the array is quite large and the total field pattern

$$E_{2D} = E_{dipole}\sum_{n=1}^{N}\sum_{m=1}^{M} \cos((2n-1)kd\sin\theta\sin\phi + (-1)^{(n+m)}(2m-1)kd\sin\theta\cos\phi), \quad (3.17)$$

will be dominated by the array factor shown in Equation 3.16.

Equation 3.9 gives the field pattern of a dipole oriented in the y-direction. This

can be converted to spherical coordinates and expressed as

$$E_{dipole_y} = \frac{\cos[(\pi/2)\sin\theta\sin\phi]}{\sin(\cos^{-1}(\sin\theta\sin\phi))}. \tag{3.18}$$

If the dipoles are oriented along the x-axis then this becomes

$$E_{dipole_x} = \frac{\cos[(\pi/2)\cos\phi\sin\theta]}{\sin(\cos^{-1}(\cos\phi\sin\theta))}. \tag{3.19}$$

Use of Equation 3.17 with $N = M = 8$ produces a FWHM of 6.35°. The solid angle of the main lobe can be approximated using Equation 3.6 as $\Omega_A = 0.0123$ sr. Assuming there are no losses in the antenna array, the effective aperture can then be calculated using Equations 3.7 and 3.8 and comes to $A_e = 4000$ m^2.

3.2.2 The Antenna Array Design

The layout of the CUSTAR antenna array is shown in Figure 3.12 and Figure 3.13. Figure 3.14 contains a photograph of the completed array. The transmitter is connected (via the transmit-receive switch) to the antenna array by a feed line which fans out so that each element receives the same signal in phase. Each dipole is mounted on the top of a capped wooden pole approximately 3 metres above the ground. The feed lines run perpendicular to the dipoles approximately 1 metre below them. To obtain an effective ground plane (as the site was unable to be levelled due to environmental considerations), each dipole has a reflector placed 0.17 λ below it. This increases the gain significantly and also minimises the power being absorbed by the ground.

The length of the dipole and reflector and the spacing between them was determined experimentally. The length of the dipole was tuned to have maximum resonance at 42.5 MHz. This occurred when the total length of the dipole was 3.06 m. This is slightly shorter than would be expected from a $\lambda/2$ dipole because of the construction of the connection to the vertical feed line at the centre of the dipole. The approximate length and spacing of the reflector was calculated using *The Yagi Optimizer*, an antenna modelling program written by *Beezley* [1990]. These initial calculations were performed to maximize the ratio of the field strength directed at the zenith to the field strength directed into the ground (the front-to-back ratio). Field tests were performed to check these measurements and the length of the reflector was adjusted to maximise the front-to-back ratio. The spacing was then adjusted to bring the dipole's impedance as close to 50 Ω as possible without

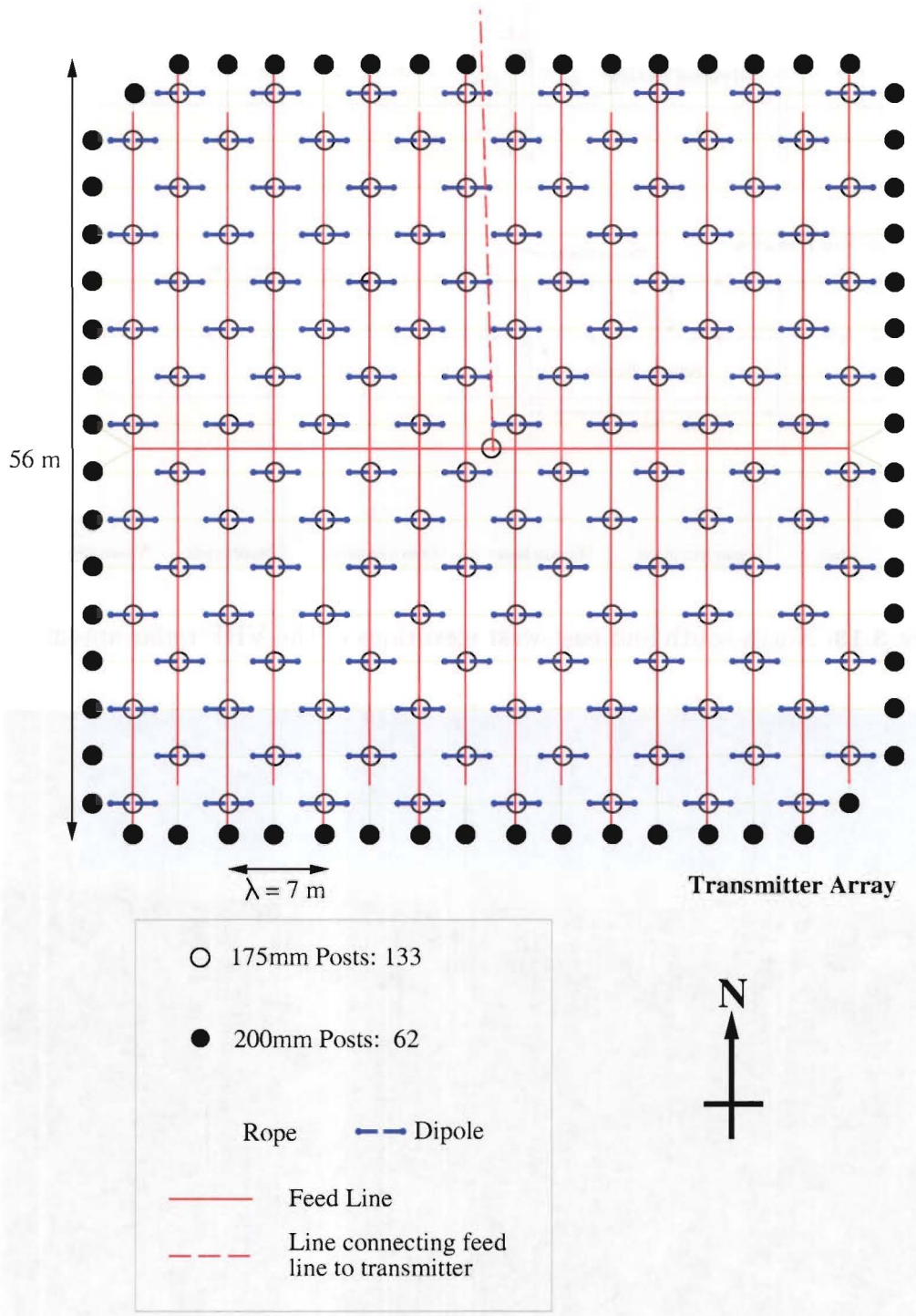

Figure 3.12: Plan view of the VHF radar antenna array showing dipoles, feed line and posts [After *Dunford*, 1999].

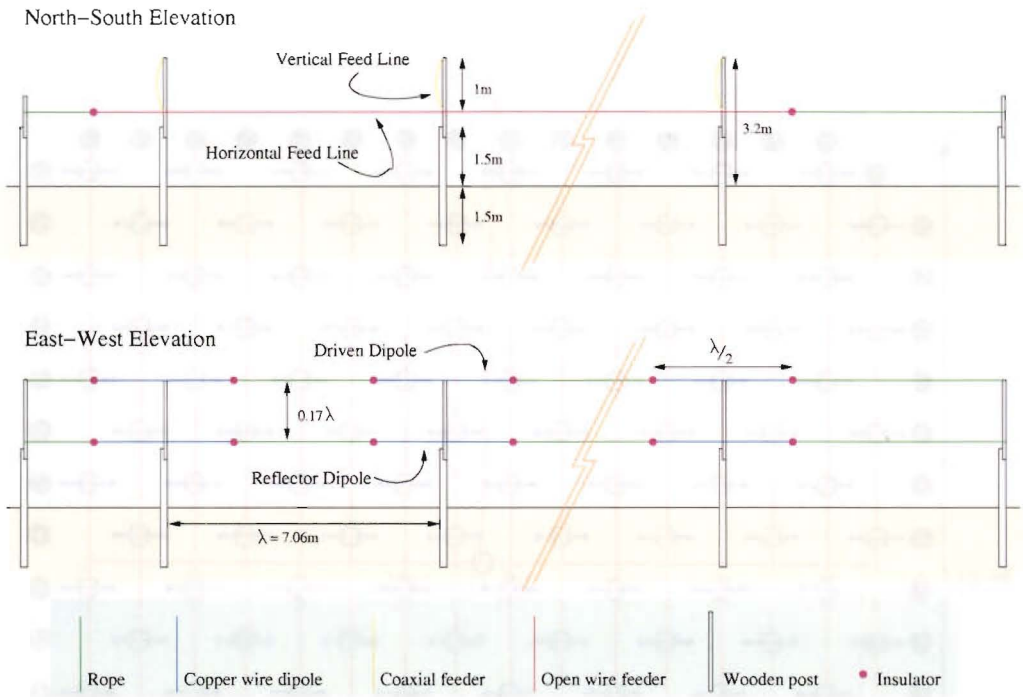

Figure 3.13: North-south and east-west elevations of the VHF radar antenna array.

Figure 3.14: A photograph of the antenna array at Birdlings Flat.

taking the antenna off tune. The optimum length of the reflector was found first as this parameter had a larger effect on the front-to-back ratio than on the impedance. The final ratio was measured to be 11.5 dB and the final impedance as 53 Ω. The optimum reflector spacing was 1.24 m and its length was 3.53 m.

The CUSTAR antenna array has been designed to obtain a vertically pointing beam. In the initial stages of development, the radar will only measure vertical wind speeds and the extension to horizontal wind measurement capabilities will be made using the spaced antenna technique. In both these modes, the antenna beam only needs to point in the vertical direction. This makes the design of the antenna feeding system simpler, as the antenna does not need to have an adjustable beam direction. If this was the case, the connections between the main feed line and the dipoles would need to be matched coaxial cable, so that different lengths of wire can be added or taken away, thereby changing the phase of the dipoles and the overall beam pointing direction. For an array with a single pointing direction, some form of open wire or balanced cable can be used to connect the dipoles to the feed line.

3.2.3 The Feed System

Where the antenna is at a distance from the generator they are connected by a transmission line made up of two conductors. Power is transferred as waves of alternating potentials and currents between and along them. In a given line, the ratio of potential difference to current is a constant known as the characteristic impedance, Z_0, which is (almost) real for high quality, low loss lines. If the end of the line is terminated by an impedance $Z_l = Z_0$ then the waves are absorbed completely, but otherwise reflection occurs, a reverse wave is generated and standing waves are produced. The reflected wave increases the loss on the line and also means that the apparent input impedance at the generator may be different from Z_0 and will vary with frequency. If the line is long, this may decrease the effective bandwidth of the system.

To avoid these problems it is usual to "match" the load to the line by transforming the antenna impedance to Z_0. A method of doing this is to use short sections of transmission line of different characteristic impedance. If the transmission line has a length of $\lambda/4$, it acts as an impedance transformer, obeying the relationship

$$Z_f = \frac{Z_0^2}{Z_i}, \tag{3.20}$$

where Z_0 is the characteristic impedance of the $\lambda/4$ transmission wire, Z_i is the impedance on one side of the transformer and Z_f is the impedance on the other side.

The characteristic impedance, Z_0, of the open wire feed line used to connect the transmitter to the array can be calculated from the diameter, d, and spacing, s, of the two wires [*Hall*, 1991] by the following relation

$$Z_0 = 276 \log_{10} \frac{2s}{d}. \tag{3.21}$$

Measurements of s and d for the transmission line utilised give a characteristic impedance of 540 Ω. A direct measurement of the line's characteristic impedance was also performed using a VHF admittance bridge and this produced a value of 520 Ω. The former of these two measurements was used for the calculations that follow as the $\lambda/4$ section of line used for the direct measurement was too short to provide a good average wire spacing. This measurement was also performed inside a laboratory and, due to the effect of the building and furniture in the room, may have produced a value different from that expected in free space. As explained in Section 3.2.2, the individual elements were designed to have a characteristic impedance of approximately 50 Ω.

The system used to connect the dipoles to the transmit-receive switch (see Section 3.3.1) is shown in Figure 3.15. The diagram at the top and running down the centre shows the entire feed system of the array, although most of the dipole lines are not shown for simplicity. The smaller diagrams around the outside of this figure show the steps needed to match the impedance of each element to the impedance of the open wire feed line.

The first diagram shows the connection of the dipole to the horizontal feed lines. This connecting wire needs to have a low impedance so that the horizontal feed line doesn't "see" an enormously high impedance. To achieve this, a pair of 75 Ω coaxial cables with their shielding joined together are used. Together, these two cables have a characteristic impedance of 150 Ω. In step A of Figure 3.15, Equation 3.20 is used to simplify the dipole and $\lambda/4$ transmission line to the 450 Ω impedance at the horizontal feed line.

Step B of Figure 3.15 takes the 450 Ω impedance calculated in step A and puts it in place of each of the eight dipoles on one horizontal line. Because the dipoles are joined at points one wavelength apart the impedances can be combined in parallel.

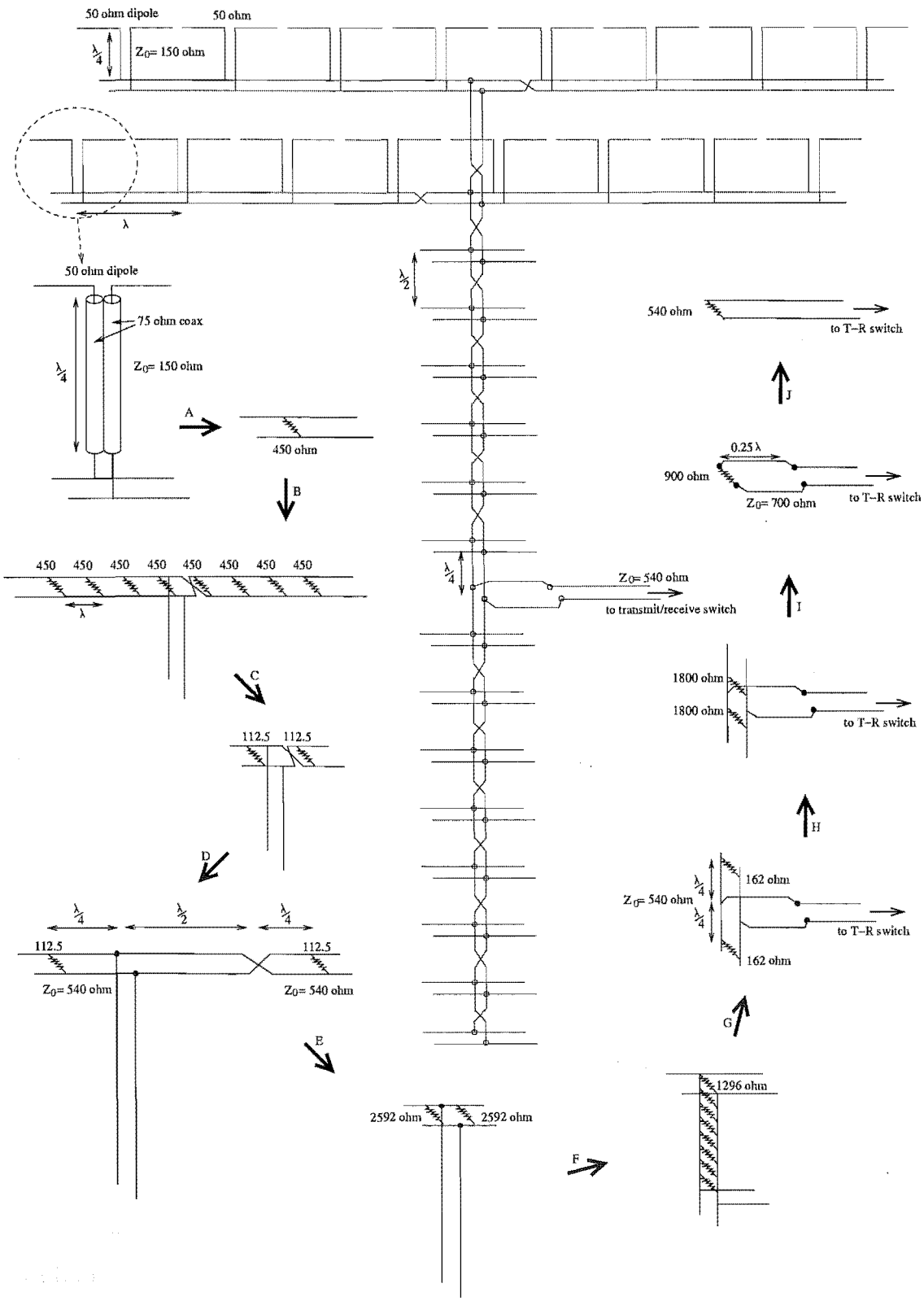

Figure 3.15: The feed system for the VHF antenna array.

This is done in step C where the four dipoles on each side of the central feed line are combined to give a total of 112.5 Ω. Step D shows a closer view of the combined impedances and their distances from the central feed line. The $\lambda/2$ section of line on the right hand side introduces a 180° phase shift which is compensated for by the addition of a twist in the open wire feed line. On each side of the central feed wire is a section of line $\lambda/4$ long. Both of these sections will be an impedance transformer according to Equation 3.20. The characteristic impedance of these $\lambda/4$ lengths is 540 Ω, so the impedances seen after the transformer will be 2592 Ω, as shown in step E.

The 2592 Ω impedances from each side of the central feed line are combined in parallel to one impedance of 1296 Ω. Step F shows this and also the total impedance of each of the other seven horizontal lines of dipoles above the central feed point. The horizontal lines are $\lambda/2$ apart, so a twist in the feed line is introduced to remove the phase shift. In step G, these eight impedances combine to give 162 Ω above and below the central feed point. These two impedances are separated from the central feed point by a distance of $\lambda/4$, therefore the final impedance for each half of the array is 1800 Ω. These can be added in parallel to give 900 Ω.

The final step is to match this 900 Ω to the 540 Ω transmission line connecting the antenna to the transmit-receive switch. This can be achieved by using a $\lambda/4$ section of transmission line that has an impedance of 700 Ω. The spacing of this section is increased to achieve this (as given by Equation 3.21).

The transmission line also needs to be matched to the transmit-receive switch (see Section 3.3.1) which is situated in a container about 50 m from the centre of the antenna array. The input of the transmit-receive switch is unbalanced and has an impedance of 50 Ω, whereas the feed line is balanced with an impedance of 540 Ω. This transformation was achieved using the two step process indicated in Figure 3.16. The impedance of the open wire line is first transformed down to 200 Ω using a $\lambda/4$ length transmission line of 330 Ω impedance. A line of this impedance is obtained by using copper pipe instead of wire, as a thicker wire diameter decreases the line impedance (Equation 3.21). The 200 Ω is then transformed to 50 Ω unbalanced by using a 4:1 balun made of 50 Ω coaxial cable.

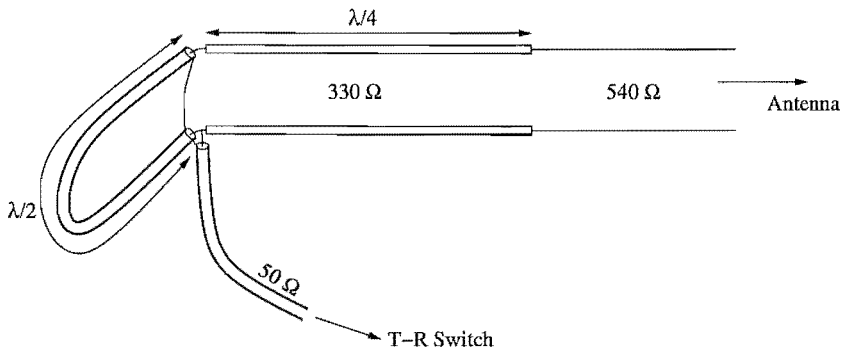

Figure 3.16: The impedance matching network inside the receiver building.

3.3 Electronic Hardware

3.3.1 Transmit-Receive Switch

When a radar system uses the same antenna for both transmission and reception, a switch is needed so that the transmitter and receiver can be connected to the antenna simultaneously. The switch needs to allow the very small signal received by the antenna through to the receiver and it must be capable of stopping the very large signal produced by the transmitter from entering the receiver input. It also needs to be able to switch between these two states very quickly and at a high frequency. This switch is often called a transmit-receive switch (T-R switch) or a duplexer.

The T-R switch in the form discussed here was first used in 1940 in a radar system used for the detection of low-flying aircraft [*Banwell*, 1946]. This was constructed from spark-gaps and sections of $\lambda/4$ transmission line arranged so that the receiver was shorted on transmission and the transmitter shorted on reception. A spark-gap is a device which is an open circuit for low voltages, but when a large voltage appears between the terminals, the gas between them ionises and the gap is bridged by a spark, thus forming a short circuit. The composition of the terminals and the gas between them is chosen so that the striking time and deionisation time are short and that the striking voltage is low.

A diagram for a spark-gap duplexer is shown in Figure 3.17. Using this arrangement, there is no need for an external signal to switch the duplexer between states, as the large voltage from the transmitter triggers the spark-gaps. When the radar is in transmission mode, the spark-gaps fire, causing short circuits at points B and E. From Equation 3.20 which gives the impedance transformation characteristics of a

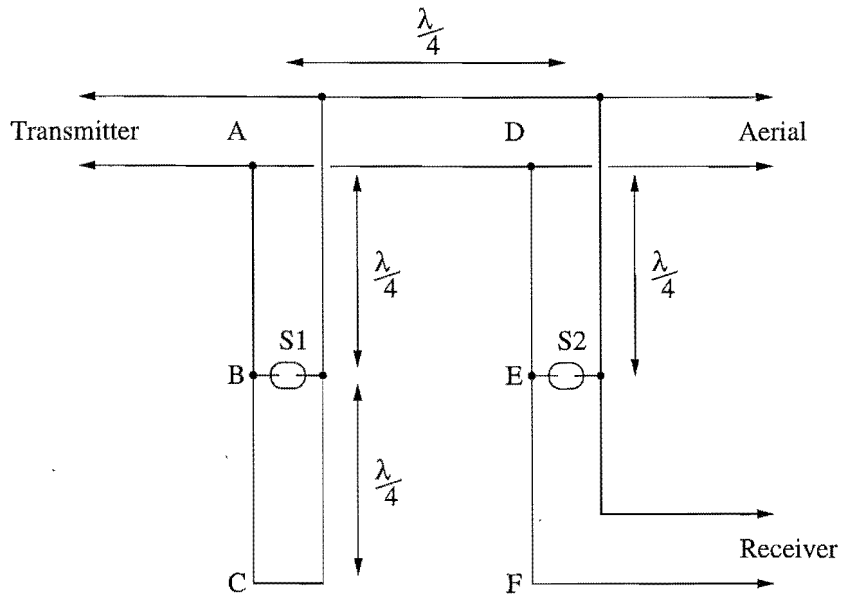

Figure 3.17: A T-R switch using spark-gaps and $\lambda/4$ transmission line sections.

$\lambda/4$ transmission line, short circuits at these points correspond to open circuits at points A and D. In this case then the aerial receives the transmitter pulse unimpeded and the receiver "sees" a short circuit.

When the radar is in reception mode, the transmitter is not producing a large voltage and the spark-gaps will remain open. Point B then is an open circuit due to the short circuit at point C and point A is a short circuit due to the open circuit at point B. The receiver is directly coupled to the aerial and isolated from the transmitter to prevent unwanted leakage.

Spark-gaps are not readily available and have some disadvantages. They have slow response times, high striking voltages, high losses and they do not have long lives. However, they can be replaced by either normal semi-conductor diodes or PIN diodes. PIN diodes normally need to have a separate trigger pulse to switch them into conduction mode and high-voltage, fast-recovery types are uncommon and expensive. *Hocking* [private communication] suggested the BAV21 fast recovery diode as a possibility for switching without the need for a trigger pulse.

With BAV21 semi-conductor diodes to replace the spark-gaps, a circuit very similar to that in Figure 3.17 can be used. For ease of construction, the $\lambda/4$ transmission line sections can be replaced with artificial lines made up of circuit elements. The circuit shown in Figure 3.18 is equivalent to a $\lambda/4$ transmission line. The impedance,

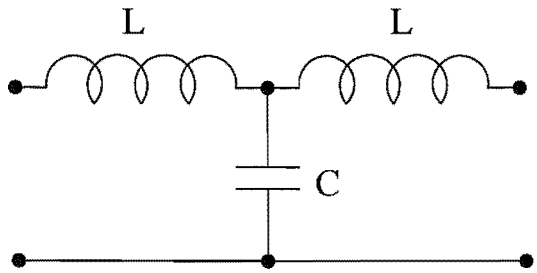

Figure 3.18: An artificial $\lambda/4$ transmission line.

Z_0, of the line can be chosen by adjusting the values of L and C.

$$L = \frac{X_L}{2\pi f} \tag{3.22}$$

$$C = \frac{1}{2\pi f X_C} \tag{3.23}$$

where f is the radar frequency and X_L and X_C are the impedance of the inductor and capacitor respectively. X_L and X_C both need to be set numerically equal to the required characteristic impedance, Z_0.

The final transmit-receive switch circuit used is shown in Figure 3.19. At points B and E, twelve BAV21 diodes replace the spark-gaps of Figure 3.17. They are arranged so that there are six diodes in each direction allowing both the negative and positive part of the R.F. signal to pass through. The diodes will be biased forward when there is more that 0.6 volts across them. This means they will be "on" when the radar is transmitting and "off" when it is receiving. A third identical set of diodes is placed at point F to reduce further the signal reaching the receiver during transmission. The values for L_1 and C_1 are chosen so that the artificial line between points A and D has a characteristic impedance of 50 Ω. This is to ensure that the transmitter and antenna, which are designed to see 50 Ω, are matched correctly. L_2 and C_2 are chosen so that all the other sections of line are at 75 Ω. This is done so that points B and E are at a higher impedance and therefore less current will flow through the diodes. According to the impedance transformation equation (see Equation 3.20) point E will have an impedance of

$$Z_E = \frac{Z_0^2}{Z_D},$$

$$Z_E = \frac{75^2}{50} = 112.5\ \Omega. \tag{3.24}$$

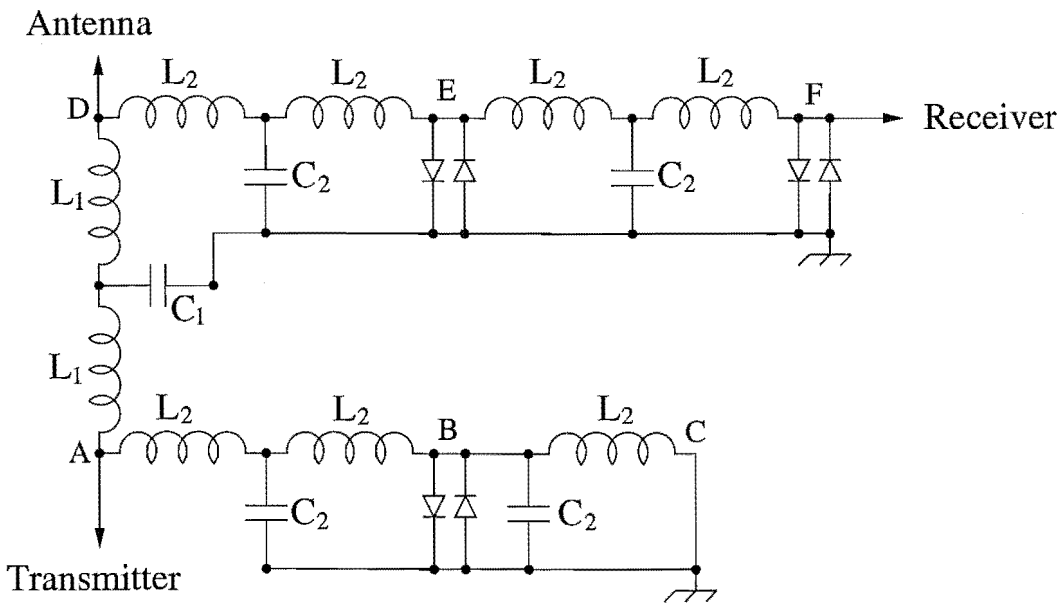

Figure 3.19: A circuit diagram of the T-R switch used in the Canterbury University VHF radar.

This impedance will be transformed back to 50 Ω to match the receiver input by the 75 Ω section of line between points E and F. By the same argument as above, point B will be at 112.5 Ω and point C at 50 Ω. One of the inductors can be left out of the section between points B and C as that section of artificial line only needs to resemble a $\lambda/4$ line from point B and not from point C.

Each BAV21 diode can take a maximum of 250 mA continuous forward current. If this is taken as the maximum average forward current, then for 12 diodes the maximum current is 3 A. The maximum average power, P_{av}, that the T-R switch can withstand is limited by the amount of current the diodes at points E and B can cope with. This power is given by

$$\begin{aligned} P_{av} &= I^2 Z, \\ P_{av} &= (3)^2(112.5) \approx 1 \text{ kW}. \end{aligned} \tag{3.25}$$

The completed device was tested using a peak output from the transmitter of approximately 1.5 kV ($P_{pk} \simeq 45$ kW). This produced a voltage of approximately 10 V after the first stage of the T-R switch (point E) and after the second stage (point F) the signal peak was reduced to 0.7 V. This is a much larger signal than the receiver is designed for (1-100 μV), but is not large enough to do any damage.

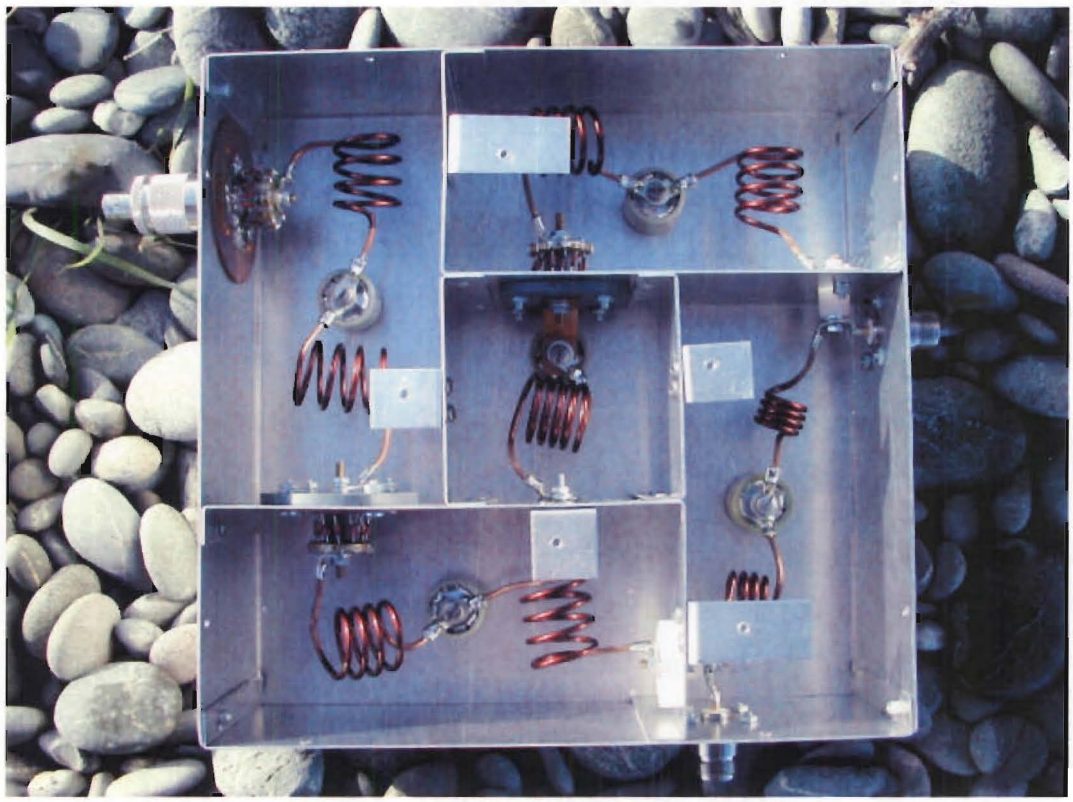

Figure 3.20: A photograph of the T-R switch used in the Canterbury University VHF radar.

As the photograph in Figure 3.20 indicates, each section of artificial line is shielded from the other sections. This prevents mutual inductance between the coils, making them easier to design and test and also helps to shield the higher voltage sections connected to the transmitter from those connected to the receiver.

Each section of artificial line was tested to ensure they all resembled $\lambda/4$ sections and that they were the correct impedance. These tests were done with the diodes in place so that the extra capacitance they added was taken into account. After completion the T-R switch was tested for the attenuation it adds to the received signal. This was found to be 1.1 ± 0.1 dB.

3.3.2 Transmitter

A transmitter is used to amplify radio frequency (R.F.) pulses so they are large enough to reflect off small changes in the radio refractive index of the atmosphere. The transmitter built for the University of Canterbury VHF radar was designed by

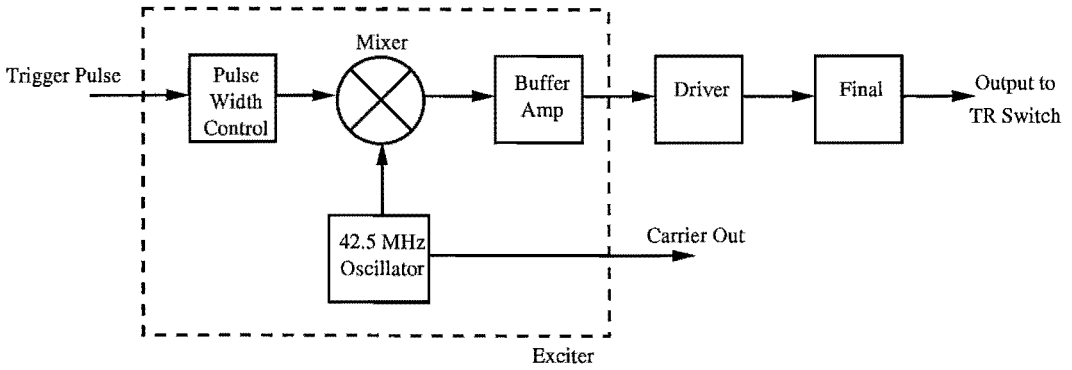

Figure 3.21: A block diagram of the transmitter.

Bob Bennett and operates at 42.5 MHz. It uses vacuum tube technology and is capable of 100 kW peak power with a duty cycle[2] of 1.4 %.

A block diagram of the transmitter is shown in Figure 3.21. The R.F. signal to be transmitted first needs to be produced and this is done by an oscillator using a 42.5 MHz crystal. From the oscillator, this continuous signal is passed to the mixer in the transmitter and also to the receiver so that coherent measurements can be made. The transmitter also needs to produce a square pulse that determines the pulse width. The device that produces this pulse is triggered by the analogue to digital converter (see Section 3.3.4). The pulse width can be changed manually from 1 to 7 μs.

The continuous R.F. signal and square pulse are mixed to produce a short pulse of R.F. signal. This pulse is amplified in a solid state buffer amplifier which has a peak output power of 40 W. All the devices described so far help to form the signal which is transmitted and together they are called the exciter. The signal is amplified to its final power in two further sections both of which use vacuum tubes. These two sections use a common cathode configuration and are class C amplifiers. The first of these is called the driver. This section uses two valves working in parallel and has a peak output power of 800 W. The final section uses two vacuum tubes in a push-pull circuit design. The final output has a peak power of 100 kW.

The transmitter is capable of producing an average power output of up to 1.4 kW. Under usual operation, however, the transmitter typically produces between 250 and 500 W.

[2]The duty cycle is the ratio of the pulse length to the repetition frequency. See Section 3.4.

3.3.3 Receiver

The purpose of the receiver is to convert the R.F. signals reflected from the atmosphere into a form that can be recorded and analysed. The type of receiver used was a direct-conversion phase-sensitive detector.

When an R.F. pulse is reflected from the atmosphere, it returns with a much reduced amplitude and also with the possibility of a small frequency shift. This reflected signal can be described as a function of time by

$$x(t) = a(t)\cos[2\pi f_0 t + \psi(t)] \tag{3.26}$$

where $a(t)$ is the amplitude, $\psi(t)$ is the phase modulation and f_0 is the carrier frequency [*Skolnik*, 1970]. It is this amplitude and phase modulation that the receiver needs to extract from its input signal. Equation 3.26 can be written alternatively as

$$\begin{aligned} x(t) &= I(t)\cos 2\pi f_0 t - Q(t)\sin 2\pi f_0 t \qquad (3.27)\\ \text{where } I(t) &= a(t)\cos\psi(t) \\ \text{and } Q(t) &= a(t)\sin\psi(t). \end{aligned}$$

$I(t)$ and $Q(t)$, which are called the in-phase and quadrature components of the returned signal, contain the amplitude and phase information needed. They are obtained by mixing the received signal with two reference signals at the carrier frequency having a phase difference of 90°. The resultant signals will have a frequency that is the difference between the transmitted and received signals, or the Doppler shift.

Figure 3.22 shows the main components of the receiver. The input signal is first sent through an R.F. filter. This ensures that only signals of around 42.5 MHz are accepted. There are many interfering R.F. signals that can be received by the antenna such as those from the other radars at the Birdlings Flat site. These other radars have frequencies of 26.2 MHz and 2.4 MHz, so any signal received from them is filtered out in this first section. The bandwidth of the input stage, however, is still much larger than the overall bandwidth of the receiver.

The 42.5 MHz signal is then amplified in two stages before being split and sent to separate mixers. The mixers are also fed with the two reference signals, one advanced by 45° from the carrier signal and one retarded by 45°, which are produced in the phase-splitter. The output of each mixer will be made up of the sum beat frequency,

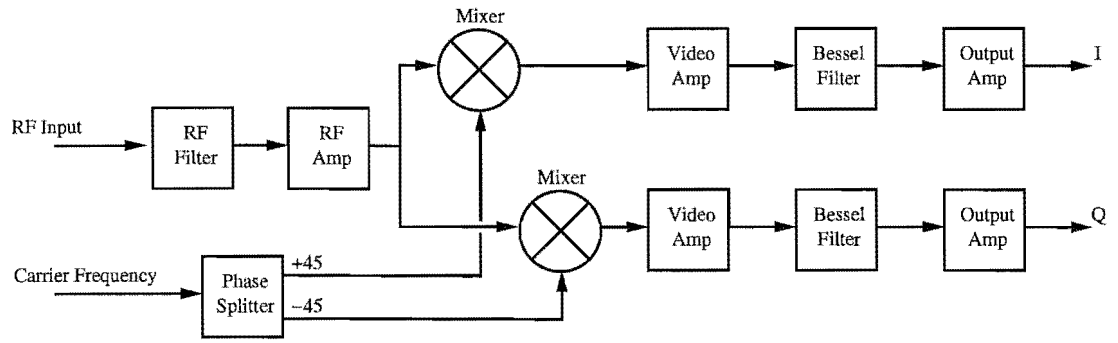

Figure 3.22: A block diagram of the receiver.

which will be very high (85 MHz) and can be filtered out in the next two sections of the receiver, and the difference beat frequency, which will be the Doppler shift, so therefore relatively small. The phase difference between the two carrier frequency signals means that the outputs of the two mixers, the I and Q signals, will be 90° out of phase.

The receiver is phase-sensitive because the reference signal sent to each mixer is coherent with the transmitted signal. This means that over a series of pulses the phase can be monitored for any variations. Also, if the phase of a reflected signal is known to change slowly (i.e. the target has a small velocity) then pulses can be added coherently without any loss of phase information.

The receiver is called a direct-conversion receiver because it transforms its input signal from 42.5 MHz down to DC in one step. It does this by using the original carrier frequency as the mixing signal. A direct-conversion system is a much simpler version of the more common superheterodyne receiver that incorporates an intermediate frequency (I.F.). Superheterodyne receivers require at least two local oscillators for coherent dectection, one, the "local oscillator", to convert the receiver's input signal to the intermediate frequency and a second one, the "beat frequency oscillator", used to convert the I.F. signal to the required output. The combination of the two local oscillators needs to be coherent with the transmitted signal so that phase information from the returned pulses is not lost. This is sometimes achieved by mixing the signal from the first oscillator with the R.F. signal from the transmitter and using that to phase-lock the second oscillator. With a direct-conversion receiver, the I.F. is 0 Hz so the reference frequency comes directly from the exciter in the transmitter.

If direct-conversion is used care must be taken to ensure that unwanted signal from the exciter is not picked up on the input to the receiver as this can cause instability. By using modern surface mount components and carefully shielding the receiver front-end and the phase-shifting circuit these problems can be avoided.

After the mixers, each channel is amplified in a video amplifier and then passed through an 8 pole low-pass Bessel filter. A Bessel filter was used as it has a linear phase variation with frequency, meaning that below the cut-off frequency of the filter, the signal is transmitted without a change in shape [*Jones*, 1986]. The optimum bandwidth, Δf, for this filter depends on the width of the transmitted pulse, τ,

$$\Delta f = \frac{1}{\tau}. \tag{3.28}$$

The receiver was initially designed for a 2 μs pulse width which gives a bandwidth of 500 kHz, however, the actual bandwidth was found to be close to 250 kHz. The experiments conducted in this thesis used a pulse width of 4 μs, so the receiver, although not being within its initial design specifications, was very close to the optimum operating point.

The final stage in the receiver is an output amplifier. This ensures that the output signals are in the range from 0 to 5 V and centered on 2.5 V. This is necessary to make the outputs compatible with the analogue to digital converter.

3.3.4 Analogue to Digital Converter

The system used to convert the analogue output from the receiver into a digital signal is dual channel to cope with both the I and Q receiver outputs simultaneously. Each of these channels contains an 8-bit analogue to digital converter (ADC) capable of 500 000 samples per second. The two channels sample at this rate 64 times for each transmitter pulse. This data is stored in a buffer and sent to a computer between each pulse.

Each ADC is controlled by a CMOS 8-bit microcontroller. This microcontroller determines the pulse repetition frequency of the transmitter and the sampling frequency of the ADC. Because the microcontroller handles the timing of the transmitter and ADC, the interface computer only needs to tell it when to start and stop, allowing the computer to perform other tasks while the radar is operating.

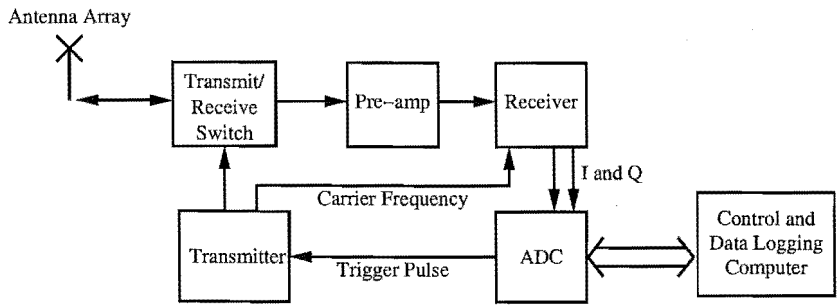

Figure 3.23: The Canterbury University VHF radar system.

3.4 Operational Details

This section describes the typical operation of the radar, including the overall system set-up and the details of each experimental run. Figure 3.23 displays a block diagram of the radar system and indicates how the individual components described in the previous section interconnect. The radar operates by sending a short pulse of radio frequency energy into the atmosphere and receiving the reflected signal. An analogue to digital converter (ADC) samples the echoes from this pulse at a high rate, separating the signal into range gates. This process is rapidly repeated a large number of times and the result is a time-series of echoes for each height bin. This data is then stored or analysed. Figure 3.24 shows the different time-scales involved in this procedure.

3.4.1 Radar Parameters

There are a number of parameters that need to be carefully chosen to ensure that the radar operates under optimal conditions. These parameters, which are discussed below, include the run length, pulse repetition frequency, pulse width and ADC sampling rate.

For each wind speed calculation, data needs to be collected for times in the order of $10 - 100$ seconds [*Rastogi*, 1986]. The chosen length is a trade-off between velocity resolution and temporal resolution. The velocity resolution, v_{res}, is related to the run length, t_r, by

$$v_{res} = \frac{\lambda}{2t_r}, \tag{3.29}$$

where λ is the radar wavelength. For a radar operating at 42.5 MHz, a run length of 130 seconds gives a velocity resolution of approximately 0.027 $\mathrm{m\,s^{-1}}$. It should

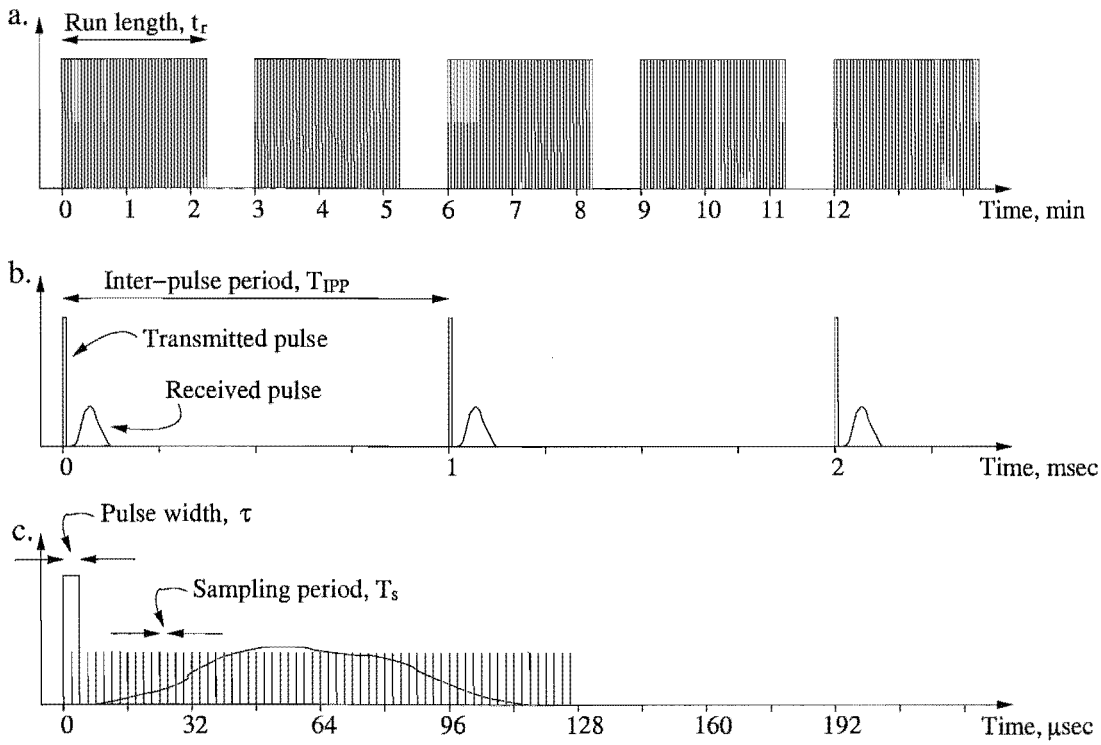

Figure 3.24: Characteristic timescales of operation. Shown are **(a)** the run length, in this case 130 seconds, **(b)** the individual transmitted pulses with their associated echoes and **(c)** a single pulse and its echo overlayed with vertical lines to represent the range gate sampling times. Note the different x-axis scales on each plot.

be noted that a large t_r not only gives a better velocity resolution, it also increases the signal detectability because of the increased number of pulses. However, a long run time also reduces the temporal resolution because the velocity calculated will be an average over the whole run. To observe short time-scale variations in the atmosphere, the run time needs to be comparable in length to those changes.

The pulse repetition frequency (PRF) should be as large as possible, but there are a number of limiting factors. Firstly, the transmitter has a maximum average power output, P_{av}, and a peak power output, P_{peak}, related by the duty cycle. The duty cycle is the fraction of time for which the transmitter is actually transmitting and can be defined as

$$\text{Duty Cycle} = \tau \times \text{PRF} \tag{3.30}$$

$$P_{av} = \text{Duty Cycle} \times P_{peak} \tag{3.31}$$

where τ is the pulse width. So the PRF can only be increased until the average

power reaches its maximum allowed value. The data collection computer will have a maximum collection rate that may also limit the PRF.

With a high PRF there is also the possibility of range aliasing. That is when the signal from a distant reflector is received after the next pulse has been transmitted. To ensure this does not happen the largest distance from which signal can be received needs to be identified. This distance is the unambiguous range, r_u. The time between pulses (or inter-pulse period, T_{IPP}) must then be

$$T_{\mathrm{IPP}} = \frac{1}{\mathrm{PRF}} > \frac{2r_u}{c}, \tag{3.32}$$

where c is the speed of light and the factor of two arises from the two-way propagation of the signal [*Morris and Harkness*, 1996]. For an ST radar with a power-aperture product[3] similar to the Canterbury University radar, approximately 2.0×10^6 W m^2, signal is very unlikely to return from altitudes greater than 20 km [*Hocking*, 1997a]. This means the PRF needs to be less than 7500 pulses per second. With a smaller power-aperture product, the PRF can be increased and for some VHF boundary layer radars it is as large as 50 kHz [e.g. *Vincent et al.*, 1998].

Another ambiguity that can occur relates to measurement of the scatterer's velocity [*Doviak and Zrnić*, 1993]. The Doppler frequency, and therefore velocity, is determined from the phase difference between the in-phase and quadrature channels. There is no unique Doppler frequency, because the phase difference can include any number of 2π phase changes and can occur with a positive or negative phase change. The maximum frequency that can be measured without aliasing is the Nyquist frequency

$$f_N = \frac{1}{2T_p}, \tag{3.33}$$

where T_p is the period between each individual sample in the time series used for determining atmospheric information. The maximum velocity that can be unambiguously derived is

$$v_{max} = \frac{\lambda}{4T_p}, \tag{3.34}$$

where λ is the radar wavelength [*Woodman and Guillen*, 1974]. For data that has not been coherently integrated, $T_p = T_{\mathrm{IPP}}$, but for integrated data, T_p becomes larger, reducing v_{max}. For a radar at 42.5 MHz operating at 1000 pulses per second,

[3]The power-aperture product is a measure of the overall output of the radar and is simply the product of the average transmitter power and the effective aperture of the antenna.

v_{max} is 1750 m s^{-1} for raw data and 27.3 m s^{-1} for data integrated over 128 samples. However, both of these are much larger than the maximum velocities expected from a vertically orientated beam.

The choice of pulse width is a trade-off between the amount of back-scattered power and the obtainable range resolution. A short pulse length will give a higher range resolution, for example $\tau = 1$ μs will produce a pulse that is 300 m long, giving a resolution of $\Delta r = 150$ m. However if the pulse length is increased to say $\tau = 6$ μs the resolution will drop to $\Delta r = 900$ m, but the size of the scattering volume will be six times as great, producing an increase in backscattered power. The range resolution is practically attainable only if the range bin size is small enough.

The range bin size, r, is related to the ADC sampling period, T_s, by

$$r = \frac{T_s c}{2}. \tag{3.35}$$

The maximum range, R_{max}, is given by

$$R_{max} = r(N_s - 1) - \frac{t_{delay} c}{2}, \tag{3.36}$$

where N_s is the number of samples and t_{delay} is the time lost in transmission and reception. Contributions to t_{delay} arise mainly in the transmitter where the R.F. pulse is formed and amplified and also in the receiver. Delays are also produced in the cables connecting the ADC to the transmitter, the T-R switch to the receiver and the receiver to the ADC.

3.4.2 Radar Operation

The control of the system and the collection of data is handled by the same computer. This computer instructs the ADC when to send the trigger pulse to the transmitter and for how long, determining the run length. The ADC controls the PRF of the transmitter via this trigger pulse and the R.F. pulse width is set manually at the transmitter.

After returning through the transmit-receive switch, the received signal is amplified by an R.F. pre-amplifier with a very low noise figure. A HamTronics LNW-50 which has a gain of 24 dB and a noise figure of 0.6 dB was used. The signal is then sent to the receiver where it is amplified further and mixed with the original 42.5 MHz carrier frequency which is sent directly from the transmitter (see Figure 3.23). The receiver, as described in Section 3.3.3, produces the in-phase and quadrature signals which are passed to the ADC.

The ADC sampling speed (in this case $T_s = 2$ μs) determines the size of the range bin (or range gate). The ADC begins sampling when the trigger pulse is sent and continues until a set number of samples (64) have been taken. After each pulse and the associated sampling, the computer collects the data from the ADC and stores it in memory. The amount of time between the last sample and the next transmitter pulse is not long enough to access the hard-drive, so the data needs to be stored in RAM. At the end of each run, the data is moved as one block from RAM to the hard drive which can be easily done in the time available.

The system has the ability to coherently integrate the data as it is being collected by the computer. The main purpose of this procedure is to reduce the amount of data that needs to be stored and analysed. Coherent integration is achieved in software by summing over the required number of successive pulses before storing the result in RAM. The number of pulses integrated over can be set by the user, and a value of 128 was used for much of this study. The effects of coherent integration are discussed in Section 5.3.

After the data has been transferred to the hard drive, the run is complete. The next stage is to process the data. This could be done in the time between runs or during the next run, but for the work done in this thesis, the processing was done off-line. For an explanation of the processing scheme used see Section 5.2.

3.4.3 Meteor Radar Operational Details

A system used to obtain head echoes from meteors (see Section 2.5) could be operated in conjunction with the ST system described above. The main difference between the two systems is the range that needs to be sampled by the ADC. Because the two height regions (0 – 18 km and 80 – 110 km) are completely separated, a second ADC with a very similar design to that described in Section 3.3.4 could be used to record the meteor echoes.

The ADC used for meteor detection would need to have a high sampling rate, similar to that of the existing ADC, in order to obtain an accurate range measurement for the meteoroid. The sampling could be triggered (with an appropriate delay) by the same pulse, produced by the existing ADC, that is used to trigger the transmitter. Ideally, a separate computer would record the data produced by the second ADC and analyse the results in real time.

Software for this system has not yet been developed, but the following method

could be utilised. The data could be recorded and briefly stored in memory. If successive pulses showed a significant increase in power, those pulses and a certain number before and after them would be stored for later analysis, or, if time permitted, analysis between meteor echoes. If no increase in power were observed, that data would not need to be retained.

If an increase in power were found to occur as a result of a meteor echo, its line-of-sight velocity would be first estimated from the time taken to traverse a number of range bins. The accuracy of this estimate could then be improved by calculating the phase difference between successive pulses. As explained in Section 2.5, the angle off zenith of the meteoroid trajectory could be calculated by noting the number of range bins that showed an increase in power. If an increase was observed at all the sampled heights, this would show that the meteoroid arrived directly overhead.

Meteoric ionisation is deposited in the height regime 80 – 110 km so an ADC sampling rate can be no higher than 1000 pulses per second (the frequency currently in use) to ensure that no range aliasing of atmospheric signal will occur. The pulse width would not need to be altered from the length used by the ST system, in fact similar research has been performed with pulse widths as short as 1 μs [*Mathews et al.*, 1999].

Chapter 4

Verification of the Antenna Beam Pattern

To ensure the antenna array has been constructed correctly, it is necessary to measure parameters associated with the beam pattern and compare them to the expected values. This can be achieved by using an aircraft to transport a receiver through the beam of the radar. If the location of the plane is known when the receiver power is measured, the exact beam pattern can be mapped. *Sato et al.* [1989] used a scientific satellite to make measurements of the multi-beam MU radar. Another method known as reverse radio astronomy, which doesn't involve transporting a receiver or transmitter into the atmosphere above the radar, can also be used.

Reverse radio astronomy is a technique which uses the antenna array as a radio telescope and compares the received signal with the known transit times of common radio sources. Both the sun and extra-solar radio sources can be used as test sources for the verification of antenna beam patterns [*Aarons*, 1954; *Graf et al.*, 1971; *Czechowsky et al.*, 1983]. This radio sky noise can also be used to measure the loss factor of an antenna [*Hocking and Lawry*, 1989; *Campistron et al.*, 2001]. Reverse radio astronomy was performed using the CUSTAR antenna first with only one row of the array in operation and then with the entire array. The results from both of these tests are detailed.

4.1 Antenna Beam Patterns

The antenna array designed and built for the CUSTAR radar is described in detail in Section 3.2. A relation describing the theoretical field pattern was derived and presented in Equation 3.17 and is reproduced here

$$E_{2D} = \frac{\cos[(\pi/2)\cos\phi\sin\theta]}{\sin[\cos^{-1}(\cos\phi\sin\theta)]} \sum_{n=1}^{8}\sum_{m=1}^{8} \cos\Big((2n-1)kd\sin\theta\sin\phi + \\ + (-1)^{(n+m)}(2m-1)kd\sin\theta\cos\phi\Big), \quad \text{for } 0 \le \theta \le \frac{\pi}{2} \text{ and } 0 \le \phi \le 2\pi. \quad (4.1)$$

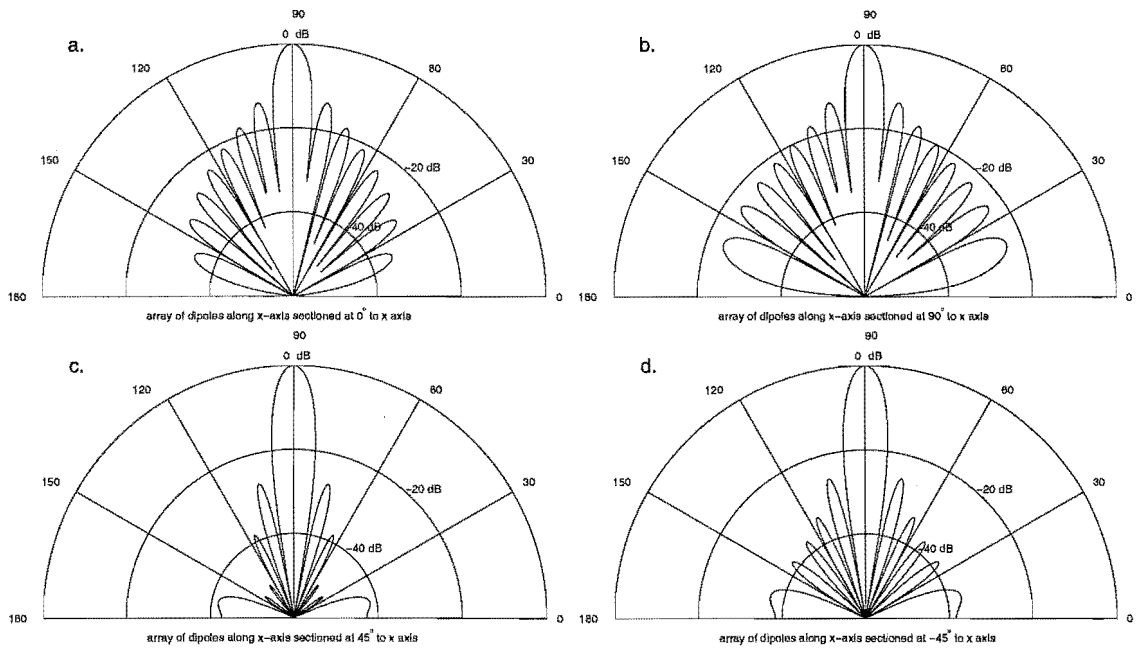

Figure 4.1: Polar diagrams of the completed CUSTAR antenna array. The sections are oriented **(a)** E-W, **(b)** N-S, **(c)** NW-SE and **(d)** NE-SW.

This equation is valid when the individual elements are oriented along the x-axis, which, for the geometry of the antenna, is E-W.

Figure 4.1 shows vertical sections of the array at different azimuth angles produced using Equation 4.1. The difference in beam shape between Figure 4.1a and b is solely due to the orientation of the elements. Figure 4.1a has smaller lobes near the ground, compared to Figure 4.1b, as the dipoles only radiate radially, not from their ends. As explained in Section 3.2.2 the ground-lobes in Figure 4.1c and d are due to the dipole spacings of 0.707 λ in those directions. The side-lobes are much smaller compared to the E-W and N-S sections because of the tapering effect of the diamond shape.

Equation 4.1 can also be used to calculate the beam-width of the main lobe (or any of the other lobes if necessary). The theoretical full-width at half-maximum (FWHM) for the main beam of the CUSTAR array was found to be 6.35° in the N-S and E-W directions and 4.49° in the NW-SE and NE-SW directions.

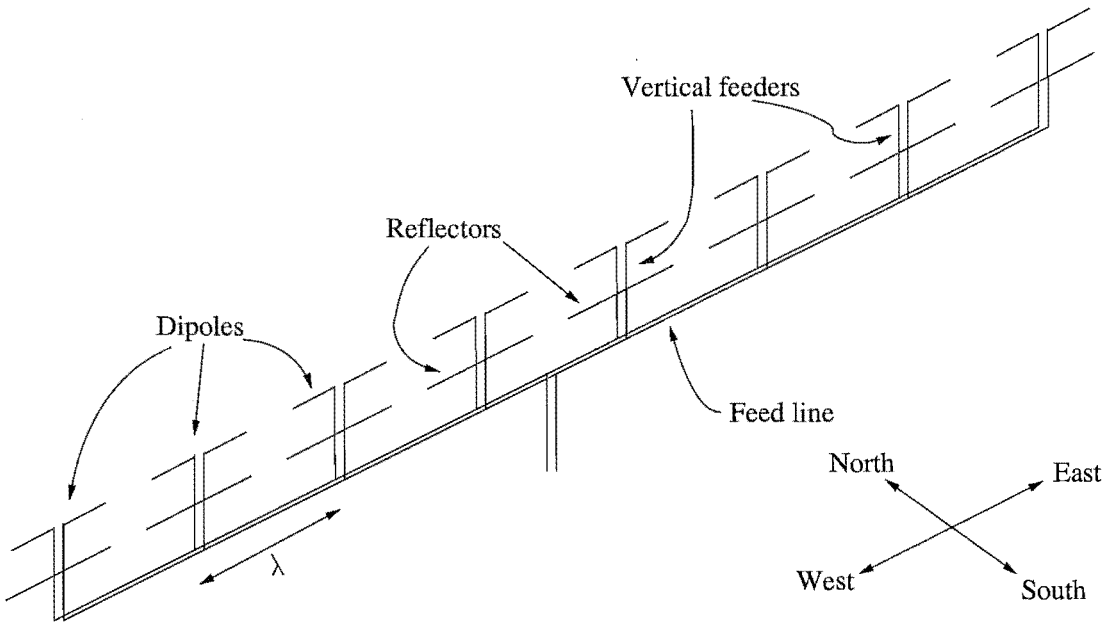

Figure 4.2: The layout of a single row of dipoles; showing the vertical feeders, feed lines and reflectors.

4.1.1 Single Row Beam Shape

Reverse radio astronomy was used to test a single row of eight dipoles while construction of the rest of the array was continuing. Using only one row gives a thin fan-shaped beam instead of the pencil-shaped beam expected from the complete array. If this fan is aligned N-S, a large variety of radio sources can pass through the beam.

The design of the full array dictated the details of the single row. Figure 4.2 shows the row of dipoles, each spaced by one wavelength, orientated in the E-W direction. The feed line ran in parallel with these dipoles, so the vertical feeders were longer than in the final design to keep the feed line below the reflectors. The vertical feeders were extended from $\frac{1}{4}\lambda$ to $\frac{3}{4}\lambda$ which gives ample length without altering the electrical properties.

Using the method described in Section 3.1, the beam pattern corresponding to a single row of dipoles is found to be

$$E_{2D} = \frac{\cos[(\pi/2)\cos\phi\sin\theta]}{\sin[\cos^{-1}(\cos\phi\sin\theta)]} \sum_{n=1}^{4} \cos\Big(2(2n-1)kd\sin\theta\cos\phi\Big), \quad \text{for } 0 \le \theta \le \frac{\pi}{2} \text{ and } 0 \le \phi \le 2\pi, \qquad (4.2)$$

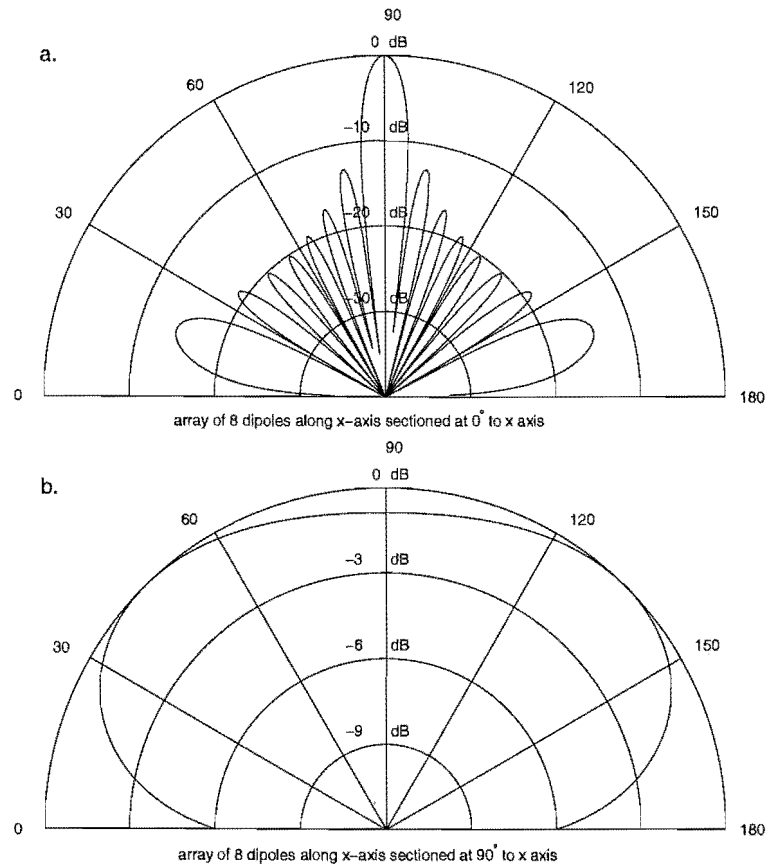

Figure 4.3: The theoretical beam shape from a single row of dipoles spaced by one wavelength. **(a)** In the E-W plane a thin beam is observed and **(b)** in the N-S plane a fan-shaped beam is observed.

where d is one quarter of a wavelength. Figure 4.3a shows the beam shape in the E-W plane obtained using this equation. Comparison of Figure 4.3a and Figure 4.1a shows that these beam shapes are very similar, as should be expected. The main difference is observed in the side-lobes closest to the ground, which are much larger in Figure 4.3a due to the dipole spacing. In the complete array, the effective spacing is 0.5λ, whereas here the spacing is exactly one wavelength so the pattern adds constructively in the ground plane. A line of point sources spaced by one wavelength would produce ground-lobes of the same magnitude as the main lobe, similar to those shown in Figure 3.7b. The actual pattern of this single row of dipoles goes to zero at 0° and 180° due to the power pattern of each individual dipole. The FWHM in this direction is the same as that for the entire array, that is 6.35°.

Figure 4.3b shows the N-S elevation of the beam power pattern. If this row of

dipoles was suspended in free space, then this pattern would be symmetric around the axis. However, due to the reflectors the beam is generally directed vertically with little radiation near the ground. The pattern in Figure 4.3b was not calculated using Equation 4.2, as this equation does not include the effects of the reflectors, instead it was created with the help of NEC (Numerical Electromagnetics Code), an antenna modelling program originally written by *Burke* [1981]. The FWHM in this plane was calculated to be 158°.

4.2 Positional Astronomy

To determine which stars will pass through the beam of the array and when this will occur, it is necessary to use positional astronomy. This section will introduce the concepts and details relevant to reverse radio astronomy.

4.2.1 Celestial Coordinate System

By imagining that all the heavenly bodies are situated on a sphere which has the same centre as the Earth, the coordinates of a particular star may be defined in a relatively easy manner. This imaginary sphere is called the *celestial sphere*, shown in Figure 4.4. The *celestial poles* and *celestial equator* are projections of their Earthly counterparts onto the celestial sphere and the point directly above the observer is called the *zenith*. Any semi-circle that runs from one celestial pole to the other is called a *meridian*, and the meridian that runs through the zenith is called the *observer's meridian*, highlighted in Figure 4.4 by a bold line. When an object lies on the observer's meridian it is said to be *in transit* [*Roy and Clarke*, 1994].

4.2.2 Star Coordinates

Any point on a sphere needs two coordinates to represent its location. For a heavenly body, the first is called the *declination*, δ, and is analogous to latitude as shown in Figure 4.5. This coordinate is measured in degrees from the celestial equator and like terrestrial latitude is positive for north and negative for south. This coordinate does not change with time. The second coordinate is known as the *hour angle*, HA, and is the angle from the observer's meridian westward to the star's meridian. This coordinate is not useful for cataloguing because it changes with time as the celestial sphere rotates relative to the Earth.

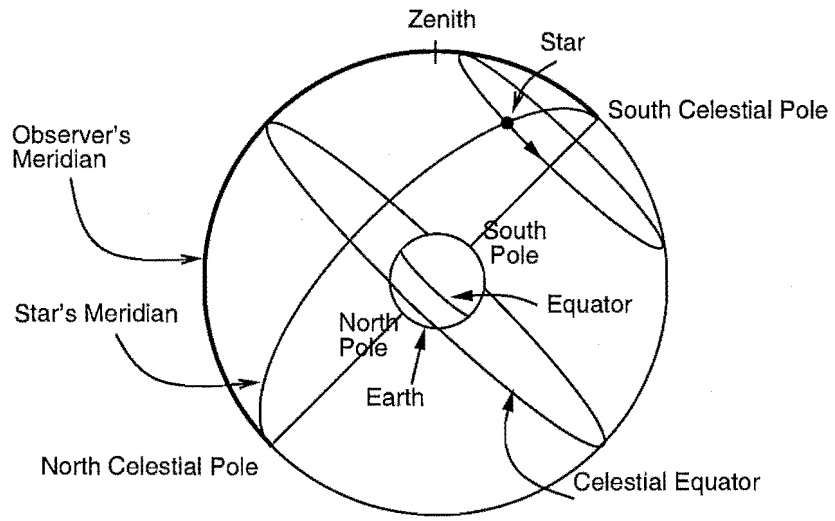

Figure 4.4: The celestial sphere showing the celestial poles, celestial equator, observer's meridian and zenith. The south celestial pole is on the upper half of the sphere because the zenith is positioned for an observer in the southern hemisphere.

To overcome this problem of rotation, a fixed point on the celestial sphere is chosen. The "longitude" of a star can then be measured from that fixed point in a similar way to longitude on Earth, which is measured from Greenwich in London. The point chosen is the *First Point of Aries*, Υ, also referred to as the *vernal equinox*. The angle measured eastward from Υ to the star is called the star's *right ascension*, RA, and is measured from 0^h to 24^h or $0°$ to $360°$.

Using the star's declination and right ascension, its position can be catalogued, but the observer still needs to know the position of Υ relative to the observer's meridian. Here, a time system called *sidereal time* is used. Instead of being based on the Earth's rotation relative to the sun it is based on its rotation relative to the stellar background, therefore the sidereal day is $3^m\,56^s$ shorter than the solar day [*Ridpath*, 1989]. The sidereal time at a particular longitude is the time that has elapsed since Υ last crossed the meridian associated with that longitude. This elapsed time is also the local hour angle of Υ. Greenwich sidereal time, GST, is the time elapsed since Υ last crossed the Greenwich meridian and its value for any particular day can be found in an astronomical almanac [e.g. *Nautical Almanac*

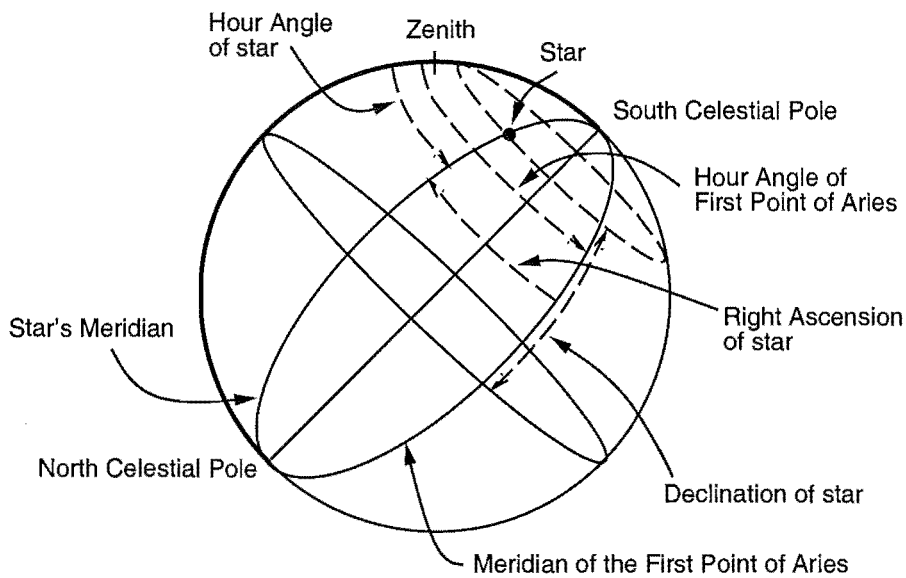

Figure 4.5: The celestial sphere, showing a star's declination, δ, hour angle, HA, and right ascension from the First Point of Aries, RA.

Office, 2001]. The local sidereal time, LST, can be found by simply adding the local longitude to GST, (or subtracting the longitude if it is west of Greenwich).

Once the LST is found, the hour angle of a star is simply

$$\mathrm{HA} = \mathrm{LST} - \mathrm{RA} \tag{4.3}$$

where HA is the time elapsed since the star crossed the observer's meridian. If this value is negative, then after that time, the star will cross the observer's meridian.

When the hour angle is zero, the star will cross the meridian and thus LST = RA. By calculating the GST, it is possible to obtain, using an astronomical almanac, the Greenwich Mean Time, or Universal Time, corresponding to the local time of meridian transit. New Zealand Standard Time can then be found by adding twelve hours to the Greenwich Mean Time. In summer, Daylight Savings must also be taken into account.

To illustrate, the sidereal time at which Centaurus A crossed the Birdlings Flat meridian on April 25, 2001, is found. Centaurus A is a strong radio source having a right ascension of $13^{\mathrm{h}}\,25^{\mathrm{m}}\,27^{\mathrm{s}}$. The source will be in the zenith when the LST is

equal to the source's right ascension, RA. Therefore,

$$\text{LST} = 13.42417^{\text{h}}.$$

Birdlings Flat is at a longitude of 172° 41.4′ E, which is equivalent to an angle of 11.5127^{h} east of Greenwich. Subtracting this angle from the LST gives

$$\text{GST} = 1.9115^{\text{h}}.$$

Greenwich Sidereal Time at 0^{h} UT on that particular day can be subtracted from this value to give the interval, in sidereal time, from 0^{h} to the star's transit. To convert this value into Universal Time, the interval is multiplied by 0.997270, changing it from sidereal time to solar time. From an astronomical almanac, Greenwich Sidereal Time at 0^{h} UT on April 25, 2001 is

$$\text{GST}_{\text{UT=0}} = 14.2052^{\text{h}}.$$

The sidereal time interval from 0^{h} UT is then -12.2937^{h} or, by adding 24 hours, 11.7063^{h}. Multiplying this by 0.997270 gives

$$\text{UT} = 11.6743^{\text{h}}.$$

New Zealand Standard Time is obtained by adding 12 hours to the Universal Time.

$$\text{NZST} = 23.6743^{\text{h}} = 23^{\text{h}}\,40^{\text{m}}\,28^{\text{s}}.$$

If this time was greater than 24 hours, then the transit time for the 26th of April would have been found.

4.3 Radio Sources

There are various radio sources in the sky; the sun, moon, planets and many stars are all sources of sky noise to varying degrees. Of primary concern here is the strength of these radio sources and whether they will pass through the beam of the antenna. The moon and planets are too weak to be useful for this project and therefore only stellar and solar sources will be discussed.

First, it is necessary to consider which objects will pass through the beam of the aerial. In Section 4.1.1, a single row of dipoles was found to have a FWHM of 158°.

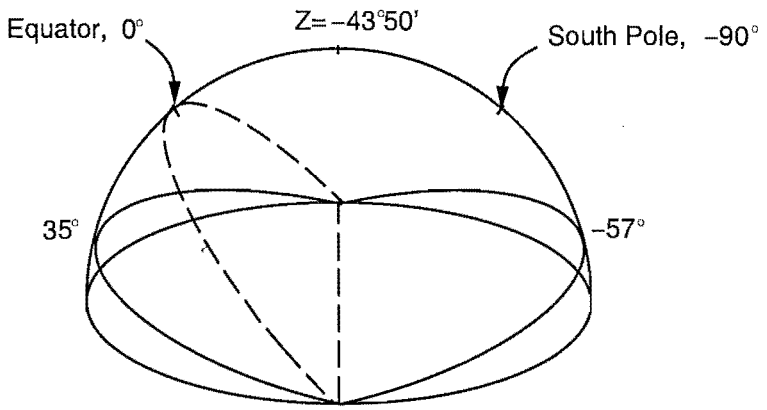

Figure 4.6: The celestial sphere with Birdlings_Flat (latitude 43° 49.5′ S) at the zenith showing, not to scale, the beam-width of a single row of dipoles. Stars with declinations between 35° and −57° will pass through the beam at some point during the day. Those with a declination between −57° and −90° will pass through the beam twice each day.

Figure 4.6 shows how this beam-width relates to declination on the celestial sphere. Any object with declination

$$\delta < 35^\circ \text{ N} \tag{4.4}$$

will at some time be within the beam of the aerial.

When the full antenna array is used the number of radio sources that will pass through the beam is greatly reduced as they have to be within 3.2° of the zenith. In terms of declination, this range corresponds to

$$40^\circ\ 37'\ \text{S} < \delta < 47^\circ\ 00'\ \text{S}. \tag{4.5}$$

4.3.1 The Sun

The most obvious source to consider is the sun itself, which passes through the beam of a single row of dipoles, but not through the beam of the entire array. The sun has a very strong radio emission and consequently has been used to verify the beam shape and pointing direction of radar antennas for many years [*Aarons*, 1954; *Eastwood*, 1960; *Riddle*, 1986]. The flux density of the sun varies considerably depending on whether it is quiet or disturbed and this variability makes the sun's flux difficult to predict from day to day. The large differences in solar emission between the

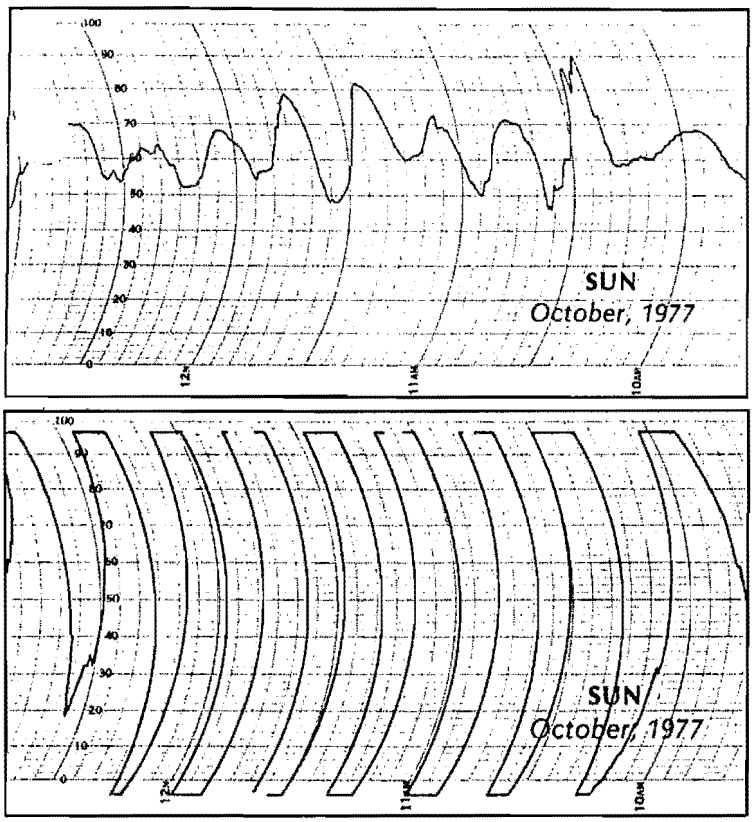

Figure 4.7: Solar activity as recorded on a phase-switching interferometer by *Swenson* [1978] on two different days in October, 1977; the first chart showing a quiet sun, the second showing the intense solar emissions of the sun when disturbed. The scale is the same in both cases emphasising the large differences that can occur.

quiet and disturbed sun, shown in Figure 4.7, are caused by sunspot activity on the surface of the sun. This varying emission from the sun can be divided into three groups, the quiet or undisturbed sun, the slowly varying component of the disturbed sun and the rapidly varying component of the disturbed sun.

The quiet sun has little or no sunspot activity and a quite stable emission. The effective temperature and flux density is shown in Figure 4.8. The slowly varying component of the disturbed sun has a time scale of days, weeks or even months. This component is caused by sunspot activity and is therefore at a maximum when a maximum number of sunspots occurs. The slowly varying component will have a small effect on measurements using the 42.5 MHz aerial ($\lambda = 7.06$ metres) as its radio emission is predominantly in the 3 to 60 cm wavelength range [*Kraus*, 1966].

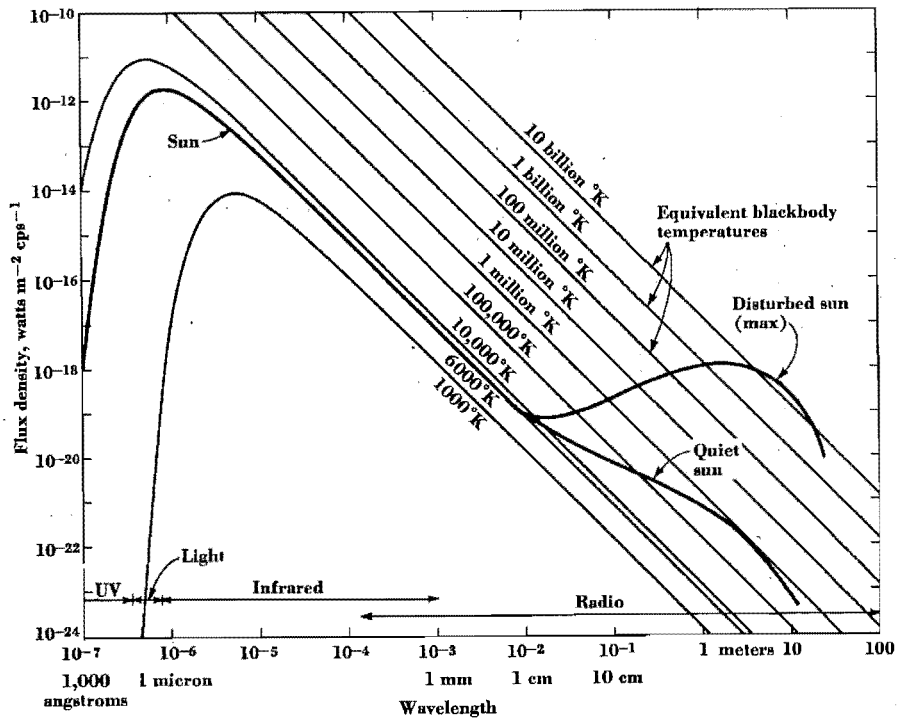

Figure 4.8: The solar spectrum of the quiet and disturbed sun showing flux density and equivalent black body temperature [*Kraus*, 1966].

The rapidly varying component of the disturbed sun does, however, emit over all radio frequencies. This component consists of solar flares, or bursts of radiation, that occur near sunspots. Typically, these last for time scales of seconds to hours. The effect on the temperature and flux density emitted when the disturbed sun is at its maximum is displayed in Figure 4.8. Examination of the region centred about wavelengths of seven metres indicates that the equivalent black body temperature of the quiet sun is around $T_s = 10^6$ K and the flux density is around 5×10^{-23} W m^{-2} Hz^{-1}. However, for the disturbed sun, the temperature is closer to $T_s = 10^{10}$ K and the flux density near 1×10^{-18} W m^{-2} Hz^{-1}. These figures are summarised in Table 4.1.

In addition to the above slow and rapid variations in the sun's emission, there is also the very slow sunspot cycle. The sun goes through an eleven year cycle from a maximum number of sunspots to a minimum number and back again. The most recent sunspot maximum was in June/July 2000, so in April 2001 when these measurements were taken the sun was still near its sunspot maximum. Figure 4.9

	Equivalent Black Body Temp, T_s	**Flux Density** (10^{-26} W m^{-2} Hz^{-1})
Quiet Sun	10^6 K	5000
Intermediate Sun	10^8 K	10^6
Disturbed Sun	10^{10} K	10^8

Table 4.1: Equivalent black body temperature, T_s, and flux density emitted from the sun at wavelengths of approximately 7 metres [*Kraus*, 1966].

shows the variation in sunspot number over the last two sunspot cycles.

The angular diameter of the sun varies with frequency. At 42.5 MHz it is approximately 0.75° which is slightly larger than the optical angular diameter [*Aarons*, 1954]. However, compared to the angular width of the CUSTAR antenna of 6.35°, this is quite small and approximates a point source.

The sun will pass through the beam of the single row antenna once every day and, although it will cross the observer's meridian at about 12 midday, the exact time will vary. To determine, for a particular day, when the sun will pass through

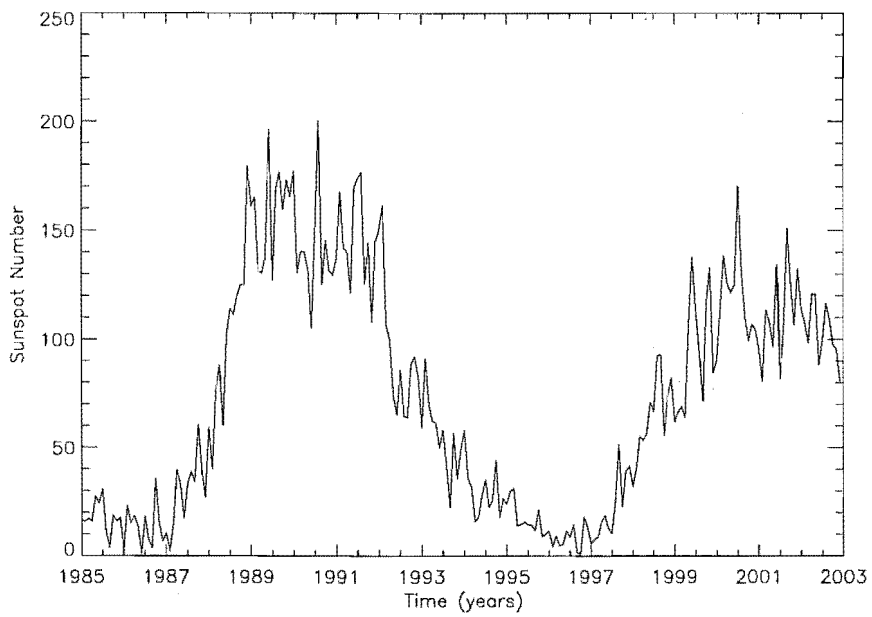

Figure 4.9: Monthly mean sunspot number from 1985 to 2003. Data provided by the National Geophysical Data Center (NGDC) (http://www.ngdc.noaa.gov/).

the beam the right ascension of the sun on that day needs to be known. This value can be found in an astronomy handbook [e.g. *Nautical Almanac Office*, 2001].

4.3.2 Extra-Solar Sources

There are many extra-solar radio sources, but most of them are quite weak. Table 4.2 shows a selection of the stronger radio sources that are within the beam of the antenna when it consists of only one row of dipoles.

Source	**Right Ascension** (1950)	**Declination** (1950)	**Flux Density** (10^{-26} W m^{-2} Hz^{-1})
Crab Nebula	$05^h\,31.5^m$	$+21°\,59'$	1420
LMC Centroid	$05^h\,22.0^m$	$-69°\,00'$	4000
Virgo A	$12^h\,28.3^m$	$+12°\,40'$	970
MSH16-61	$16^h\,10.8^m$	$-60°\,48'$	1190
Centaurus A	$13^h\,22.5^m$	$-42°\,46'$	2010
Vela XYZ	$08^h\,32.8^m$	$-45°\,37'$	1400
Galactic Nucleus	$17^h\,42.9^m$	$-28°\,50'$	1800

Table 4.2: The declinations and right ascensions, for epoch 1950, of some strong radio sources [*Kraus*, 1966].

Three strong radio sources pass through the beam of the complete array and these are the Vela-Puppis region, Centaurus A and part of the galactic equator. The galactic equator is a broad ridge of high radio emission so does not have exact coordinates, but the Vela-Puppis region and Centaurus A have relatively small angular sizes and these sources are now discussed in detail.

4.3.3 The Vela-Puppis Region

The Vela-Puppis complex consists of Vela XYZ and Puppis A. Vela XYZ is made up of three radio peaks commonly thought to be the remnant of a supernova explosion that also left behind the Vela pulsar [*Dwarakanath*, 1991; *Frail et al.*, 1997]. Puppis A is also thought to be a remnant from a supernova explosion. *Dwarakanath* [1991] published a 34.5 MHz map of the Vela-Puppis region which is shown in Figure 4.10a. The three peaks associated with Vela XYZ are labelled and Puppis A is observed

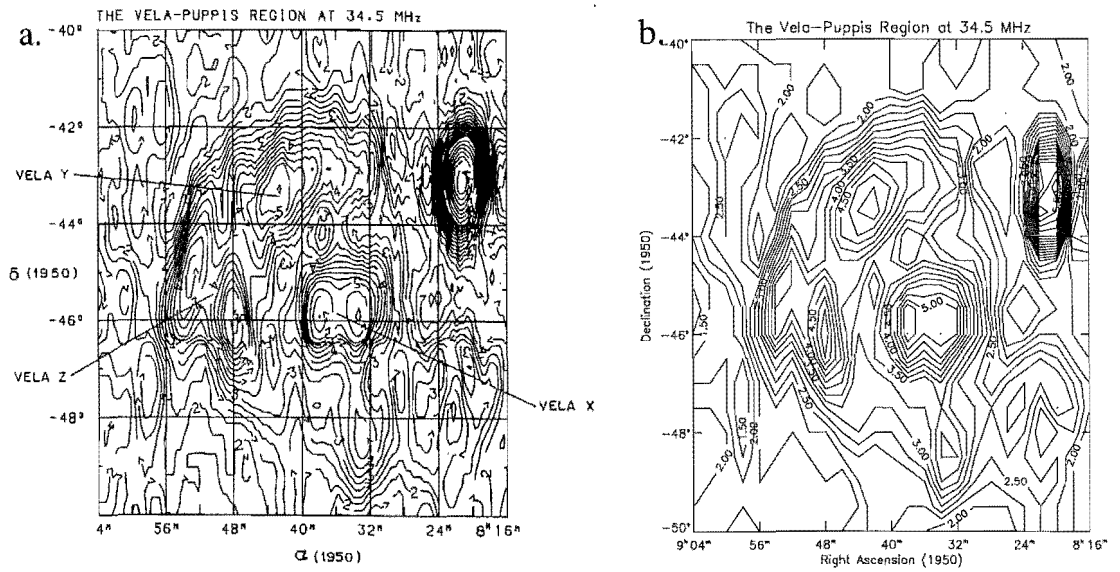

Figure 4.10: **(a)** A 34.5 MHz map of the Vela-Puppis region [*Dwarakanath*, 1991]. This has a resolution of $26' \times 84'$ in right ascension and declination, respectively. **(b)** A copy of **(a)** used to estimate the centre of the Vela-Puppis region as observed by the CUSTAR antenna. In both plots, the contours are labelled in units of 10^4 K and have a step size of 0.25×10^4 K.

at $\alpha = 08^{\mathrm{h}}\,22^{\mathrm{m}}$, $\delta = -43°$.

The angular size of the CUSTAR antenna beam corresponds to approximately 24 minutes of right ascension and 6° of declination. This means that the features in Figure 4.10a will not be resolved and will therefore be observed as one broad peak. The three Vela peaks have maxima ranging from 5.25×10^4 K to 5.75×10^4 K and Puppis A has a maximum of 6.75×10^4 K. Even though Puppis A has a larger maximum, it will not produce a stronger signal on the CUSTAR antenna than the other peaks because of its limited angular width.

An estimate of the right ascension at the centre of the broad peak that would be observed by the CUSTAR antenna was obtained by extracting the temperature data from Figure 4.10a and gridding it in a similar fashion (Figure 4.10b). Then, for each point in right ascension, a Gaussian curve centred at $-43°\,32'$, was multiplied by the associated vertical slice from Figure 4.10b. The total area under each resulting curve was found and is shown by the solid line in Figure 4.11. The declination of $-43°\,32'$ was chosen as it is the latitude of Birdlings Flat in epoch 1950 coordinates. The

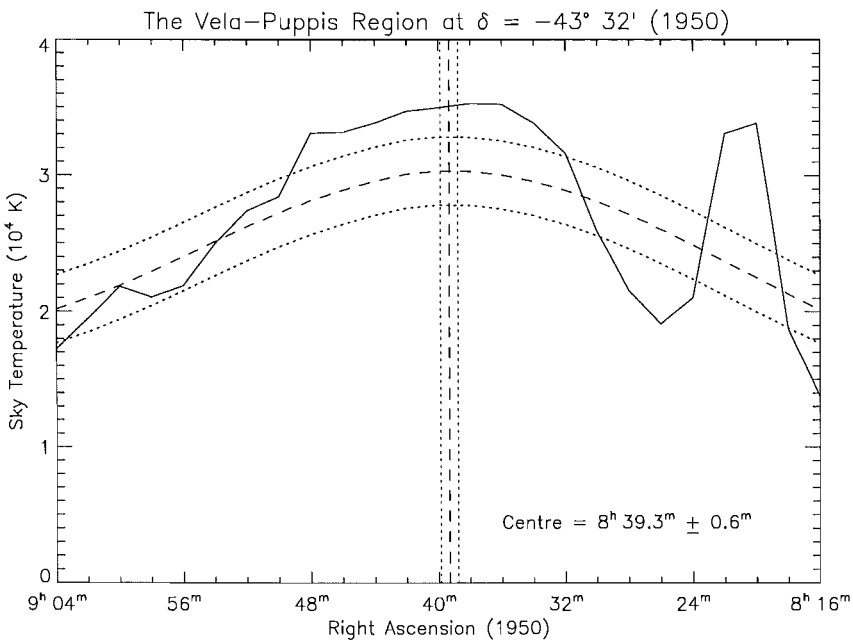

Figure 4.11: The Vela-Puppis region as observed by an antenna with a FWHM of 6.35° and centred at a declination of −43° 32′. The solid line shows the profile before convolution and the dashed line represents what the CUSTAR antenna should observe. The dashed vertical line shows the centre of the Vela-Puppis region as observed by the CUSTAR antenna. Dotted lines represent uncertainties.

width of the Gaussian curve needs to represent the width of the CUSTAR antanna, but because Figure 4.10b has already been smoothed to a resolution of $84' = 1.4°$ (in declination), the Gaussian will be slightly narrower than 6.35°. When two Gaussian curves are convolved with one another, the standard deviation of the resulting curve σ_c is

$$\sigma_c = \sqrt{\sigma_a^2 + \sigma_b^2}, \tag{4.6}$$

where σ_a and σ_b are the standard deviations of the original curves [*Aarons*, 1954]. The resolution of Figure 4.10b can be approximated as a Gaussian curve with a FWHM of 1.4°, so the Gaussian curve used to find each point in right ascension needs to have a width of

$$\sqrt{6.35^2 - 1.40^2} = 6.19°.$$

The solid line in Figure 4.11 represents what would be observed by an antenna with a resolution of 0.43° × 6.35° along right ascension and declination, respectively.

A Gaussian curve, this time oriented in right ascension and with width

$$\sqrt{6.35^2 - 0.43^2} = 6.34°,$$

was then convolved with the solid line, resulting in the dashed curve in Figure 4.11. The dotted lines show the uncertainty in this curve due to errors in the regridding of the data. This dashed line represents what the CUSTAR antenna should theoretically observe when the Vela-Puppis region passes through its beam. None of the individual features in Figure 4.10 are observed in this curve, because the width of the beam is too large to resolve them and acts as a low pass filter. The centre of the curve, shown by the vertical dashed line, is at a right ascension of $08^{\mathrm{h}}\,39.3^{\mathrm{m}} \pm 0.6^{\mathrm{m}}$, which in epoch 2002 coordinates is

$$\alpha = 08^{\mathrm{h}}\,41.1^{\mathrm{m}} \pm 0.6^{\mathrm{m}} \qquad \delta = -43°\,50' \tag{4.7}$$

where the declination is the latitude of Birdlings Flat and does not represent the centre of the Vela-Puppis region.

Unfortunately, due to the limited scope of Figure 4.10, the width of the Vela-Puppis region, as observed by the CUSTAR antenna, could not be directly estimated. However, if it is assumed that the region around this map is flat, Figure 4.11 can be extended so that the edges of the Gaussian curve can be observed. The temperature value used to extend the map was taken as the average of the end points of the solid line in Figure 4.11 and the uncertainty on these additional points was taken as 1×10^4 K. The resulting curves, obtained in the same manner as those in Figure 4.11, are displayed in Figure 4.12. The dashed line again represents what the CUSTAR antenna should theoretically observe. The width of the Gaussian curve mapped out by this line has a FWHM $= 9.2° \pm 0.4°$.

4.3.4 Centaurus A

Centaurus A is an active galaxy that has a radio emission spanning approximately 2° in right ascension and 6° in declination [*Sheridan*, 1958; *Burns et al.*, 1983]. However, most of the emission comes from a central nucleus. Figure 4.13 shows the central region of Centaurus A mapped at a frequency of 1.4 GHz. The nucleus is in the centre of this map and the two lobes are called the inner jets. The radio emission is strong for all these features, but the dimensions of the whole central source are less than a quarter of a degree.

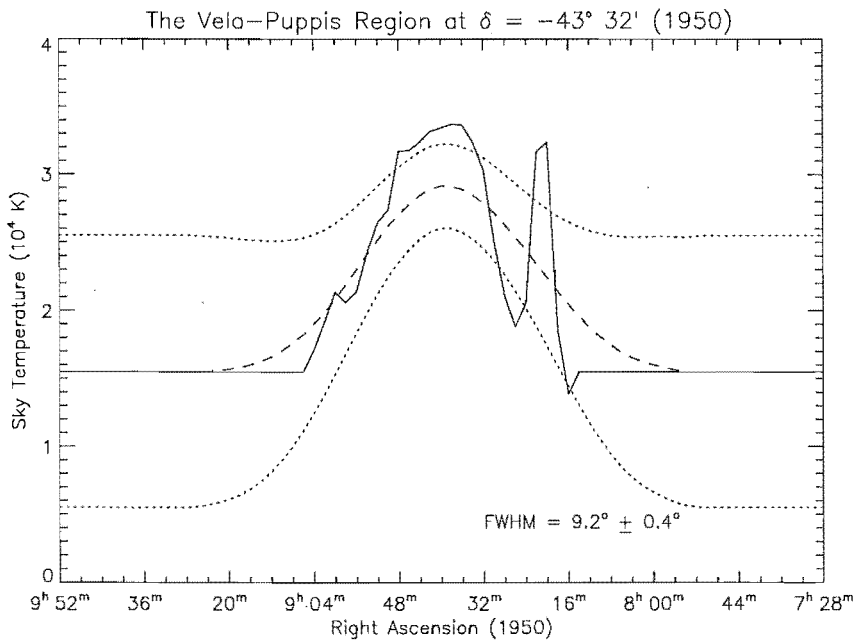

Figure 4.12: As Figure 4.11, but with an estimate of the surrounding region also included. The width of the dashed Gaussian curve is shown on the plot.

Sheridan [1958] performed a survey of Centaurus A at 85 MHz using an antenna with a beam-width of 50 minutes. At this resolution the central source appeared circular with the peak at $\alpha = 13^{\mathrm{h}}\,22.4^{\mathrm{m}} \pm 0.2^{\mathrm{m}}$, $\delta = -42^{\circ}\,41' \pm 4'$. Converted to epoch 2002 these coordinates become:

$$\alpha = 13^{\mathrm{h}}\,25.4^{\mathrm{m}} \pm 0.2^{\mathrm{m}} \qquad \delta = -42^{\circ}\,57' \pm 4'. \tag{4.8}$$

Shain [1958] compared the radio structure of Centaurus A measured at 19.7 MHz using a 1.4° beam-width with that measured at 85.5 MHz using a 0.8° beam-width. At declinations of −41° and −44.5° the FWHM of Centaurus A was found to be 1.7° and 1.4°, respectively, at 85.5 MHz and 2.2° and 2.4°, respectively, at 19.7 MHz. The frequency of the CUSTAR radar is approximately the geometric mean of these two frequencies so an estimate of the FWHM at 42.5 MHz will be the average of these values, that is 1.9° ± 0.5°. The declinations −41° and −44.5° are slightly above and below the centre of Centaurus A. The FWHM at the centre was deduced from a temperature map at 19.7 MHz [*Shain*, 1958] as approximately 2° which agrees well with the previous value.

Centaurus A as observed by the CUSTAR antenna will be broader than 1.9° ± 0.5°

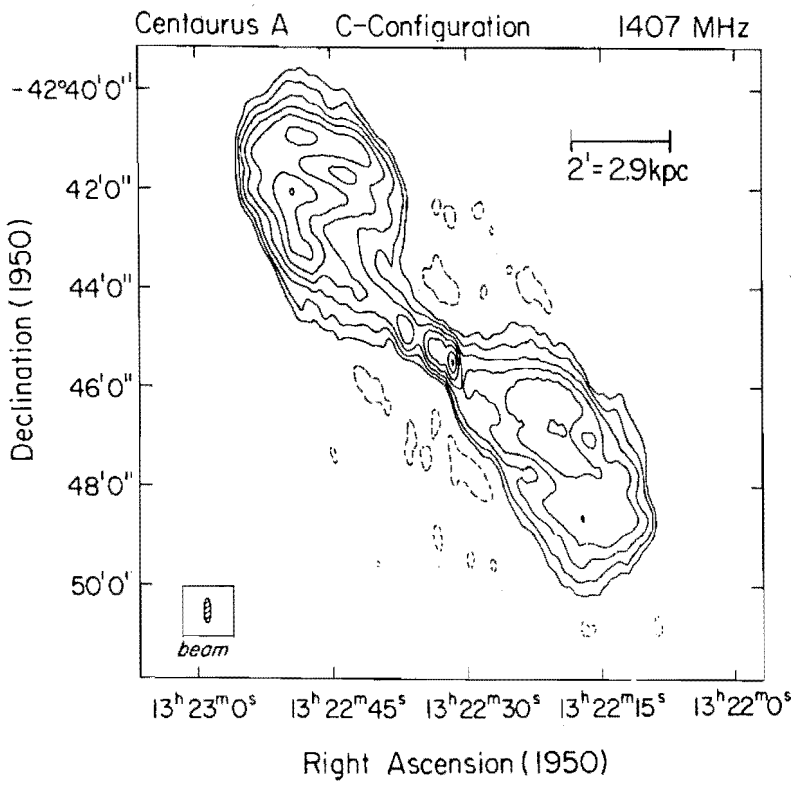

Figure 4.13: A 1.4 GHz map of the central Centaurus A region [*Burns et al.*, 1983]. The antenna used for this study had a resolution of $10'' \times 31''$ along R.A. and Dec. respectively. The map has contours of -2, 2, 4, 8, 16, 32, 64 and 95% of the peak.

due to the width of the antenna beam. Using Equation 4.6 the theoretical observed width is calculated to be $6.6° \pm 0.2°$.

4.4 Results for a Single Row

4.4.1 Single Row Receiver System

For measurements using a single row of the antenna array, the "total power" method of radio astronomy was used. This method involves recording the total noise power received on the aerial, so that when a radio source passes through the beam, a peak will be observed at the receiver output [*Kraus*, 1988].

The system used in this study is shown in Figure 4.14. The balanced output from the row of eight dipoles is converted to a 50 Ω unbalanced signal using a 1:1 balun. A

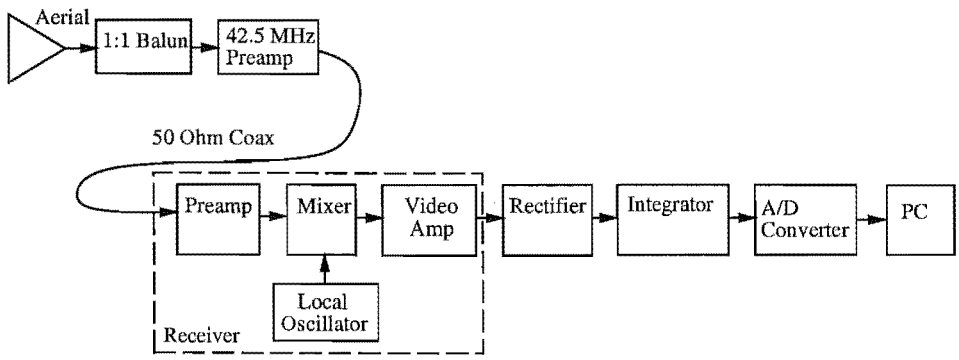

Figure 4.14: The receiver system used for the single row beam verification experiments.

24 dB HamTronics pre-amplifier was placed next to the aerial to amplify the signal well above any noise picked up on the long 50 Ω co-axial line back to the receiver hut.

Once inside, the signal is fed to a 42.5 MHz receiver which contains an R.F. amplifier, a mixer and a video amplifier. This receiver was a prototype of the receiver described in Section 3.3.3. For a total power receiver, no phase information is necessary, so only one of the two receiver channels was used. As in the final receiver, the R.F. signal is mixed with a local oscillator of frequency 42.5 MHz. This produces a signal with a much lower frequency which is amplified in a video amplifier and passed through a Bessel filter.

The output from the video section is then rectified and filtered to direct-current. Using a digital multimeter this DC voltage was transferred to a computer once every five seconds.

The prototype receiver had problems with the stability of its output. Due to the sensitive nature of direct-conversion receivers (see Section 3.3.3) the front-end or first section needs to be shielded very well. If this is not done satisfactorily then any local oscillator signal that is received by the front-end will lead to large shifts in the DC levels at the output. This was the case with the prototype receiver, and there were often large drifts and sometimes distinct steps in the output signal.

4.4.2 April 24-27, 2001

The reverse radio astronomy system was operational using a single row of dipoles for approximately one month from the middle of April, 2001, to the beginning of May.

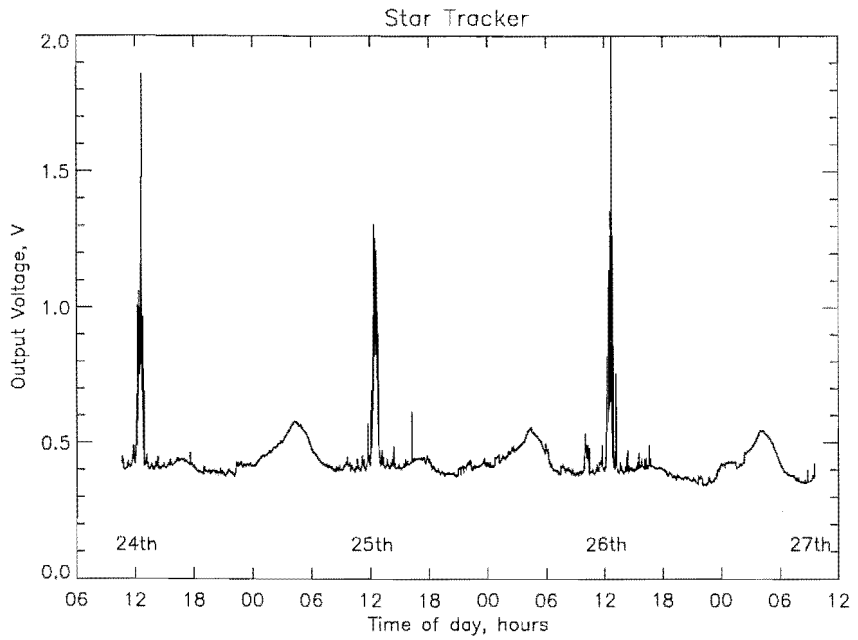

Figure 4.15: Output voltage measured by the digital multimeter from the 24th to the 27th of April, 2001.

As explained above, much of this data could not be used and to find satisfactory results, it was necessary to manually examine the data to remove periods where large unrealistic discontinuities were observed. One relatively stable period which contained very interesting results, was from the 24th to the 27th of April. The sky noise detected by the antenna array during this period is displayed in Figure 4.15. The data clearly shows a daily cycle, the most obvious sign being the large peak just after noon each day. This corresponds to the sun passing through the beam of the antenna. The wide peak at around 04:30 NZST each day is produced by the galactic plane, which includes the galactic nucleus. The small peak near 17:00 NZST is the other side of the galactic plane passing through the beam. These features, and others, can be observed more clearly by focussing on just one of the days.

Figure 4.16 shows data from the 25th of April. Also shown on this graph are the transit times of some major radio sources. The sun is the dominant feature and is studied in detail in the next section. The next largest feature is associated with the Galactic Nucleus, but it should be noted that the transit time does not match up exactly with the peak. This is because the Galactic centre is near the middle of a ridge which runs along the galactic equator. This ridge has very large radio

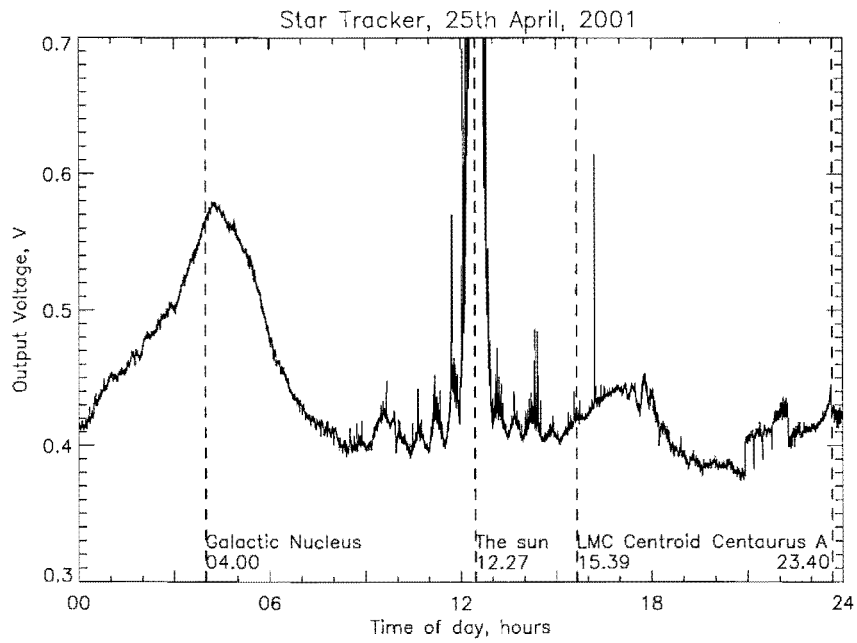

Figure 4.16: Results from the 25th of April, 2001, showing the transit times of the Galactic Nucleus, the sun, the LMC Centroid and Centaurus A.

emissions and stretches from a right ascension of approximately $16^{h}\,00^{m}$ to $20^{h}\,00^{m}$. This corresponds to between about 02:00 and 06:00 NZST, hence the broad peak at this time.

The galactic equator passes over the antenna array for a second time at around 17:00 NZST. This part of the equator produces a smaller signal because the radar beam is now orientated so that the edge of the galaxy is observed instead of the centre. The Large Magellanic Cloud (LMC) Centroid and Centaurus A have much smaller signals, but are also visible above the background noise level.

4.4.3 The Sun and the Sidelobes

The sun was particularly active near the end of April, 2001, and the signal received by the aerial system was therefore very large. As described in Section 4.3.1, the sun was near a sunspot maximum during 2001. The daily sunspot index and the 10.7 cm (2.8 GHz) flux density are good indicators of the strength of the sun's radio emission and both these variables show a large peak near April 25 (Figure 4.17). Comparison of the flux density at this time (200×10^{-22} W m^{-2} Hz^{-1}) with the solar spectrum in Figure 4.8 places it around half way between the curves shown for the quiet and

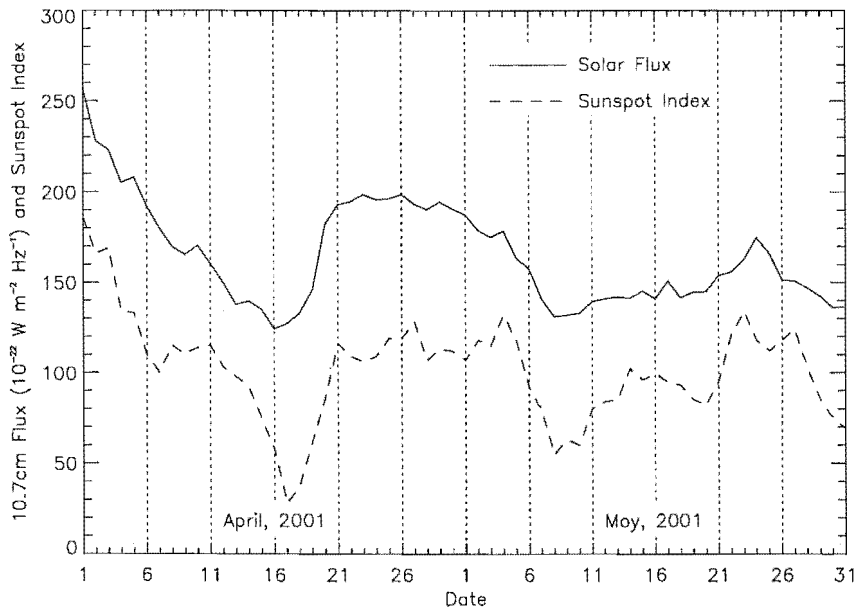

Figure 4.17: The Sunspot number and 10.7 cm solar radio flux recorded during April and May, 2001. Data provided by the National Geophysical Data Center (NGDC) (http://www.ngdc.noaa.gov/).

disturbed sun. The sunspot index of approximately 120 is not exceptionally large, as the maximum daily sunspot index for 2001 was 240, which occurred on March 27. However, it is above the average value for 2001 of 111, which is itself a large index due to the sunspot maximum at this time. The mean sunspot number for the last 11 year sunspot cycle is 65.

On April 25, the flux observed from the sun was large enough that, in addition to the large maximum associated with the sun passing through the antenna's main lobe, secondary maxima, associated with the sun passing through the antenna' side-lobes, were also observed. These secondary maxima are clearly visible in the output voltage measured by the digital multimeter, displayed in Figure 4.18. The voltage measured by the digital multimeter can be compared with the idealised theoretical beam pattern by comparing the solid line in Figure 4.18 with the dashed line.

Although quite noisy, it is clear that the theoretical beam shape matches well to the received signal, as the position and magnitude of many of the side-lobes are similar to the side-lobes observed within the data. There are, however, a number of discrepancies which need to be discussed. Firstly, before 08:00 NZST, the edge of

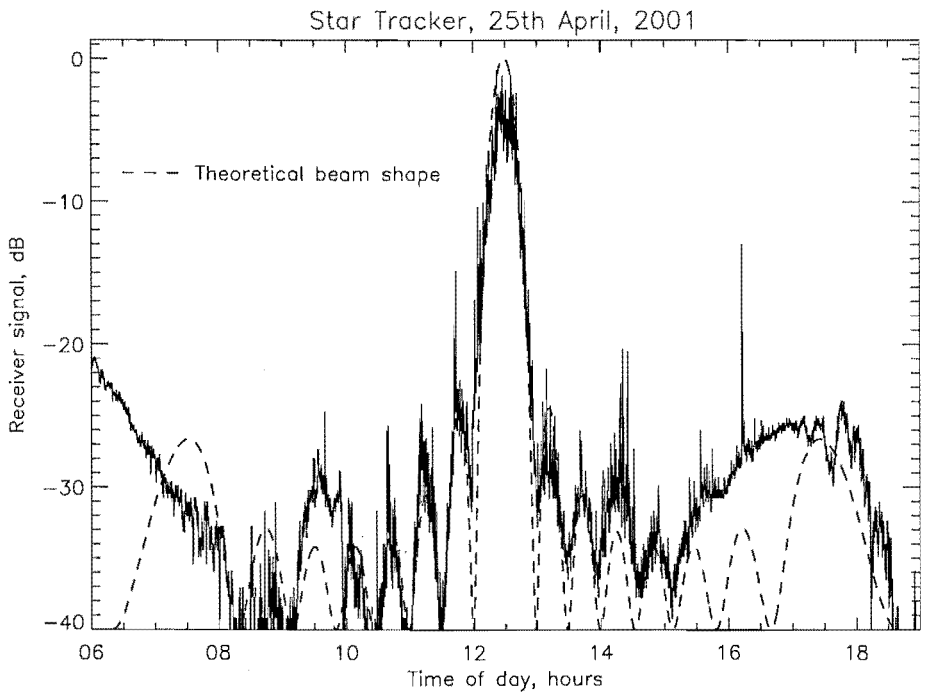

Figure 4.18: The sun passing through the beam on the 25th of April. The full beam pattern can be seen, including the large main lobe and the smaller sidelobes. The theoretical beam shape (dashed line) is shown for comparison.

the galactic equator is observed in the main lobe. The sun is not observed in the ground-lobe at 07:30 because it does not rise above the Banks Peninsula hills, which are to the east of the antenna, until later in the morning. At 09:30 the galactic equator passes through the antenna ground-lobe, and thus the increase in signal at this time is a superposition of the galactic equator in the ground-lobe and the sun in one of the side-lobes. Between 16:00 and 18:00 the quieter side of the galactic equator passes through the main lobe and the increased signal between 15:30 and 16:00 is due to the Large Magellanic Cloud. These sources obscure the signal from the sun received in the side-lobes, but the variable signal between 17:30 and 18:30 is likely to be the sun passing through the western ground-lobe.

The other differences throughout this time are probably due to variability in the sun's output. As explained in Section 4.3.1 solar flares can happen over a period of minutes, causing solar emission to vary considerable over short time scales. This makes the signal received from the sun very noisy. A possible example of this is the difference in magnitude between the second and third side-lobes of the afternoon.

The second side-lobe, beginning at 13:30, receives a signal that is smaller than that received by the third sidelobe, beginning at 14:00, when theoretically the third side-lobe should be smaller than the second. These variations could be reduced by averaging data over a number of days and examination of Figure 4.15 shows that the pattern observed in Figure 4.18 is repeatable. Unfortunately, due to the short measurement campaign and the difficulties experienced with the receiver, a large enough dataset to pursue this theory was not produced.

Despite these discrepancies, the antenna array behaves as expected. The main feature that shows this is the null points between the lobes. If there was a problem with the spacing of the dipoles or the feed system used, the lobes would be shifted from their theoretical position. It can be observed in Figure 4.18 that even though the sizes of the lobes do not match the pattern exactly, their positions match well. This means that the theoretical FWHM of 6.35° is an accurate representation of the actual beam-width. Although this result was obtained using only a single row of dipoles, it is indicative of that expected for the complete array, since the final array is made up of 16 rows identical to the one detailed here.

4.5 Results for the Complete Array

Reverse radio astronomy has also been performed using the completed antenna array. Theoretically, the full array should produce a thin vertically pointing beam with a FWHM of 6.35° (see Section 4.1). This means that only radio sources that pass near the zenith will be observed by the antenna. Two radio sources, Vela XYZ and Centaurus A, pass quite close to the zenith (see Table 4.2) and these are observed when the entire array is in operation.

The transit times of Centaurus A and Vela XYZ were compared to the right ascension calculated in Section 4.3 and also to a 45 MHz sky map obtained from *Alvarez et al.* [1997].

4.5.1 Full Array Receiver System

In a similar fashion to that used for the measurements using a single row, the full antenna array was used as a stellar radio receiver from November 1, 2001, to August 19, 2002. The experiment did not run continuously as the receiver equipment was being constructed and developed during this time. From August 28, 2002, onwards,

the radar was in operation and the sky noise was calculated as part of the signal processing scheme.

As the equipment was developed the receiving arrangement underwent a number of configuration changes. Initially, the system was similar to that for a single row (Section 4.4.1) except with the balun as described in Section 3.2.3 and the preamplifier located inside the receiver hut. During the first month of operation it was found that the computer did not keep accurate time. This was remedied on December 7, 2001, by repeatedly resetting the CMOS clock to an external clock which was much more accurate. When the analogue to digital converter was completed at the beginning of July, 2002, this replaced the digital multimeter that had been in use to this date. With the new ADC in place, the rectifier and integrator circuits were removed and these processes were performed in software. On the 9th of August, the new receiver replaced the prototype, and from the 19th onwards the antenna was used for both transmission and reception as part of the completed radar system.

From August 28, 2002, when the radar was in operation, the sky noise was calculated from the background noise. The signal processing scheme described in Section 5.2 calculates the background noise of each range bin for each radar run. Figure 4.19 shows the background noise for a typical day as a function of time and height. Below 5 km the background noise is dominated by instrumental noise, mainly due to the receiver being overloaded by the transmitter pulse (see Section 5.1.2). Above this, however, the sky noise is dominant. For most of the day, the magnitude of the noise is constant for all heights above 5 km, which suggests that the noise is almost solely due to sky noise. The strong features, namely the peaks at approximately 08:00, 13:00 and 16:00 NZST, are repeated each day and are due to Vela XYZ, Centaurus A and the galactic equator.

Some features can be seen that are not due to sky noise. For instance at 09:00 NZST between 12 and 14 km there is a large increase associated with reflections from an aircraft. There are other sources of noise, not observed in Figure 4.19, that can also increase the noise level. During rain or in misty weather conditions, moisture can collect on the wires of the antenna array and, due to the static in the rain droplets, the noise level (over all range bins) can increase. Canterbury has relatively dry weather conditions, so only a small percentage of days are affected by rain static.

For each day, a time-series of the sky noise was produced by averaging over 25

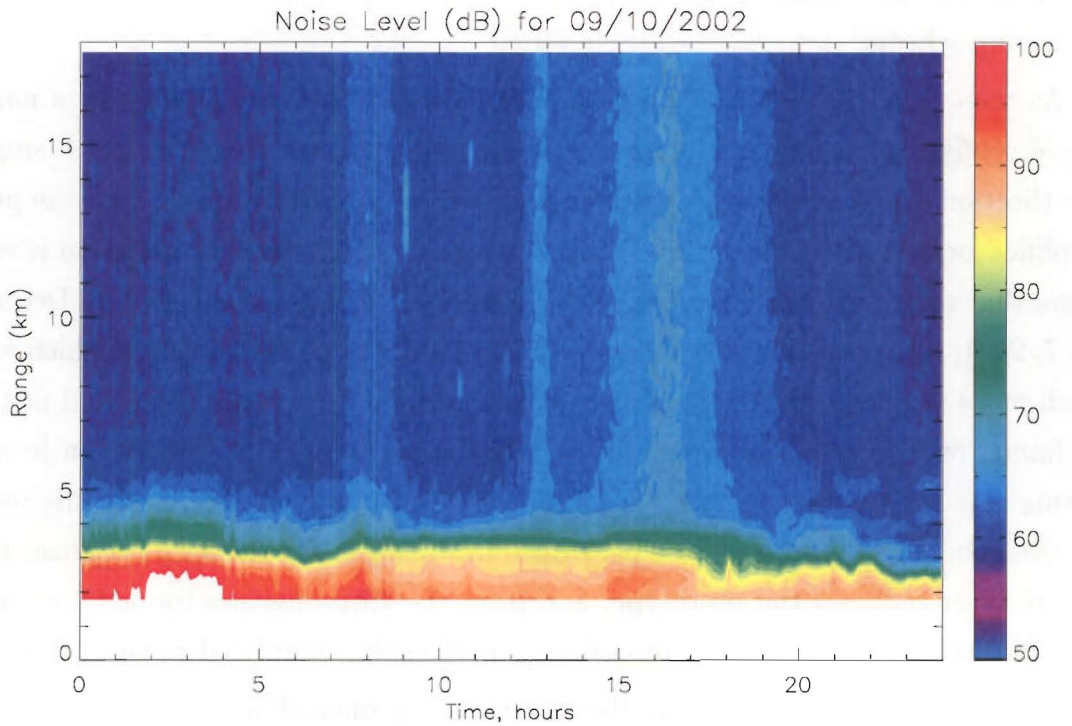

Figure 4.19: Background noise on the 9th October, 2002, plotted in dB. This noise data was obtained from power spectra using the method proposed by *Hildebrand and Sekhon* [1974] (see Section 5.2.3).

selected range bins. It is clear that if all the range bins were used, the sky noise would be contaminated by instrumental noise and signals from aircraft. Instrumental noise and reflections from aircraft tend to produce noise levels that are significantly higher than the sky noise and, because sky noise is always present, the measured noise level should never be below the sky noise level. Because of this, a good estimate of the sky noise at any particular time can be obtained from the range bin containing the lowest noise value. There are 54 (usable) range bins, and a better estimate of the sky noise could be achieved by averaging over all the range bins that contain only sky noise. By choosing the 25 range bins with the lowest noise levels, the time series is smoothed considerably, while the possibility of including areas of unwanted noise, such as aircraft reflections, is minimised. The chosen bins were generally those at ranges above 10 km, except when reflections from aircraft were received.

This method of processing the background noise does not remove all unwanted noise. Slow fluctuations in the system noise will still be included as will noise sources

that affect all range bins, such as interference from other radio equipment and rain static on the antenna array. However, these effects should be irregular and can therefore be reduced by integrating the sky noise data over many days.

4.5.2 Results Obtained Between December 2001 and April 2002

Before September, 2002, the radar was not operational and the antenna array was used solely as a receiver. As explained above, the receiver equipment was being developed during this time and it was not until the radar became operational, that the equipment was finished and working correctly.

Due to the computer timing error before December 7, 2001, the data collected over this period could not be used to verify the beam pointing direction, as accurate positioning of the radio sources requires accurate knowledge of their transit times. For this reason, data collected before December 7 is not presented in this study.

Before the radar became operational, sky noise data was collected at 5 second intervals. The time stamp for each data point was altered so that it was the point's right ascension. This alteration is described in Section 4.2.2. The data was then smoothed and regridded at two minute intervals, so that an average could be taken over many days.

For almost all of the remainder of the time until the radar was operational, the prototype receiver was used to collect the cosmic noise. As discussed in Section 4.4.1, this receiver was not very stable and caused severe noise level fluctuations throughout this time period. Figure 4.20 contains some typical results from four consecutive days in February, 2002. The data is obviously unstable and no clear pattern can be observed, although there is a peak at a right ascension of $17^{h}\,00^{m}$ on each day.

Until the new ADC was put in place at the beginning of July, 2002, data was collected for a total of 46 days and is shown in Figure 4.21a. This graph shows the large spread in the results obtained during this time. In order to make the mean of these results more representative of the actual sky noise, data points that varied by more than half of one standard deviation away from the median were removed, leaving the data shown in Figure 4.21b. The removal of such a large proportion of the data (22 %) was necessary to remove most of the spurious points seen above 1.0 in Figure 4.21a.

Figure 4.22 contains the median of the data from Figure 4.21b. The median was used because of its ability to resist outlying points. Despite the fluctuations caused

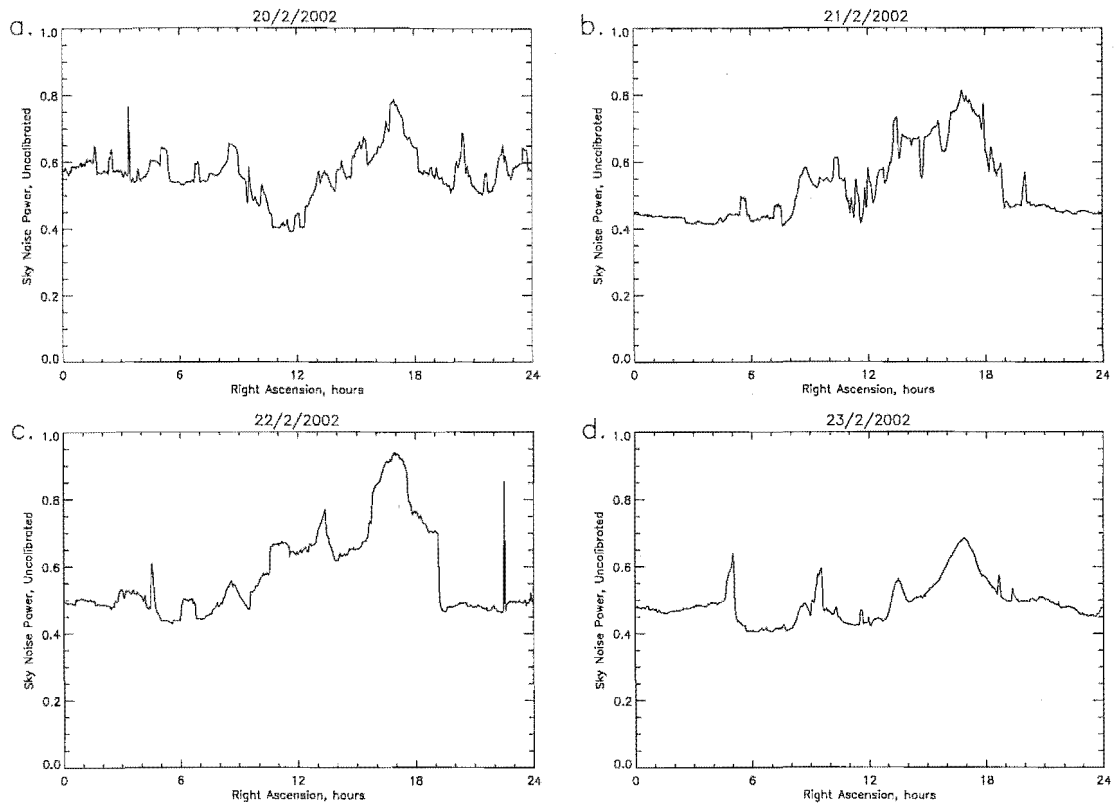

Figure 4.20: Typical sky noise data obtained using the prototype receiver. The data has been plotted against right ascension.

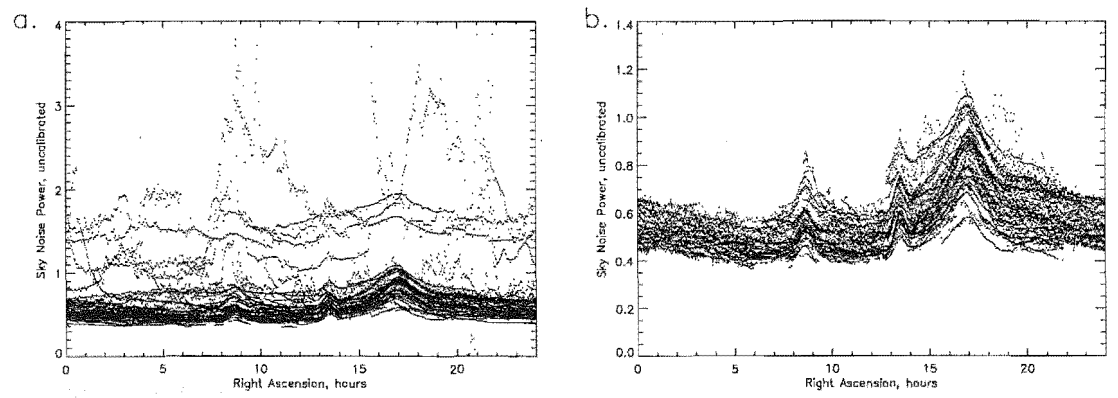

Figure 4.21: Scatter plots of **(a)** all data points recorded between December 7, 2001, and April 18, 2002, and **(b)** only those points deviating by less than half of one standard deviation from the median. Note the change in y-axis scale.

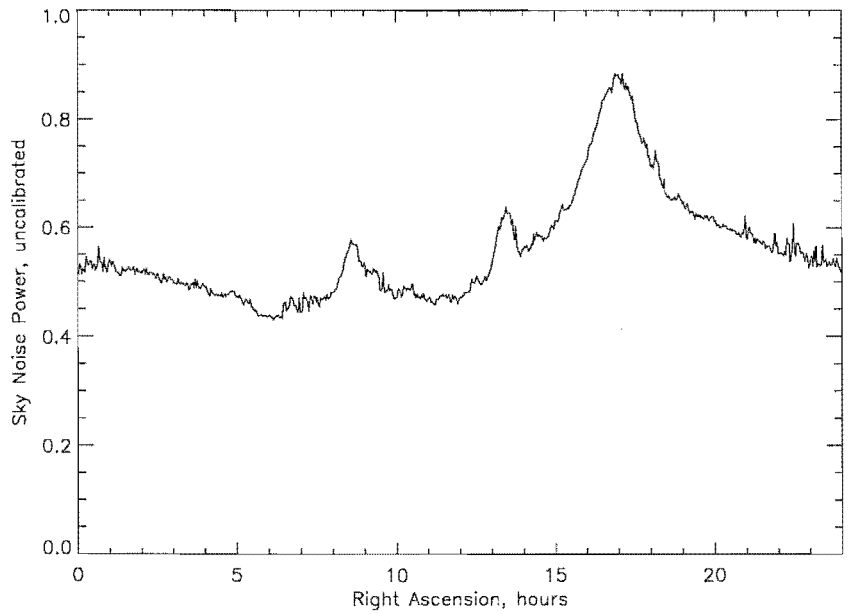

Figure 4.22: Sky noise measured by the CUSTAR antenna between December 7, 2001, and April 18, 2002. The graph is a median of the data shown in Figure 4.21b. The first peak is Vela XYZ, the second is Centuarus A and the third and largest is the galactic equator.

by the receiver, the expected radio sources are observed clearly. The three prominent peaks at right ascensions of $08^{\mathrm{h}}\,30^{\mathrm{m}}$, $13^{\mathrm{h}}\,30^{\mathrm{m}}$ and $17^{\mathrm{h}}\,00^{\mathrm{m}}$ are the Vela-Puppis region, Centaurus A and the galactic equator, respectively.

To make comparisons between the theoretical right ascensions found in Sections 4.3.3 and 4.3.4 and those measured by the CUSTAR antenna, Gaussian curves were fitted to the peaks associated with Vela XYZ and Centaurus A. This procedure was not performed for the peak associated with the galactic equator as it does not have exact coordinates. Using the data in Figure 4.22 and the standard deviation at each point in right ascension calculated from Figure 4.21b, a non-linear least squares fit was found using the Levenberg-Marquardt method [*Press et al.*, 1992]. The function $f(t)$ used to fit the data was a Gaussian plus a second-order polynomial given by

$$f(t) = A \exp\left[-\frac{\left(\frac{t-B}{C}\right)}{2}\right] + D + tE + t^2F, \tag{4.9}$$

where A to F are the fitting parameters. B gives the position of the centre of the

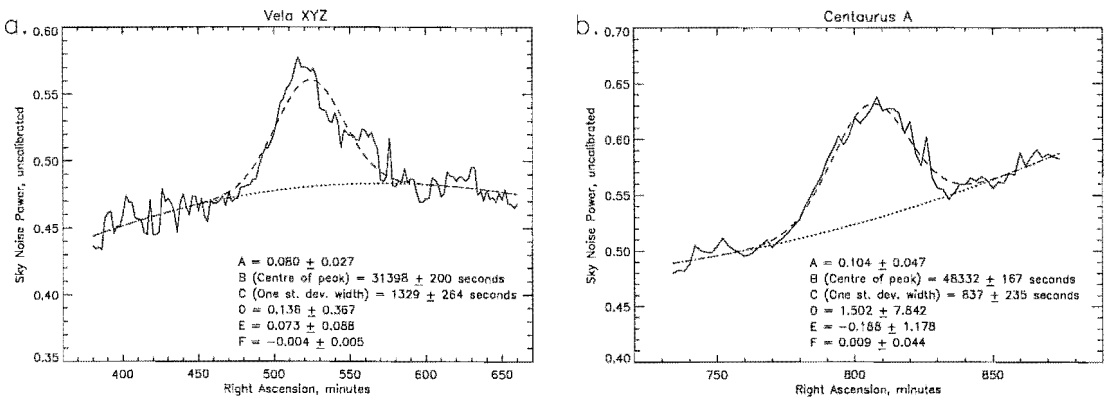

Figure 4.23: A Gaussian and second-order polynomial fit to CUSTAR data for **(a)** Vela XYZ and **(b)** Centaurus A. The solid line is the CUSTAR data (obtained between December 7, 2001, and April 18, 2002), the dotted line is the polynomial fit and the dashed line is the Gaussian plus polynomial fit.

Gaussian and C is its one standard deviation width. The polynomial was included to account for changes in the background sky noise. The additional curve's parameters are most important for Centaurus A which is superimposed on the edge of the galactic equator.

The fits for Vela XYZ and Centaurus A are shown in Figure 4.23a and 4.23b, respectively. In each case the data is displayed as a solid line and the Gaussian plus polynomial fit as a dashed line. The fitting parameters have been included on the plots, along with one standard deviation uncertainty estimates.

The centres of the fitted Gaussian curves have right ascensions of $\alpha = 08^{\mathrm{h}}\,43^{\mathrm{m}}\,18^{\mathrm{s}}$ for Vela XYZ and $\alpha = 13^{\mathrm{h}}\,25^{\mathrm{m}}\,32^{\mathrm{s}}$ for Centaurus A. The one standard deviation uncertainty estimates for these values are 200 and 167 seconds, respectively. The differences between these right ascensions and the theoretical ones given in Equations 4.7 and 4.8 come to $132^{\mathrm{s}} \pm 236^{\mathrm{s}}$ and $8^{\mathrm{s}} \pm 179^{\mathrm{s}}$ for Vela XYZ and Centaurus A, respectively. These results show that, within uncertainties, the antenna beam is pointing vertically. However, the large uncertainties, which are mainly due to the spread in the CUSTAR data, mean that the results are not convincing. The much larger difference in the Vela XYZ position is most likely due to the extra peak on the right-hand side of the curve in Figure 4.23a. The fitting routine attempts to include this peak in the Gaussian fit which shifts its centre to the right.

The widths of these peaks can also be compared to those calculated in Sec-

tions 4.3.3 and 4.3.4. Converted to FWHM, the values for C in Figure 4.23 are $13.0° \pm 2.6°$ and $8.2° \pm 2.3°$ for Vela XYZ and Centaurus A, respectively. Both of these widths are larger than expected, the differences coming to $3.8° \pm 3.0°$ and $1.6° \pm 2.5°$, respectively. That the widths are larger than expected, suggest that the antenna beam is broader than predicted by theory. However, the uncertainties are large and, in the case of Centuarus A, allow for a beam-width difference of zero degrees. For Vela XYZ, the measured width does not agree, within uncertainties, to the theoretical width and this may be due to the additional peak on the right-hand side of the Vela XYZ curve mentioned earlier.

4.5.3 Results Obtained in July and August 2002

Near the beginning of July, 2002, the new analogue to digital converter replaced the digital multimeter and was used to collect sky noise data until August 6. The results from this time period have been analysed in a similar manner to that described in the previous section. Although this data set contained a large spread, there was a much smaller number of outlying points than that from the previous section. This meant that it was not necessary to remove such a large proportion of the data, so only those points that did not deviate by more than 2 standard deviations from the median were removed, and the remaining points are shown in Figure 4.24a. Using a two standard deviation cut-off point resulted in the removal of only 1.3% of the data.

Figure 4.24b contains the median of the data from Figure 4.24a. The three main peaks corresponding to Vela XYZ, Centaurus A and the galactic equator can again be observed. The main difference between this figure and Figure 4.22 is the large increase between 5^h and 8^h. This right ascension corresponds to approximately 09:00 NZST. It is thought that the increase is due to temperature changes in some part of the receiver system, as the receiver output increases abruptly at dawn, stays relatively constant for 7 or 8 hours before beginning to decrease. The piece of equipment most likely to be the cause of this instability was the ADC, which, during its first month of operation, had not been shielded adequately.

A Gaussian curve and second-order polynomial was fitted to both the Vela XYZ and Centaurus A peaks and the results are displayed in Figure 4.25. The centres of the fitted Gaussian curves have right ascensions of $\alpha = 08^h\,39^m\,52^s \pm 5^m\,24^s$ for Vela XYZ and $\alpha = 13^h\,28^m\,15^s \pm 5^m\,10^s$ for Centaurus A. The differences between

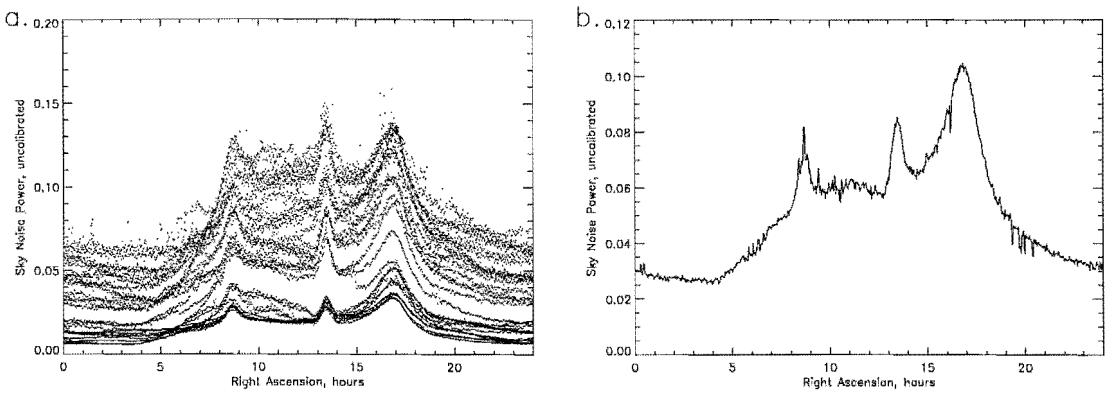

Figure 4.24: Sky noise measured by the CUSTAR antenna between July 5 and August 6, 2002. **(a)** Scatter plot of all data points deviating by less than 2 standard deviations from the median. **(b)** Median of the data shown in **(a)**. Note the change in y-axis scale.

these right ascensions and the theoretical ones are $-74^s \pm 360^s$ and $171^s \pm 322^s$ for Vela XYZ and Centaurus A, respectively. Like those from Section 4.5.2, these results suggest that the antenna beam is pointing vertically, but again the uncertainties are very large. It should be noted that Vela XYZ is now observed before expected, whereas in the previous section is was observed later than expected. Also, the position of Centaurus A has moved in the opposite direction, that is, it is observed later than in the previous section.

The FWHM of these peaks are $9.1° \pm 3.6°$ and $9.2° \pm 4.8°$ for Vela XYZ and Centaurus A, respectively. The width of Vela XYZ agrees well with the expected value and Centaurus A is again wider than expected. The differences between the measured and theoretical values are $-0.1° \pm 4.0°$ and $2.6° \pm 5.0°$, respectively.

The uncertainties for the results in this section are larger than for the previous section as there is a larger vertical spread in the data (compare Figures 4.21b and 4.24a). In Figure 4.21b the vertical spread at any right ascension is approximately 0.2 while the range through which the median varies over the whole day is just under 0.46. In this case the spread is then 43% of the range. In Figure 4.24a, the corresponding values are 0.06 and 0.08, resulting in a spread that is 75% of the range, which is almost twice as large. The very large spread observed in Figure 4.24a may be caused by the same effect that produced the increase in noise level during daylight hours. If this increase is a temperature effect (as explained above), then

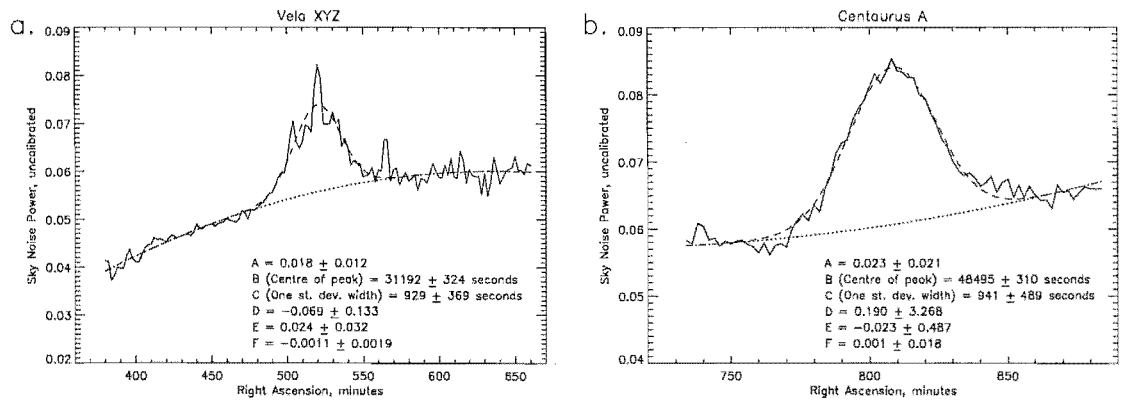

Figure 4.25: A Gaussian and second-order polynomial fit to CUSTAR data for **(a)** Vela XYZ and **(b)** Centaurus A. The solid line is the CUSTAR data (from between July 5 and August 6, 2002), the dotted line is the polynomial fit and the dashed line is the Gaussian plus polynomial fit.

variations in the temperature from day to day could also cause variations in the average noise level. The large spread and the increase during the day are not observed before or after the period discussed in this section (see Figures 4.21a and 4.26a) so it is reasonable to assume that it is not a real effect, but something arising due to the equipment used during this time.

4.5.4 Results Obtained After August 2002

From August 28th, 2002, onwards, the ST radar system was in full operation. Using the scheme described in Section 4.5.1, 480 sky noise data points were calculated each day, each having a time stamp in New Zealand Standard Time. These were altered so that the associated time for each point was the point's right ascension. After conversion to right ascension, the data needed to be gridded regularly so that at each point, an average over many days could be taken. Using a cubic spline the data was interpolated at two minute intervals starting at $00^{h}\,00^{m}$ and finishing at $23^{h}\,58^{m}$. This grid was chosen as it matches that used by *Alvarez et al.* [1997] for the 45 MHz continuum survey described in Section 4.5.5.

From September 1 to December 28, 2002, 113 full days of data were collected and the noise level values calculated using the scheme described above are shown in Figure 4.26a. Most of the points are grouped near the bottom of the chart and

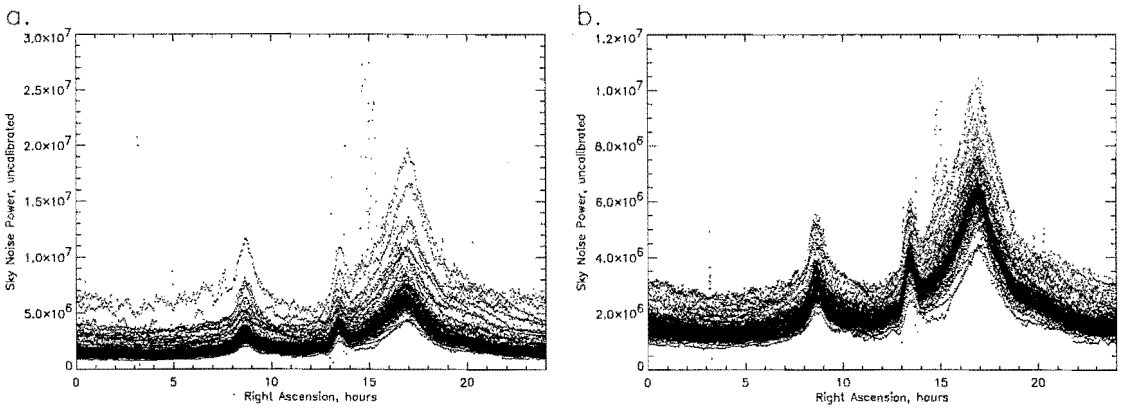

Figure 4.26: Scatter plots of **(a)** all data points recorded between September 1 and December 28, 2002, and **(b)** only those points deviating by less than two standard deviations from the median. Note the change in y-axis scale.

follow a pattern similar to that observed in Figures 4.22 and 4.24b. However, there are a number of points which do not and these clearly do not represent the sky noise alone. There were further points, not shown in Figure 4.26a, with a sky noise power higher than 4.0×10^7 which are possibly related to aircraft echoes. Figure 4.26b shows a similar plot which includes only data deviating by less than two standard deviations from the median. This scatter plot is much smoother and will produce a more accurate representation of the mean sky noise. About 5 % of the data was removed using the standard deviation limiting procedure.

The median sky noise calculated from the data displayed in Figure 4.26b is shown in Figure 4.27. This graph contains a much smoother profile than those observed previously in Figures 4.22 and 4.24b. This is due to the more stable receiver equipment and also the larger sample size.

The Gaussian fitting routine described earlier was performed again on Vela XYZ and Centaurus A with the data displayed in Figure 4.27 and the results are given in Figure 4.28. The centres of the Gaussians have right ascensions of $\alpha = 08^h\,40^m\,02^s$ for Vela XYZ and $\alpha = 13^h\,25^m\,41^s$ for Centaurus A. The uncertainties are smaller than in the previous sections and come to 104 and 61 seconds, respectively. The differences between these right ascensions and the theoretical values in Equations 4.7 and 4.8 are $-64^s \pm 140^s$ and $17^s \pm 73^s$ for Vela XYZ and Centaurus A, respectively.

In this case the widths of the fitted Gaussian curves are both larger than expected. For Vela XYZ, the FWHM is $11.9^\circ \pm 1.3^\circ$ and for Centaurus A it is

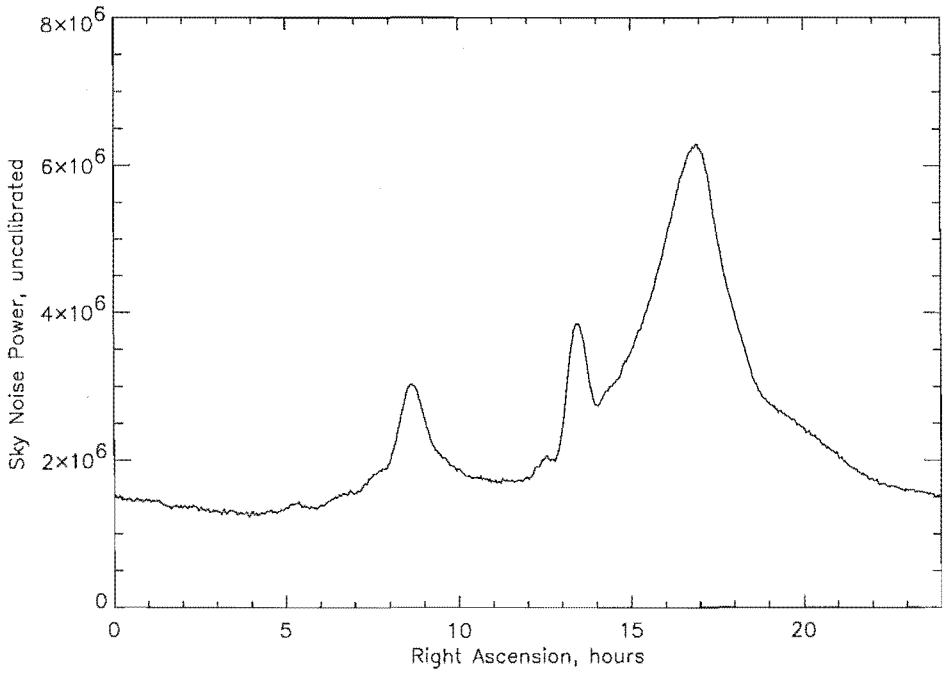

Figure 4.27: Sky noise measured by the CUSTAR radar. The graph is an average over 113 days between September, 2002, and December, 2002. The first peak is Vela XYZ, the second is Centuarus A and the third and largest is the galactic equator.

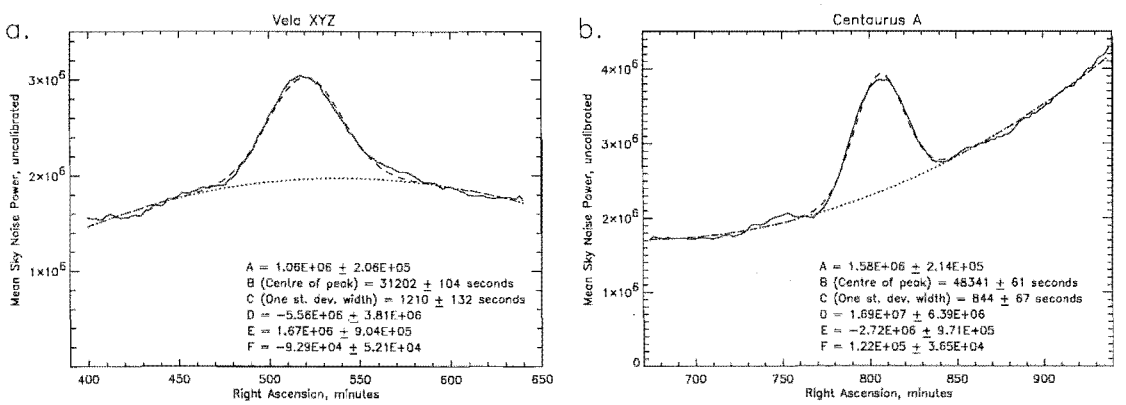

Figure 4.28: A Gaussian and second-order polynomial fit to CUSTAR data for **(a)** Vela XYZ and **(b)** Centaurus A. The solid line is the CUSTAR data (from between September 1 and December 28, 2002), the dotted line is the polynomial fit and the dashed line is the Gaussian plus polynomial fit.

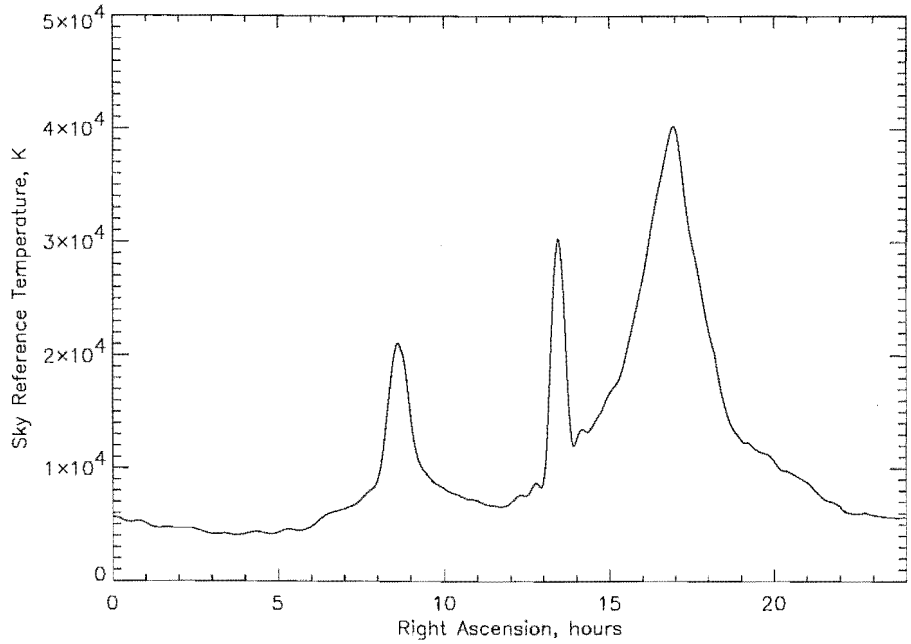

Figure 4.29: Sky temperature data at declination of 43° 34′ plotted against right ascension. Obtained from *Alvarez et al.* [1997].

$8.3° \pm 0.7°$. These are wider than expected by $2.7° \pm 1.7°$ and $1.7° \pm 0.9°$, respectively, and do not agree within uncertainties. These results suggest that the antenna beam is wider than theoretically expected.

Of all the sky noise results obtained using the full antenna array, those covered in this section have the smallest associated uncertainties. As mentioned earlier, this is probably due to the increased stability in the receiver and ADC, which allowed for more consistent results.

4.5.5 Comparison with a 45 MHz Sky Map

As indicated previously, *Alvarez et al.* [1997] has published a 45 MHz continuum survey of the Southern Hemisphere. This survey was made using an array telescope in Chile with an angular resolution of 4.6° in right ascension and 2.4° in declination. Sky temperature data was obtained from *Alvarez et al.* [private communication] at a declination of 43° 34′ which is very close to the longitude of Birdlings Flat. This data is plotted in Figure 4.29.

Sky temperature data was also obtained from *Alvarez et al.* after it had been

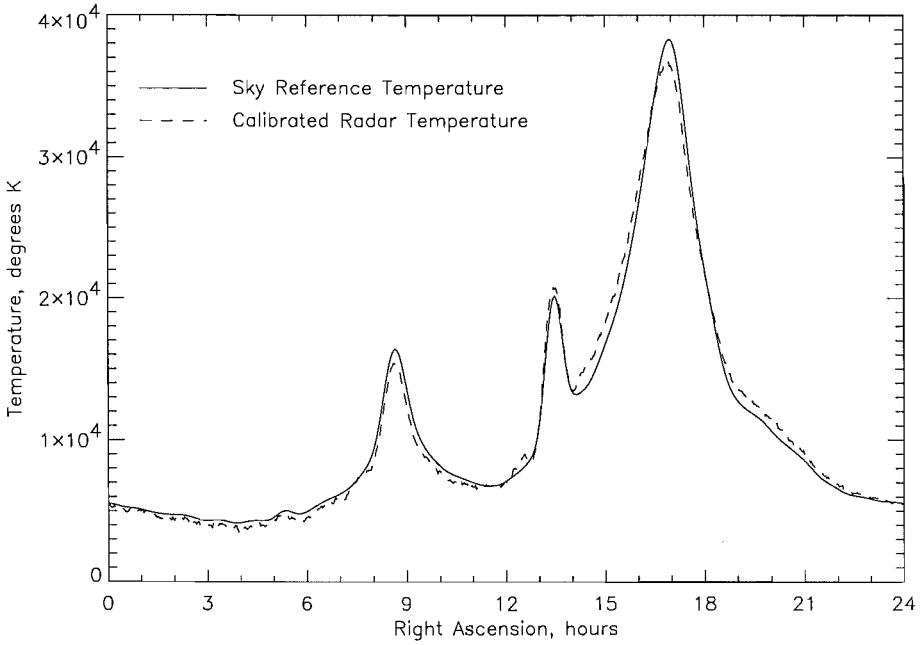

Figure 4.30: Sky temperature data smoothed to 6.4° × 6.4° resolution. The dashed line shows CUSTAR sky noise data from September to December, 2002.

smoothed to a resolution of 6.4° × 6.4° to match that of the CUSTAR antenna. This data is displayed in Figure 4.30 along with sky noise data from the radar plotted as a dashed line. The radar data is a repeat of that in Figure 4.27, but has had a constant of 6.95×10^5 removed and has been multiplied by a factor of 6.58×10^{-3}. The two data sets agree very well, which is to be expected as they are not only of the same resolution and declination, but they are also at very similar frequencies.

The CUSTAR data was compared to the 45 MHz data in a similar way to that described in Section 4.5.4. A Gaussian and second-order polynomial were fitted to each of the three peaks in the radar data and the sky map data. Each peak in the radar data was compared to the corresponding peak in the sky map data to ascertain the delay between the measurements and the sky map data. The galactic equator could also be included, as the comparison was between two sky noise profiles rather than to an exact right ascension and declination.

The results are shown in Figure 4.31. The CUSTAR radar data for Vela XYZ, Centaurus A and the galactic equator are shown in Figures 4.31a, b and c, respectively. The *Alvarez et al.* [1997] data is shown in Figures 4.31d, e and f. The one

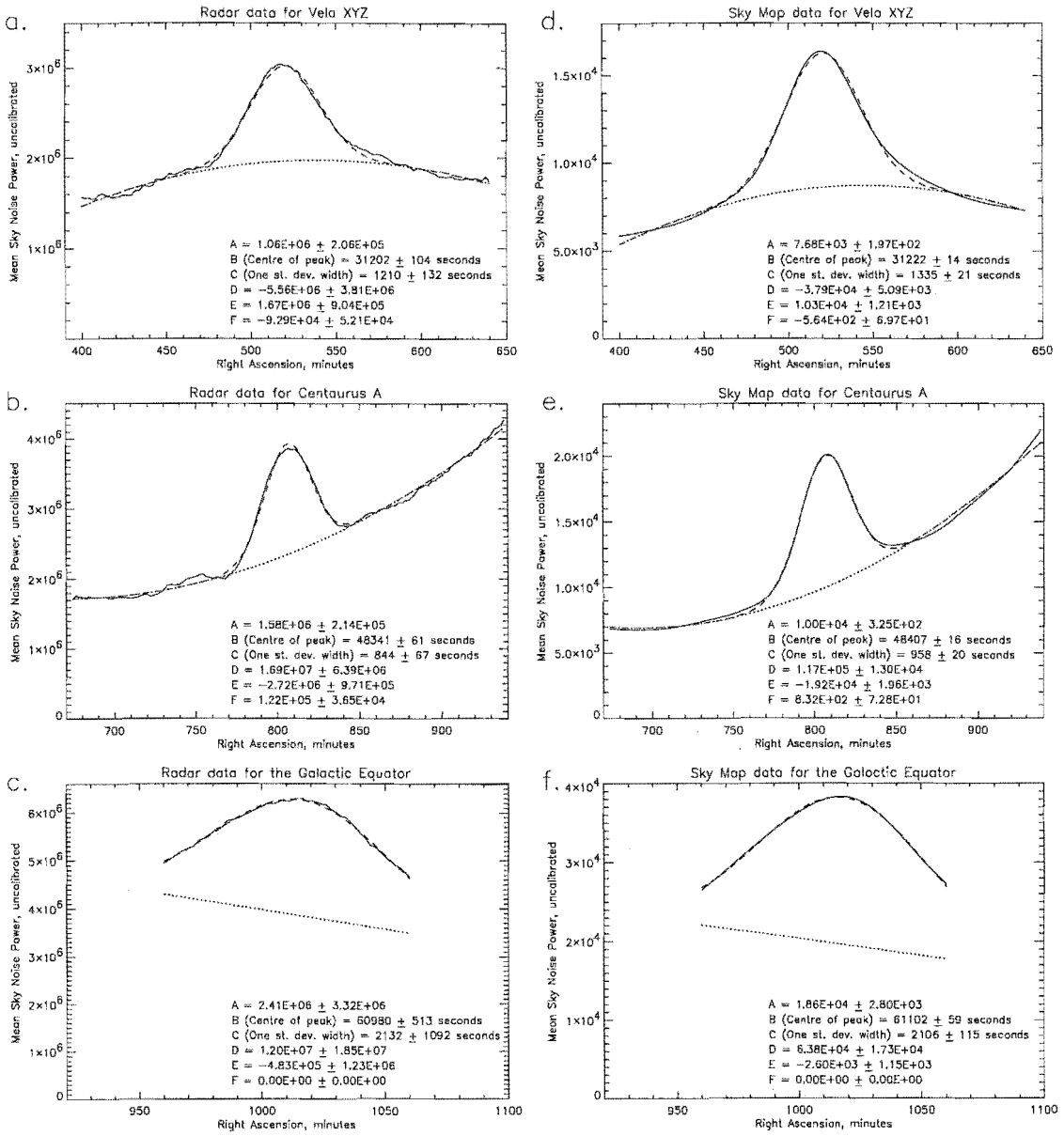

Figure 4.31: A comparison between the CUSTAR data and 45 MHz sky map data. In all cases the data is represented by solid lines, the polynomial fits by dotted lines and the Gaussian plus polynomial fits by dashed lines.

standard deviation uncertainty estimates are much smaller for the 45 MHz data because no measurement errors have been included in the fitting procedure as these were unavailable. It is assumed that the sky map is an accurate representation of the sky temperature and the uncertainties shown on Figures 4.31d, e and f are solely due to imperfect fits.

The differences between the centres of the Gaussian curves are $-20^s \pm 128^s$, $-66^s \pm 77^s$ and $-122^s \pm 572^s$ for Vela XYZ, Centaurus A and the galactic equator, respectively. The uncertainty for the galactic equator is very large, because the peak due to the galactic equator does not approximate a Gaussian curve very closely. In order to obtain a reasonable fit, only a small range of points from the central part of the peak could be used, therefore increasing the uncertainty of the fit.

The widths of the Gaussian curves fitted to Vela XYZ and Centaurus A in the sky map data theoretically should be identical to those fitted to the radar data, as the sky map was convolved to the same resolution. In actual fact, the widths corresponding to the radar data were smaller than for the sky map data, the differences coming to $-1.2° \pm 1.5°$ and $-1.1° \pm 0.9°$ for Vela XYZ and Centaurus A, respectively. The width of the galactic equator is too wide for it to be used to estimate the CUSTAR antenna beam-width.

A further method of comparing the 45 MHz sky survey with the CUSTAR data is to perform a cross-correlation using data at all right ascensions. A cross-correlation finds the similarity between two different data sets by producing a correlation coefficient. This coefficient is 1 if the data sets are positively correlated, -1 if they are anti-correlated and 0 if there is no correlation between them. A cross-correlation can be performed at different lags, that is when one data set is shifted left or right with respect to the other. The discrete correlation of two sampled functions g_k and h_k, each periodic with period N, is defined by

$$\mathrm{Corr}(g,h)_i = \sum_{k=0}^{N-1} g_j h_k \qquad j = \begin{cases} k+i & \text{if } k+i < N \\ k+i-N & \text{if } k+i \geq N \\ k+i+N & \text{if } k+i < 0 \end{cases} \tag{4.10}$$

where i is the lag and can vary from $-(N-1)$ to $(N-1)$ [*Press et al.*, 1992].

As explained earlier, the CUSTAR data was interpolated using the same grid as the sky map data. Using this grid, each point is spaced by two minutes which means that the lag can only be adjusted in two minute increments. The correlation

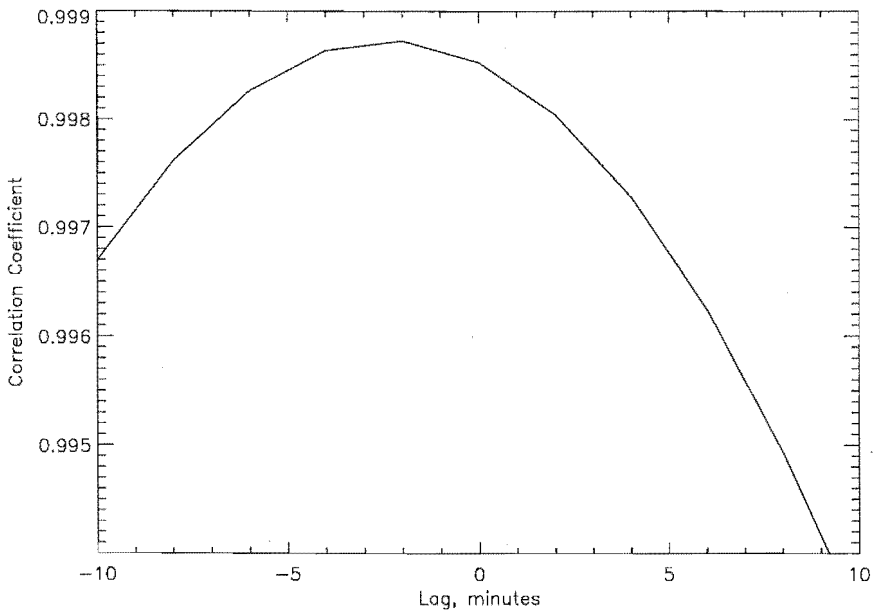

Figure 4.32: Correlation coefficients from a cross-correlation performed between the sky map data and the CUSTAR data.

coefficients for lags of −6 to 6 minutes are:

Lag (min)	−6	−4	−2	0	2	4	6
Corr. Co.	0.99827	0.99864	0.99873	0.99853	0.99805	0.99728	0.99624

Figure 4.32 shows the correlation coefficients plotted as a function of lag. Maximum correlation occurs at a lag of −2, but it is clear that with better resolution this point would be shifted slightly to the left. If a Gaussian curve is fitted to this data then the maximum point of that Gaussian occurs at a lag of −2.44 minutes. An estimate of the uncertainty in this value was taken as the spacing between the points being correlated, or 120 seconds.

4.5.6 Increasing the Temporal Resolution

The data used in the above discussion was obtained at three minute resolution. For each point, the background noise was calculated from a $2^m\,11^s$ time series. As explained in Section 4.5.1, this data was then re-gridded in right ascension at two

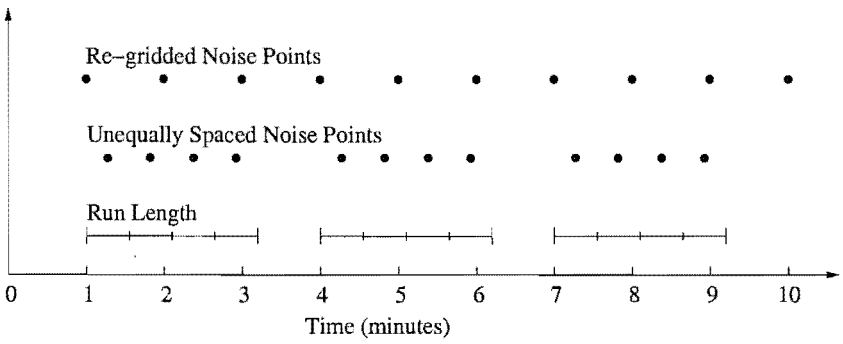

Figure 4.33: A representation of the method used to increase the temporal resolution of the sky noise data.

minute intervals. In an attempt to increase the temporal resolution, the data used above has also been re-gridded at one minute intervals using the following method.

To increase the resolution each 2.18 minute time series is first split into four sections of equal length. These sections are then processed individually to obtain the noise level. The resulting noise points will be unequally spaced due to the 49 second gap between runs, but in order to perform an average over many days, the points need to be gridded regularly in right ascension. This is achieved using a cubic spline resulting in data points evenly spaced by one minute (see Figure 4.33). As a result of the shorter sections, there will be greater variance in the noise level values, but as is shown below, the larger number of points acts to reduce the overall uncertainty.

The results were analysed using the procedure described previously and are presented in Figure 4.34. The increased variance can be noted by comparing this figure to Figures 4.27 and 4.31 in which the sky noise shows a much smoother profile.

The lag between the centres of the Gaussians in Figures 4.34b and c and the theoretical positions of Vela XYZ and Centaurus A are $-104^s \pm 118^s$ and $46^s \pm 61^s$, respectively. When compared to the 45 MHz sky map these lags become $-60^s \pm 96^s$ for Vela XYZ, $-37^s \pm 65^s$ for Centaurus A and $-173^s \pm 578^s$ for the galactic equator. Apart from the galactic equator, all these differences have smaller uncertainties, due to the increased number of points in each fit.

The differences between measured and expected beam-widths also have smaller uncertainties. Compared to the theoretical widths the measured widths are wider by $2.6° \pm 1.4°$ and $1.8° \pm 0.7°$ for Vela XYZ and Centaurus A, respectively. Compared to

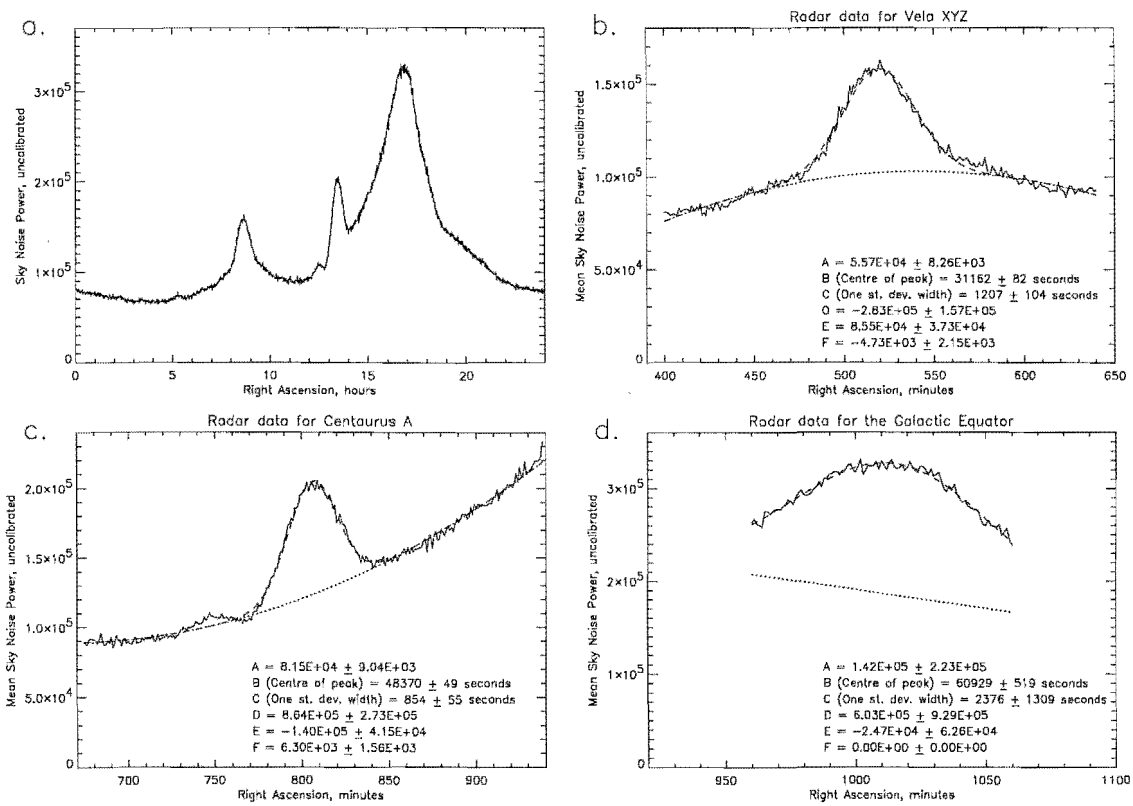

Figure 4.34: Sky noise measured by the CUSTAR radar with a high temporal resolution. The median for **(a)** the full 24 hours, **(b)** Vela XYZ, **(c)** Centaurus A and **(d)** the galactic equator. In the final three plots the data is represented by solid lines, the polynomial fits by dotted lines and the Gaussian plus polynomial fits by dashed lines.

the sky map, they are again narrower by $-1.3° \pm 1.2°$ and $-1.0° \pm 0.7°$, respectively.

4.5.7 Summary of Results

A summary of all the lag values found in the the previous sections, along with their estimated uncertainties, is shown in Table 4.3 and plotted in Figure 4.35. Not all of this data could be used to calculate the best estimate of the beam pointing direction, as some values are not independent. Instead, the best estimate of the positions of Vela XYZ and Centaurus A, as measured by the radar, were compared to the best estimates of their actual position.

The best estimates of the central points of Vela XYZ and Centuarus A for the CUSTAR antenna were found by taking the average over the three time periods

	Description	Lag (seconds)
1	Vela X from 12/2001 to 4/2002	132 ± 236
2	Centaurus A from 12/2001 to 4/2002	8 ± 179
3	Vela X from 7/2002 to 8/2002	-74 ± 360
4	Centaurus A from 7/2002 to 8/2002	171 ± 322
5	Vela X from 9/2002 to 12/2002	-64 ± 140
6	Centaurus A from 9/2002 to 12/2002	17 ± 73
7	Vela X compared to 45 MHz sky map	-20 ± 104
8	Centaurus A compared to 45 MHz sky map	-66 ± 61
9	Galactic equator compared to 45 MHz sky map	-122 ± 513
10	All data cross-correlated with 45 MHz sky map	-146 ± 120
11	Vela X from high resolution data	-104 ± 118
12	Centaurus A from high resolution data	46 ± 61
13	Vela X from high resolution data (sky map)	-60 ± 96
14	Centaurus A from high resolution data (sky map)	-37 ± 65
15	Galactic equator from high resolution data (sky map)	-173 ± 578

Table 4.3: A comparison of all the lags found in the previous four sections. A negative lag means the CUSTAR antenna observes the source earlier than expected.

discussed. Only the higher resolution form of the data gathered between September and December, 2002, was used. The mean of the three values for each radio source was found, weighted toward those with lower uncertainties. The mean values obtained were $31196^s \pm 74^s$ for Vela XYZ and $48370^s \pm 46^s$ for Centaurus A.

The best estimates for the actual right ascensions of Vela XYZ and Centaurus A were found by taking the mean of the values from the sky map and those found in Sections 4.3.3 and 4.3.4, again weighted toward those values with lower uncertainties. In this case the mean values came to $31228^s \pm 13^s$ for Vela XYZ and $48354^s \pm 10^s$ for Centaurus A.

The differences between the measured and actual values found above are $-32^s \pm 87^s$ and $16^s \pm 56^s$ for Vela XYZ and Centaurus A, respectively. The weighted mean of these values comes to $2^s \pm 47^s$ and is plotted on Figure 4.35 as the solid and dashed horizontal lines. This lag means the pointing direction of the antenna beam is very slightly off-vertical, by an angle of $0.01° \pm 0.20°$ to the west.

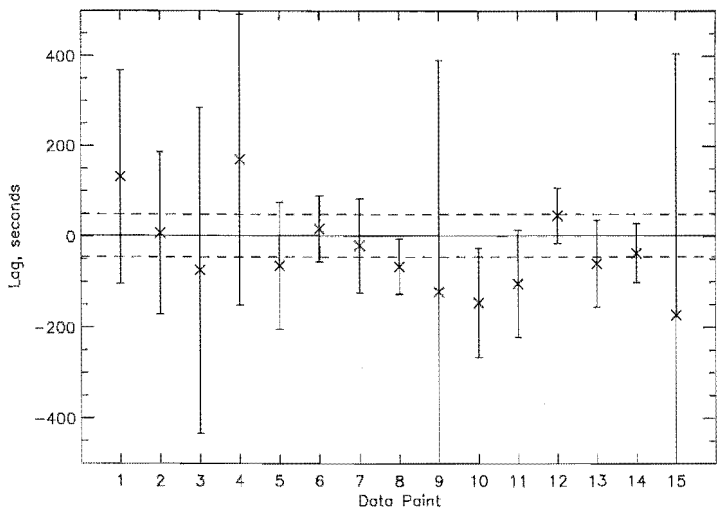

Figure 4.35: A graph of the data shown in Table 4.3. The numbers on the x-axis correspond to those in the table. The best estimate of the beam pointing direction is shown as a solid line and its one standard deviation uncertainties as dashed lines.

A list of all the deviations from the theoretical beam-width of the CUSTAR antenna found in the previous sections, along with their estimated uncertainties, is shown in Table 4.4. This data is plotted in Figure 4.36. The best estimate of the deviation from the theoretical beam-width was calculated in the same way as the best estimate of the pointing direction was determined.

The best estimate of the width of the Vela XYZ signal as measured by the CUSTAR antenna came to $11.77° \pm 0.90°$, and for Centaurus A, it was $8.40° \pm 0.49°$. The best estimate of the theoretical width of Vela XYZ and Centaurus A came to $12.32° \pm 0.18°$ and $8.00° \pm 0.14°$, respectively. The difference between the measured and theoretical values is $-0.54° \pm 1.08°$ and $0.40° \pm 0.63°$ for Vela XYZ and Centaurus A, respectively. The weighted mean of these values is $0.16° \pm 0.54°$ and this is plotted in Figure 4.36 as a solid line with dashed lines showing the uncertainty. This deviation suggests that the CUSTAR antenna is wider than the expected 6.35° and has a FWHM of $6.51° \pm 0.54°$.

4.5.8 Verification Using Mean Vertical Velocity

The pointing direction of the beam can also be checked by analysing the long-term mean of vertical wind velocities measured using the radar. At mid-latitudes, the

	Description	Deviation
1	Vela X from 12/2001 to 4/2002	$3.8° \pm 3.0°$
2	Centaurus A from 12/2001 to 4/2002	$1.6° \pm 2.5°$
3	Vela X from 7/2002 to 8/2002	$-0.1° \pm 4.0°$
4	Centaurus A from 7/2002 to 8/2002	$2.6° \pm 5.0°$
5	Vela X from 9/2002 to 12/2002	$2.7° \pm 1.7°$
6	Centaurus A from 9/2002 to 12/2002	$1.7° \pm 0.9°$
7	Vela X compared to 45 MHz sky map	$-1.2° \pm 1.5°$
8	Centaurus A compared to 45 MHz sky map	$-1.1° \pm 0.9°$
9	Vela X from high resolution data	$2.6° \pm 1.4°$
10	Centaurus A from high resolution data	$1.8° \pm 0.7°$
11	Vela X from high resolution data (sky map)	$-1.3° \pm 1.2°$
12	Centaurus A from high resolution data (sky map)	$-1.0° \pm 0.7°$

Table 4.4: A comparison of all the differences between measured and expected beam-widths found in the previous four sections. A negative deviation means the measured width is smaller than that expected.

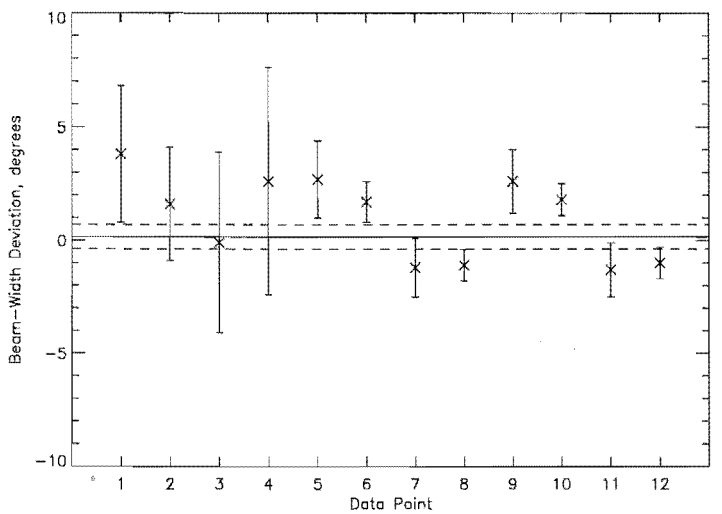

Figure 4.36: A graph of the data shown in Table 4.4. The numbers on the x-axis correspond to those in the table. The best estimate of the deviation is shown as a solid line and its one standard deviation uncertainties as dashed lines.

mean vertical velocity over a period of three or four months should be near zero. However, most long-term means measured using existing VHF radars have shown a typical downward vertical velocity of a few $\mathrm{cm\,s^{-1}}$ [e.g. *Nastrom and VanZandt*, 1994]. This trend has been explained using a number of models, some of which assume the bias is due to false radar measurements and some which attribute it to real atmospheric phenomena, such as gravity waves. *Worthington et al.* [2001] recently published a theory that suggested the bias could be due to the location of VHF radars, which are often close to significant orographic features. This is not the case for all radars, as is shown by the Flatland radar, which is situated in very flat terrain and still shows a significant downward vertical velocity bias [*Green et al.*, 1988].

Despite this bias, which could possibly occur in the CUSTAR observations because the site is in close proximity to the Banks Peninsula hills, the long-term mean of the vertical velocity should still be close to zero. This will not be the case, however, if the radar antenna beam is tilted off-vertical, as a component of the horizontal wind, which is significantly stronger than the vertical wind (typically by an order of magnitude or more), will be measured along with the vertical wind.

The mean wind at mid-latitudes is westerly at all heights in the troposphere (see Figure 2.4). Figure 4.37 contains the mean horizontal wind from September 1 to December 28, 2002, obtained from the NCEP/NCAR (National Centers for Environmental Prediction/National Center for Atmospheric Research) reanalysis dataset. It is very close to westerly and reaches a maximum velocity at just above 10 km. In the previous section it was found that the CUSTAR antenna beam is pointing off vertical by $\theta = 0.01° \pm 0.20°$ to the west. The magnitude of the vertical bias, Δw, produced by a horizontal wind, v, for an off-vertical beam is given by

$$\Delta w = v \sin\theta, \tag{4.11}$$

where θ is the angle off vertical in the direction of v.

The mean vertical velocity as measured by the radar from September 1 to December 28, 2002, is shown in Figure 4.38. Section 5.2 explains the signal processing technique used to calculate vertical velocities from the radar observations. Also included in Figure 4.38 is the expected bias caused by the mean wind calculated using Equation 4.11. There is clearly a significant downward vertical velocity in the radar profile, but the features of the vertical velocity profile do not match those of the

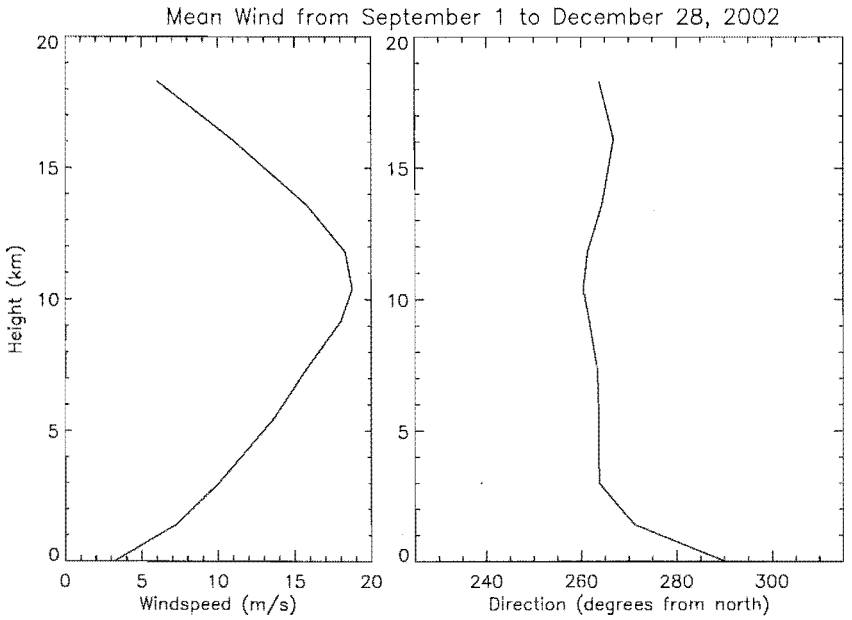

Figure 4.37: Background wind speed above Christchurch from September 1 to December 28, 2002. Data provided by the NOAA-CIRES Climate Diagnostics Center, Boulder Colorado (http://www.cdc.noaa.gov/) [*Kalnay et al.*, 1996].

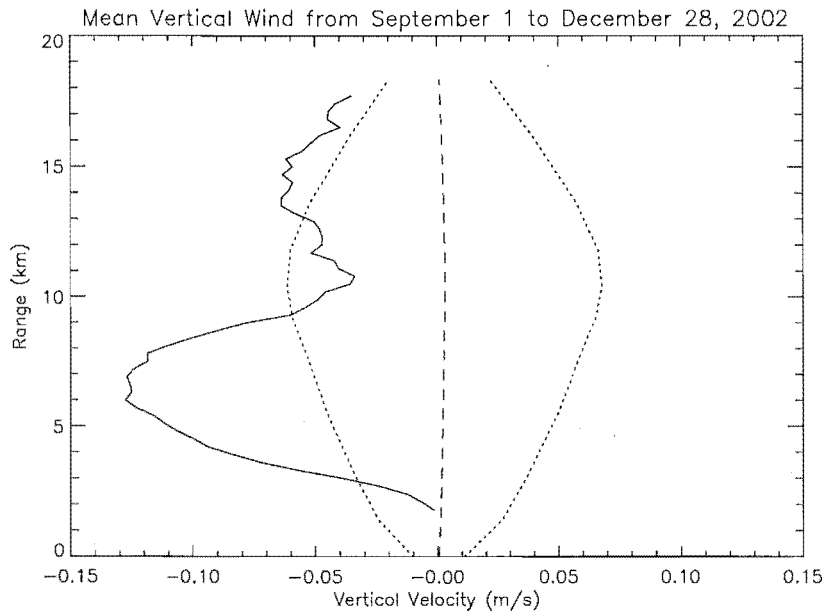

Figure 4.38: Mean vertical wind speed measured by the radar from September 1 to December 28, 2002 (solid line). The dashed line is the expected bias caused by horizontal wind contamination and the dotted lines are its uncertainty.

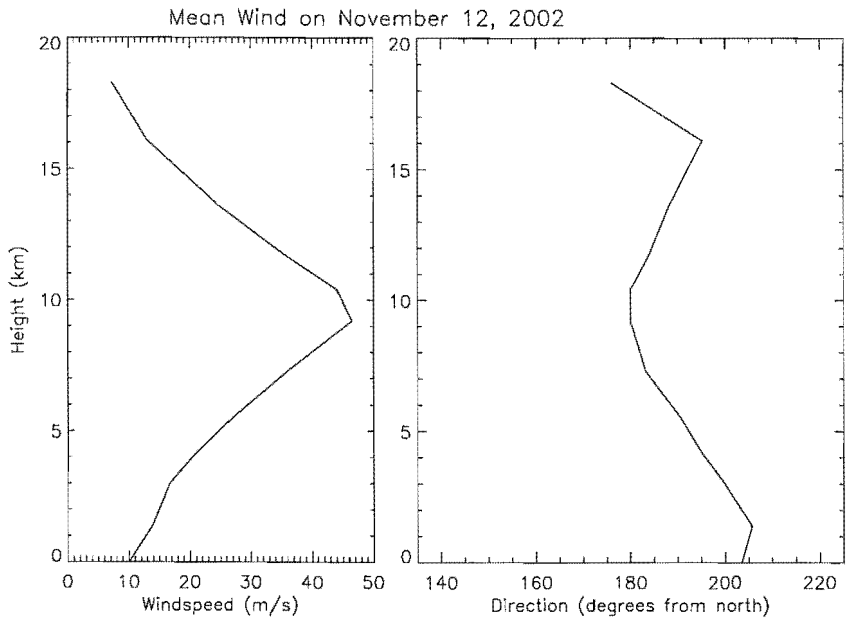

Figure 4.39: Background wind speed above Christchurch on November 12, 2002. Data provided by the NOAA-CIRES Climate Diagnostics Center, Boulder Colorado.

expected bias, in fact, the peaks are in quite different locations. This suggests that the non-zero mean vertical velocity is unlikely to be caused by horizontal wind contamination. The pattern observed in the vertical velocity profile is, however, quite similar to that observed by *Nastrom and VanZandt* [1994], although the maximum amplitude of the bias in their case was only 0.08 $\mathrm{m\,s^{-1}}$ for bimonthly means.

Figure 4.39 contains data from the NCEP/NCAR reanalysis dataset for November 12, 2002, during which time there was a strong southerly flow. The background wind flow was compared using Equation 4.11 to the mean vertical velocity measured by the radar on this day and this comparison is displayed in Figure 4.40. Again, there seems to be no correlation between the horizontal bias and the vertical velocity, suggesting that, in the north-south direction, the antenna beam is not tilted off-vertical by a significant amount.

It should be noted that this technique will only provide conclusive evidence of a tilted antenna beam if it is tilted off-vertical by a significant amount. This is because the mean vertical wind speed is quite large relative to the expected horizontal wind contamination, so unless the beam is tilted by a large amount, e.g. 0.2°, the vertical wind will obscure the bias.

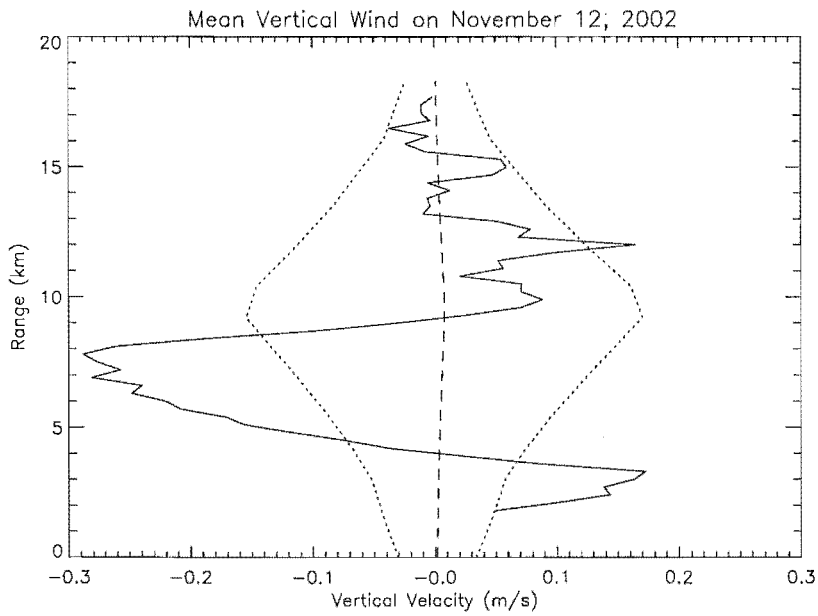

Figure 4.40: Mean vertical wind speed measured by the radar on November 12, 2002 (solid line). The dashed line is the expected bias caused by horizontal wind contamination and the dotted lines are its uncertainty.

4.6 Summary

This chapter has described experiments that were performed to verify the beam pattern of the CUSTAR antenna array. A technique which involved measuring the variation of sky noise over the sidereal day was utilised. The results obtained show that the antenna array behaves almost exactly as expected.

Initially, tests were performed using only a single row of the antenna. This produced a broad beam which allowed measurements of the sun's radio emission to be obtained. This was very beneficial as the strong signal produced by the sun was observed in all of the antenna lobes and provided a means of checking the side-lobe positions. The results showed that the measured lobes had very similar positions and magnitudes to those calculated theoretically.

Measurements of the sky noise were also made after the antenna array had been completed. It was found that the most accurate method (that with the lowest uncertainty) of finding the beam pointing direction and beam-width was the comparison of individual radio source patterns, as measured by the radar, with their expected patterns. It should be noted that the best results were obtained while the radar

was in normal operation. This demonstrates the value of this technique, as it can be used to continuously monitor the antenna beam pattern and also the system stability. The latter could be monitored by measuring the day to day variation in the mean sky noise. If this changed by a large amount, it could indicate a problem with the radar system, such as a fault in the receiving equipment [*Campistron et al.*, 2001].

The final pointing direction of the antenna beam in the east-west plane was found to be $0.01° \pm 0.20°$ to the west. This is an excellent result and even at the extremes of the uncertainty range, a strong horizontal wind of 50 $\mathrm{m\,s^{-1}}$ would produce a bias in the measured vertical wind velocity of only 0.18 $\mathrm{m\,s^{-1}}$. The width of the main antenna beam was estimated to be FWHM $= 6.51° \pm 0.54°$. Assuming there are no ohmic losses in the antenna, the effective aperture can be calculated using Equations 3.6 to 3.8 and comes to $A_e = 3900 \pm 400$ $\mathrm{m^2}$.

Chapter 5

ST Radar Results

This chapter details the signal processing scheme and some interesting initial atmospheric results which show the efficacy of the radar. The first two sections show some typical results and explain in detail how the data used in this thesis has been processed. The third section discusses the effects of both coherent and incoherent integration using data collected from the CUSTAR radar. The remainder of this chapter is devoted to interpreting the radar measurements with respect to atmospheric phenomena. Section 5.4 explains how the radar can be used to routinely observe the height of the tropopause and in the next section comparisons between the height of the tropopause measured by the radar and by radiosondes are covered. In the final section, observations of a frontal passage and gravity waves are presented along with a discussion on the likely source of the wave activity.

5.1 Initial Tests and Results

The radar system described in Chapter 3 was completed by June 2002, at which time some preliminary tests were performed to ensure the system was operating correctly. These tests and the initial results obtained from the radar are covered in this section.

5.1.1 Initial Tests

The first tests were performed to estimate the time, t_{delay}, lost in transmission and reception (see Section 3.4.1) and also to verify the sampling speed of the analogue to digital converter (ADC). The system was set up as previously specified in Section 3.4, but with an additional pulse generator to create artificial echoes with a known delay. The transmitter power was kept low to prevent overloading of the receiver caused by leakage through the transmit-receive (T-R) switch. This leakage is commonly called the ground pulse, as in systems with separate arrays for

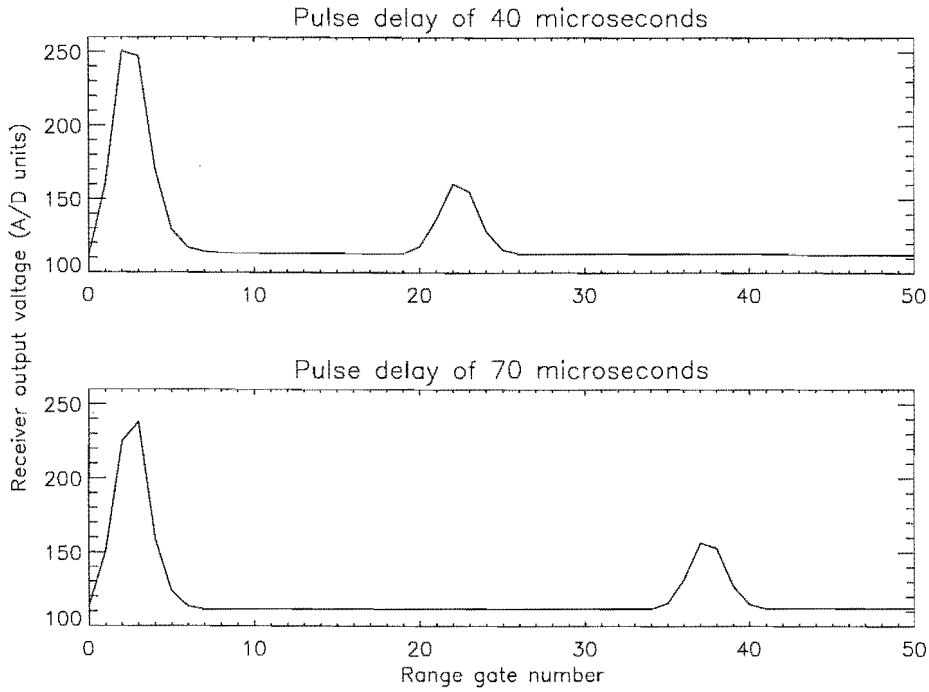

Figure 5.1: Output from the receiver showing the ground pulse and a delayed artificial radar echo. In the upper plot, the delay was set for 40 μs and in the lower plot, for 70 μs.

transmission and reception, the pulse is received along the ground.

The time delay can be estimated from the output of the ADC by measuring the time from the beginning of the trigger pulse to the centre of the ground pulse. Figure 5.1 contains the results from tests performed to estimate t_{delay}. Both graphs show the output from the ADC in units ranging from 0 to 255 plotted against range bin number, each of which corresponds to the sampling period of 2 μs. t_{delay} is then measured from 0 to the centre of the first peak which is between the 2nd and 3rd bin and equals 5 ± 1 μs. This calculation of the delay does not include that incurred in the transmission line from the T-R switch to the antenna or in the antenna itself. The transmission line is approximately 50 metres long and because it is an open wire line, the speed with which an R.F. wave travels along it is similar to that in free space, c. The time taken to traverse the line there and back therefore equals 0.33 μs. A similar amount of time will be lost in the antenna as it has dimensions of 50 metres, so the total delay time will come to 6 ± 1 μs.

Figure 5.1 also includes artificially created radar echoes. These were produced to

ensure that the bin size is exactly 2 μs. The echoes were set, using an oscilloscope, to have delays from the centre of the ground pulse to the centre of the artificial pulse of 40 μs and 70 μs in the upper and lower plot respectively. The position of these echoes with respect to the ground pulse is 20 bins and 35 bins, which corresponds to the previous figures exactly. According to Equations 3.35 and 3.36, the sampling period of 2 μs gives a range bin size of 300 m and with 64 samples each run, the maximum range is 18 km. Due to a timing problem in the ADC, the top range bin was not usable, reducing R_{max} to 17.7 km.

When calculating a Doppler radial velocity, the direction of motion of the target is determined by the sign of the Doppler frequency shift. If the target is moving toward the antenna, then the frequency of the signal is increased (blue-shifted) and the Doppler frequency shift has a positive sign. If the target is moving away then the frequency shift is negative (red-shifted). These relations will be reversed if the two outputs from the phase splitter are reversed or the I and Q channels are swapped anywhere in the hardware chain or the signal processing scheme. To ensure that this is not the case, signals with frequencies slightly above and below the carrier signal were fed into the receiver and the power density spectrum was compared for each different frequency.

The carrier signal produced in the exciter has a frequency of 42503.77 ± 0.10 kHz. The uncertainty is due to a slow drift which does not affect the coherence of the radar as the same signal is used in both the transmitter and receiver. The signal used to verify the sign of the Doppler frequency shift was produced in a commercial signal generator which was precise down to 0.01 kHz. This precision was not large enough to verify the numerical accuracy of Doppler frequency shift, but was adequate to check its sign. Results were obtained using four different input signals nominally at $+70$, $+120$, -70 and -120 Hz from the carrier frequency. The first three of these signals had input voltages of 0.3 μV and the fourth, 0.6 μV. The four corresponding power density spectra are shown in Figure 5.2.

Each plot shows a spike within 15 Hz of the expected frequency shift. This value is less than the combined uncertainty of the signal generator and the exciter, suggesting that the Doppler frequency estimation is reliable. More importantly, the sign of each frequency shift matches, proving that the hardware configuration and signal processing scheme are working correctly.

Figure 5.2 also reveals the sensitivity of the receiver system. The data for each

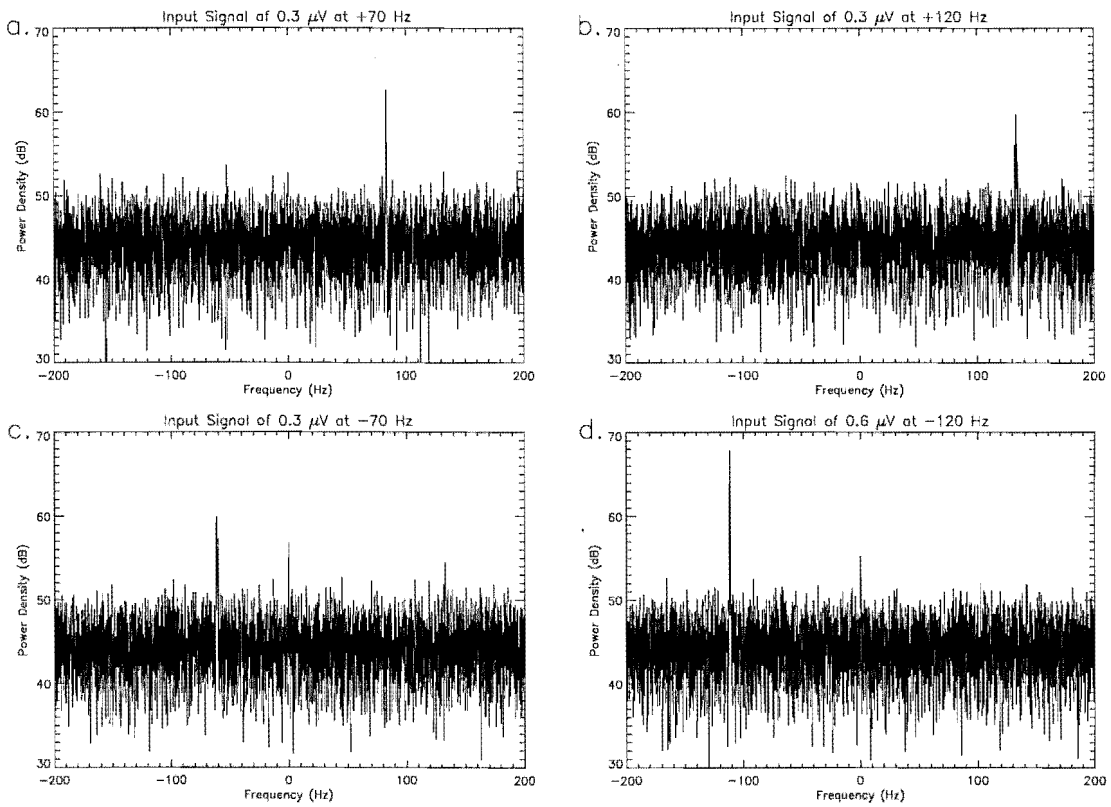

Figure 5.2: Power density spectra from the tests performed to verify the Doppler frequency shift.

plot was produced as though the system were in normal operation, except that the transmitter was off and the antenna replaced with a signal generator. Each plot is one height bin from a run of 131072 pulses (2.18 minutes) with no coherent integration. With input signals of only 0.3 μV, the signal is 10 dB above the noise, and with an input of 0.6 μV, the signal is nearly 20 dB above the noise. When the transmitter is running and the antenna connected, the noise level will of course be higher than it is in these plots, but this test shows that the receiver sensitivity is very good.

On some of the plots of Figure 5.2, there is also a spike at 0 Hz, due to instrument clutter. The reason for this spike is likely to be leakage of the carrier signal directly into the input of the receiver. This carrier signal will be seen as real signal with no frequency shift and produce an output at 0 Hz. This spike is easily removed in software by using a notch filter (see Section 5.2.2).

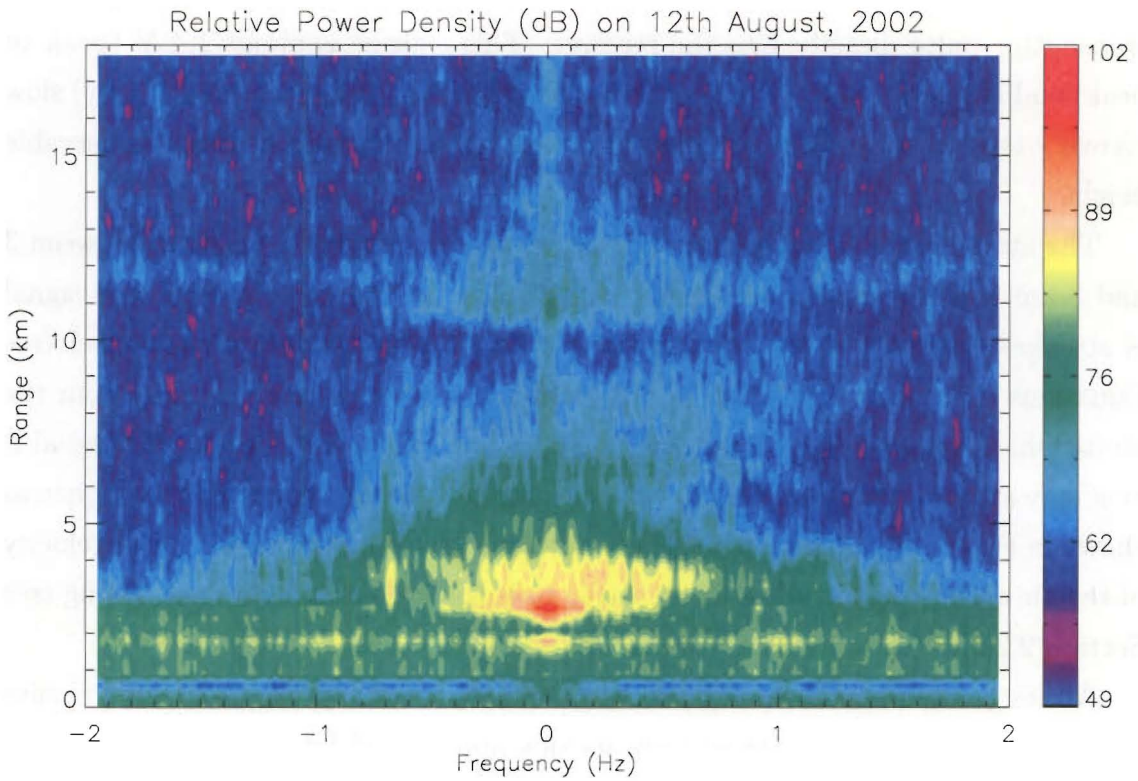

Figure 5.3: Average power density spectrum over 15 minutes on August 12, 2002.

5.1.2 First Results

The first returns from the atmosphere were observed on August 12, 2002. These were obtained with a pulse repetition frequency of 1 kHz, a pulse width of 4 μs and a run length of 2.18 minutes (which corresponds to 131072 pulses). The data was not coherently integrated. Using the signal processing scheme described in Section 5.2, power density spectra were found at each height for each run. The average of five runs between 12:09 and 12:24 NZST is displayed in Figure 5.3. This plot shows the received signal power plotted against range and Doppler frequency. The power density is plotted in decibels, relative to an arbitrary reference which depends on receiver gain, the ADC conversion ratio and the signal processing procedure.

The power density spectrum of Figure 5.3 reveals a large amount about the radar system and the received signal. Firstly, below a range of about three kilometres, there is an area of large signal power that does not vary with frequency. This region, which corresponds to 20 μs, is associated with the receiver recovery time. Despite

the very large attenuation provided by the T-R switch, there is still leakage of the transmitter pulse directly into the receiver. This leakage is about 1.4 V (peak to peak) and is enough to swamp the receiver filter section, which has a (relatively) slow recovery time. The receiver response time determines the radar's lowest observable height[1].

The atmospheric signal is concentrated in two main regions, the first between 3 and 8 km and the second between 10 and 13 km. In the lower section, the signal is strongest at the bottom and decreases with height as would be expected (see Equations 2.31 and 2.34). The upper section corresponds to reflections from the stratosphere and also decreases with height. At any particular height, the signal is generally strongest at around 0 Hz and has a roughly Gaussian shape in frequency as shown in Figure 5.4. The centre of this Gaussian curve relates to the vertical velocity of the air and the spectral width is related to turbulence and beam broadening (see Section 2.2.4).

Although the main beam of the antenna points vertically, the radar does receive some clutter or unwanted signal from its side and ground-lobes. In Figure 5.4 and between 3 and 8 km in Figure 5.3 there is an increase in power at -0.7 Hz associated with sea clutter. *Crombie* [1955, 1971] showed that the dominant scattering mechanism associated with ocean waves is Bragg scatter. When a radar signal is scattered from the ocean surface, the strongest returns arise from wave crests that are separated by half the radar wavelength. This is because the reflected signals from different crests will be in phase and therefore add constructively. The velocity of an ocean wave with wavelength $\lambda_{ocean} = \lambda/2$, where λ is the radar wavelength, is given by

$$v_{ocean} = \sqrt{\frac{g\lambda_{ocean}}{2\pi}} = \sqrt{\frac{g\lambda}{4\pi}}. \tag{5.1}$$

The frequency shift of the carrier signal is (see Equation 2.37)

$$f_{ocean} = \pm\sqrt{\frac{g}{\pi\lambda}} \tag{5.2}$$

and is positive for ocean waves moving toward the radar and negative for those moving away. For the CUSTAR radar this comes to $f_{ocean} = \pm 0.67$ Hz. The actual

[1]A new receiver, which has been in use since March, 2003, contains improved circuitry that decreases the receiver recovery time. Receiver blanking, which involves grounding the receiver input during transmission, is also being implemented and will allow the radar to observe at lower altitudes.

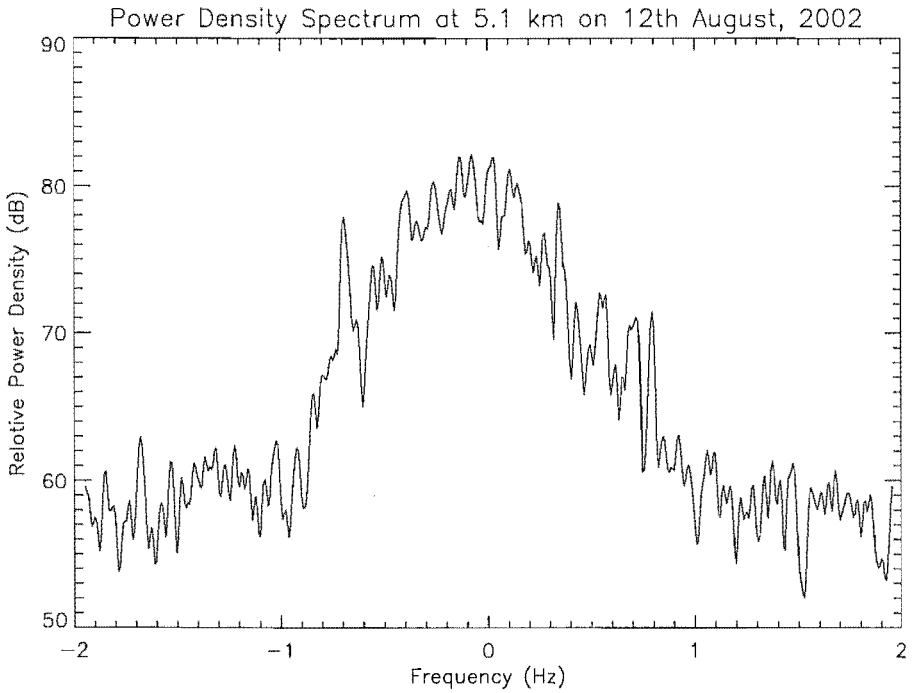

Figure 5.4: A horizontal slice taken through Figure 5.3 at 5.1 km.

sea clutter peak may vary from this value depending on the background ocean current. It is also dependent on the weather conditions and as a result the peak is not always observed. A survey of Doppler spectra over a one month period showed that the ocean peak was present about 30% of the time and only at ranges of less than 8 km. In most (around 80%) of the spectra containing sea clutter, the peak is completely separated from the atmospheric signal and therefore will have little effect on the deduced atmospheric parameters.

Figure 5.3 also shows an increase in signal power at 0 Hz at all ranges. This is a mixture of ground clutter and instrumental clutter, which can be removed by subtracting a linear or polynomial fit from the raw data (see Section 5.2.1) and by using a notch filter around 0 Hz (see Section 5.2.2). As shown in Figure 5.4, when the atmospheric signal is large, the clutter peak is negligible, however in regions of low signal, it is important to account for the clutter peak.

A final observation from Figure 5.3 is the increase in signal power across the entire spectrum at a range of 12 km. This was instrumental in origin and caused by the negative going edge of the trigger pulse going from the ADC to the transmitter. This was remedied by extending the length of the trigger pulse to well beyond the

region sampled by the ADC.

5.2 Signal Processing

Chapter 3 discussed the hardware which transmits R.F. signal into the atmosphere and receives the backscattered signal. This section details how these observations are processed in order that useful information can be derived from the in-phase (I) and quadrature (Q) outputs from the coherent receiver. Good reviews of spectral signal processing associated with MST radar can be found in *Woodman and Guillen* [1974], *Röttger and Larsen* [1990] and *Hocking* [1997a].

Signal processing techniques vary depending on what type of radar system is in use. For systems with three or more receiving antennas, the SAD (spaced antenna drifts) technique [*Mitra*, 1949; *Vincent et al.*, 1987] or a technique involving interferometry [*Pfister*, 1971] can be used. To obtain three dimensional wind speeds using systems with only one receiving antenna, the DBS (Doppler beam swing) method, which requires a steerable antenna beam, must be used [*Green et al.*, 1975]. The Doppler method can also be applied to systems with only a vertically pointing beam to calculate vertical wind speeds. It is the Doppler method that has been applied to the data collected by the CUSTAR system thus far.

The Doppler method involves the conversion of the I and Q components from the time to the frequency domain using a discrete Fourier transform (DFT). In the frequency domain the power spectrum arising from the atmosphere seldom deviates from a Gaussian form [*Woodman*, 1985]. The atmospheric signal can be described in terms of the Gaussian's three parameters. These are the frequency shift, which gives the wind velocity, the spectral width of the signal and the signal power.

5.2.1 Time-Domain Processing

The in-phase and quadrature outputs from the receiver both have a DC offset of approximately 2.5 V. This is to ensure that the full range of the ADC (0 to 5 V) is used to maximum potential. Examples of in-phase and quadrature time series are shown in Figure 5.5. The simplest way of removing this offset is to subtract from the time series its mean value [e.g. *Rao et al.*, 1995].

The receiver outputs may also contain some slow instrumental drift and fading from ground clutter. When power from one of the side or ground-lobes reflects off

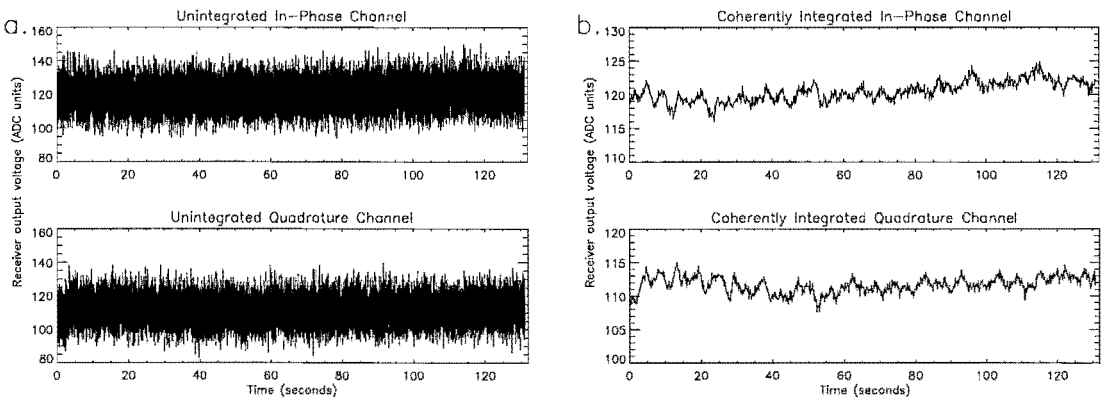

Figure 5.5: Typical time series for **(a)** unintegrated and **(b)** coherently integrated data. Note the change in y-axis scale. Both the in-phase and quadrature channels are shown.

orography, the frequency of the received signal will be nearly identical to that of the transmitted signal and will produce an increase in the power density spectrum near 0 Hz. Due to the non-uniform nature of the air between the antenna and orography, there may be some fading or slight change in frequency of the signal, which can broaden the ground clutter spike. There may also be reflections from moving targets seen in the ground-lobes (for example vegetation) which will broaden and increase the ground clutter spike. As mentioned in Section 5.1.1, instrumental clutter can also contribute to this peak at 0 Hz. This type of drift is clear in the in-phase channel in Figure 5.5b, where from about 20 to 120 s there is a slow increase in signal. These low frequency components can be removed by fitting a curve to the time series and then subtracting that fit from the data. This technique is usually called a trend removal and is most easily achieved by fitting a straight line to the raw data using a least squares fitting routine and then subtracting that fit from the data [e.g. *Ruster*, 1994]. *Hocking* [1997a] used a simple polynomial instead of a straight line to achieve better results when using long sample lengths.

The in-phase and quadrature components of the received signal should be separated in phase by 90° and have the same amplification. This is often not the case, due to instrumental drift in the two channels. These errors can be allowed for by exploiting the fact that the average intensity will be the same for both channels [*Ruster*, 1994]. This correction has yet to be implemented in the CUSTAR radar, but examination of the I and Q components showed that amplitudes varied by only

a few percent and the phase difference was within a few degrees of 90°. These differences are small enough that they will not have a great effect on the signal properties.

When a time series is transformed into the frequency domain, its finite length introduces side-lobes in the Doppler spectrum. The spectral leakage from these side-lobes increases the noise level across the spectrum's entire width. To correct for this, the data can be weighted with a windowing function to smooth the abrupt edges of the time series [*Hooper*, 1999].

There are a number of different windows and *Hooper* [1999] suggests the use of the Hanning or Kaiser-Bessel windows. The coefficients of the Hanning window are

$$w_n = \frac{1}{2}\left(1 - \cos\left(\frac{2\pi n}{N-1}\right)\right) \tag{5.3}$$

where $n = 0, 1, ..., N-1$ [*Hamming*, 1989] and the coefficients for the Kaiser-Bessel window are

$$w_n = \frac{\mathrm{I}_0\left[\alpha\sqrt{1-\left(\frac{2(n-N/2)}{N}\right)^2}\right]}{\mathrm{I}_0[\alpha]} \tag{5.4}$$

where I_0 is the zeroth order Bessel function [see *Press et al.*, 1992]. α is a constant that is normally set to 2.5 [*Hooper*, 1999]. These coefficients are multiplied with the original samples to produce a weighted (or windowed) version of the data. The Hanning and Kaiser-Bessel (with α set to 2.5 and 5.0) window functions are shown in Figure 5.6. The Hanning window was used in this work due to its ability to provide a lower average noise level (see Section 5.2.2).

Figure 5.7 contains the time series from Figure 5.5 after trend removal and windowing. Both the coherently integrated and unintegrated data have had a linear trend removed and have been weighted with the Hanning window function. These samples can now be transformed into the frequency domain using the fast Fourier transform (FFT) algorithm, which is an adaption of the discrete Fourier transform [*Press et al.*, 1992].

5.2.2 Frequency-Domain Processing

The Fourier transform of complex data points in the time domain results in complex data points in the frequency domain (H_k). The power received in each frequency bin, or the spectral power density (S_k), is the sum of the real and imaginary parts

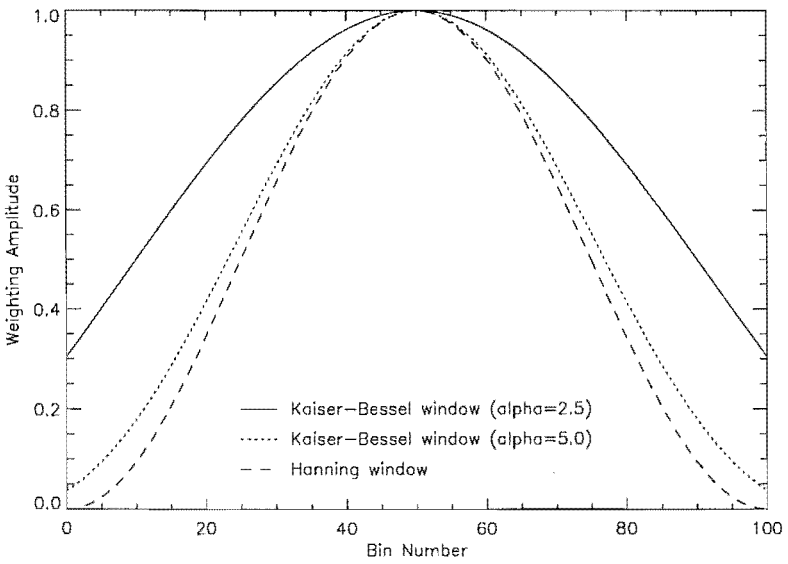

Figure 5.6: The Hanning and Kaiser-Bessel window functions.

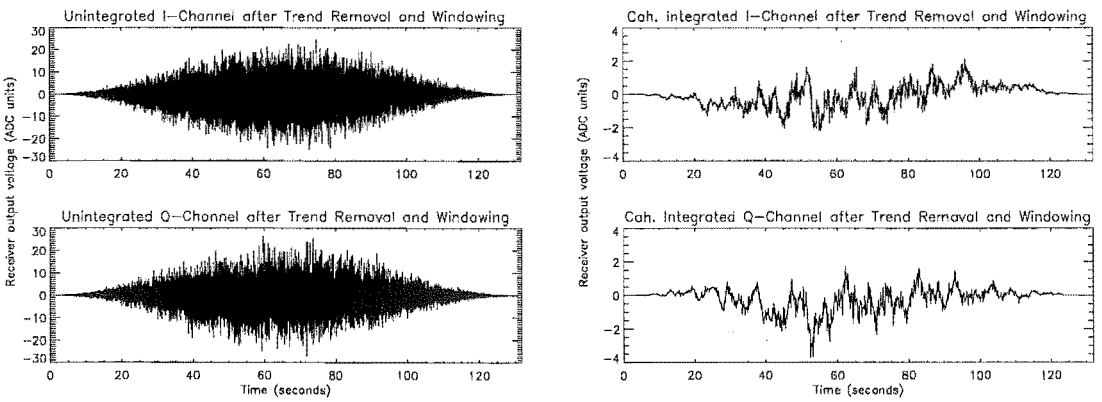

Figure 5.7: The same time series as shown in Figure 5.5 for **(a)** unintegrated and **(b)** coherently integrated data. A straight line fit has been subtracted from each time series and they have been weighted with the Hanning window function. Note the change in y-axis scale. Both the in-phase and quadrature channels are shown.

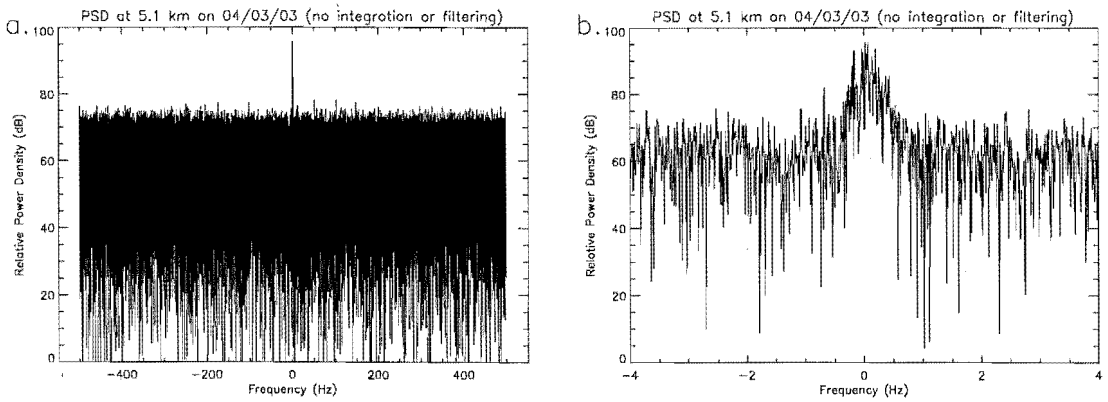

Figure 5.8: Power density spectrum at 5.1 km for unintegrated data showing **(a)** the full spectrum and **(b)** the central ±4 Hz. (Dates are presented in the form DD/MM/YY.)

squared

$$S_k = [\mathrm{Re}(H_k) + \mathrm{Im}(H_k)]^2, \qquad k = -\frac{N}{2}, ..., \frac{N}{2}. \tag{5.5}$$

The spectrum made up from the S_k values is used to determine the parameters of the received atmospheric signal.

A typical power spectrum at a height of 5.1 km for a single run is shown in Figure 5.8a. The maximum frequency of the spectrum (the Nyquist frequency, f_N) is determined by the time between pulses, which in this case is 1 ms. Using Equation 3.33, the maximum frequency is $f_N = 500$ Hz. This graph has a clear background noise level with one peak at 0 Hz, which is 20 to 25 dB above this level. This peak is atmospheric signal. There are also a number of other much smaller peaks that are mostly multiples of 50 Hz. These are due to power supply interference which could not be completely removed.

The frequency of signals reflected from the atmosphere will be much lower than 500 Hz and the atmospheric signal can be observed by concentrating on the central region of the spectrum as shown in Figure 5.8b. This spectrum is similar to that in Figure 5.4, except that it is from a single run rather than an average of 5 runs.

The power density spectrum shown in Figure 5.8b is very similar to one that would be obtained from data coherently integrated over 128 points. This integration increases the sampling period to 128 ms and using Equation 3.33, the Nyquist frequency is $f_N = 3.91$ Hz. The differences between coherently integrated and unintegrated data are discussed in Section 5.3 and the remainder of this section will

focus solely on unintegrated data.

At this stage it is quite common for the power density spectrum to have a large spike at 0 Hz corresponding to clutter. This could be a mixture of instrumental clutter and ground clutter. By removing the central point (or a small number of central points) and replacing it with the average of the two adjacent points, the clutter can be excluded. This gives much better Doppler estimates especially when the velocities are small and the signal span includes 0 Hz.

The signal processing scheme described here does not attempt to reduce the effects of any sea clutter that may be present in the Doppler spectra. However, if necessary, a possible method of removing the clutter peak would be to fit a double peak to the spectra with one peak centred on f_{ocean} (see Equation 5.2) and having a limited width. This scheme would have similarities to other schemes used to separate double spikes, such as those used for spectra containing both precipitation and clear-air echoes [e.g. *Sato et al.*, 1990; *Rajopadhyaya et al.*, 1994]. These schemes are generally successful only when both peaks are strong and separate from one another. A technique for fitting double peaks may perform more consistently for ocean clutter as the associated peak is centred at a constant frequency, however it is expected that problems would still occur when the two peaks overlap. For this reason, and also because it is thought that ocean clutter will affect the atmospheric signal in only a small number of cases (see Section 5.1.2), this scheme has not yet been implemented.

Minimal smoothing can also be utilised to reduce noise spikes in the spectrum. The Hanning window (see Equation 5.3) can be used as a three point sliding window by letting $N = 5$. This reduces it to what is commonly known as the quarter-half-quarter filter and is implemented as follows,

$$S_{sk} = \frac{1}{4}S_{k-1} + \frac{1}{2}S_k + \frac{1}{4}S_{k+1}, \qquad k = -\frac{N}{2} + 1, ..., \frac{N}{2} - 1, \tag{5.6}$$

where S_k is the kth element in the power spectrum, S_{sk} is the kth element in the smoothed power spectrum and N is the number of points in the power spectrum. The endpoints, $k = -\frac{N}{2}$ and $k = \frac{N}{2}$, are replaced by their average. A filter of this type was applied to each Doppler spectrum.

Figure 5.9a contains data from the same run as Figure 5.8, but from a range bin with a much smaller atmospheric signal. The clutter peak is very clear here as it is over 20 dB higher than the atmospheric signal. As is shown in Figure 5.9b the

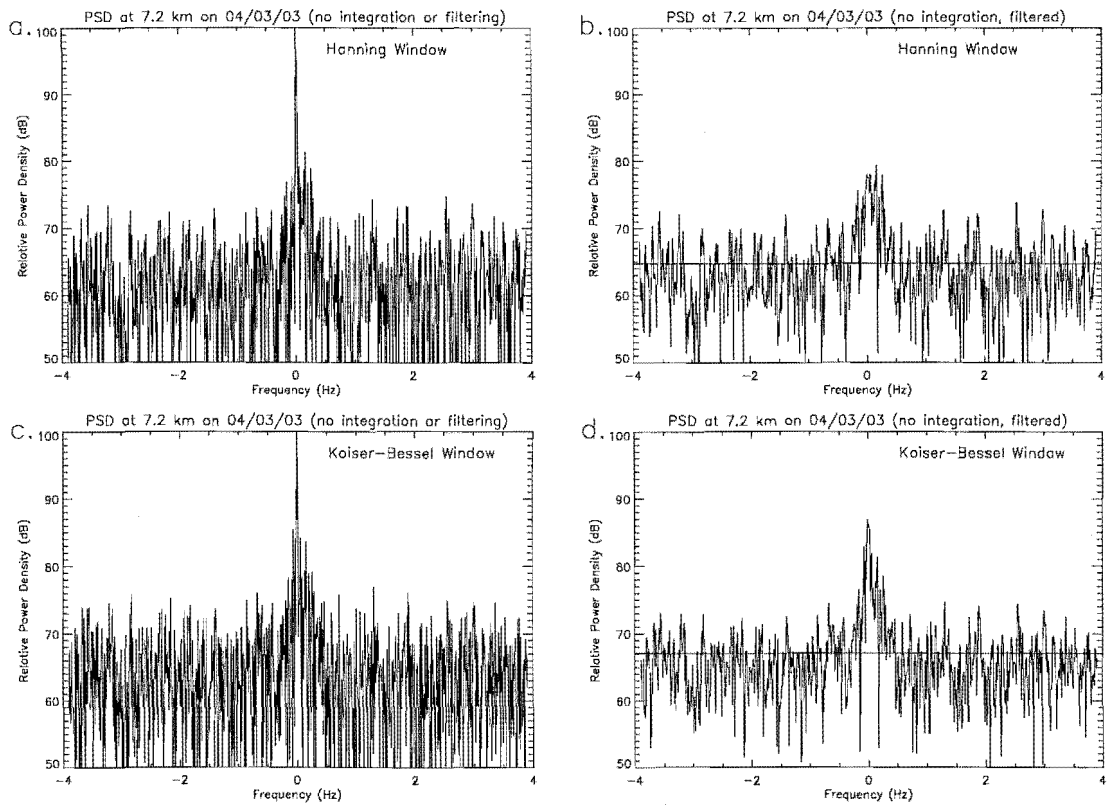

Figure 5.9: Power density spectra at 7.2 km for unintegrated data showing **(a)** unfiltered data windowed using the Hanning function and **(b)** the same data after being filtered with a notch filter at 0 Hz and a quarter-half-quarter filter. Also shown are spectra for **(c)** unfiltered and **(d)** filtered data windowed using the Kaiser-Bessel function.

clutter peak can be removed completely using a notch filter at 0 Hz that replaces the three central bins. The data in Figure 5.9b has also been smoothed with a quarter-half-quarter filter.

This figure also shows the difference between the two window functions. The data that has been weighted with the Hanning window has a lower noise level than that weighted by the Kaiser-Bessel window. The noise level, which was found using the method described in Section 5.2.3, is depicted by the horizontal lines in Figures 5.9b and 5.9d and is at 64.7 and 67.1 dB respectively. The difference can also be observed by noting that the noise spikes are generally higher across the whole spectrum for the Kaiser-Bessel window. In this particular case the extra noise near 0 Hz means that the clutter peak was not completely removed by the notch filter. The Hanning

window produces a greater reduction in noise because it drops to zero at the edges of the window, whereas the Kaiser-Bessel window only drops to 0.3 (see Figure 5.6). This abrupt end to the time series will produce larger side-lobes, causing more noise to be folded back into the spectrum. When the Kaiser-Bessel window was used with $\alpha = 5.0$, which lowers the edges of the window down to less than 0.05, the result was very similar to that obtained when using the Hanning window.

5.2.3 Noise Level Determination

To determine which part of the power spectrum contains signal, the noise power density, S_{noise}, needs to be determined. This needs to be calculated at each range bin, as it varies with range, particularly at lower levels. Below about 3 km, the receiver is completely swamped due to leakage from the transmit-receive switch (see Section 5.1.2) and consequently the noise level is higher than any atmospheric signal that is received. Between 3 and 5 km the receiver is still recovering, but the noise level is low enough that atmospheric signals can be observed. Above about 5 km, the noise level is nearly at its minimum and is almost entirely due to sky noise (see Section 4.3). Determining the noise level at each range bin is also useful for removing large signals produced by aircraft as these usually increase the signal across the entire spectrum.

The method used to determine the noise level is adapted from *Hildebrand and Sekhon* [1974] and relies on the fact that atmospheric signal and system noise are both Gaussian. The noise, however, will have a white spectrum and the atmospheric signal will be coloured (enhanced at certain frequencies). To find the noise level, a cut-off value is chosen and every point in the spectrum that is higher than this is removed. If the remaining spectrum looks like white noise, the noise ceiling has been determined, and if not, the cut-off value is lowered and the process repeated until the noise ceiling is found. To test for white noise, the following ratio, R, is computed:

$$\begin{aligned} R &= \frac{P^2}{Q}, \\ \text{where} \quad P &= \frac{\sum S_k}{N}, \\ Q &= \sum(\frac{S_k^2}{N}) - P^2, \end{aligned} \tag{5.7}$$

and N is the number of points in the spectrum. If $R > 1$ then the spectrum in

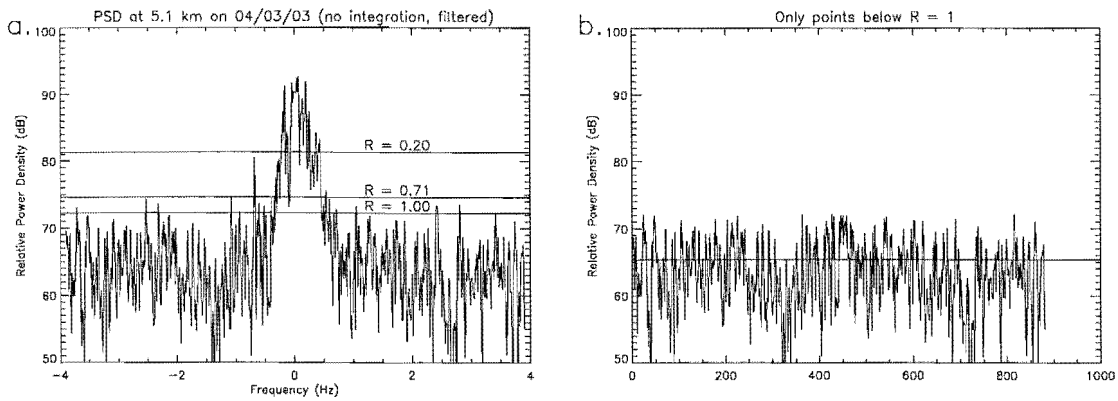

Figure 5.10: A power density spectrum at 5.1 km illustrating the noise level determination method. **(a)** shows three different cut-off levels, depicted by horizontal lines, with their associated R values. **(b)** contains only the data points that are below the cut-off level with an R value of 1. The mean of these points, which is the average noise level, is shown by the horizontal line. The data contained in these plots is the same as that displayed in Figure 5.8b, but has been filtered as described in Section 5.2.2.

question contains only white noise.

Figure 5.10 displays how this method works. The uppermost cut-off level in Figure 5.10a has an R value of 0.20. This value is very low because little of the atmospheric signal is above the cut-off level and so not much has been removed. The data points below the second cut-off level contain only a small amount of atmospheric signal and consequently the value for R is increased to 0.71. The final line marks the noise ceiling as R has reached 1.00. All the points below the noise ceiling are displayed in Figure 5.10b and the average noise level can easily be calulated by finding the mean of these points.

The initial cut-off value is determined by taking the average signal level near the edges of the spectrum (between 3 and 4 Hz and also between -3 and -4 Hz) where no atmospheric signal is expected. This value is then multiplied by a factor of 30 to ensure the initial cut-off is not below the noise ceiling. For the example shown in Figure 5.10, the initial noise level calculated from the edges of the spectrum is 66.5 dB which after multiplication by 30 comes to 81.3 dB. The final noise ceiling was calculated to be 72.1 dB and the final noise level as 65.4 dB, which as expected is quite close to the initial estimate.

Figure 5.11 shows why it is especially important to calculate the noise level at each range bin when an aircraft is observed by the radar. The plots in this figure are from different range bins for the same run at 09:06 NZST on February 26, 2003. Figure 5.11a at 10.5 km contains data with a fairly typical noise level, showing that the aircraft was not seen in this range bin. At 10.8 km the noise level has jumped by more than 15 dB and at 11.1 km it has jumped by another 15 dB. Figure 5.12 contains spectra from the runs taken either side of that shown in Figure 5.11 (09:03 and 09:09 NZST). The spectra are from a range of 11.1 km where the signal from the aircraft was largest and these plots contain no evidence of a substantial increase in the noise level. The transitory nature (in time and range) of this large increase in the noise level strongly suggests that it is caused by an aircraft. By calculating the noise level at each range bin, the signal to noise ratio at the affected ranges will be small even though the total power is very high. Aircraft such as this are not seen more than 2 or 3 times per day, so do not greatly affect the collection of atmospheric data.

5.2.4 Moment Estimation

The signal received from the atmosphere is expected to be approximately Gaussian. To parameterise this accurately it is necessary to know in what part of the spectrum the signal exists. The fitting, or moment estimation, can then be performed in the desired region.

To find the signal area, a copy of the spectrum is taken and then smoothed using a triangular window with a width of 0.5 Hz. The maximum point in the spectrum is then found and all the contiguous points either side of this maximum that are larger than the average noise level are included as part of the signal area. The smoothing needs to be performed to ensure that any brief fluctuations in the signal that might be below the noise level are removed so that their effect on the signal area is minimised. If the resulting signal area is not wider than a certain value, it is ignored and considered as noise.

Figure 5.13 contains an example of a power density spectrum and its associated signal area. Figure 5.13a shows the smoothed plot used to find the signal area and Figure 5.13b shows the original data, that will be used to calculate the moments.

This method for finding the signal gives better results if the search area for the maximum value is restricted to ± 1 Hz which corresponds to $\pm 3.6\ \mathrm{m\,s^{-1}}$. This means

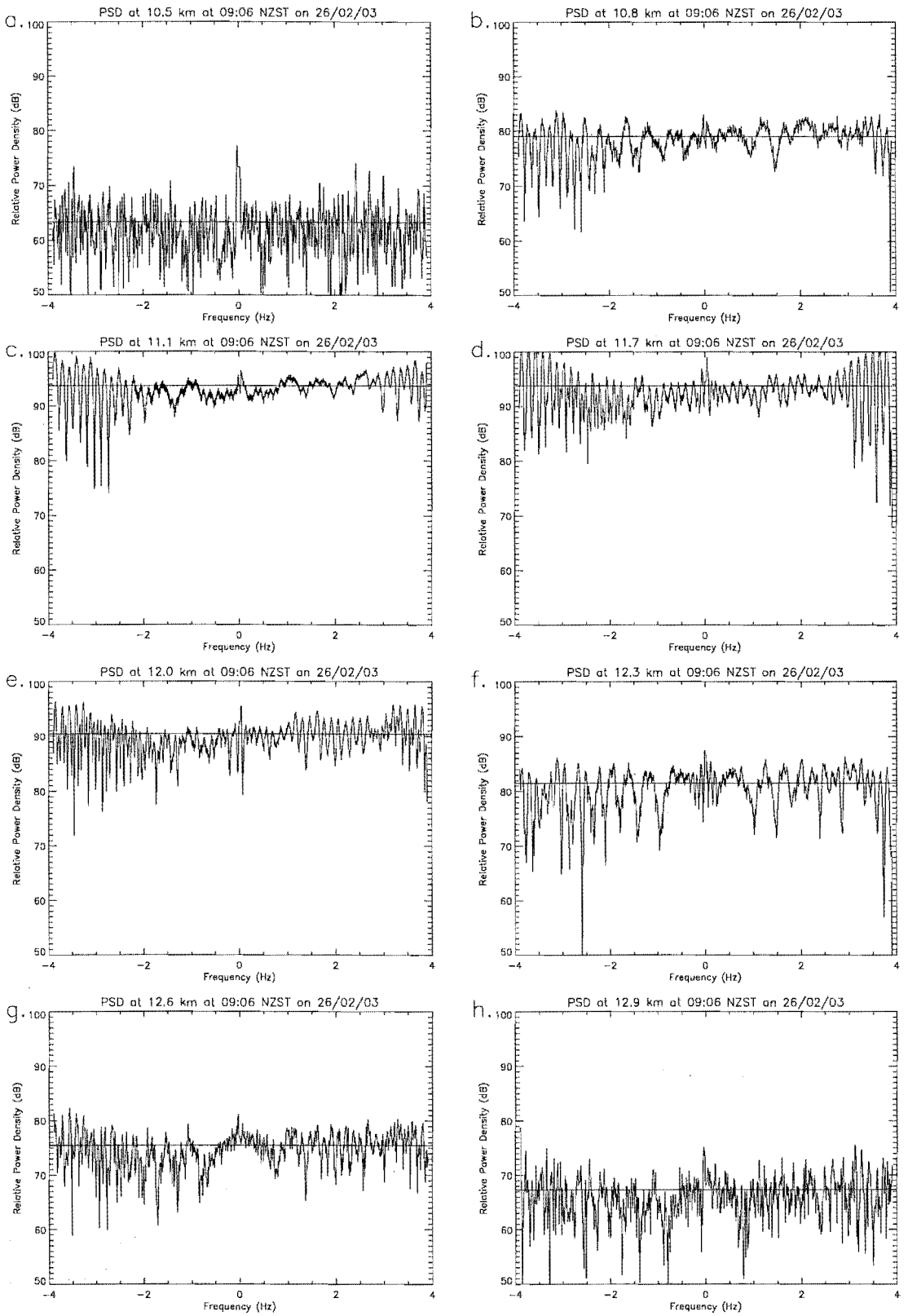

Figure 5.11: The effect an aircraft has on the noise power density level. Figures (**a**) to (**h**) increase in range from 10.5 to 12.9 km.

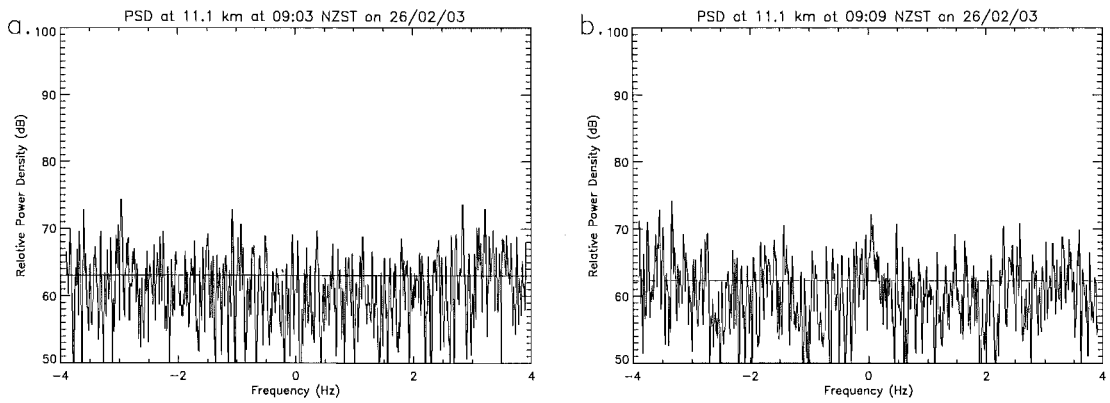

Figure 5.12: Power spectra at 11.1 km obtained before and after the passage of the aircraft shown in Figure 5.11.

that large noise peaks, which sometimes occur near the edges of the spectra, are not falsely labelled as signal area. The vertical velocities measured with the radar are not expected to exceed $\pm 3.6\ \mathrm{m\,s^{-1}}$, and in the first few months of operation, the vertical velocties measured by the CUSTAR radar seldom exceeded $\pm 2\ \mathrm{m\,s^{-1}}$.

The final signal processing step is to calculate the useful atmospheric parameters. By assuming that the atmospheric signal is Gaussian in nature, it can be approximated by a Gaussian power spectrum which has the form

$$S(\omega) = \frac{P}{\sqrt{2\pi W^2}} \exp\left[-\frac{(\omega - \Omega)^2}{2W^2}\right], \tag{5.8}$$

where ω is the frequency in radians [*Woodman*, 1985]. The signal is then completely described by three parameters, P, the total power, Ω, the Doppler shift, and W, the one standard deviation width of the spectrum. These three parameters are also the first three moments of $S(\omega)$

$$P = \int S(\omega) d\omega \tag{5.9}$$

$$\Omega = \frac{1}{P} \int \omega S(\omega) d\omega \tag{5.10}$$

$$W^2 = \frac{1}{P} \int (\omega - \Omega)^2 S(\omega) d\omega. \tag{5.11}$$

Because $S(\omega)$ is in practise made up of discrete points the above moments can be

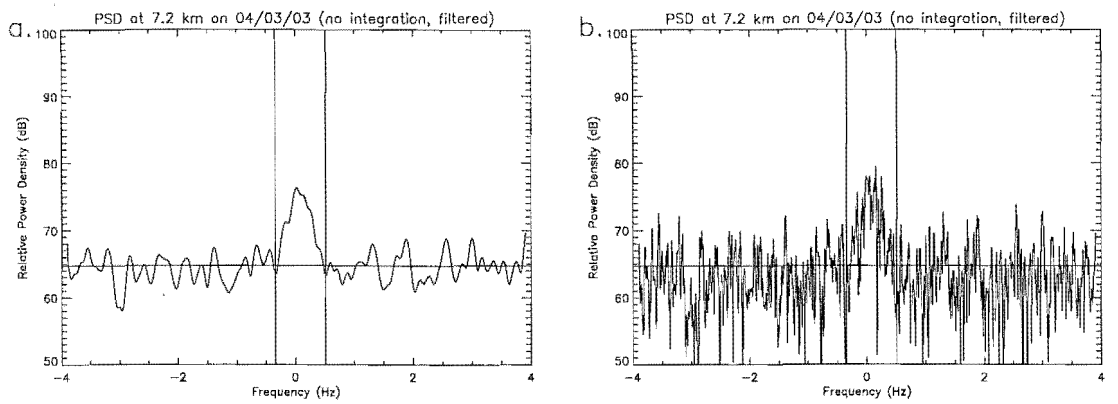

Figure 5.13: A power density spectrum at 7.2 km illustrating the method used to detemine the signal area. **(a)** shows the spectrum after it has been smoothed and **(b)** shows the original spectrum. On both of these plots the horizontal line is the noise level found using the method indicated in Section 5.2.3 and the vertical lines mark the signal area. The data used in these plots is the same as that in Figure 5.9b.

calculated using the following sums

$$P = \frac{2\pi}{T} \sum_{k=-\frac{N}{2}}^{\frac{N}{2}-1} S_k \tag{5.12}$$

$$\Omega = \frac{2\pi}{T} \frac{1}{P} \sum_{k=-\frac{N}{2}}^{\frac{N}{2}-1} \omega_k S_k \tag{5.13}$$

$$W^2 = \frac{2\pi}{T} \frac{1}{P} \sum_{k=-\frac{N}{2}}^{\frac{N}{2}-1} (\omega_k - \Omega)^2 S_k, \tag{5.14}$$

where T is the length of the time series and N is now the number of points in the signal area.

The signal to noise ratio, SNR, can be defined as the total signal power P divided by the average noise power per signal bandwidth, P_{noise} [*Röttger and Larsen*, 1990]. P_{noise} can be found by multiplying the noise power density, S_{noise}, by the width of the signal area.

5.3 The Effects of Integration

5.3.1 Coherent Integration

Coherent integration, which is the summing of a number of coherent sequential samples prior to transformation into the frequency domain, reduces the number of mathematical operations performed during the spectral analysis without significantly affecting the resulting spectrum [*Balsley and Gage*, 1980]. However, if the computing resources are available, there are a number of advantages associated with processing the raw data without coherent integration [*Hocking*, 1997a]. This section is concerned with the effect coherent integration has on the CUSTAR data.

Coherent integration is effectively a low-pass filter. Any received signal that has a frequency greater than the cut-off for this filter (the Nyquist frequency) will be aliased into the final spectrum [*Blackman and Tukey*, 1958]. Signals in this category include power supply noise, signals received from other radio equipment, reflections from aircraft and reflections from meteor trails. If coherent integration is not performed these signals normally don't affect the atmospheric signal as they are usually at much higher Doppler frequencies. *Hocking* [1997a] describes spectral processing techniques to remove such effects in both the time and frequency domains.

For the CUSTAR radar, the unwanted signals mentioned above (meteor and aircraft returns) are not likely to cause significant problems. Birdlings Flat is not under a major flight path and reflections from aircraft happen only once or twice a day, so are not a great concern. Meteor ablation trails occur at altitudes of between 80 and 120 km and because the CUSTAR inter-pulse period is relatively large ($T_{\mathrm{IPP}} = 1$ ms, which corresponds to a maximum range of 150 km) there is little possibility that reflections from meteors could be aliased into the data. Also, power supply noise has been almost completely removed, as has interference from the other radar experiments at Birdlings Flat (see Figure 5.8a).

The aliasing which results from coherent integration will still have an effect on the final spectra even if these additional signals do not exist. This has been investigated for radar by *Rastogi* [1983], who shows that coherent integration weights the power spectrum with a factor $G(f_k)$ given by

$$G(f_k) = \left[\frac{\sin(\pi f_k(T_{\mathrm{IPP}})M)}{M\sin(\pi f_k(T_{\mathrm{IPP}}))}\right]^2, \qquad k = -\frac{N}{2}, ..., \frac{N}{2}, \tag{5.15}$$

where T_{IPP} is the inter-pulse period and M is the number of data points in the inte-

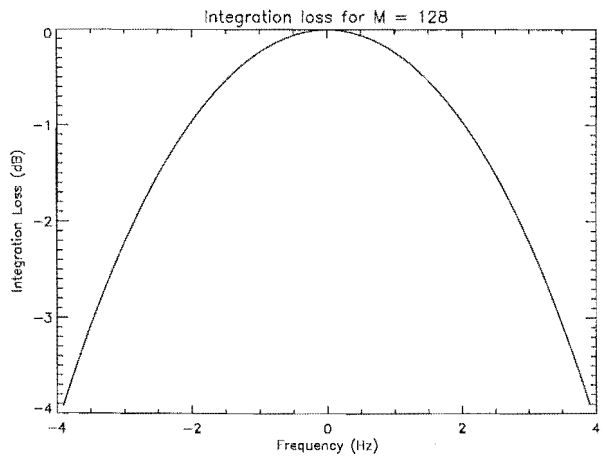

Figure 5.14: The integration loss for typical operational parameters used in this work ($T_{\mathrm{IPP}} = 1$ ms, $N = 128$).

gration. This weighting function can be inverted and applied to the signal portion of the spectrum to correct for the low-pass filtering effect [*Hooper*, 1999].

The power loss associated with this weighting has the greatest effect near the Nyquist frequency and a very small effect at frequencies near zero as shown in Figure 5.14. For frequency shifts of less than 2 Hz, the expected loss is less than 1 dB. This means that for signals with small Doppler shifts, such as those expected from a vertically pointing beam, it is not essential that this correction is performed.

During this project, raw data was stored on the radar control computer and the processing of this data was performed off-line using computing resources available in the Department of Physics and Astronomy. To make continuous operation feasible in terms of data storage space, it was necessary to integrate the data in the radar control computer. In order to test the effect of this process, 25 runs, each 2.18 minutes in length, were collected without coherent integration and examined off-line. An example of an unintegrated power spectrum is shown in Figure 5.8.

The data from the 25 runs was also coherently integrated over 128 pulses, giving a time between samples of 128 ms and a Nyquist frequency of 3.91 Hz. Figure 5.15 shows power density spectra for the coherently integrated data and the unintegrated data at heights of 5.1 and 7.2 km. Atmospheric signal can be seen in all four plots, although at the higher altitude the signal is much weaker. The data in these plots has been filtered using a notch filter and a quarter-half-quarter filter (see Section 5.2.2).

The shape of the atmospheric signal in the integrated and unintegrated data is

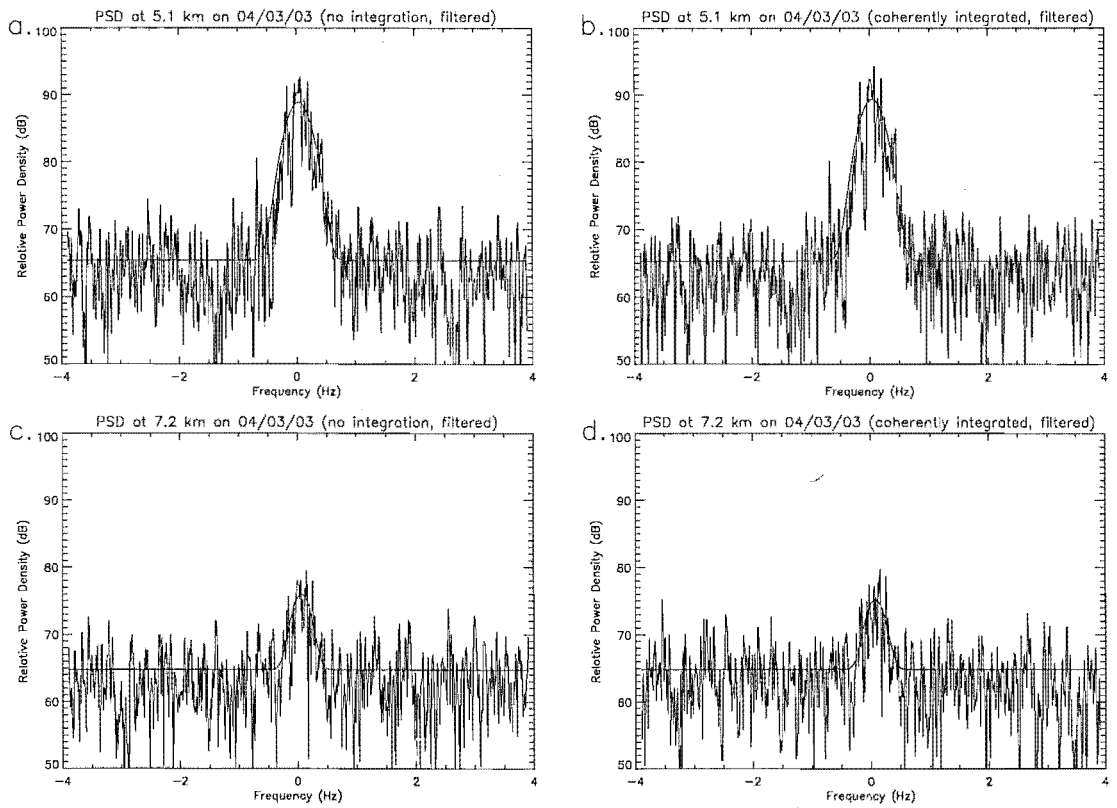

Figure 5.15: Comparison between power density spectra for unintegrated data and coherently integrated data. **(a)** and **(c)** contain unintegrated data at 5.1 and 7.2 km respectively, showing only the central ± 4 Hz. **(b)** and **(d)** contain coherently integrated data at 5.1 and 7.2 km, respectively. This data has been filtered using a notch filter at 0 Hz and a quarter-half-quarter filter (see Section 5.2.2).

very similar. The major difference between the two processing methods is the characteristics of the noise. The individual noise spikes are of different magnitudes and in different positions and even larger anomalies, such as at 2.75 Hz in Figure 5.15a, are quite different. However, at both heights, the noise levels (and signal levels) are approximately the same, as shown by the Gaussian curves plotted over the spectra. These show the noise level and signal characteristics calculated by the signal processing scheme.

The differences between coherently integrated and unintegrated data for all the points in the 25 runs mentioned above are shown in Figure 5.16. There is little difference between the signal to noise ratio for the different data sets, the comparison producing a very good correlation and a mean difference of only 0.09 dB. Fig-

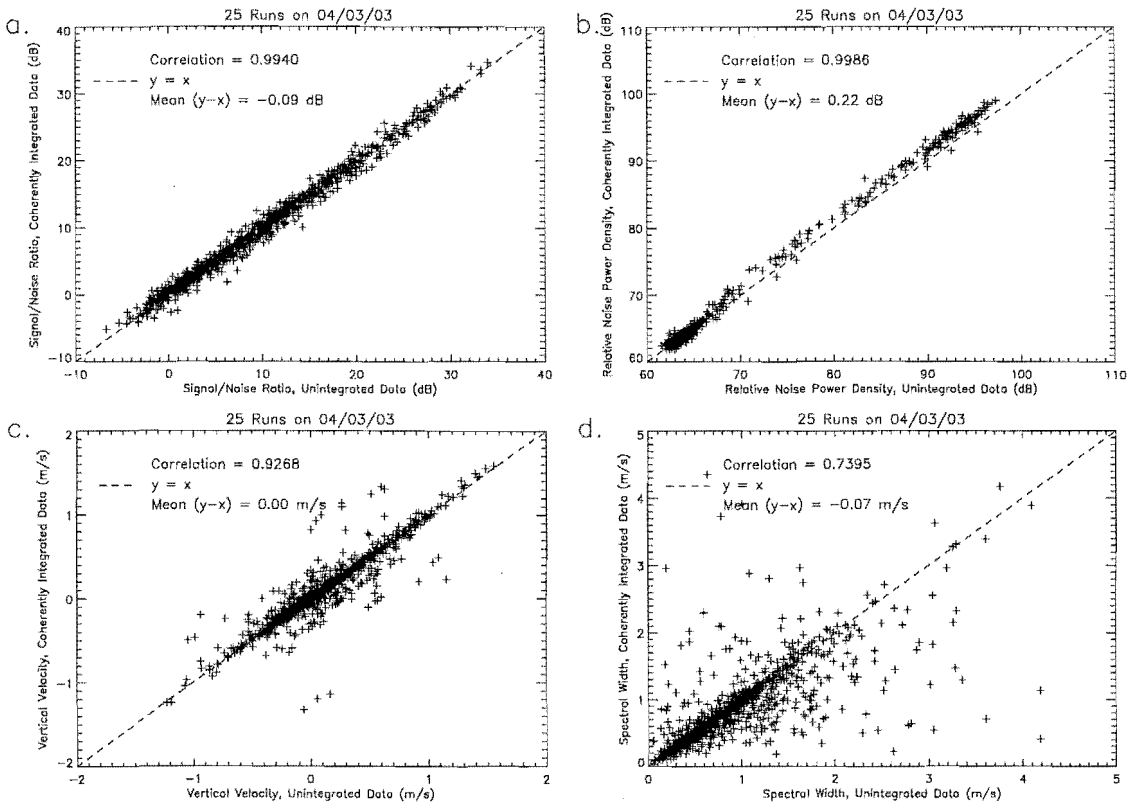

Figure 5.16: Comparisons between coherently integrated data and unintegrated data for **(a)** signal to noise ratio, **(b)** noise power density, **(c)** vertical velocity and **(d)** spectral width.

ure 5.16b shows an excellent correlation between the noise density values, although the coherently integrated data has a noise level that is on average 0.22 dB higher than the noise level of the unintegrated data. This is not a very large difference and occurs mainly where the noise level is already high.

The comparisons for vertical velocity and spectral width have a larger spread than those for signal to noise ratio and noise power density. This is because all points are included in these plots, even those with a low signal to noise ratio, and so some of the points will be poor estimates of the true values. Even so, the vertical velocities seen in Figure 5.16c have a correlation coefficient of 0.93, showing that there is still very good agreement. The correlation coefficient for the spectral width comparison is quite low (0.74), but the mean difference is only 0.07 $\mathrm{m\,s^{-1}}$ suggesting that the spread is more a measure of the uncertainty in the spectral width rather than a consistent difference between the two processing methods.

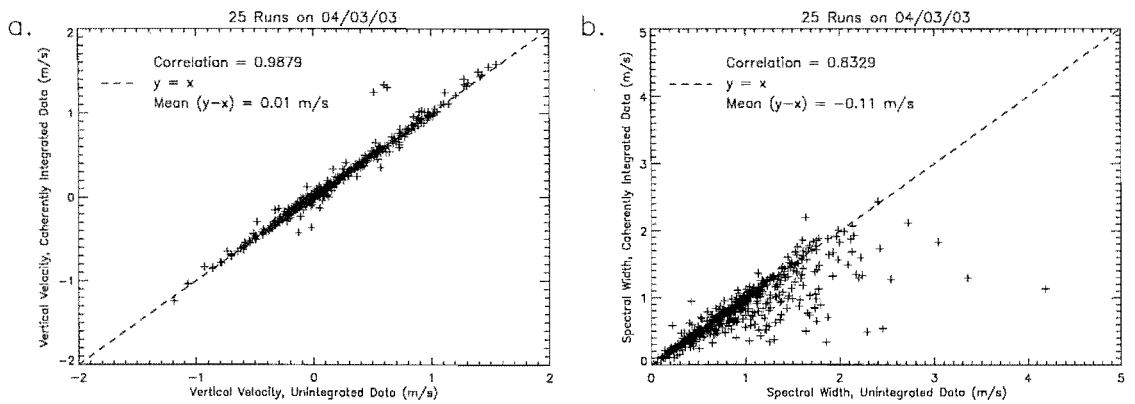

Figure 5.17: Comparisons between coherently integrated data and unintegrated data for **(a)** vertical velocity and **(b)** spectral width, including only those data points with a signal to noise ratio greater than 5 dB.

Figure 5.17 contains a repeat of Figures 5.16c and 5.16d, except that all data points with a signal to noise ratio less than 5 dB have been removed. The correlations are now much better, although the spectral widths calculated from the unintegrated data are (on average) slightly larger than those calculated from the integrated data.

The coherently integrated data and unintegrated data were also compared after the theoretical weighting function in Equation 5.15 was removed from the integrated data. The "correction" was applied after the noise level and signal area had been found, and therefore only affected the signal area. Comparisons between the "corrected" data and unintegrated data were performed and produced nearly identical results to those in Figure 5.16. The mean difference between the signal power was 0.08 dB, which is a change of only 0.01 dB from the "uncorrected" data. The mean difference between the vertical velocity was negligible and the mean difference between the spectral width was 0.10 $\mathrm{m\,s^{-1}}$ (for data with a signal to noise ratio greater than 5 dB), which is a change of only 0.01 $\mathrm{m\,s^{-1}}$ from the "uncorrected" data. This shows, as expected, that the theoretical weighting given by Equation 5.15 has very little effect on signal received from a vertically pointing antenna beam.

While coherent integration can have some adverse effects on results from the radar, they are not substantial enough to overcome the pratical advantages gained in the operation of the system. The results from this section show that for the CUSTAR radar there is no significant difference between the coherently integrated data and unintegrated data.

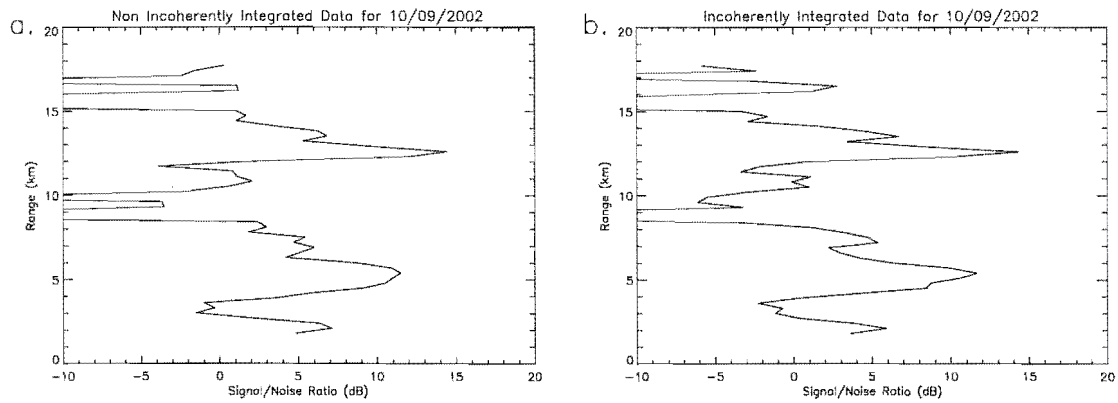

Figure 5.18: Vertical signal to noise profiles for one 2.18 minute time period for **(a)** non-incoherently integrated data and **(b)** incoherently integrated data.

5.3.2 Incoherent Integration

To improve signal detectability, two or more power spectra can be summed and this process is called incoherent integration. The CUSTAR radar collected time series of length 2.18 minutes and did not perform incoherent integration. This section compares results from data with no incoherent integration to results from data that has been incoherently integrated.

The comparison was performed by taking each time series from the radar and splitting it into four lengths of 33 seconds. Each of these four time series was processed using the same technique as the non-incoherently integrated data and then summed. The results were then compared with results from the original data that had been processed in the normal manner. The radar data used for this comparison was coherently integrated over 128 pulses at the radar site, so a full day's worth of data (September 10, 2002) could be used.

Figure 5.18 contains vertical signal to noise ratio profiles for data which has been incoherently integrated and data which has not been incoherently integrated. The profiles are from the same raw data. The large scale structure of these plots is almost identical, although on scales of $\sim$ 300 m, there are small deviations.

Figure 5.19 contains comparisons for all the points taken during the 480 runs over the day. The correlation coefficients for these comparisons are very good, although the signal to noise ratio comparison has a much larger spread. The signal to noise ratio for the incoherently averaged data is on average 1.59 dB lower than that for

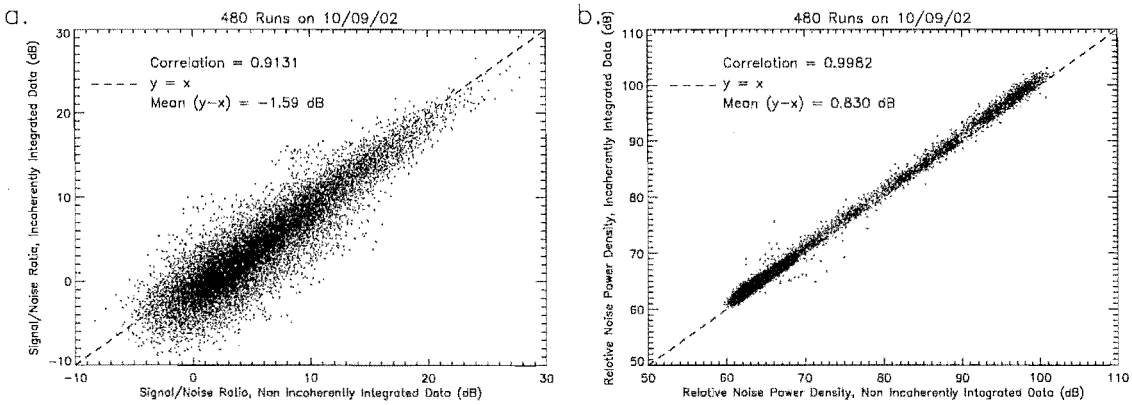

Figure 5.19: Comparisons between data which has been incoherently integrated and data which has not, for **(a)** signal to noise ratio and **(b)** noise power density.

the unaveraged data and the noise power is 0.83 dB higher.

The disadvantage in not incoherently integrating the data is that the time taken to perform the Fourier transforms is longer. However, as the data has already been coherently integrated the extra time is not of great significance.

5.4 The Radar Tropopause

The tropopause is the boundary between the troposphere and stratosphere. These two regions differ in vertical temperature structure, potential vorticity and in the concentration of various chemical species such as ozone and water vapour [*Holton et al.*, 2003]. VHF radars are very sensitive to changes in the gradient of the potential temperature and so can be used to investigate the tropopause [*Gage and Green*, 1979; *Vaughan et al.*, 1995; *Hooper and Arvelius*, 2000]. The tropopause was first detected with radar by *Atlas et al.* [1966] who used ultra-high frequencies and assumed that the increase in backscattered power arose from turbulence.

For turbulent scatter and Fresnel scatter, the backscattered power for a VHF radar is approximately proportional to M^2/r^2 (see Section 2.3.2 and 2.3.3) where r is the range from the radar and M is the vertical gradient of the potential refractive index. Above the first few kilometres of the atmosphere, where the humidity contribution can be assumed negligible, M can be approximated as

$$M = -77.6 \times 10^{-6} \left(\frac{p}{T}\right) \left(\frac{\partial \ln \theta}{\partial z}\right), \tag{5.16}$$

where p is atmospheric pressure in mb, T is absolute temperature and θ is potential temperature (see Section 2.2.4). Radar signal strength is therefore closely related to the potential temperature gradient. This gradient and the absolute temperature gradient are related by Equation 2.5 which is reproduced below

$$\frac{1}{\theta}\frac{d\theta}{dz} = \frac{1}{T}\left(\Gamma_d - \Gamma\right), \tag{5.17}$$

where Γ_d ($= 9.8\ \mathrm{K\,km^{-1}}$) is the dry adiabatic lapse rate. In the troposphere, the observed lapse rate, Γ, is approximately $6\ \mathrm{K\,km^{-1}}$ (excluding inversions) and in the stratosphere Γ is typically less than $2\ \mathrm{K\,km^{-1}}$ [*Gage et al.*, 1986]. The transition between these gradients is normally abrupt and causes a sudden increase in the radar signal strength. The radar tropopause can then be defined as the point (above some minimum height, e.g. 4 km) at which the vertical gradient of the signal strength is at its maximum.

Figure 5.20 shows the signal to noise ratio of CUSTAR radar data plotted against altitude. Twenty profiles over a one hour period from 10:00 to 11:00 NZST on October 12, 2002, have been averaged to produce this plot. It shows a clear increase in signal strength at 10 km and the strongest vertical gradient in the signal power is observed at 9.3 km, represented by the horizontal line. The profile shown in Figure 5.20 is an example of a strong tropopause. This is by no means an unusual profile, but it should be noted that the strength of the tropopause can vary quite considerably and in some cases no appreciable increase in signal power is observed.

5.4.1 Tropopause Determination Algorithm

In simple cases where there is a distinct and strong radar tropopause, its altitude is the point at which the vertical gradient in the radar signal power, evaluated over a certain height range (e.g. 1500m), has its maximum value [*Hooper and Arvelius*, 2000]. *Vaughan et al.* [1995] showed that the point at which the radar signal power reached a secondary maximum above the minimum normally observed in the upper troposphere could also be used to estimate the radar tropopause height, provided a suitable offset was incorporated into this value. In many cases, however, the tropopause can be indefinite or occur in two distinct steps and in these cases, a more sophisticated method of determining the tropopause is necessary.

The method used in this thesis to find the radar tropopause height is now described. First, the signal to noise ratio, SNR, is averaged over one hour. SNR is

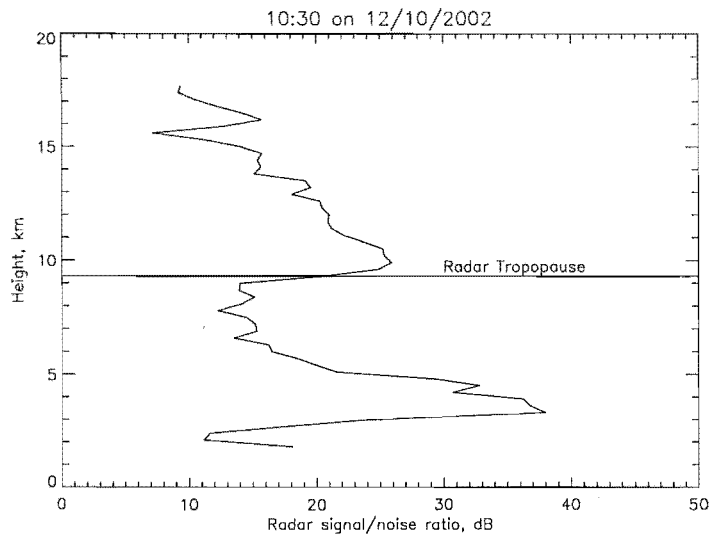

Figure 5.20: Radar signal to noise ratio averaged over one hour. The height of the radar tropopause is indicated by a horizontal line.

used, instead of the total signal power, to reduce the amount of bad data included in the tropopause estimation process. Some unwanted signals, such as those from airplanes, produce a high noise level as well as a high signal level (see Figure 5.11), so that when the signal to noise ratio is used, these areas of bad data are greatly reduced. The averaging improves the profile by removing the small fluctuations between runs and also provides a useful hourly average of the radar tropopause which can be readily compared with tropopause heights deduced from other sources, such as radiosondes (see Section 5.5). However, as shown later, the radar tropopause height can be calculated quite accurately at a temporal resolution as high as 9 minutes.

Next, the vertical gradient in the profile of SNR is found (over a height of 1500 metres) for each range gate between 5.85 km and 14.25 km. In this analysis, the vertical gradient between 5.1 and 6.6 km is calculated and assigned to the height of 5.85 km, then the vertical gradient between 5.4 and 6.9 km is assigned to 6.15 km and so on, up to 14.25 km which contains the gradient between 13.5 and 15 km. This produces 30 gradients, from which the four largest are extracted. The largest of these gradients and any of the other three that are at adjacent heights are used to determine the main tropopause height. An average of these heights is taken, weighted by the magnitude of each associated gradient.

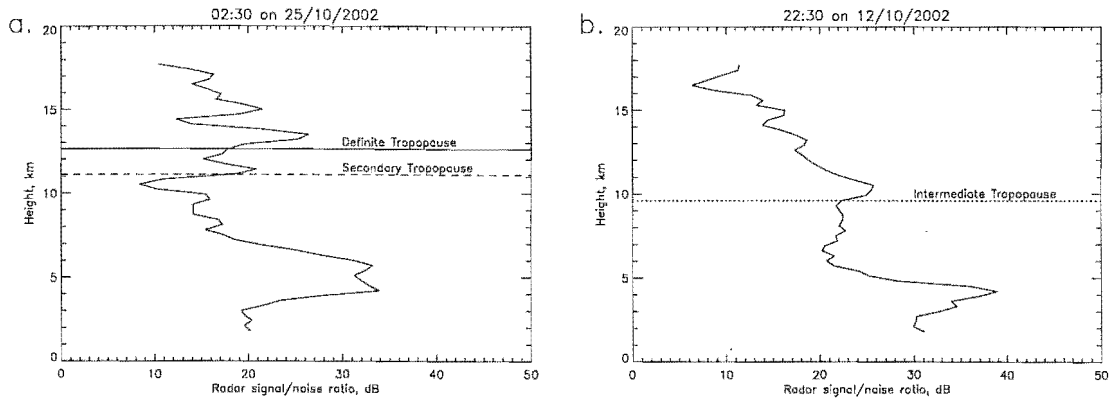

Figure 5.21: Examples of **(a)** a two-step tropopause and **(b)** an intermediate tropopause. The profiles are of radar signal to noise ratio averaged over one hour.

This main tropopause is categorised as either a definite, intermediate or indefinite tropopause using a similar method to that used by *Hooper and Arvelius* [2000]. If the magnitude of the largest gradient is greater than 5 dB km^{-1}, then it is defined as a definite tropopause. The tropopause is indefinite if the largest gradient is less than 2 dB km^{-1} and intermediate if the gradient is between these two values. These categories are a measure of the sharpness of the tropopause.

The height of the secondary tropopause, if one exists, can be calculated from the remainder of the four largest gradients calculated earlier. If two of the remaining gradients are adjacent then the weighted average of their heights is used. If none of the remaining gradients are adjacent and the largest is greater than 2 dB km^{-1}, it alone is taken as the height of the secondary tropopause. Figure 5.21 contains examples of a two-step tropopause and an intermediate tropopause. Figure 5.20 is a good example of a definite tropopause.

5.4.2 Radar Tropopause Results

The radar tropopause was found once each hour from August 27, 2002 to February 4, 2003. The tropopause height was plotted each day as a function of time. These plots showed that the tropopause height and structure varied considerably between days and often during the day.

Figures 5.22 and 5.23 contain contour plots of the radar signal to noise ratio, SNR, for two typical days. The first shows data for September 1, 2002, when there

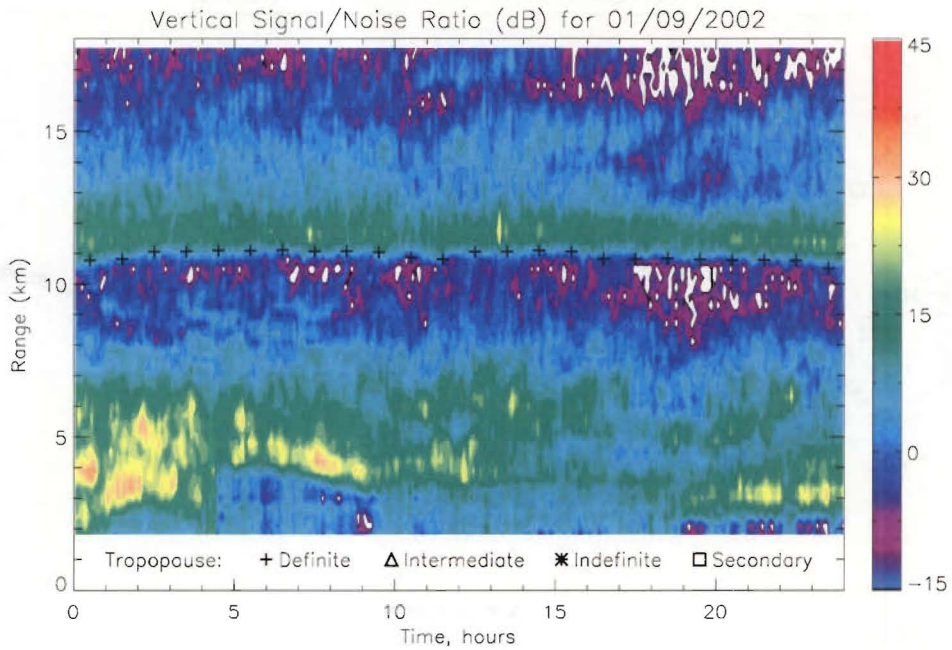

Figure 5.22: Radar signal to noise ratio plotted as a function of range and time. Tropopause height is shown each hour and little variation is seen through the day.

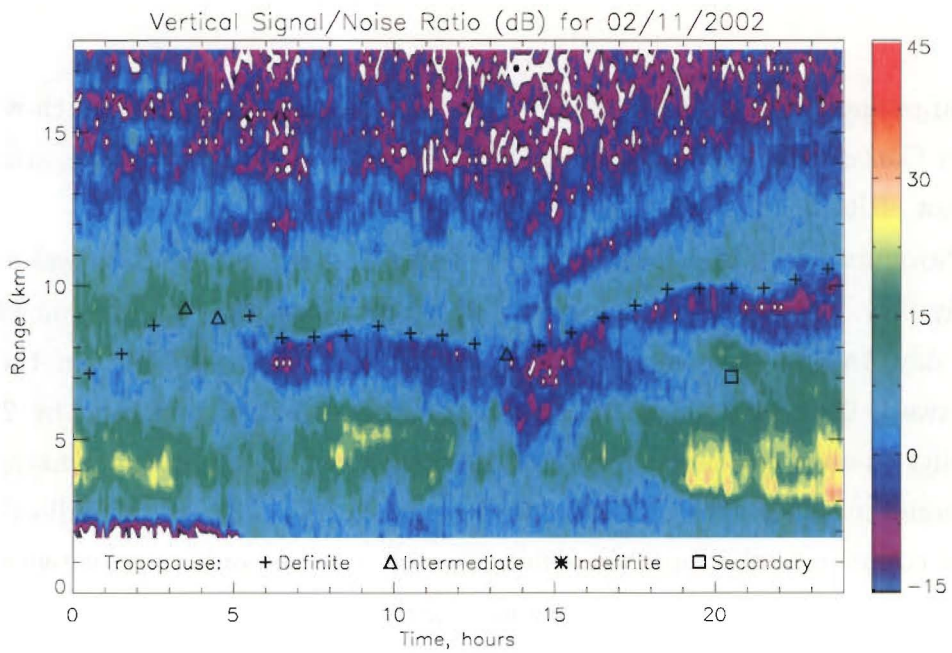

Figure 5.23: Same as Figure 5.22, but showing a large variation in the tropopause altitude through the day.

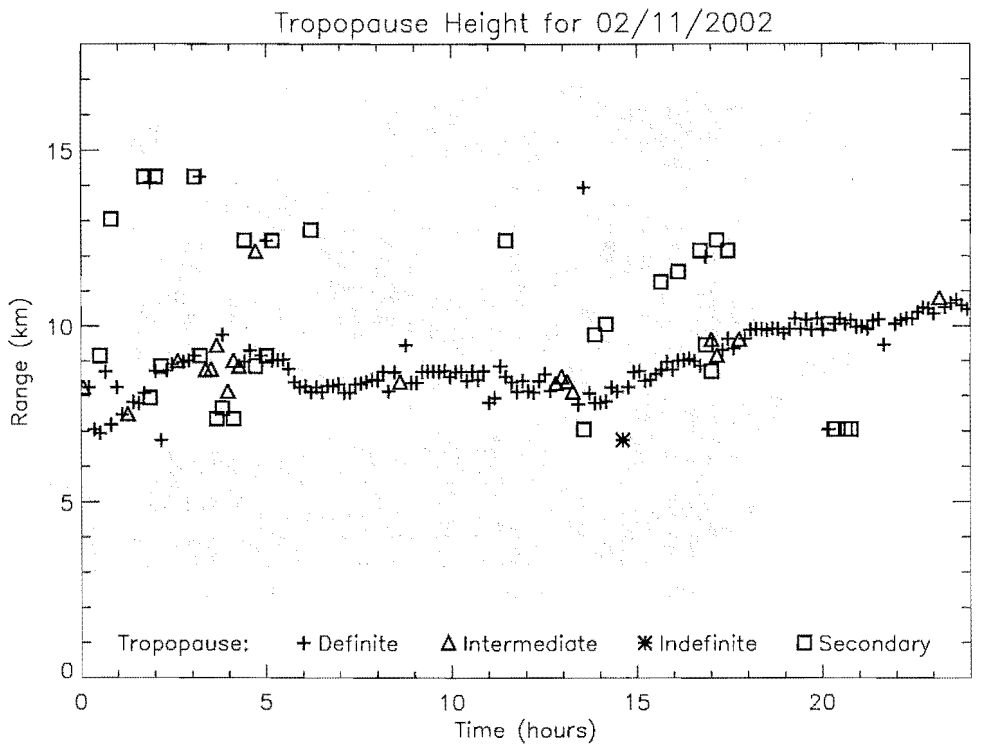

Figure 5.24: Radar tropopause altitudess for the same day as Figure 5.23, but calculated with a temporal resolution of 9 minutes instead of one hour.

was a large anti-cyclone situated over most of New Zealand and a north-westerly flow over Canterbury. The radar tropopause on this day was very stable, staying at a constant altitude of about 11 km.

On November 2, 2002, a cold front passed over Canterbury and there was a strong southerly flow. As shown in Figure 5.23, the tropopause varied quite considerably on this day, ranging between just over 7 km to 10.5 km. In fact, in the short time between 00:00 and 04:00 NZST the tropopause height increased by 2.5 km. The ability to observe changes on this time scale gives the radar an advantage over conventional methods of determining tropopause height. The use of radiosondes is the most common method and these are generally released only once or twice a day.

Tropopause heights can be determined with a temporal resolution as high as 9 minutes using a radar, although the results are more prone to spurious height derivations. Figure 5.24 shows tropopause heights calculated for the same day as Figure 5.23, but with only 9 minutes of averaging. Most of the results follow a similar curve to Figure 5.23 suggesting that little information is lost when the radar data

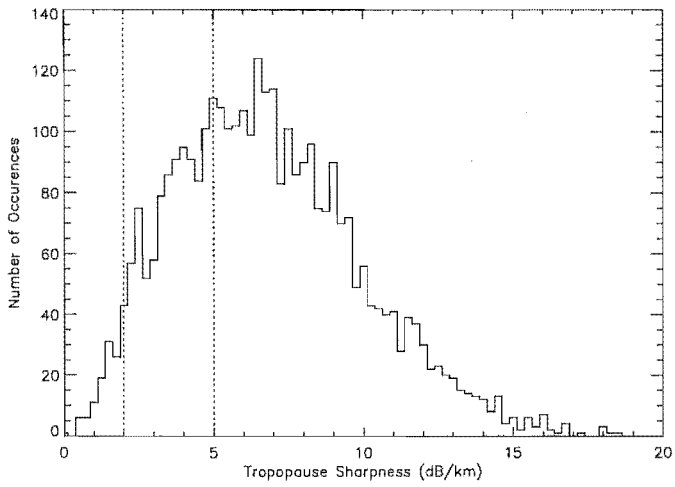

Figure 5.25: The distribution of tropopause sharpness as measured by the radar. Dotted vertical lines mark the transitions between indefinite, intermediate and definite tropopauses.

is averaged over one hour periods. If this higher temporal resolution was necessary, the spurious data points could be separated out based on what type of tropopause is observed, as most of the spurious points have been defined as secondary tropopauses. Spurious points could also be excluded by fitting a piecewise polynomial fit and removing those points that are not within a certain distance (say 1 km) of this fit, as has been done for wind velocity measurements by *Hocking* [1997b].

Between August 27, 2002 and February 4, 2003, approximately 3800 individual tropopause heights were calculated (including secondary ones). Of these, the majority (62%) were definite tropopauses, 25% were intermediate, 3% were indefinite and 10% were secondary. Figure 5.25 shows the distribution of tropopause sharpness values using a bin size of 0.25 $\mathrm{dB\,km^{-1}}$. Secondary tropopauses are included in this plot and placed depending on their sharpness.

Figure 5.26 shows the height distributions for the four different tropopause groups. The bin size is 250 metres for all plots. Figure 5.26a shows a clear maximum at 10.5 km with most points grouped between 8.5 and 12.5 km. The two secondary peaks at 9.25 and 11.75 km are probably artifacts of the low sampling size. Figures 5.26b, c and d show progressively less grouping, which is to be expected as there will be more uncertainty in these results, particularly for the indefinite and secondary tropopause heights.

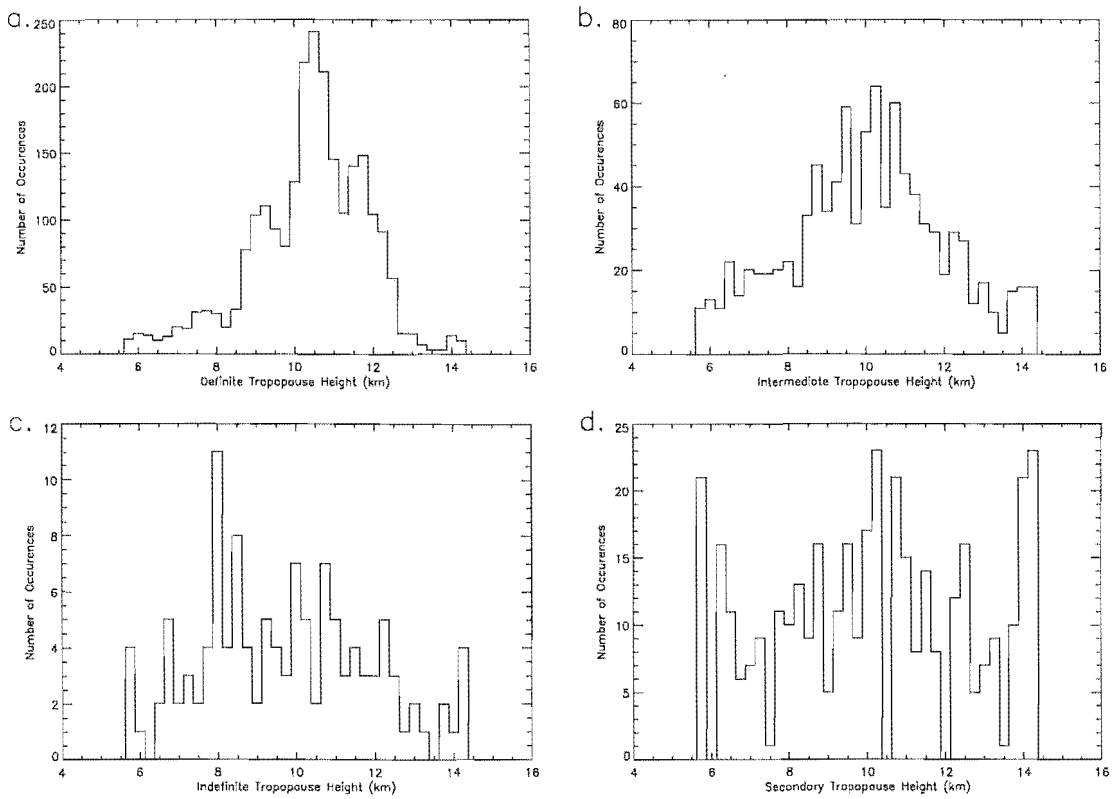

Figure 5.26: The distribution of tropopause heights as measured by the radar. Included are distributions for **(a)** definite, **(b)** intermediate, **(c)** indefinite and **(d)** secondary tropopauses.

5.5 Comparisons with Temperature Tropopause

The conventional definition of the tropopause uses the differing vertical temperature profiles of the troposphere and stratosphere as a basis. In the troposphere, the temperature decreases with height and in the stratosphere, it increases with height and the point where the lapse rate changes is defined as the tropopause. The World Meteorological Organisation (WMO) defined the temperature tropopause as the lowest altitude at which the vertical temperature gradient becomes more positive than $-2\ \mathrm{K\,km^{-1}}$ and remains so between this point and every point in the next 2 km. In addition, the tropopause can not be lower than 4 km in altitude to avoid boundary layer temperature inversions being categorised as the tropopause [*WMO*, 1986].

A method of determining the sharpness of the temperature tropopause has been

proposed by *Price and Vaughan* [1993]. The sharpness is calculated by finding the vertical distance taken for the lapse rate to decrease from 6 $\mathrm{K\,km^{-1}}$ (the lapse rate in the troposphere) to 2 $\mathrm{K\,km^{-1}}$ (the lapse rate at the tropopause). The tropopause is definite if this distance is less than 0.5 km, indefinite if it is greater than 1.2 km and intermediate if it is between these values. *Vaughan et al.* [1995] used this method with the refined value of 5 $\mathrm{K\,km^{-1}}$ for the tropospheric lapse rate. This modification makes very little difference to the data obtained in New Zealand, as the lapse rate in the tropopause is seldom less than 7 $\mathrm{K\,km^{-1}}$.

5.5.1 Annual Variation of the Tropopause

In the mid-latitudes, the average height of the tropopause varies through the year (see Figure 2.2). The variation can be investigated by taking monthly or bi-monthly means of the tropopause height. This was done using the radar tropopause data and the results were compared with radiosonde data collected in Christchurch by the New Zealand Meteorological Service (NZMS) between 1958 and 1962 [*NZMS*, 1963].

The NZMS data was recorded at Christchurch Airport (43° 29′ S, 172° 32′ E) which is 40 km away from Birdlings Flat (43° 49.5′ S, 172° 41.5′ E). Tropopause heights, calculated using the WMO definition described above, were available for the period 1958 to 1962 and had been summarised to give monthly statistics. The data was presented as a distribution of tropopause heights with a bin size of 500 metres.

Tropopause heights were calculated from the CUSTAR radar data from August 27, 2002 to February 4, 2003. Due to a technical fault, the radar was not in operation for more than half of January, so only data for the four full months of September through to December, inclusive, was used for this comparison. Secondary tropopauses were not included. The tropopause heights were binned with a 250 metre resolution and grouped into two sets, September plus October and November plus December (Figures 5.27a and 5.27c). Similarly, the NZMS data was also grouped into two lots containing the same months as the radar data (Figures 5.27b and 5.27d). The average over two months was taken to increase the sample size.

The first thing to note in Figure 5.27 is that the radar data has a much greater number of points than the radiosonde data. The number of points in the Sep/Oct and Nov/Dec plots for the radar data is 1438 and 1391 respectively, whereas for the radiosonde data the equivalent numbers are 297 and 292. Although the radiosonde

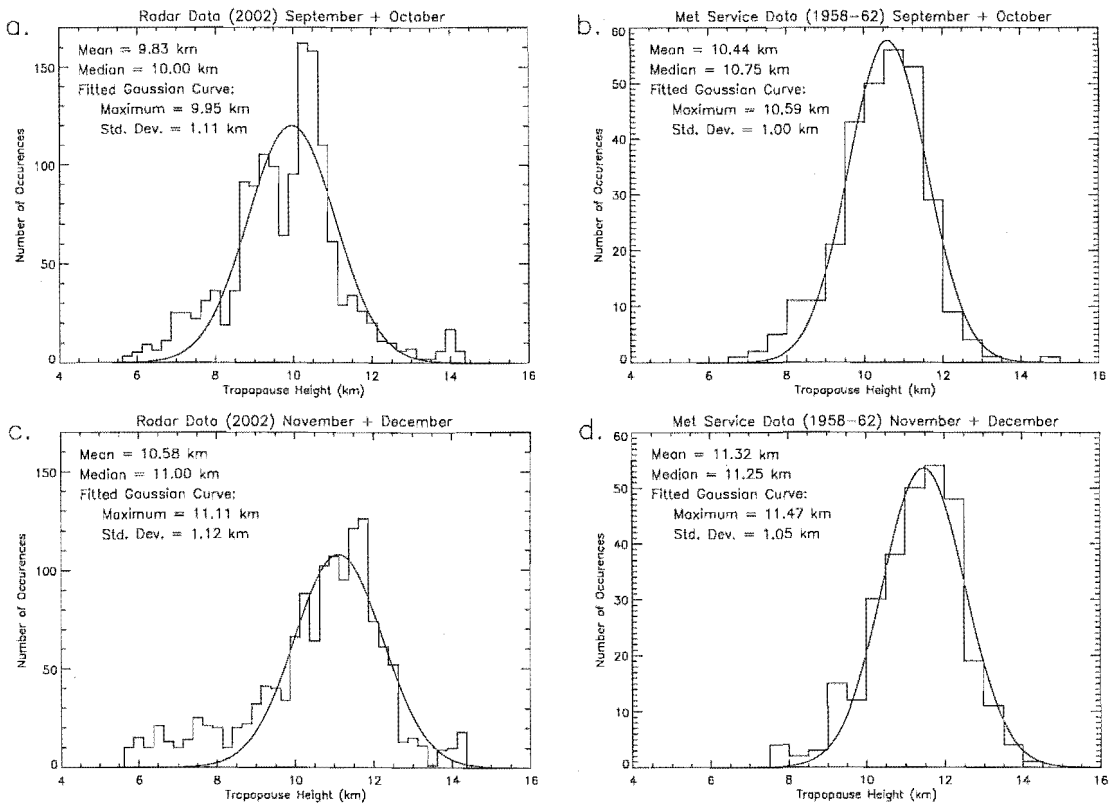

Figure 5.27: Histograms showing the distribution of tropopause heights for different months of the year. **(a)** and **(c)** show radar data while **(b)** and **(d)** contain radiosonde data. Included on each graph are the mean and median of the sample populations and also the maximum point and standard deviation of a Gaussian curve fitted to the data.

data contains four years worth of points, the sample size is small because the radiosonde data only contains one point per day compared to the radar's 24 points per day.

The variation in tropopause height through the year can be seen in Figure 5.27 by noting that the average tropopause height in the Sep/Oct plots is lower than that in the Nov/Dec plots for both the radar and radiosonde data. To quantify this height difference, Δh, the mean for each sample population was calculated, but because of the large number of outlying points, particularly in the radar data, this value did not accurately find the centre of the main peak. For this reason, the median was also calculated, but due to the coarse binning of the NZMS data, the values produced had a large uncertainty of ± 0.25 km. A third technique, which was

used for the comparisons, involved fitting a Gaussian curve to each population and finding its centre. This produced values that were consistent with the median values and their associated uncertainties (± 0.125 km for the radar data and ± 0.25 km for the radiosonde data), and slightly larger than the mean values due to the outlying points which are mainly at lower heights.

For the radar data, the centre of the fitted Gaussian curve is at 9.95 km for Sep/Oct and 11.11 km for Nov/Dec. For the NZMS data, the centre is at 10.59 km for Sep/Oct and 11.47 km for Nov/Dec. These figures correspond to a difference of $\Delta h_{radar} = 1.16$ km for the radar data and $\Delta h_{sonde} = 0.88$ km for the NZMS data. The magnitudes of Δh_{radar} and Δh_{sonde} are similar (approximately 1 km) and the trend in both sets of data is for increased tropopause height in the warmer months.

The tropopause height determined from the radiosonde data is, in both Sep/Oct and Nov/Dec, higher than that determined from the radar data. In Sep/Oct the difference is 0.64 km and in Nov/Dec it is 0.36 km. This discrepancy is due to the fact that the two datasets are from different years and so are unlikely to be the same. The inter-annual variation will be reduced in the NZMS data as it is an average over four years, but the radar data only contains data from one year, so may not be a good measure of the "typical" average tropopause height.

This comparison shows that, on average, tropopause heights calculated from the CUSTAR radar data are similar to those obtained using a radiosonde. The next section attempts to show that individual tropopause heights calculated using the radar agree with those calculated from radiosondes.

5.5.2 Direct Radiosonde Comparison

In order to make direct comparisons between tropopause heights detected by the radar and those found using radiosondes, data was obtained from three different radiosonde sites for the months of October and November, 2002. The three sites available were Whenuapai (36° 47′ S, 174° 37′ E), Paraparaumu (40° 54′ S, 174° 58′ E) and Invercargill (46° 25′ S, 168° 20′ E) which are 790, 370 and 440 km away from Birdlings Flat, respectively. Data from Whenuapai was available from October, 2002, right through to February, 2003.

Radiosondes were launched from each location twice daily, at around 10:00 and 22:00 NZST. The Whenuapai radiosonde took measurements every 10 seconds of the pressure, temperature, relative humidity, wind speed, wind direction and also the

ascent rate and height of the sonde. The Paraparaumu and Invercargill radiosondes took measurements every 2 seconds, but only of the pressure, temperature and relative humidity. To find the tropopause height, both temperature and height are needed, so for Paraparaumu and Invercargill, the *hypsometric equation* was used to calculate the altitude at each point from the pressure and temperature data. This equation is written as

$$z_2 - z_1 = -H \ln\left(\frac{p_2}{p_1}\right), \tag{5.18}$$

where p_1 is the pressure at altitude z_1, p_2 is the pressure at z_2 and H is the mean scale height. H is given by

$$H = \frac{R\langle T\rangle}{g_0}, \tag{5.19}$$

where R is the gas constant, g_0 is the global average of gravity at sea level and $\langle T\rangle$ is the mean temperature of the layer [*Holton*, 1992]. If z_1 is taken to be sea level, then

$$z = -H \ln\left(\frac{p}{p_0}\right), \tag{5.20}$$

where p is the pressure at z and p_0 is the pressure at sea level.

For each radiosonde flight, the tropopause height and sharpness was found using the method described at the beginning of this section. The radar tropopause was then found for the one hour period closest to the radiosonde flights. The flight time of each sonde was taken to be the time that the sonde reached 10 km as this is the approximate mean height of the tropopause. The average of the flight times for Whenuapai, Paraparaumu and Invercargill were then calculated and used when finding the radar tropopause.

Figure 5.28 contains a plot of radar signal to noise ratio together with temperature profiles from the three radiosonde sites for the same time and date. Also shown are the four tropopause heights calculated from this data. This is a particularly good example showing a clear lapse rate of about 7 $\mathrm{K\,km^{-1}}$ in the troposphere and very little temperature change in the stratosphere for all three radiosonde profiles. The change in lapse rate occurs at nearly the same height in all cases and also agrees well with the radar tropopause height.

While not unusual, the good agreement between all four sites shown in Figure 5.28 did not occur in the majority of cases. Figure 5.29 shows a more typical result. Again all three radiosondes show a lapse rate of about 7 $\mathrm{K\,km^{-1}}$ in the lower half of the plot, but while the lapse rates for Paraparaumu and Invercargill decrease

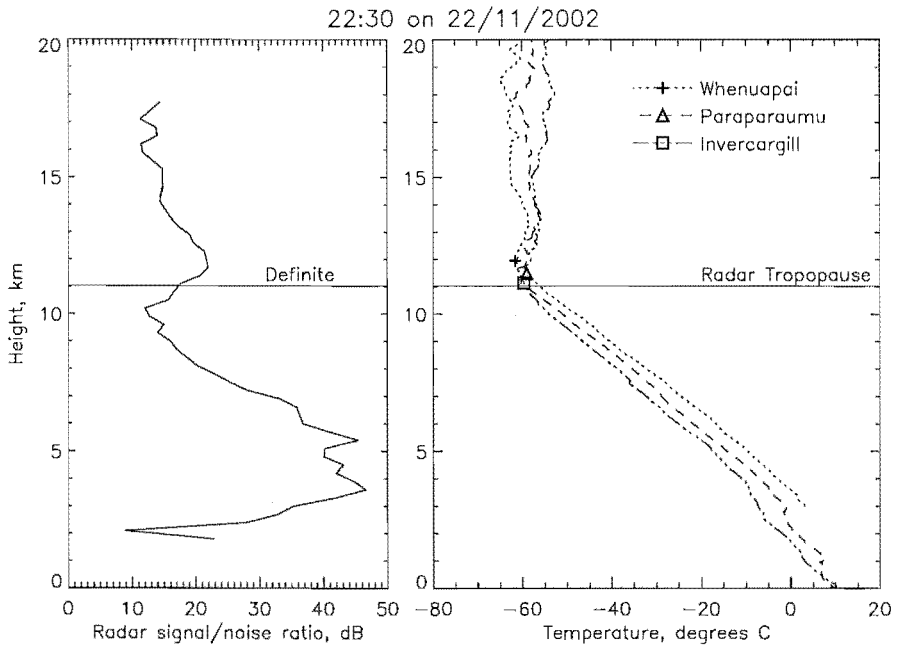

Figure 5.28: Comparison of tropopause heights calculated from radar signal power and from temperature measured by radiosonde. The radar tropopause is shown by the horizontal line and the symbols represent the temperature tropopause found at the different radiosonde sites. Data shown is for 22:30 NZST on November 22, 2002.

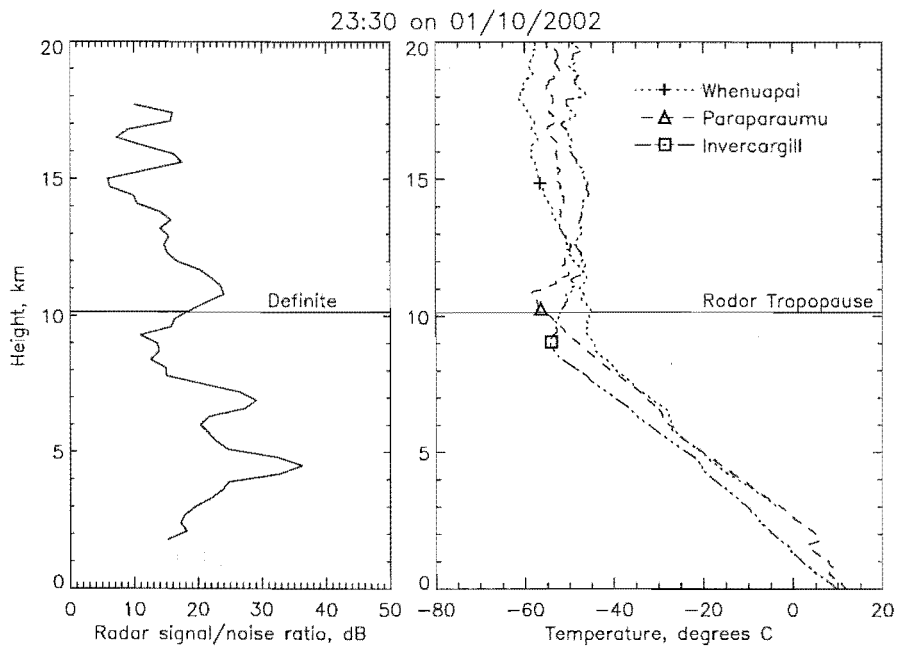

Figure 5.29: Same as Figure 5.28, but for 23:30 NZST on October 1, 2002.

to zero (and in fact become negative for a short time), for Whenuapai the lapse rate only decreases to about 3 $\mathrm{K\,km^{-1}}$. This lapse rate lasts for around 5 km until an altitude of approximately 15 km when it starts to slowly decrease. Although the most distinct change in lapse rate is at 9.5 km, the tropopause is placed, using the WMO definition, at nearly 15 km.

For the Whenuapai radiosonde data, the gradual decrease in lapse rate observed in Figure 5.29 occurred in over a third of the profiles obtained. A similar tropopause structure was observed in very few of the profiles obtained from Paraparaumu and Invercargill. The differing shape of the Whenuapai profile is due to its latitude which places it in the sub-tropics. As explained in Section 2.1.3, there is a break in the tropopause in this region, which often results in multiple or overlapping tropopauses.

Scatter plots are shown in Figure 5.30 comparing the radar tropopause altitudes with the temperature tropopause altitudes found at the three radiosonde sites. These plots contain all tropopause heights calculated, regardless of their sharpness, except if there is a double tropopause, where the tropopause altitude associated with the highest sharpness coefficient is taken. The correlation coefficient for each pair of sites has been calculated and is displayed, along with the number of points used in the correlation, on the relevant plot.

The Invercargill and Paraparaumu sites, which are separated from the radar by approximately 400 km, show much better correlation than the Whenuapai site which is nearly 800 km away from the radar. The low correlation coefficient of $C_{RW} = 0.40$ for the Whenuapai data is due to the large number of points between 14 and 18 km on the y-axis which do not correlate well with the radar tropopause altitudes. These points correspond to the Whenuapai temperature profiles that have a smooth decrease in lapse rate as described earlier (see Figure 5.29).

Although larger than Whenuapai, the correlation coefficients for Paraparaumu and Invercargill ($C_{RP} = 0.55$ and $C_{RI} = 0.53$) are still quite low. This is mainly due to the large spatial separation of the different sites. To gain an understanding of the effect of spatial separation, the tropopause altitudes determined from the three radiosondes have been compared with each other (Figure 5.31).

These comparisons reinforce the incompatability of the Whenuapai tropopause altitudes with those from the other two sites. There is almost no correlation between Whenuapai and Invercargill ($C_{WI} = 0.05$), which should not be surprising as they are separated by 1180 km. However, if distance was the only factor involved, When-

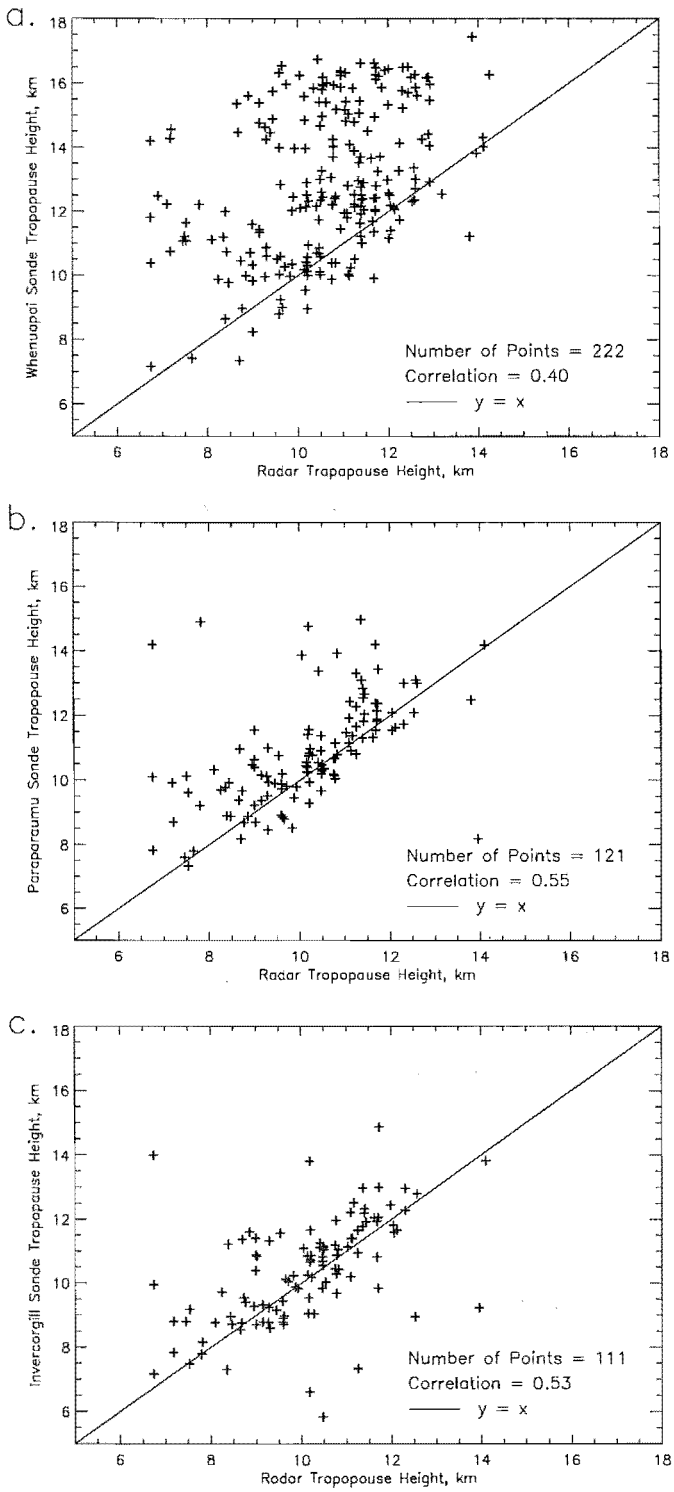

Figure 5.30: Scatter plots of radar tropopause height vs. radiosonde tropopause height for **(a)** Whenuapai, **(b)** Paraparaumu and **(c)** Invercargill. The plots contain all types of tropopause except for secondary tropopauses.

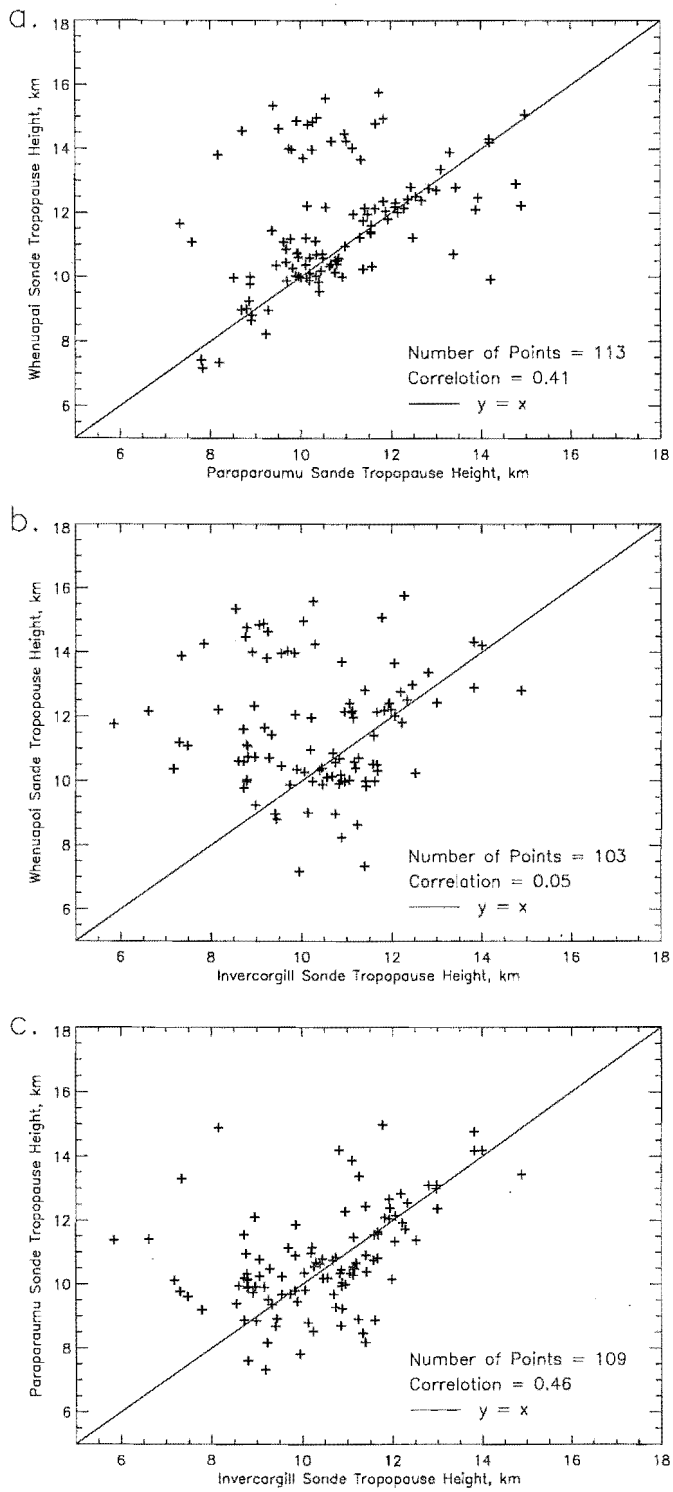

Figure 5.31: Scatter plots of radiosonde tropopause height for **(a)** Whenuapai and Paraparaumu, **(b)** Whenuapai and Invercargill, and **(c)** Paraparaumu and Invercargill.

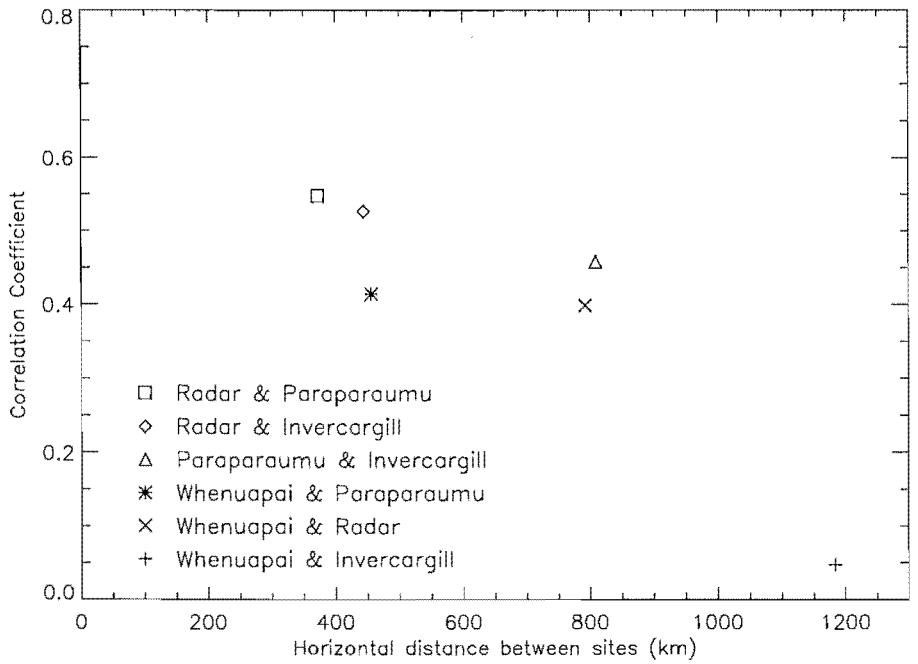

Figure 5.32: Correlation coefficients from Figures 5.30 and 5.31 plotted against site separation.

uapai and Paraparaumu (460 km separation) should have a higher correlation than Paraparaumu and Invercargill (810 km separation). In actual fact their correlation coefficients are $C_{WP} = 0.41$ and $C_{PI} = 0.46$, respectively. Figure 5.31a contains two distinct groups, one with good correlation that follows the $y = x$ line well and one in which the Whenuapai tropopause heights are higher than those from Paraparaumu. It is this second group which decreases the correlation coefficient and if it were removed this plot would have a higher correlation coefficient than Figure 5.31c.

From the results shown so far, it is clear that the Invercargill and Paraparaumu radiosondes are much more suitable than the radiosonde at Whenuapai for comparisons with the CUSTAR radar. Comparisons using these sites are now studied in more detail. The radar is closer to both Paraparaumu and Invercargill than these sites are too each other. This means that C_{RP} (the correlation between the radar and Paraparaumu) and C_{RI} (the correlation between the radar and Invercargill) should be greater than C_{PI} (the correlation between Paraparaumu and Invercargill). This is indeed the case, and if the correlation coefficients are plotted against distance between sites a downward sloping trend is observed (Figure 5.32).

The fact that C_{RP} and C_{RI} are both larger than C_{PI} suggests that the radar measures the height of the tropopause with an accuracy similar to that of the radiosondes. *Hooper and Arvelius* [2000] compared the height of the temperature tropopause with height of the tropopause measured by the ESRAD MST radar in a similar manner to that described above. With a radiosonde launch site nearby to the radar, they produced correlation coefficients of 0.41 and 0.63 for sample sizes of 45 and 68, respectively. Due to the large site separation of the CUSTAR data, a lower correlation would be expected. In actual fact, C_{RP} and C_{RI} both fall between the ESRAD values. The low correlations found by *Hooper and Arvelius* [2000] may be due to the location of the ESRAD radar which is in the Swedish Arctic at 68° N. This location is at the edge of the polar tropopause where the tropopause often has a two-step structure and therefore may produce results similar to those shown here from the Whenuapai radiosonde. *Gage and Green* [1979], when using the Sunset radar near Boulder, Colorado, obtained a correlation coefficient of 0.84 when comparing tropopause heights with those measured by radiosonde in Denver, less than 50 km away.

Kitchen [1989] performed comparisons between radiosonde measurements taken using 13 radiosonde stations spread throughout the United Kingdom. The root mean squared (RMS) differences between spatially and temporally separated sonde measurements of vector wind, temperature, geopotential and humidity were calculated. It was found that at an altitude of 250 hPa (the approximate height of the tropopause) the RMS temperature difference was around 3 K for a spatial separation of 400 km and around 4 K for a separation of 800 km. Although these temperature differences cannot be directly related to tropopause altitude differences, useful comparisons can be made with the results from this study.

Table 5.1 contains the mean and standard deviation of the tropopause height differences between each pair of data sets. It also contains the RMS differences which were calculated using the relation

$$\mathrm{RMS}_{xy} = \sqrt{\frac{\sum_{i=1}^{N}(x_i - y_i)^2}{N}}. \tag{5.21}$$

where x_i and y_i are the individual tropopause heights at the two locations under consideration. Again, the comparisons which contain Whenuapai have larger standard deviations and RMS differences than those without. The RMS differences between the radar and Paraparaumu and the radar and Invercargill are both lower

Sites	Mean (km)	St. Dev. (km)	RMS Diff. (km)	Corr.	Separation (km)
When. – Radar	2.31	2.20	3.18	0.40	790
Para. – Radar	0.68	1.50	1.64	0.55	370
Inver. – Radar	0.31	1.52	1.54	0.53	440
When. – Inver.	1.26	2.44	2.74	0.05	1180
When. – Para.	0.83	1.95	2.11	0.41	460
Para. – Inver.	0.36	1.69	1.72	0.46	810

Table 5.1: Statistics produced from comparisons between tropopause height measured by radar and radiosonde. The first column shows which data set was subtracted from which to produce the mean difference. The standard deviation of the values used to produce the mean is shown in the third column. The RMS difference between the two data sets is in the fourth column and the correlation coefficients calculated previously are included for reference along with the site separation.

than the RMS difference between Paraparaumu and Invercargill. However, the ratio of differences seen at 400 km to those seen at 800 km (approximately 0.9) is not the same as the ratio of temperature differences at similar separations observed by *Kitchen* [1989] (approximately 0.75). This is because the tropopause has a relatively constant lapse rate, which means that if the temperature changes by a certain amount at one height, it is likely to change by a similar amount at other heights, so the overall shape of the temperature profile will not be greatly affected. As the tropopause height is calculated from the gradient in the temperature profile not the absolute temperature measurement, the height of the tropopause will therefore not change as much as the absolute temperature measurements.

The mean height of the tropopause is expected to change with latitude and have a general downward sloping trend between the tropics and the polar region (see Figure 2.5). From Table 5.1 the mean difference in the tropopuase height between Paraparaumu and Invercargill is 360 metres, which agrees with this trend. The mean height of the tropopause in Christchurch should be approximately half way between that of Invercargill and Paraparaumu. The mean radar tropopause height in Christchurch was actually lower than the Paraparaumu and Invercargill mean heights. The difference is such that, if the temperature tropopause is assumed to be

half way between that in Paraparaumu and Invercargill, the radar underestimates the tropopause height by $\simeq$ 500 metres. This is contrary to the result obtained by *Rastogi and Röttger* [1982] who found that the radar-determined tropopause is higher than the radiosonde tropopause by 0.1-1 km.

It should be noted that, in this study, the radar tropopause height has been calculated using data with an effective height resolution of 600 m (due to a pulse length of 4 μs). This relatively coarse resolution (the height resolution of radiosonde data is typically less than 50 m) may produce discrepancies between the temperature and radar determined tropopause, such as that described above.

Another common method of determining the tropopause height with a VHF radar is to use the point at which the signal to noise ratio reaches a maximum above the dip normally observed in the upper troposphere [*Vaughan et al.*, 1995]. This was found for the CUSTAR data in two different ways. The first method took the tropopause height deduced using the steepest gradient method outlined previously and then found the first maximum in signal to noise ratio that occured above this point. The second method took the steepest gradient tropopause height and then found the global maximum above this point.

Figure 5.33 contains a radar signal to noise profile with the three different tropopause heights displayed. Also included is the radiosonde data for the same time period. In this particular case the three radar tropopause heights are all separate, with the "maximum gradient" tropopause matching well with the Paraparaumu temperature tropopause and the "first maximum" tropopause matching well with the Invercargill temperature tropopause. The "global maximum" tropopause is higher than all the other tropopause heights.

All three methods of determining the tropopause height were performed on the available data and in approximately half the radar power profiles, the "first maximum" tropopause was at the same height as the "global maximum" tropopause. Correlations were performed similar to those shown in Figure 5.30, and the correlation coefficients obtained were very similar to those obtained using the "maximum gradient" method. The mean difference between the tropopause heights for the radar, Paraparaumu and Invercargill were calculated for the three different methods. Table 5.2 contains these figures, the second column being a repeat of the figures in Table 5.1.

If the temperature tropopause above Birdlings Flat is again assumed to be half

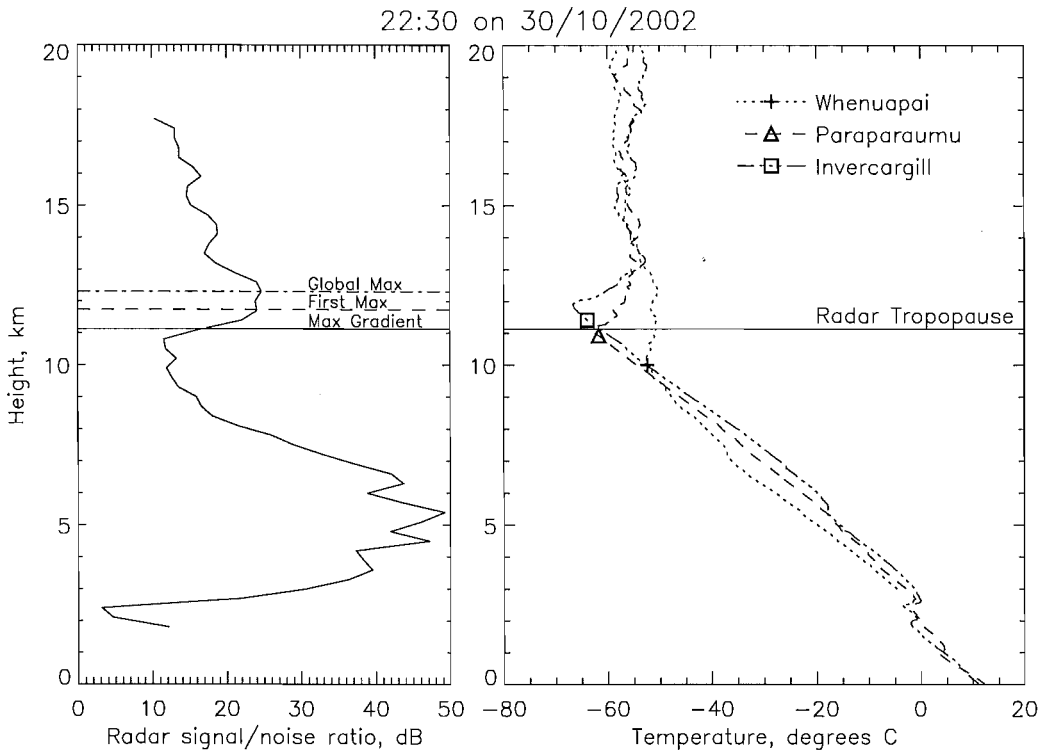

Figure 5.33: A profile of radar signal to noise ratio showing three different methods of calculating the radar tropopause. Corresponding radiosonde temperature measurements are also included.

way between that in Paraparaumu and Invercargill, the radar tropopause determined by the "first maximum" method is only $\simeq$ 20 metres too low. However, the "global maximum" method overestimates the tropopause height by $\simeq$ 500 metres. It would seem from these results that the "first maximum" method is the most accurate way of determining the radar tropopause height. However, there could be other factors affecting the height of the tropopause, such as the location of the radar in the lee of the Southern Alps, and this comparison needs to be repeated using data from a radiosonde located near to the radar before any firm conclusions can be made.

Other individual events show that there is often a good correlation between the radar and one or more of the radiosonde sites. For the evening of October 20, 2002, the radar data shows a double tropopause which is also clearly observed in the data from Paraparaumu (see Figure 5.34). There are two distinct enhancements in radar signal power at altitudes of 10 and 15 km. In the Paraparaumu temperature profile there are two corresponding regions where the lapse rate decreases from the

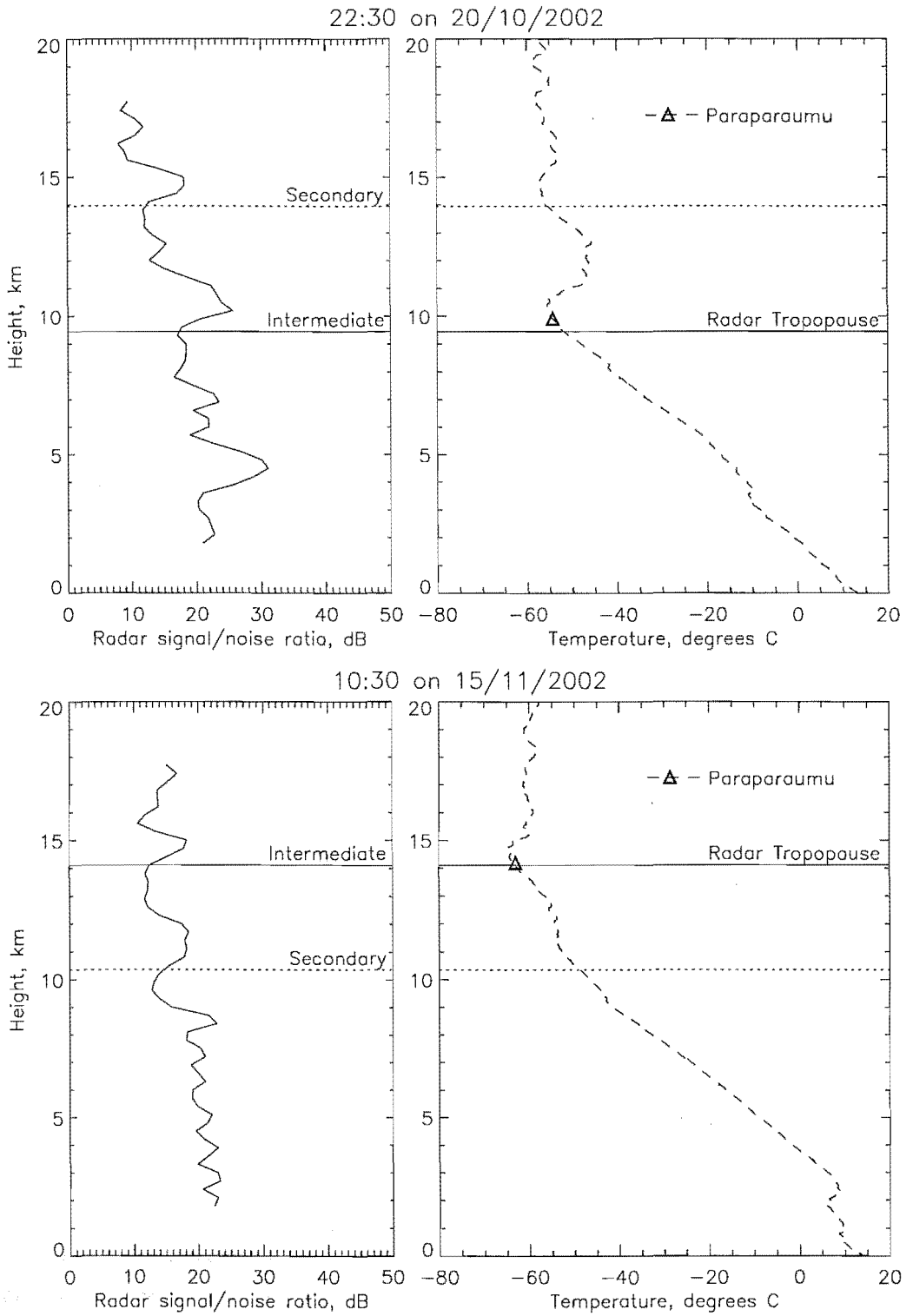

Figure 5.34: Two examples of a double tropopause observed in both the radar data and the Paraparaumu radiosonde data.

Sites	Mean (km)		
	Max. Gradient	First Max.	Global Max.
Paraparaumu – Radar	0.68	0.20	−0.33
Invercargill – Radar	0.31	−0.17	−0.67
Paraparaumu – Invercargill	0.36	0.36	0.36

Table 5.2: The mean difference between the tropopause height measured with radiosondes and the CUSTAR radar for three different methods of determining the radar tropopause. The first method is the maximum gradient method and the figures shown are a repeat of those from Table 5.1. The second and third methods determine the tropopause height where the signal to noise ratio is at a maximum.

tropospheric value of $\simeq 7\ \mathrm{K\,km^{-1}}$ to values below zero. A similar double tropopause is also observed on the morning of November 15, 2002, where there are again two distinct enhancements in radar signal power. However, in the temperature profile the lower tropopause is not so well defined. A decrease in lapse rate to nearly zero can be observed at about 11 km (corresponding to the secondary radar tropopause), but it only lasts for 1 km. Using the WMO definition, the tropopause is placed at an altitude of 14 km, which corresponds to the upper radar tropopause.

5.5.3 Calculating M^2 from Radiosonde Data

As explained in Section 2.3.2, power received by the radar from Fresnel scattering processes is proportional to M^2/r^2, where M is the gradient of potential refractive index (see Equation 2.11) and r is range. M is dependent on pressure, temperature and humidity, all of which are commonly measured by radiosondes. M^2 profiles calculated from radiosonde data have been used by *Hocking and Mu* [1997] to ascertain the difference between conditions above their VHF radar and the region measured by a nearby radiosonde. M^2 can also be calculated directly from the radar returned signal to derive temperature profiles [*Gage and Green*, 1982] and humidity profiles [*Gossard et al.*, 1998] without the need for radiosondes.

For this work, comparison of M^2 profiles calculated at each radiosonde site, provides a quantitative method of determining the effect of geographical separation on the expected radar signal power. Profiles of M^2 were calculated for each radiosonde ascent and low pass filtering, using a cut-off period of 4 km, was performed to re-

move the effects of small scale fluctuations. Two sections of each profile, one from 4 to 8 km in altitude and the other from 12 to 16 km, were extracted in order to examine the differences between the troposphere and stratosphere. The upper limit of 8 km and the lower limit of 12 km were chosen so that, for the majority of cases, the tropopause was between the two regions (see Figure 5.26a). The correlation coefficient and gradient between the M^2 profiles for each pair of radiosonde sites was found for the two altitude ranges. If both of these variables are equal to unity for a particular pair of profiles, it means they have identical shapes.

This technique was performed on all the available radiosonde data and it was found that the M^2 profile above the tropopause was likely to be more consistent between radiosonde sites than the profile below the tropopause. Figure 5.35 shows a typical comparison between M^2 profiles for the three radiosondes. The correlation coefficients and gradients for comparisons between the upper sections are clearly closer to 1.0 than those for the lower sections. This is due to the fact that in the troposphere M^2 is more dependent on humidity, which has large variations over small spatial scales.

The figures in Table 5.3 also show the same difference above and below the tropopause. The table contains the means and standard deviations of all the correlation coefficients and gradients calculated. The correlation coefficients and gradients are consistently closer to 1.0 for the stratospheric region than they are for the tropospheric region. Also, the standard deviations are always larger for the 4 to 8 km region suggesting that there is more variation between radiosondes below the tropopause.

The relatively good mean correlation coefficients and gradients found between Whenuapai and Paraparaumu compared to the corresponding values between Paraparaumu and Invercargill were unexpected, given the different shape of the Whenuapai temperature profile with respect to the other two sites. The results in Table 5.3 show, in fact, that despite the differing tropopause structure observed above Whenuapai, the profile of the refractive index gradient (above Whenuapai) is quite similar to that above Paraparaumu. The relatively good values found between Whenuapai and Paraparaumu could be due to the site separation, as Whenuapai is only 460 km from Paraparaumu, whereas Paraparaumu is 810 km from Invercargill.

The M^2 profiles can be used to decide whether radiosonde data and radar data, taken at similar times but at different locations, correspond to similar atmospheric

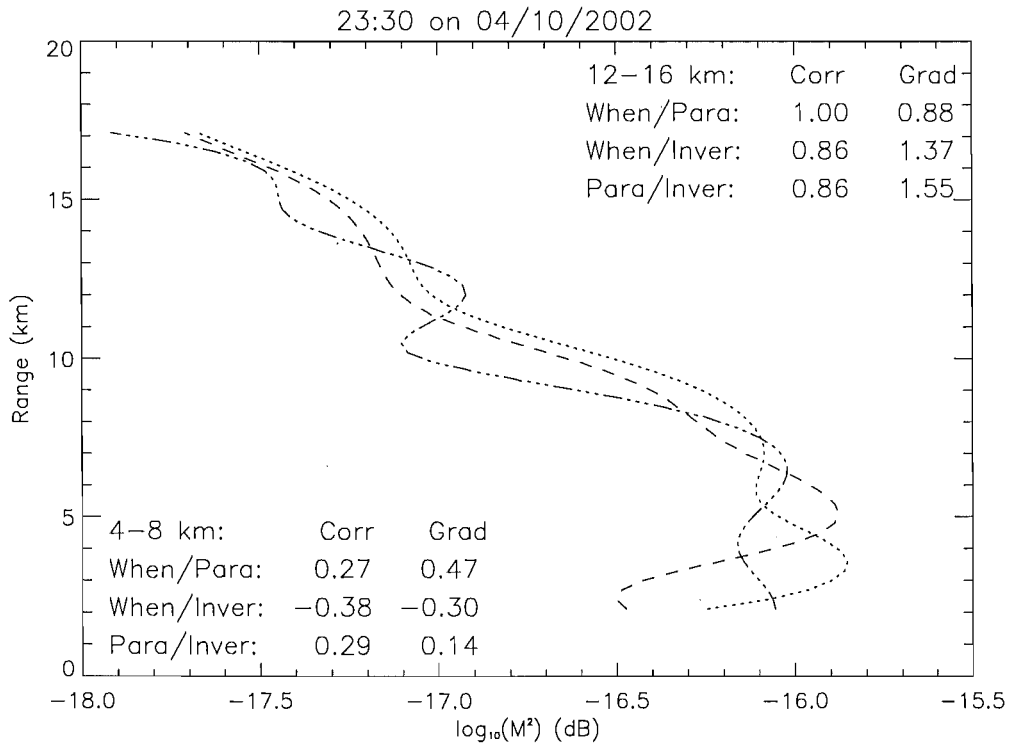

Figure 5.35: A comparison of M^2 profiles from the Whenuapai (dotted line), Paraparaumu (dashed line) and Invercargill (dashed-dotted line) radiosonde sites. The correlation coefficients and gradients from comparisons between two different sections of each profile are included.

conditions. Although the conditions in the troposphere are likely to be different due to humidity etc., if the stratospheric conditions are similar, other atmospheric parameters such as the temperature profile (and therefore the tropopause height) may be the same. This was checked by comparing the M^2 radiosonde profiles with received power profiles from the radar, corrected for range (power $\times$ range^2). This was initially performed for altitudes between 12 and 16 km and, as done previously with the radiosondes, both the correlation coefficient and the gradient between the profiles were found. For those with good correlation and a gradient close to 1.0, the radar and radiosonde tropopause heights were compared. The definition of a "good" correlation was when the correlation coefficient was higher than 0.6 and the gradient between 0.6 and 1.6.

For the radar and Whenuapai, the number of "good" correlations was 72 (32%) and the correlation between tropopause heights was 0.43. As with other comparisons

Sites		Correlation Coefficient		Gradient	
	Altitude Range	Mean	St. Dev.	Mean	St. Dev.
Whenuapai & Paraparaumu:					
	12 to 16 km	0.79	0.38	0.89	0.68
	4 to 8 km	0.33	0.65	0.34	1.23
Whenuapai & Invercargill:					
	12 to 16 km	0.67	0.44	0.70	0.79
	4 to 8 km	0.15	0.63	0.13	1.63
Paraparaumu & Invercargill:					
	12 to 16 km	0.64	0.45	0.71	0.69
	4 to 8 km	0.15	0.63	0.20	1.41
Totals:	12 to 16 km	0.70	0.42	0.77	0.72
	4 to 8 km	0.21	0.64	0.22	1.42

Table 5.3: Statistics produced from comparisons between M^2 calculated at the three different radiosonde sites. Correlation coefficients and gradients have been calculated between the M^2 profiles of different radiosondes flown at the same time. For each comparison, these calculations were separated into two sections, one below and one above the tropopause. For each height range and pair of radiosondes, the mean and standard deviation of all the correlation coefficients and gradients were found and these are displayed here. Also shown is the mean of the above figures for the three sites.

between these two sites, the correlation is very low and is indicative of the differing tropopause structures involved. For the radar and Paraparaumu, there were 27 "good" correlations (22%), and for Invercargill, there were 34 (31%). Both of these groups produced a tropopause correlation coefficient of 0.76 which is significantly better than those found for the complete data set (see Table 5.1).

The percentage of "good" correlations is similar for all three sites, even though the resulting correlation between tropopause heights for Whenuapai and the radar is still very low. This means that this procedure cannot be relied on with confidence to show when two different locations will have similar tropopause heights and it is only prior knowledge of the differing tropopause structure above Whenuapai that allows any conclusion to be drawn.

When performing the same procedure for altitudes between 4 and 8 km, the number of points satisfying the "good" correlation criteria is much smaller. For comparisons between the radar and Whenuapai, Paraparaumu and Invercargill, the numbers were 8, 4 and 5, respectively. These produced correlation coefficients between tropopause heights of 0.86, 0.92 and −0.49, but nothing of significance can be drawn from these results due to the small number of points.

The results from this section show that the similarity between tropopause heights deduced at different locations is dependent on the atmospheric conditions. When the atmosphere above the radar site is similar to that above a spatially separated radiosonde site, then the tropopause height calculated using the different instruments is more likely to be comparable.

5.6 Frontal Activity and Gravity Waves

5.6.1 Radar Measurements of Frontal Activity

The passage of cold and warm fronts can be observed clearly in VHF radar data due to the increase in static stability in the frontal region and the distortion or breaking of the tropopause that often occurs (see Section 2.1.4). The increase in reflectivity associated with enhanced static stability has been used by *Röttger* [1979], *Larsen and Röttger* [1983, 1985], *Ruster et al.* [1998] and many others to investigate frontal activity. UHF and VHF radars were used by *Browning et al.* [1998] to study upper- and lower-level jets and other aspects of the circulation near a cold front.

There have been a number of frontal passages observed with the CUSTAR radar in its first few months of operation. Figure 5.36 shows one clear example which occurred between the 9th and 11th of September, 2002. Information about the frontal surface and tropopause height during this time can be obtained by investigating variations in the radar signal to noise ratio. From 18:00 NZST on September 9 until 09:00 NZST on September 10, the tropopause altitude increases slowly and reaches just over 12 km. Underneath this level, between 4 and 8 km there is a large increase in backscattered power from 05:00 to 09:00 NZST, which is possibly associated with the frontal surface. At 09:00 NZST, the tropopause can no longer be observed at 12 km and emerges from the previously mentioned enhancement in signal power at about 8 km. The altitude of the tropopause increases slightly and then stays at about 9 km for the remainder of the time period. However, from 06:00 NZST on

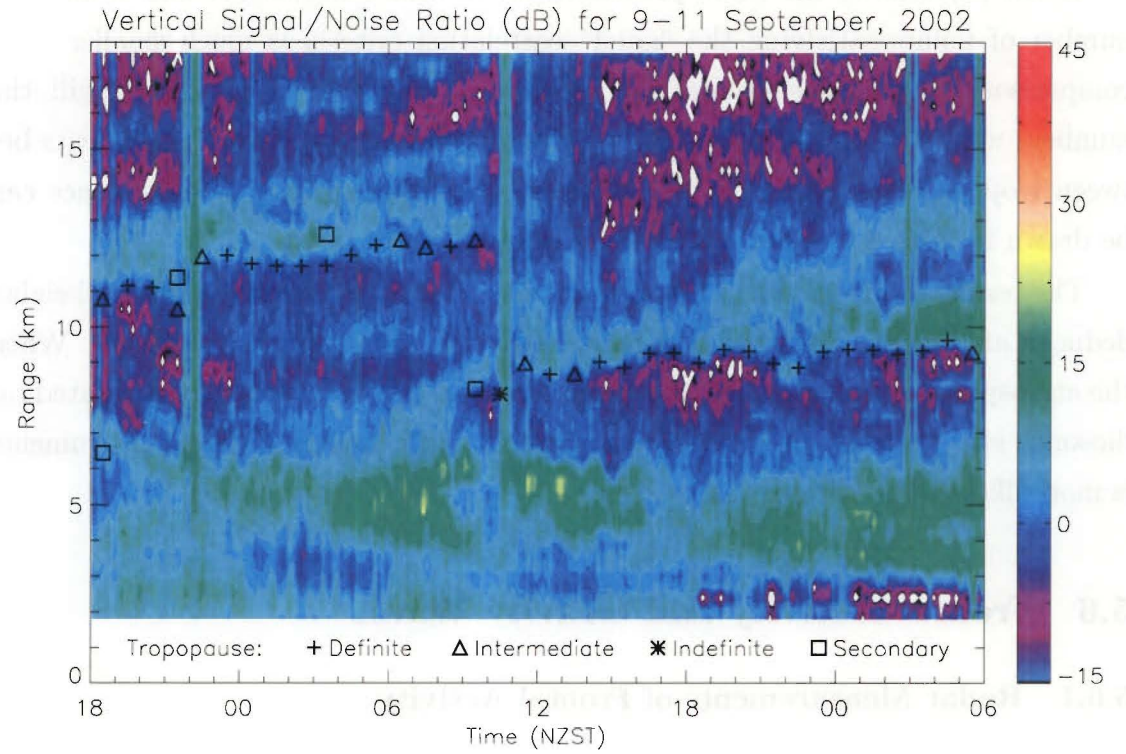

Figure 5.36: Contours of radar signal to noise ratio from 18:00 NZST on September 9 to 06:00 NZST on September 11, 2002.

the 10th until 06:00 NZST on the 11th, the increased signal power which is initially observed at 7 km, moves upward at a constant rate to 13 km. This increase in signal power may be associated with an upper level frontal surface.

Figure 5.36 shows the atmospheric conditions over a stationary location as a function of time. If it is assumed that the atmosphere does not evolve as it moves, this picture is equivalent to a spatial slice of the atmosphere, parallel to its direction of motion, at a single point in time. If Figure 5.36 is viewed in this way, the direction of motion is from the right side of the diagram to the left. The assumption that the atmosphere does not evolve is obviously not strictly true and Figure 5.37, which is discussed below, shows how the front gradually weakens from about 12:00 NZST on September 10 onwards.

Figure 2.9 shows the typical structure of a cold front which, in this diagram, is moving from left to right. The main features of this figure correspond closely to the CUSTAR echo intensity measurements from the 10th of September (see Figure 5.36),

although the pattern is reversed due to the orientation of the diagrams. On the lee (or cold) side of the front in Figure 2.9, the tropopause is at an altitude of 7 km. It decreases to 5 km when the tropopause fold is most developed and then abruptly increases to 10 km. These heights are all slightly lower than those for Figure 5.36, but the pattern is very similar.

Figure 5.37 contains mean sea level analysis plots, obtained from the Australian Bureau of Meteorology (BoM), which describe the synoptic situation during the above time period. The first plot, for 18:00 NZST on September 9, shows a deep low pressure system, accompanied by a cold front, situated to the south-west of the South Island (SI). The low pressure system initially produces strong north-westerly winds over the SI, which gradually become south-westerly as the low moves eastward during the 48 hour period. The front also moves to the east and the first four plots show it passing over the SI. By 12:00 NZST it has reached the radar site and the remaining plots show the weakening front continue to move to the north-east.

Figure 5.38 contains MSL analysis plots over the same time period produced by the New Zealand MetService (NZMS). These plots more accurately reflect the effect of the Southern Alps than those from the Bureau of Meteorology. In particular the kink in the isobaric surfaces above the South Island is much more pronounced and is an indication of the large effect orography has on synoptic scale disturbances. In most respects the plots are similar, although the frontal surface appears above Christchurch at 06:00 NZST in the NZMS data which is 6 hours earlier than in the BoM data.

The synoptic situation appears to correlate well with the radar data which shows the break in the tropopause between 06:00 and 12:00 NZST on September 10. However, if the frontal surface of Figure 5.36 is extrapolated to ground level, it would pass the site at approximately 00:00 NZST on September 10. This appears to contradict the time of the frontal passage obtained from the MSL analysis plots.

From the analysis plots, the speed of the front relative to the radar site was estimated to be approximately 10 $\mathrm{m\,s^{-1}}$. This speed can be used to calculate the slope of the upper level frontal surface which stretches from 7 to 13 km in Figure 5.36. It takes 24 hours (from 06:00 NZST on the 10th to 06:00 NZST on the 11th) for this increase in altitude to occur and this corresponds to a distance of 900 km and a slope of 0.4°. This is a fairly typical value for the slope of an upper level cold front. A previous investigation by *Caccia and Cammas* [1998] used VHF radar

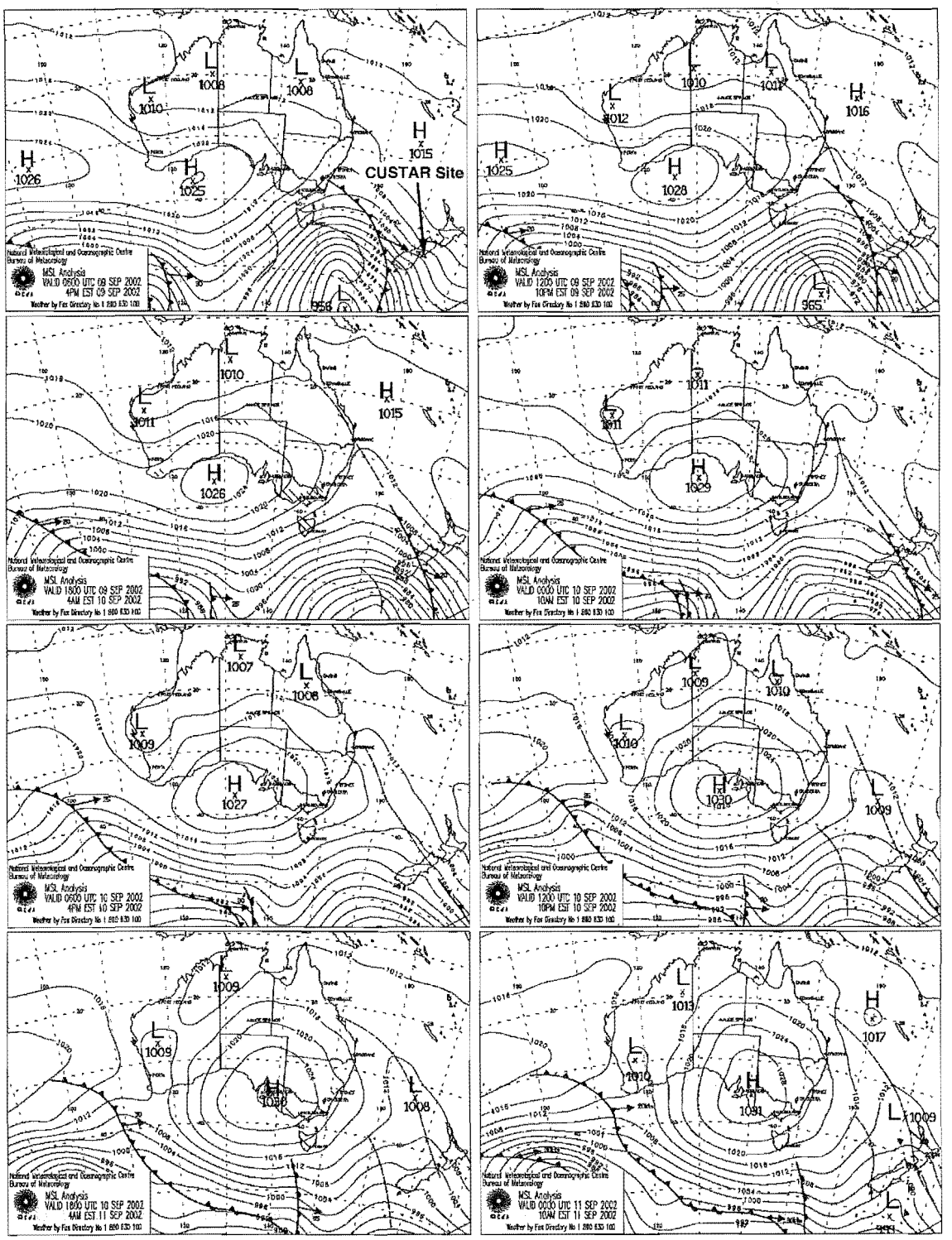

Figure 5.37: Mean sea level (MSL) 6 hourly analysis plots from 18:00 NZST on September 9 to 00:00 NZST on September 11. Obtained from the Bureau of Meteorology (http://www.bom.gov.au/.

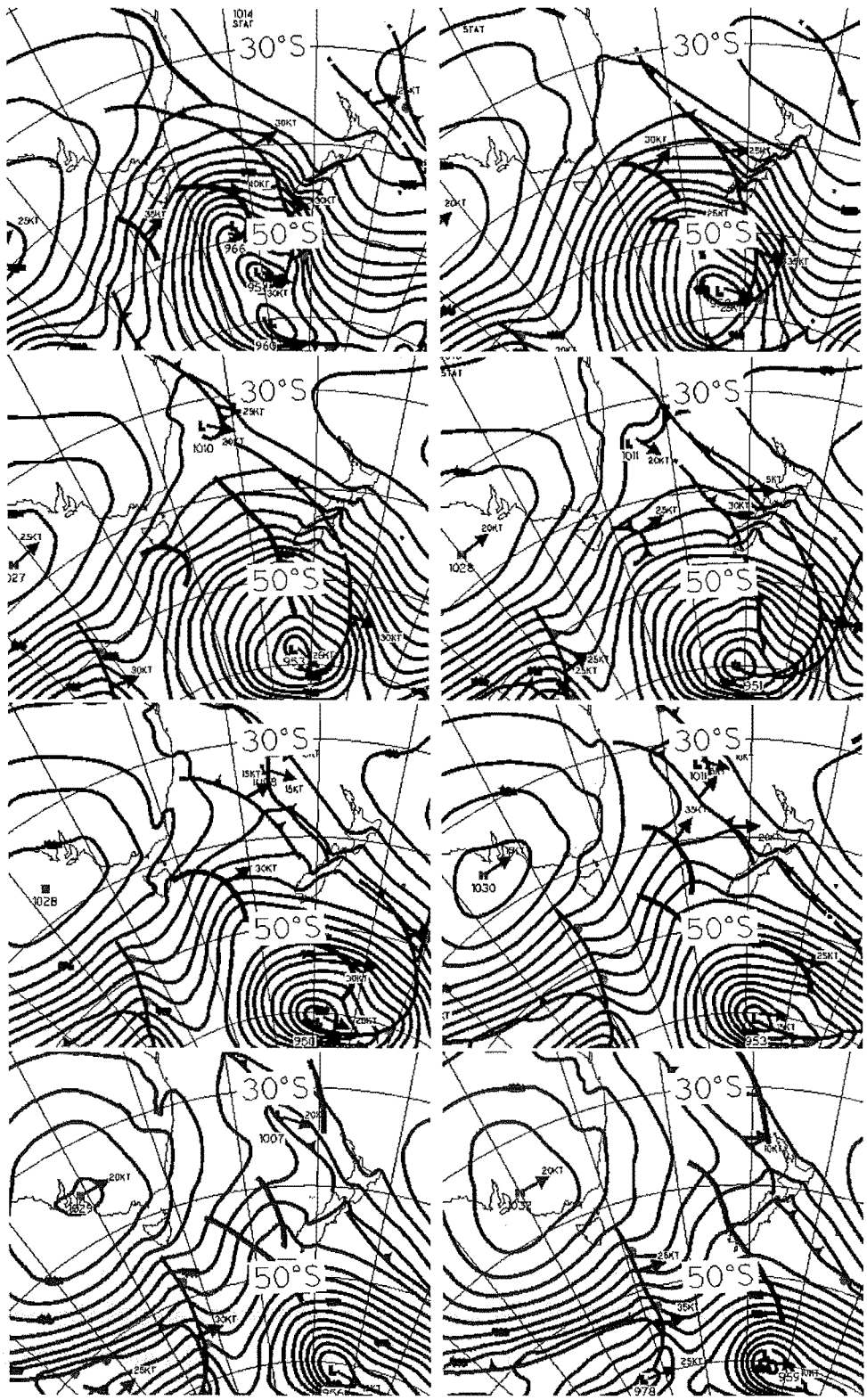

Figure 5.38: MSL 6 hourly analysis plots for the same time period as Figure 5.37. Obtained from the New Zealand MetService (http://www.metservice.co.nz/).

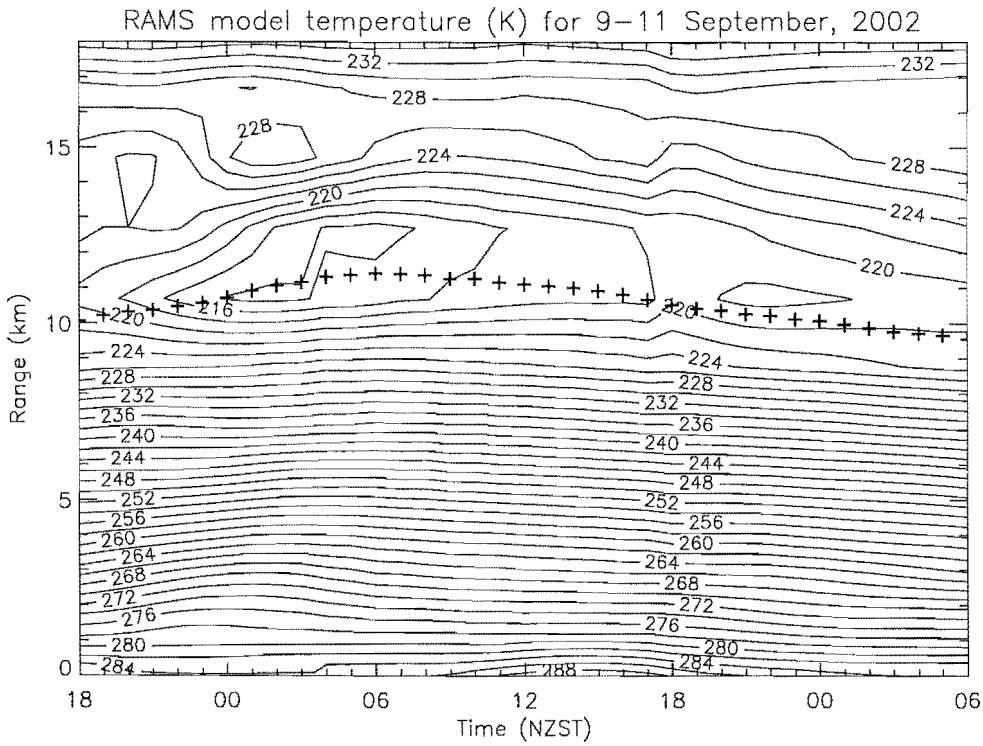

Figure 5.39: RAMS model temperature data (20 km × 20 km × 1000 m) over Christchurch for the 9th to the 11th of September, 2002. Included are tropopause heights calculated each hour using the WMO definition. Model data courtesy of *R. Turner*, NIWA.

and radiosonde measurements to examine a cold front over Western Europe and calculated a slope of 0.3°.

Figure 5.39 contains model temperature data over Christchurch for the same time period as Figure 5.36 obtained using the Regional Atmospheric Modelling System (RAMS). RAMS is a highly versatile numerical code developed for simulating and forecasting meteorological phenomena. It has been designed for mesoscale grids, but can also perform global scale or microscale simulations. The data shown in Figure 5.39 was obtained from *R. Turner* [private communication] of the National Institute of Water and Atmospheric Research (NIWA), who used a model with 20 km horizontal resolution and 1000 m vertical resolution above 3000 m.

The height of the tropopause calculated hourly from the RAMS temperature data is depicted in Figure 5.39 by '+' symbols. The tropopause starts at 10 km and increases to a maximum of 11.5 km at 06:00 NZST on the 10th of September,

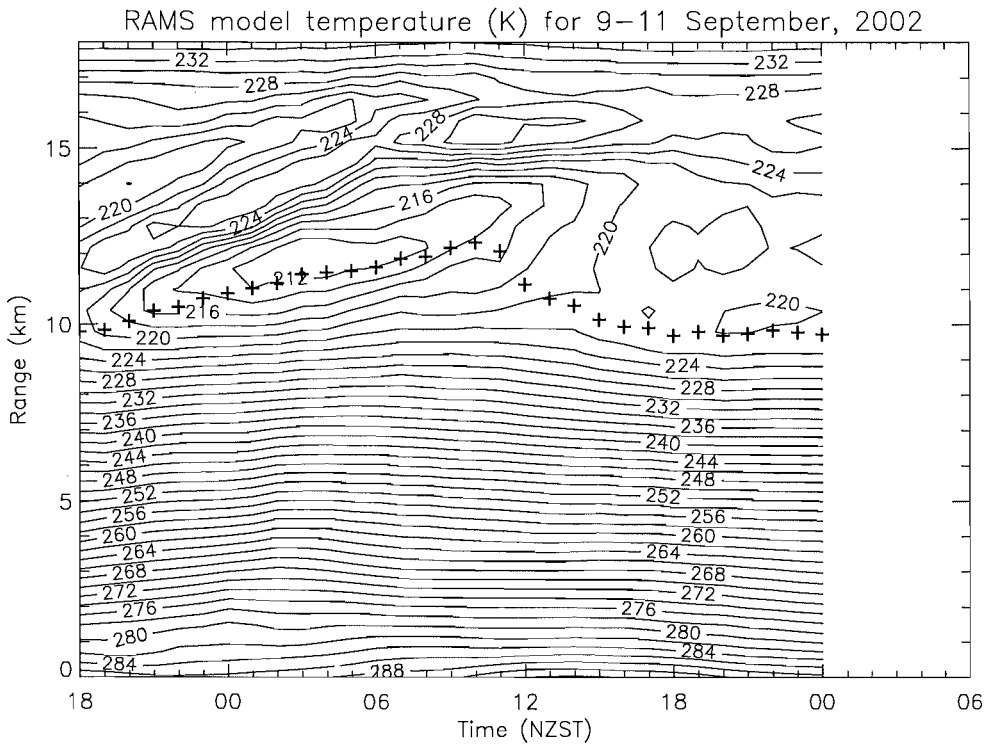

Figure 5.40: RAMS model temperature data (5 km × 5 km × 600 m) over Christchurch for the 9th to the 11th of September, 2002. Included are tropopause heights calculated each hour using the WMO definition. Model data courtesy of *R. Turner*, NIWA.

before decreasing to an altitude of 9.5 km by 06:00 NZST on the 11th. These three points agree well with the tropopause height detected by the radar, but the model data fails to replicate the abrupt change observed at 09:00 NZST on September 10. The model resolution is not high enough to resolve the frontal surface, so the discontinuity, which is a result of this surface crossing the radar site, is not observed in the RAMS data.

The above simulation was also performed with a horizontal resolution of 5 km and a vertical resolution of less than 600 m, producing the results shown in Figure 5.40. At this resolution, the model shows greater agreement with the results obtained from the radar. The point at which the tropopause reaches its maximum altitude before abruptly decreasing, occurs at 10:00 NZST on the September 10. This corresponds exactly to when the discontinuity is observed in Figure 5.36, although the step is again not as sharp as that observed by the radar. This difference may be due to

the limited temporal and spatial resolution of the model, but it may also arise from differences between the radar tropopause and the temperature tropopause. The radar tropopause is effectively the point where the gradient in the static stability is at its largest. A frontal surface has a large static stability and during a frontal passage it may not coincide with the temperature tropopause. In this situation, an ST radar can not distinguish between two surfaces and the algorithm utilised will usually place the tropopause at the height of the lower surface. In this particular case, however, the upper surface seems to disappear completely at 10:00 NZST (see Figure 5.36) suggesting that the tropopause drops abruptly at this point.

Comparisons between the CUSTAR radar data and the two mesoscale simulations presented here show that the results obtained by the radar could be used as an aid in weather forecasting and also to verify the performance of nowcasting models. Although it is currently not configured to do so, the radar is capable of calculating the tropopause height and the vertical wind velocity in real time. This means that results from the radar could be used for current weather predictions. The radar will be even more valuable for these purposes when its capabilities are extended to include measurement of the horizontal wind velocity.

5.6.2 Radar Measurements of Gravity Waves

The high resolution temporal and height measurements achievable by radar lend themselves to studies of smaller-scale time-varying phenomena such as gravity waves.

As mentioned in Section 2.1.5 gravity waves can be formed from a number of sources. These include fronts, thunderstorms, jet streams and convection, which have all been investigated with VHF radar [e.g. *Lu et al.*, 1984; *Nastrom et al.*, 1990; *Fritts and Nastrom*, 1992; *Muschinski*, 1997; *Ralph et al.*, 1999; *Kusunoki and Eito*, 2003]. Orography is a well known source of gravity waves and the focus of this section is a case study of wave activity, in which topography is the suggested source. *Röttger* [2000] gives a good review of mountain wave research performed with ST radars.

Mountain waves have been studied in depth using VHF radars [e.g. *Ecklund et al.*, 1982; *Ralph et al.*, 1992; *Pritchard et al.*, 1995] and have been found to be very dependent on the direction and strength of the background wind. Waves produced in the lee of orography are usually stationary waves with zero horizontal phase speed and therefore measurements of the wave pattern above a single location are

expected to be reasonably constant with time [*Shutts and Broad*, 1993]. However, it has been shown that in regions of lee wave activity, a wide spectrum of waves can be generated. The power spectra of mesoscale horizontal velocity fluctuations show a $f^{-5/3}$ dependence which has been related to buoyancy waves [*Vanzandt*, 1982]. *Worthington and Thomas* [1996b, 1998] showed that the frequency spectra of vertical velocity oscillations also show a f^n dependence, where n approaches $-5/3$ for regions of mountain wave activity and $n = 0$ for regions without wave activity.

Energy dissipation and momentum transfer have also been the focus of much VHF radar research due to the importance of gravity wave drag in weather forecasting and climate prediction models. Convective and dynamical instabilities associated with gravity waves are thought to contribute significantly to the generation of turbulence in the middle atmosphere [*Fritts and Rastogi*, 1985]. Radars have been used to investigate the gravity wave momentum flux [e.g. *Vincent and Reid*, 1983; *Worthington and Thomas*, 1996a] and the energy dissipation rate [e.g. *Hocking*, 1985] which can both be closely related to the breaking of gravity waves. Additionally, breaking mountain waves can produce turbulence near the tropopause and have an important impact on the vertical mixing and transfer of air masses [*Worthington*, 1998].

Lee waves are common over the Canterbury Plains during north-westerly winds and are often seen in cloud patterns such as those shown in Figure 5.41. *Farkas* [1958] and *Cherry* [1972] studied winds over Christchurch using radiosonde data and both found many examples of mountain wave activity. Lee waves seen in cloud patterns over the Southern Alps have also been studied using satellite data by *Revell* [1982] and *Auer* [1992]. *Sturman* [1980] has investigated lee wave activity caused by the orography of Banks Peninsula, which is to the south-east of Christchurch. More recently, *Lane et al.* [2000] observed and modelled mountain waves as part of the New Zealand Southern Alps Experiment (SALPEX).

The topography of the South Island is dominated by the Southern Alps, which is a roughly linear mountain range oriented SW-NE. When the wind is from the north-west, it is perpendicular to the Southern Alps and arrives above Christchurch after having passed over the mountains (see Figure 5.42).

Associated with the cold front described in Section 5.6.1 was a region of gravity wave activity detected in the vertical velocities measured by the radar. Figure 5.43 contains the vertical wind data collected from 18:00 NZST on September

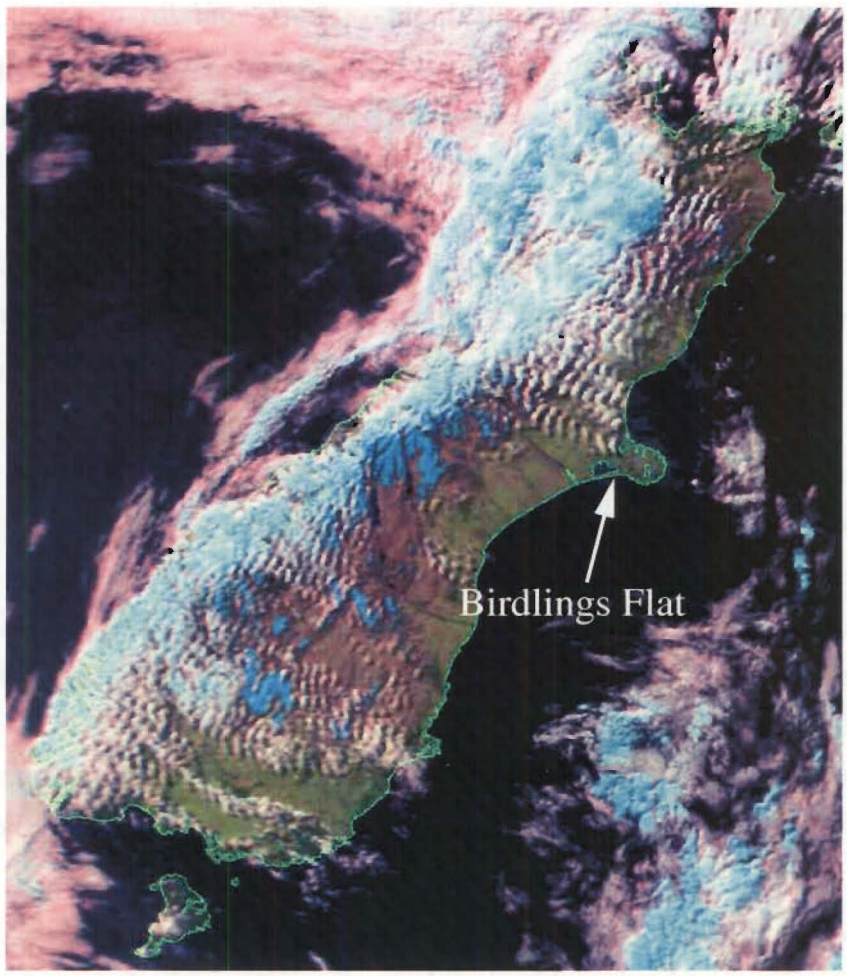

Figure 5.41: Wave cloud formations in the lee of the Southern Alps at 14:35 NZST on September 4, 2002. NOAA-17 satellite image provided by Landcare Research Ltd. (http://www.landcareresearch.co.nz/).

9 to 06:00 NZST on September 11 and shows regions with large vertical motion occurring throughout the troposphere and lower stratosphere.

The largest vertical velocities occur below an altitude of about 8 km. From 22:00 NZST on September 9 to 04:00 NZST on September 10, oscillations with a period of about 1 hour can be observed, which reach an altitude of about 7 km. Following this there is a strong downward motion which lasts for about 6 hours. At 12:00 NZST on September 10, there is a clear upward trend which may be associated with circulation at the frontal surface. This time also marks the onset of some very strong oscillations reaching up to 12 or 13 km and persisting for just under 6 hours.

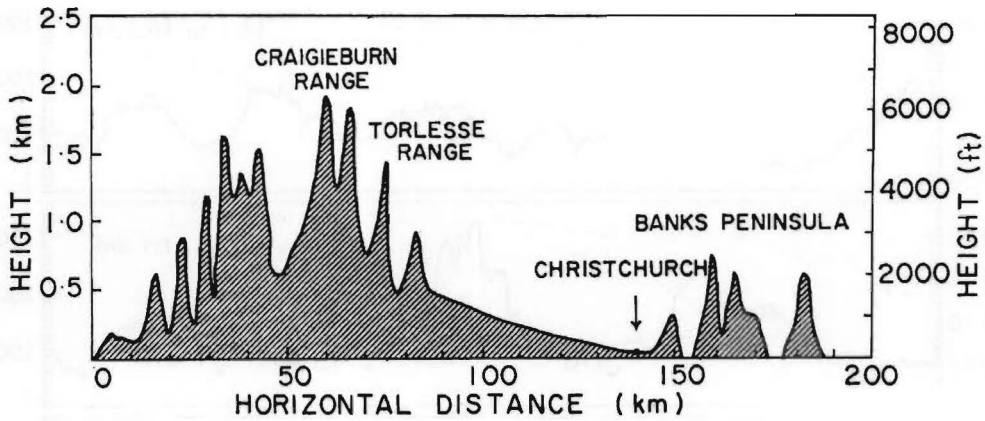

Figure 5.42: A NW-SE cross-section through Christchurch, the Southern Alps and Banks Peninsula [from *Cherry*, 1972].

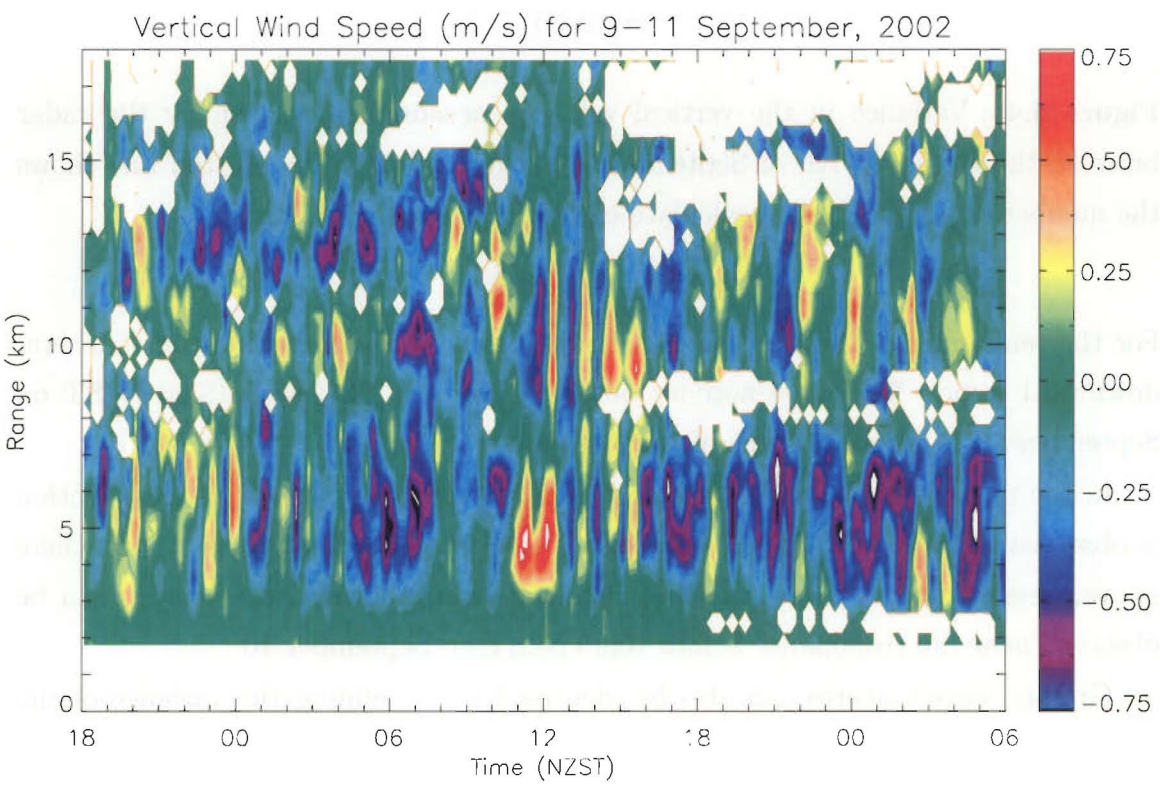

Figure 5.43: Vertical wind speed measured by the radar for the 9th to the 11th of September, 2002. Data points with a low signal to noise ratio (less than −3 dB) have not been included.

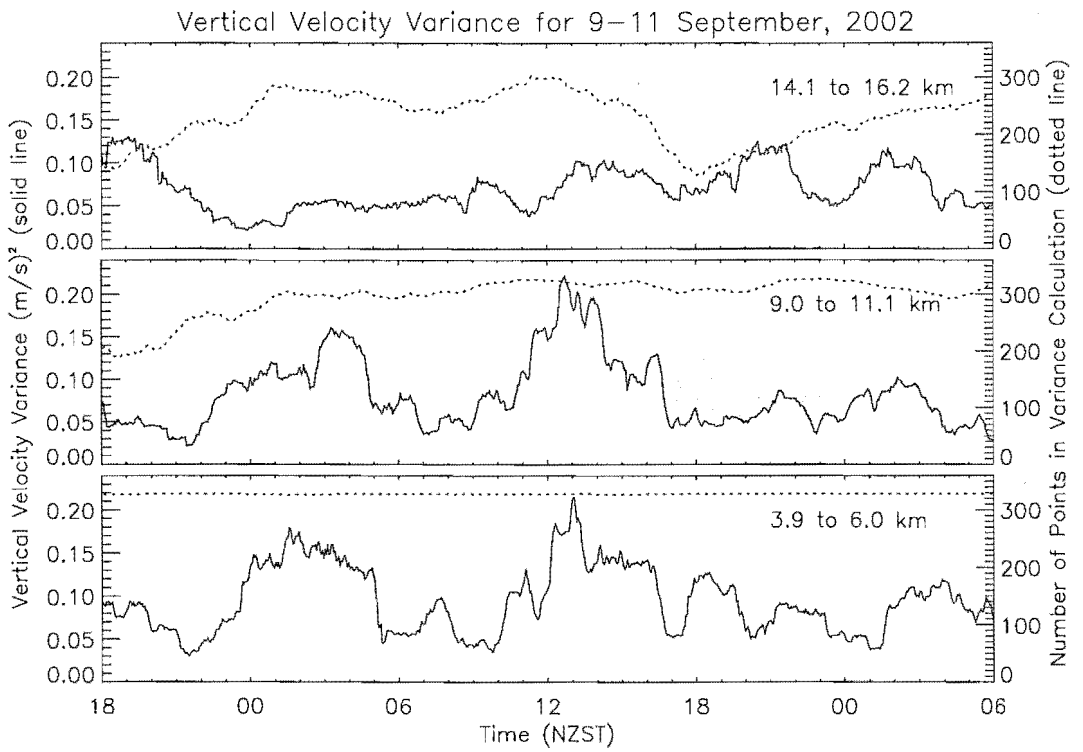

Figure 5.44: Variance in the vertical velocity measurements taken by the radar between the 9th and 11th of September, 2002 (solid line). The dotted line shows the number of points used to calculate each variance value.

For the remainder of the time-period shown, below 8 km, there is again a general downward trend. The wave activity observed between 12:00 and 18:00 NZST on September 10 is the main focus of this section.

In the region between 8 and 11 km the only evidence of strong vertical motion is observed between 12:00 and 18:00 NZST on September 10. Above 11 km there is even less evidence of wave motion, although strong downward velocities can be observed near the tropopause before 10:00 NZST on September 10.

Gravity wave features can also be identified by examining the variance of the vertical velocity measurements. This process was performed for three different height regions, each approximately 2 km thick, centred at altitudes of 5, 10 and 15 km. The vertical velocity variance was calculated at each point (in time) using two hours of data centred at that point. The results are shown in Figure 5.44, which includes a dotted line indicating the number of points used for each calculation of the velocity variance. The variation in the number of points results from the exclusion

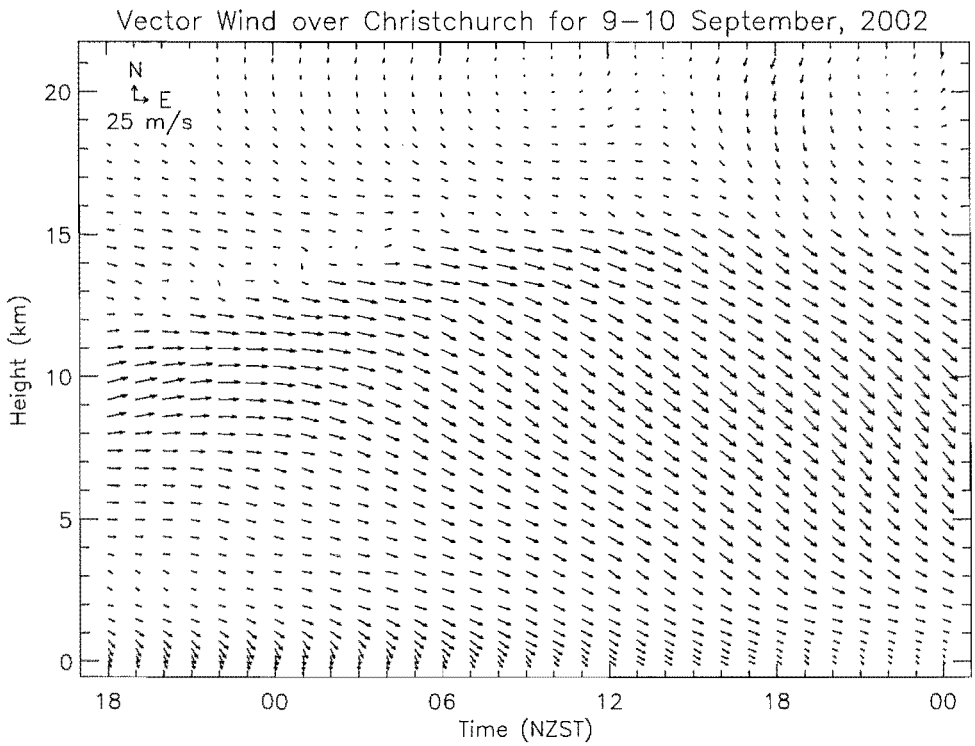

Figure 5.45: Background wind speed above Christchurch from September 9 to 10. Model data courtesy of *R. Turner*, NIWA.

of measurements with a signal to noise ratio less than −3 dB.

Within the lowest layer, there are two main regions with large variance. These regions are associated with the wave activity mentioned earlier between 00:00 and 04:00 NZST and 12:00 and 18:00 NZST on September 10. In the height region centred at 10 km, there is only one region of large variance and this is again associated with the wave event observed at midday on September 10. Between 14.1 and 16.2 km, there are no regions of large variance.

The high resolution mesoscale model discussed in the previous section, also yields the background wind and this is shown in Figure 5.45. At low levels, there is a weak north-westerly flow over Christchurch for the duration of the time period. In contrast, at heights above 4 or 5 km in altitude, the wind is quite strong and is initially westerly before changing direction between 00:00 and 06:00 NZST on September 10 to become north-westerly. This direction is maintained for the remainder of the time period. The wind is very strong between 4 and 15 km and reaches a maximum of $\simeq 45\ \mathrm{m\,s^{-1}}$ after 18:00 NZST at approximately 10 km. Above 15 km, from

Height Range (km)	Time Period (NZST)		
	00:00 - 06:00	11:30 - 17:00	00:00 - 06:00
14.1 - 16.2	−0.29	−0.03	−0.31
9.0 - 11.1	−0.16	−0.80	−0.49
3.9 - 6.0	−0.23	−0.68	−0.46

Table 5.4: Comparisons between n from frequency spectra for time periods before, during and after the frontal passage.

06:00 NZST onwards, the background wind is close to zero.

The change in wind direction to strong north-westerlies observed in Figure 5.45 occurs approximately 6 hours before the beginning of the wave motion observed by the CUSTAR radar. This suggests that the oscillations may be due to orography.

In regions of lee wave acitivity, the vertical wind obeys a power law, where the spectral density varies as $f^{-5/3}$. This dependence can be used to determine whether activity observed in vertical velocity data is likely to be caused by mountain waves. It should be noted that exact values of $-5/3$ are not always observed, for instance *Worthington and Thomas* [1996b] obtained a slope of -0.7 for an event with relatively weak mountain wave activity.

Figure 5.46 contains frequency spectra for three different height regions during the main wave event which was observed between 11:30 and 17:00 NZST on September 10. The spectra are plotted using log-log axes and a dashed line with slope $-5/3$ is shown for reference. The region between 14.1 and 16.2 km, which is an area of weak background wind, has a very flat spectrum with a slope of only -0.03. The region directly above the tropopause, which contains very strong wave activity and also has the strongest background wind, has a much larger slope of -0.80 which is closer to $-5/3$. The third region, from 3.9 to 6.0 km, has a slightly shallower slope of -0.68. Although not conclusive, these values suggest that the wave activity present may be due to lee waves.

Table 5.4 contains values of the slope, n, for time periods before, during and after the main gravity wave activity. For the time period from 00:00 to 06:00 NZST on September 10, the slopes of the frequency spectra are shallow at all heights, which corresponds well with what is expected, as the background wind is not from the north-west at this time. As expected, between 11:30 and 17:00 NZST on Septem-

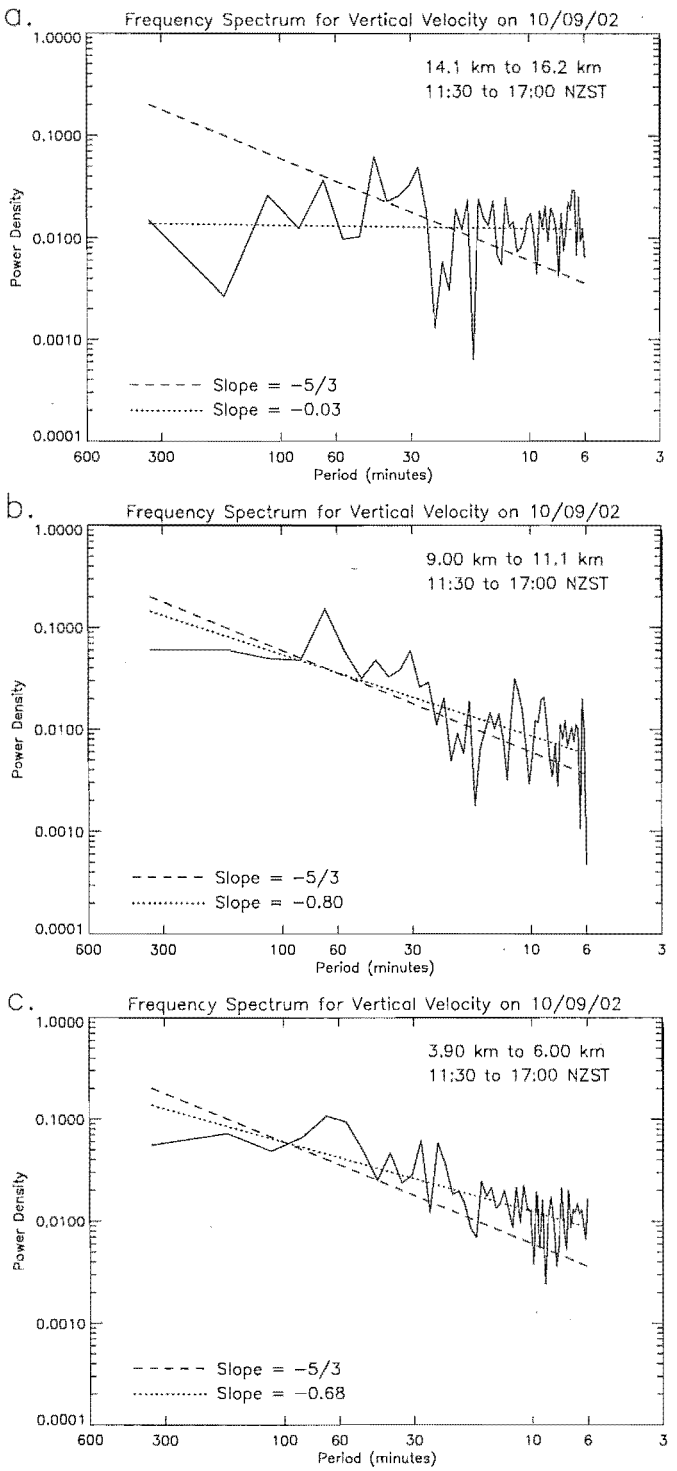

Figure 5.46: Frequency spectra for oscillations in the vertical velocity between 11:30 and 17:00 on September 10. The height ranges shown are **(a)** 14.1 to 16.2 km, **(b)** 9.0 to 11.1 km and **(c)** 3.9 to 6.0 km. In each plot the dashed line indicates a slope of $-5/3$ and the dotted line is the linear least-squares fit.

ber 10, the values for n are much larger. During the third period, the slopes of the spectra have again become more shallow, despite the continuation of strong cross-mountain winds. This suggests that there may be another factor, other than orography, controlling the production (or propagation) of these waves.

The conditions were not right for formation of clouds in the lee of the Southern Alps on September 10, so no wave patterns were observed in satellite data on this day. However, vertical velocity measurements obtained using the CUSTAR radar were analysed for the time period corresponding to the satellite image in Figure 5.41. The background wind was north-westerly on this day and lee waves can be observed clearly in the cloud pattern extending south-east as far as Christchurch. Although the lee wave clouds are not seen directly above Birdlings Flat, it is very likely that there is mountain wave activity in this region also.

Figure 5.47 contains vertical wind speed measured by the radar for 09:00 to 16:00 on this same day. The oscillations have a period of about 1 hour, which is very similar to the gravity waves observed on September 10. However, in this case the waves only reach heights of around 9 or 10 km, which may indicate that the waves are trapped, especially considering the large horizontal extent of the waves. The frequency spectrum of this data is plotted on log-log axes in Figure 5.48 and produces a slope of -0.53. Although this slope is not as steep as those observed in Figure 5.46, it shows that there is possibly some wave excitation. The satellite image in Figure 5.41 shows the lee clouds disappearing at approximately the same distance from the mountains as Birdlings Flat. If this is also where the lee wave activity reduces, it may account for the shallow slope of -0.53 observed in the frequency spectrum.

The similarity between the data on September 4, when there was almost certainly mountain wave activity, and September 10 suggests that the gravity wave activity observed on September 10 was also produced orographically.

A closer view of the vertical velocity measurements performed by the radar between 11:00 and 18:00 NZST on September 10 is displayed in Figure 5.49. The velocities shown are an average over 9 minutes and over 4 range gates (1.2 km). The wave activity begins just before 12:00 NZST and continues with an approximately constant amplitude until 16:00 NZST, when the oscillations quickly fade. By 17:00, the oscillations are almost completely gone. This plot also shows that the phase of the wave changes very little with height, which suggests the wave could be a trapped

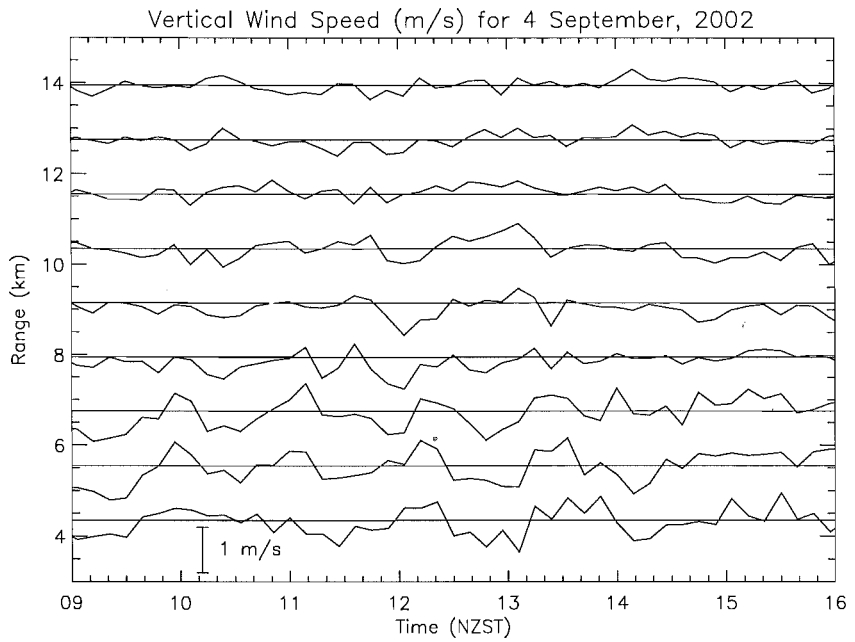

Figure 5.47: Vertical wind speed as measured by the radar for 09:00 to 16:00 NZST on September 4. The data has been averaged over 9 minutes.

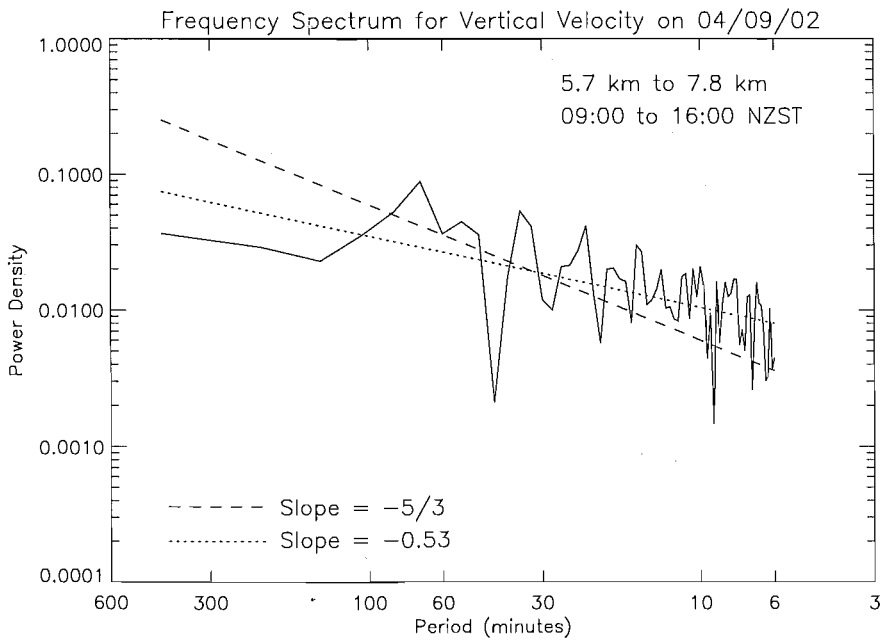

Figure 5.48: Frequency spectrum for oscillations in the vertical velocity between 09:00 and 16:00 on September 4. The dashed line indicates a slope of $-5/3$ and the dotted line is the linear least-squares fit.

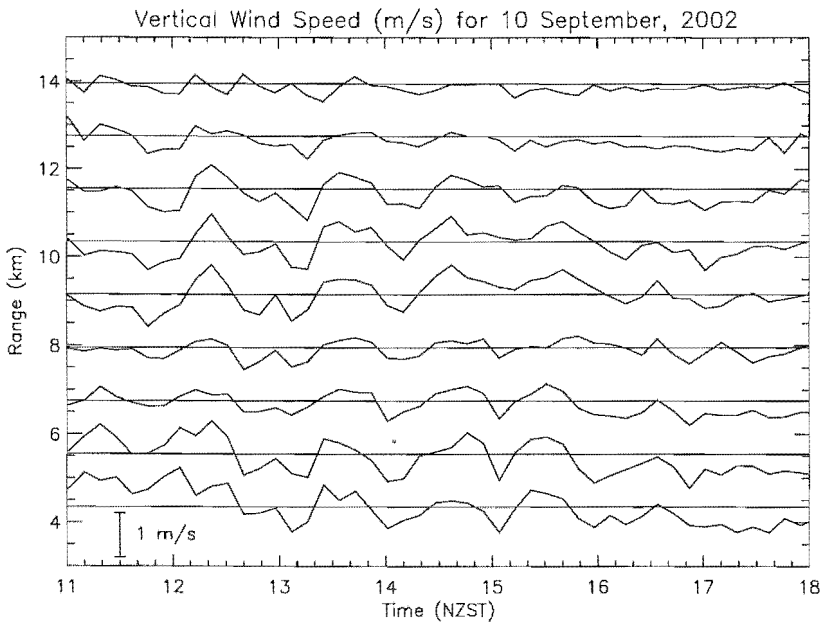

Figure 5.49: Vertical wind speed as measured by the radar for 11:00 to 18:00 NZST on September 10. The data has been averaged over 9 minutes.

lee wave [*Ralph et al.*, 1992; *Shutts et al.*, 1994].

Figure 5.49 also shows evidence that the gravity waves propagate vertically to heights above 12 km. Indeed, the oscillations can also be observed at the height of the radar tropopause. From 12:00 NZST onwards in Figure 5.50, the maximum in signal power associated with the tropopause undergoes perturbations, with a period of about 1 hour, which are very similar to those in Figure 5.49. Using the "global maximum" technique (see Section 5.5.2), the radar tropopause height was found with a temporal resolution of 9 minutes. This height is shown in Figure 5.50 by the solid line. The oscillations in the tropopause height may be an indication that wave breaking is occurring. This would cause mixing between the stratosphere and troposphere leading to variations in static stability (and therefore radar signal to noise ratio) at the tropopause level. The gravity wave activity has the largest effect on the tropopause between 13:00 and 15:00 NZST, when the oscillation has a peak-to-peak amplitude of just over 500 metres. The amplitude of the oscillation rapidly fades, however, to between 100 and 200 metres.

As explained before, the change in wind direction to strong north-westerlies suggests that the gravity waves observed may be due to orography. It is also interesting

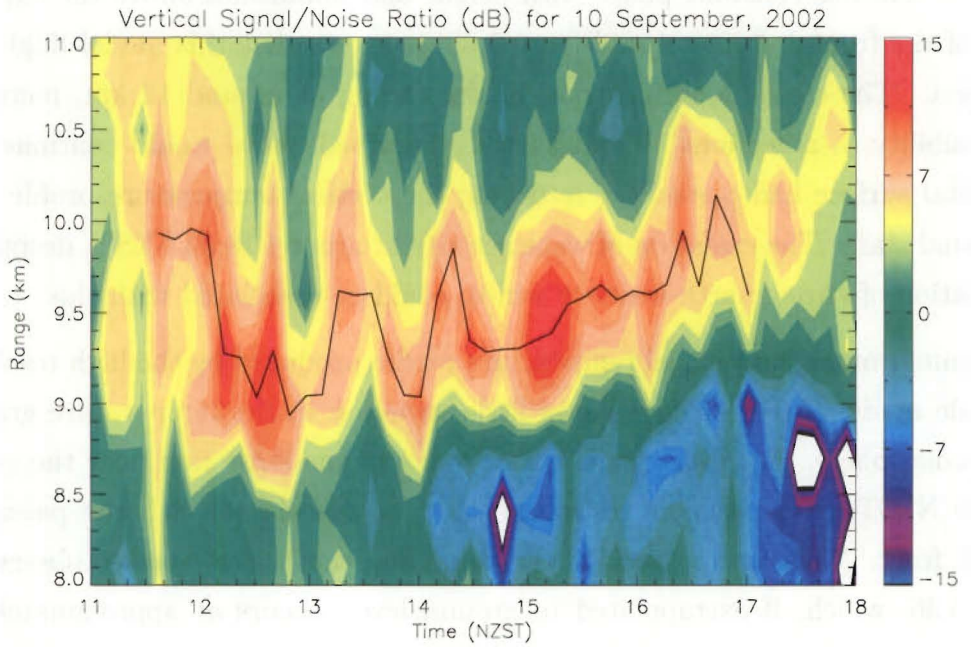

Figure 5.50: Radar signal to noise ratio for 11:00 to 18:00 NZST on September 10, showing returns from between 8 and 11 km. The increased signal power associated with the tropopause shows oscillations of about 1 hour.

to note that the wave motion diminishes to zero about 2 to 3 km below the height at which the background wind drops close to zero. If the disappearance of the wave was associated with a critical layer, the absorption of the wave should occur at the same height that the background wind approaches zero (see Section 2.1.5).

The abrupt onset of gravity waves at 11:00 NZST on September 10 could also be related to the passage of the cold front, which occurs at this time. As the cold front passes, the air temperature at the ground becomes cold relative to the air above the frontal surface. This reduces the lapse rate below the frontal surface, causing increased stability, but decreases the stability above the frontal surface. As explained in Section 2.1.5, when the static stability is high, gravity waves can propagate vertically, but when the static stability decreases (and/or the background wind increases significantly) there can exist a turning point where the waves are reflected and therefore trapped. This creates favourable conditions for the production and propagation of gravity waves under the frontal surface and allows for possible reflection of the waves from the region above the front. That the gravity wave activity observed

in Figure 5.49 has constant phase with height and diminishes above the expected height of the frontal surface (see Figure 5.36) suggests that this model might also be correct. The cross-mountain wind is also strong at around 12 km, increasing the possibility of reflections. The situation described above would continue until the frontal surface had passed by, returning the vertical temperature profile to its more usual state. The cessation of wave activity at around 18:00 NZST, despite the continuation of strong north-westerly winds, could be associated with this.

Examination of the vertical temperature profile produced by the high resolution mesoscale model (Figure 5.40), shows little variation in the temperature gradient in the troposphere. However, there is a decrease in the lapse rate near the ground at 00:00 NZST on September 10 which could be associated with the passage of the cold front. This can be verified by examining the frontal surface observed in Figure 5.36, which, if extrapolated to ground level, occurs at approximately the same time as the lapse rate reduction. The model temperature data shows no evidence of an increase in static stability at mid-tropospheric heights between 06:00 and 18:00 NZST on September 10, where the gravity waves are observed. However, there is a clear increase in the radar signal to noise ratio in this region, which, in contrast, suggests that there may be an increase in the static stability. These results do not conclusively support the theory that the observed wave activity is trapped, but this interpretation is still a possibility.

To determine whether the waves are absorbed or reflected, it is beneficial to examine the Scorer parameter (Equation 2.9). Profiles of the Brunt-Väisälä frequency and Scorer parameter were calculated from the model temperature and wind data during the main wave event. The Scorer parameter was calculated both with and without the curvature term, $(1/\overline{u})(d^2\overline{u}/dz^2)$, which is expected to have a neglible effect [*Ralph et al.*, 1992]. Figure 5.51 contains these profiles for 14:00 NZST on September 10. The Brunt-Väisälä frequency profile shows a fairly typical value of 0.01 rad s^{-1} in the troposphere, which gradually increases to 0.02 rad s^{-1} due to the stable stratospheric air at approximately 10 km. There is also a large increase at 15 km due to a brief, but strong, positive temperature gradient at this height (see Figure 5.40). The Scorer parameter is fairly constant with height in the troposphere, but increases exponentially in the lower stratosphere. The profiles with and without the curvature term follow a similar overall pattern, but there are small differences on scales of 1 or 2 km.

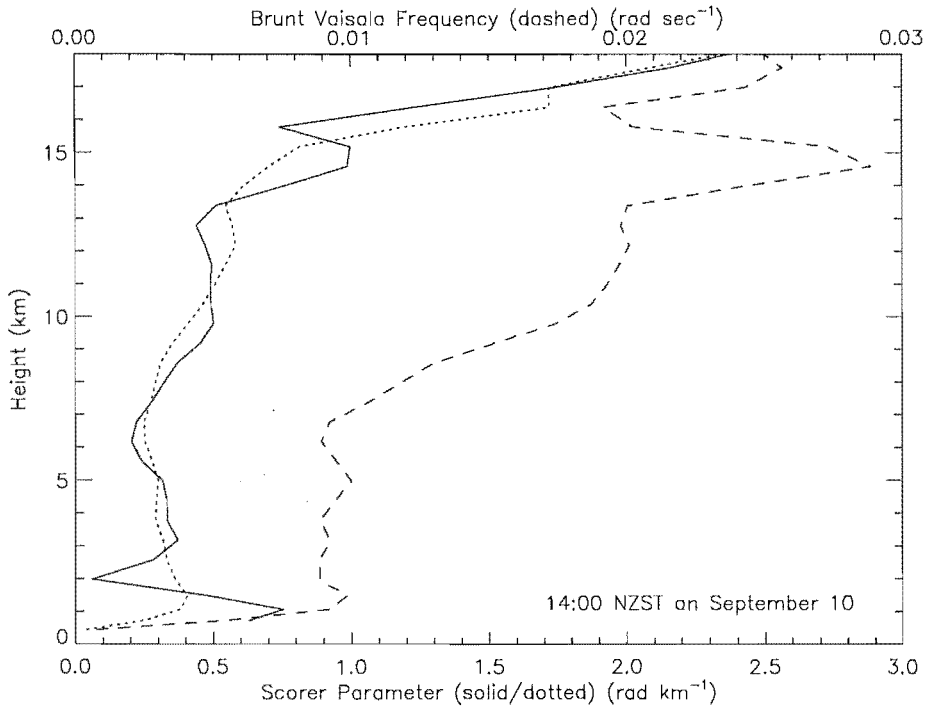

Figure 5.51: Profiles of the Brunt-Väisälä frequency and Scorer parameter above Christchurch at 14:00 NZST on September 10, 2002. The Scorer parameter is shown with the curvature term (solid line) and without (dotted line). All profiles calculated from RAMS model data.

None of the profiles in Figure 5.51 show any clear features at around 12 km, where the gravity wave activity observed in the vertical velocity measurements decreases to zero. If the wave was trapped due to reflections from a "turning point", a strong decrease would be expected in the Scorer parameter profile at this point. If the wave was absorbed due to a "critical level", a significant peak would be expected in the Scorer parameter profile. That neither of these features is observed means that no clear conclusion, as to why the wave dissipates, can be reached.

There are a number of reasons that could explain why there is not a clear correlation between the wave activity and the Scorer parameter. Firstly, the Scorer parameter has been calculated from model data which may not be able to resolve sharp increases (or decreases) occuring on small scales. For instance, the temperature data in Figure 5.40 contains very little detailed structure during the frontal passage, even though the radar signal to noise ratio clearly shows the presence of complex structure. It is possible that there was a large decrease in the Scorer pa-

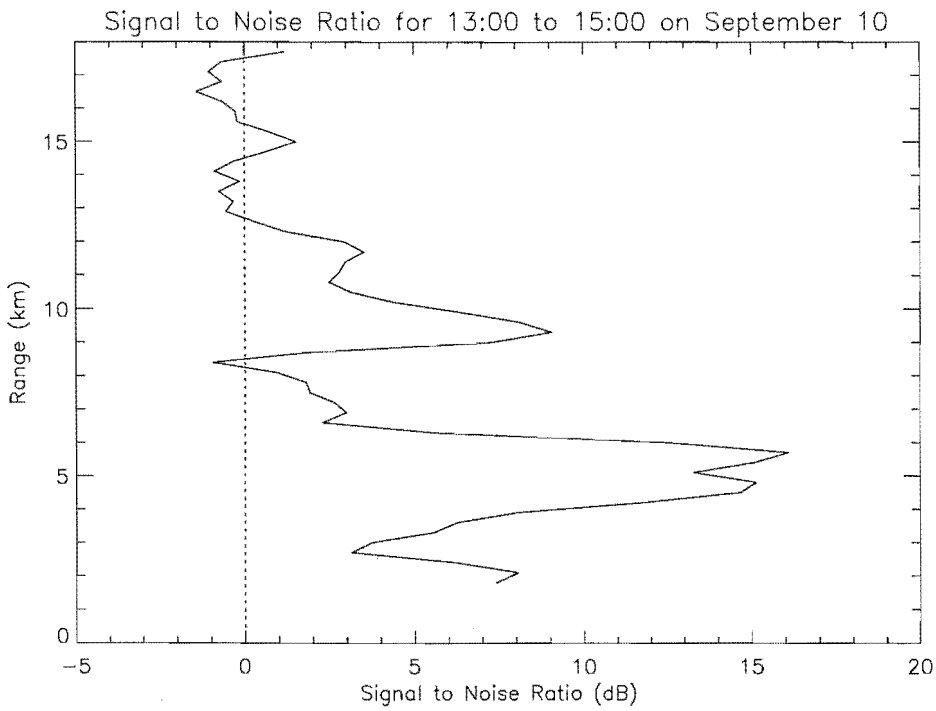

Figure 5.52: Average radar signal to noise ratio between 13:00 and 15:00 NZST on September 10, 2002.

rameter near an altitude of 12 km and that the model was unable to reproduce this. There is also a possibility that the wave activity does propagate higher than 12 km, but is not seen in the radar data due to the low signal to noise ratio found above this height. Figure 5.52 shows the radar signal to noise ratio during the main wave event and indicates that it becomes very small at both 8 km and 13 km in altitude. Investigation of Figure 5.49 shows that these two altitudes correspond to when the wave activity is smallest, suggesting that there could be a bias toward the underestimation of vertical wind speeds when the signal to noise ratio is low.

In conclusion, there is fairly strong evidence that the wave activity observed on September 10 is orographically generated and that the cold front may have had some role in producing favourable conditions for the waves. The lack of *in situ* upper air measurements during the wave event means that profiles of the Scorer parameter can not be relied upon with confidence. From the information available, it is unclear why the waves disappeared at around 12 km and neither reflection nor absorption provide a satisfactory explanation. Firstly, if the waves were absorbed due to a

critical layer, this layer would need to be at an altitude above 15 km where the cross-mountain wind becomes very small. A possible explanation for the absence of gravity waves in the radar vertical wind measurements up to this height is the low signal to noise ratio that is observed. Secondly, a strong case could be argued for wave reflection from a turning point as the waves that were observed did not change phase with height. The reflection could also be due to an unstable layer above the frontal surface, however, no evidence of this layer was observed in the model values for the Scorer parameter.

5.7 Summary

This chapter has described some initial results obtained using the Canterbury University ST radar that have been used to validate its performance. The main focus has been on determination of the tropopause height, but the results have also been used to investigate a frontal passage and gravity wave activity.

A method has been developed to determine the radar tropopause height at hourly intervals using profiles of the signal to noise ratio. Radar tropopause altitudes have been compared to those calculated from radiosonde temperature measurements and in general the agreement has been good. It was found in Section 5.5.1 that a similar seasonal variation in tropopause height between September/October and November/December was observed in both the radar data and in Christchurch radiosonde data collected over a four year period. In both datasets, an increase in the average tropopause altitude (by approximately 1 km) was observed in the warmer months.

Simultaneous measurements of tropopause height using the radar and radiosonde measurements from three sites spread across New Zealand were also performed and these show very good correlations considering the large separation between the radar and radiosonde sites. The correlation coefficients between the radar derived tropopause and radiosonde tropopause for the two closer sites (440 and 370 km away) were found to be 0.55 and 0.53, respectively. These results are quite promising, particularly in light of results discussed by *Hooper and Arvelius* [2000], who found similar results even though their comparisons were made using a radiosonde station that was located nearby.

Using the radar signal to noise ratio and vertical velocity measurements, the region associated with a frontal passage has been examined in detail. Comparisons

between the radar data and a high resolution mesoscale model show good agreement and have also demonstrated the radar's ability to observe atmospheric events with a very high temporal resolution. Gravity wave activity, thought to be orographically produced, was also observed near the frontal surface and lasted for about 6 hours. This activity attained heights of 12 km, but above this altitude the amplitude of the mountain wave was significantly reduced. From the data available, it is unclear whether the lack of waves at greater altitudes was due to reflection or absorption.

The results covered in this section show that the radar consistently operates in a satisfactory mode. It is capable of measuring the tropopause height with a temporal resolution of one hour and a height resolution of 300 metres. The radar is also capable of detailed study of the structure of atmospheric phenomena such as frontogenesis and gravity waves.

Chapter 6

Conclusion

This thesis has described the design, construction and initial operation of a VHF stratosphere-troposphere (ST) radar. The Canterbury University ST Atmospheric Radar (CUSTAR) operates at 42.5 MHz and is capable of continuous measurement of the vertical wind profile from 3 to 15 km in altitude, with a temporal resolution of 2 minutes and a height resolution of 300 metres. It can currently be used to routinely measure the height of the tropopause and also to investigate the structure of frontal surfaces and gravity waves.

6.1 Design and Construction

A large part of the work performed during this study was on the design and construction of the antenna array and its associated feed system. The Canterbury University radar uses a novel, cost-effective antenna design. By spacing the individual elements by 0.707 wavelengths instead of the more usual 0.5 wavelengths, the effective area of the antenna is increased, without significantly increasing the magnitude of the side-lobes. Using relatively cheap, bare copper wire, the elements can then be fed at one wavelength intervals (diagonal to the 0.707 wavelength spacing) and therefore remain in-phase. Two element Yagi-Uda antennas were used for the individual elements to minimise the effect of the uneven ground-plane.

The final antenna array is square, with a length down each side of 56 metres, and is made up of 128 individual elements. The antenna site was unable to be levelled due to environmental considerations, so the array was constructed using fence posts set into the ground so that the tops of the posts were level. The theoretical half-power full-width of the main beam is 6.35° and the largest side-lobe is 13 dB below the main peak.

A transmit-receive switch was constructed to allow the same antenna to be used for both transmission and reception. The switch can attenuate the transmitted

signal by more than 66 dB before it reaches the receiver and on reception, the signal is only attenuated by 1 dB. The radar is powered with a vacuum tube transmitter which has a typical peak power of 100 kW and a typical average power of 500 W. The pulse length can be adjusted from 1 to 7 μs and the pulse repetition frequency is currently set at 1 000 pulses per second. The in-phase and quadrature signals are extracted from the received signal using a direct-conversion receiver. A two channel, 8 bit analogue to digital converter, capable of 500 000 samples per second, transfers the receiver outputs to a computer.

For the majority of the measurements discussed in this thesis, the radar operated with a pulse length of 4 μs and the data was coherently integrated over 128 pulses. In Section 5.3 it was found that this coherent integration did not adversely effect the quality of the data. Signal was collected for run lengths of 2 minutes and for heights between 3 and 17.7 km using range cells of 300 metres in size. The data was then processed to find the noise level and first three moments of the atmospheric signal.

An investigation into the use of the ST radar as a probe of meteoric ionisation has been performed. Changes to the present observing system, permitting echoes to be obtained from ranges between 80 and 110 km, can be implemented. This would be very beneficial, especially with regard to the measurement of the declination of interstellar meteoroids.

6.2 Beam Verification

To make accurate measurements of wind speed with a VHF radar, the pointing direction of the antenna beam needs to be precisely known. This is even more important when examining the vertical wind as any contamination by horizontal winds, which are stronger by approximately one order of magnitude, can significantly alter the measurement. To this end, the beam pattern of the CUSTAR antenna array was investigated in great detail using astronomical radio sources. Measurements were performed at different stages throughout the construction and testing of the radar equipment. In almost all cases the beam was found to be vertical within the uncertainties of the measurement.

While the antenna array was under construction, a single row of two-element Yagi-Uda antennas was tested using measurements of the sun's radio emission. The

sun was particularly active during this time and could be observed in the main beam and the side-lobes due to the strong signal obtained. It was found that the position of the main lobe and the side-lobes matched the theoretically expected pattern closely, suggesting that the single row of dipoles under examination had been constructed correctly.

After the antenna array had been completed, its beam pattern was tested using reverse radio astronomy while the receiver equipment needed for the radar was being developed. The sky noise results obtained during this time were not of excellent quality due to instabilities in the prototype receiver used. However, peaks in the sky noise associated with Vela XYZ and Centaurus A were compared to their expected positions and it was found that the antenna beam was pointing vertically (in the east-west plane), although the uncertainties were very large, at times up to ± 6 minutes ($\pm 1.5°$).

After the radar became operational in September, 2002, the sky noise results were much improved, due to the increase in stability of the receiver equipment. Signals associated with Vela XYZ and Centaurus A were again compared to their expected positions and the results indicated that the beam was pointing vertically and the uncertainty was reduced to less than $\pm 0.5°$. A 45 MHz sky map of the Southern Hemisphere produced by *Alvarez et al.* [1997] was used as an independent measure of the positions of Vela XYZ and Centaurus A and, although this produced slightly different results, the beam direction was again shown to be vertical within uncertainties.

Using all the results obtained with the CUSTAR antenna and the best estimate of the transit times of Vela XYZ and Centuarus A, the pointing angle of the beam, in the east-west plane, was calculated to be $0.01° \pm 0.20°$ from the zenith. This result means that, aside from increasing the spectral width due to beam-broadening, horizontal wind contamination is unlikely to affect the vertical velocities measured by the radar.

Antenna measurements of sky noise were also used to estimate the width of the antenna beam. The sky noise results collected using the completed antenna were compared with the 45 MHz sky map and also to high resolution maps of the two radio sources, Vela XYZ and Centaurus A. The width of the beam was found to be narrower than expected when compared to the 45 MHz sky map and wider than expected when compared to the high resolution maps, even though the maps had

been convolved to the theoretical resolution of the CUSTAR antenna. Using the best estimates of the widths of the two sources, obtained from the available maps, the width of the antenna beam was found to be FWHM $= 6.51° \pm 0.54°$. This value is slightly wider than that expected from theory and means that the effective aperture of the antenna is $A_e = 3900 \pm 400$ m^2.

6.3 Initial Operation

The Canterbury University ST radar has been operating in the Doppler mode using a single vertically oriented beam since September, 2002. During this time, excellent results have been obtained that demonstrate the versatility of the system.

The tropopause height was measured hourly, from the signal to noise ratio of the received signal, thoughout the period that the radar was operational. Radiosonde flights are not launched from Christchurch at the present time, so the tropopause altitudes measured by the radar were not able to be compared directly to independent measurements of the tropopause height. However, the statistics of the tropopause height measured over the four months of available radar data were compared to data collected by radiosonde measurements in Christchurch between 1958 and 1962. This comparison showed that the seasonal variation between September/October and November/December was similar for both data sets (approximately 1 km higher in the warmer months), although the mean tropopause height differed, between the data sets, by about 0.5 km.

For the months of October and November, 2002, radiosonde data was obtained from three sites; Whenuapai, Paraparaumu and Invercargill, which are separated from Birdlings Flat by 790, 440 and 370 km, respectively. Individual tropopause altitudes were calculated using this data and compared to tropopause heights measured simultaneously by the radar. The correlation between the radar data and Whenuapai was very low due to their large spatial separation and the location of Whenuapai which is in the sub-tropics. The correlation coefficients between the radar and Paraparaumu and the radar and Invercargill were 0.55 and 0.53, respectively. These are good correlations, particularly in light of comparisons that were made between the different radiosondes, which produced correlation coefficients that were lower than those quoted above. This suggests that the radar is capable of finding the tropopause height with an accuracy similar to that obtainable when using

radiosondes.

To find days when the atmospheric conditions above the radar were similar to those above the radiosondes, the profile of the gradient in the potential refractive index (M^2) was calculated from each radiosonde flight and compared to the echo power profile of the radar. For times when the M^2 profile above the tropopause was well correlated with the radar power profile, it was found that the tropopause heights measured using the different instruments also had much better correlations. This process indicates that the low correlations observed between the radar and the radiosondes were most likely due to the large spatial separation between the instruments.

Radar observations of a frontal passage and associated gravity wave activity have also been examined in detail. The structure of a cold front which passed over Christchurch on September 10, 2002, was observed in the radar signal to noise profiles. The frontal surface was detected above the radar for approximately one day, during which time the slope of the surface was found to be 0.4°. During the frontal passage, gravity wave oscillations, that were thought to be caused by orography, were also observed. The wave activity had a dominant period of about one hour and extended into the lower stratosphere, above which there was a marked reduction in its amplitude. It could not be determined from the available data whether the wave was reflected or absorbed at this point, but both scenarios have been examined thoroughly. Firstly, the gravity waves showed no evidence of phase oscillation with height, suggesting that they were trapped, possibly due to reflections from an unstable layer above the frontal surface. However, no evidence of a decrease in the Scorer parameter was observed in model profiles at this time. A scenario involving wave absorption was also a possibility, because the model data did show a large increase in the Scorer parameter that could be interpreted as a critical layer. However, this layer was at 15 km and the observed wave disappeared below this, at an altitude of 12 km. It was also interesting to note that the wave activity was strongest during the passage of the front. This was thought to be due to an increase in atmospheric stability under the front and also because the background wind was strong and from the direction of the mountains.

The preliminary results obtained from the radar show that it is working as expected and that it will indeed prove to be a very useful tool in the examination of the structure and dynamics of the atmosphere in New Zealand.

6.4 Further Work

The Canterbury University ST radar has the potential to support numerous research activities. Some of these can be achieved using the current radar system and some will require further development.

It would be beneficial to perform direct measurements of the antenna beam pattern to validate the results presented in this thesis, but also to ensure that the pointing direction in the north-south plane (which has not yet been investigated in detail) is close to vertical. This could be achieved by flying a light aircraft or automated glider through the beam of the array with a small 42.5 MHz transmitter and GPS receiver on board. The known location of the aircraft could then be matched with the signal received by the antenna array and used to map the field pattern.

This thesis has only investigated a few of the interesting atmospheric events that the radar has observed. There are many more frontal passages similar to, and different from, the case discussed in Section 5.6 and these other examples could be examined in a similar manner. It also would be interesting to observe whether gravity waves are often associated with the passage of cold fronts or whether the case described in this thesis was an unusual event. If this work was to continue, it would be very beneficial to perform *in situ* upper air measurements during frontal or gravity wave events to gain a more complete understanding of the mechanisms involved. A Stratosphere-Troposphere Atmospheric measurement Glider (STAG) is currently being constructed in the Department of Physics and Astronomy at the University of Canterbury and this instrument would be ideal for this purpose.

By implementing some minor changes, the CUSTAR system would be an ideal facility for monitoring meteoric ionisation produced by near vertical trajectory meteoroids. A project to explore the characteristics of interstellar meteoroid inflow, as described in Sections 2.5 and 3.4.3, would provide a significant contribution to the current interest in the study of interstellar dust in the neighbourhood of the solar system.

There are also a number of improvements that can be made to the ST radar system itself, most notably the extension of its capabilities to include the measurement of horizontal wind. This work is underway and the construction of a versatile receiving array for measurement of horizontal winds using the spaced an-

tenna (full-correlation analysis) method has already been partly completed. Various improvements could also be made to the receiver and data-acquistion hardware. A system has been designed to prevent overloading of the receiver input by leakage of the transmitter pulse through the transmit-receive switch. This needs to be implemented to improve the radar's ability to observe low altitudes. The performance of the radar system can also be enhanced by increasing the pulse repetition frequency and by increasing the sampling rate and accuracy of the analogue to digital converter. These improvements will give the radar a higher temporal and height resolution allowing more detailed study of the structure of the atmosphere, including small scale phenomena such as turbulence.

Bibliography

Aarons, J., Antenna and receiver measurements by solar and cosmic noise, *Proc. I.R.E.*, *42*, 810–815, 1954.

Alvarez, H., J. Aparici, J. May, and F. Olmos, A 45-MHz continuum survey of the southern hemisphere, *Astron. Astrophys. Suppl. Ser.*, *124*, 315–328, 1997.

Atlas, D. (ed.), *Radar in Meteorology: Battan Memorial and 40th Anniversary Radar Meteorology Conference*, Boston. American Meteorology Society, 1990.

Atlas, D., K. R. Hardy, K. M. Glover, I. Katz, and T. G. Konrad, Tropopause detected by radar, *Science*, *153*, 1110–1112, 1966.

Auer, A. H., Wave cloud formations in the lee of southern New Zealand, *Weather*, *47*, 103–105, 1992.

Baggaley, W. J., Radar observations, in *Meteors in the Earth's Atmosphere*, edited by E. Murad, and I. P. Williams, chap. 6, pp. 123–147. Cambridge University Press, 2002.

Baggaley, W. J., and D. P. Galligan, Mapping the interstellar dust flow into the solar system, in *Proc. Meteoroids 2001 Conference*, pp. 663–666. European Space Agency – SP-495, 2001.

Baggaley, W. J., R. G. T. Bennett, D. I. Steel, and A. D. Taylor, The advanced meteor orbit radar facility: AMOR, *Q. J. R. Astron. Soc.*, *35*, 293–320, 1994.

Balsley, B. B., and K. S. Gage, The MST radar technique: Potential for middle atmosphere studies, *Pure Appl. Geophys.*, *118*, 452–493, 1980.

Balsley, B. B., W. L. Ecklund, D. A. Carter, and P. E. Johnston, The Poker Flat MST radar: first results, *Geophys. Res. Let.*, *6*, 921–924, 1979.

Banwell, C. J., The use of a common aerial for radar transmission and reception on 200 Mc/s, *Journal I.E.E.*, *93*(Part IIIA), 545–551, 1946.

Beezley, B., *The Yagi Optimiser*. California, Software package, 1990.

Bennett, R. G. T., Antenna phasing arrangements, in *Proc. MST5*, edited by B. Edwards, pp. 374–376, Illinois. SCOSTEP, 1992.

Bethan, S., G. Vaughan, and S. J. Reid, A comparison of ozone and thermal tropopause heights and the impact of tropopause definition on quantifying the ozone content of the troposphere, *Q. J. R. Meteorol. Soc.*, *122*, 929–944, 1996.

Blackman, R. B., and J. W. Tukey, *The Measurement of Power Spectra From the Point of View of Communications Engineering*. Dover, New York, 1958.

Bluestein, H. B., Fronts and jet-streaks: A theoretical perspective, in *Mesoscale Meteorology and Forecasting*, edited by S. Ray. American Meteorological Society, 1986.

Booker, H. G., and W. E. Gordon, A theory of radio scattering in the troposphere, *Proc. I.R.E.*, *38*, 401–412, 1950.

Briggs, B. H., The analysis of spaced sensor records by correlation techniques, in *Handbook for Middle Atmosphere Program*, edited by R. Vincent, vol. 13, chap. 13, pp. 166–186. ICSU, 1984.

Briggs, B. H., Radar measurements of aspect sensitivity of atmospheric scatterers using spaced-antenna correlation techniques, *J. Atmos. Terr. Phys.*, *54*(2), 153–165, 1992.

Briggs, B. H., W. G. Elford, D. G. Felgate, M. G. Golley, D. E. Rossiter, and J. W. Smith, Buckland Park aerial array, *Nature*, *223*, 1321–1325, 1969.

Browning, K. A., Organization and internal structure of synoptic and mesoscale precipitation systems in midlatitudes, in *Battan Memorial and 40th Anniversary Radar Meteorology Conference*, edited by D. Atlas, pp. 433–460, Boston. American Meteorological Society, 1990.

Browning, K. A., D. Jerrett, J. Nash, T. Oakley, and N. M. Roberts, Cold frontal structure derived from radar wind profilers, *Meteorol. Appl.*, *5*, 67–74, 1998.

Burke, G., *Numerical Electromagnetics Code*. Lawrence Livermore National Laboratory, Software package, 1981.

Burns, J. O., E. D. Feigelson, and E. J. Schreier, The inner radio structure of Centaurus A: Clues to the origin of the jet x-ray emission, *Astrophys. J.*, *273*, 128–153, 1983.

Caccia, J. L., and J. P. Cammas, VHF-ST radar observations of an upper-level front using vertical and oblique-beam C_N^2 measurements, *Mon. Weath. Rev.*, *126*, 483–501, 1998.

Campistron, B., G. Despaux, M. Lothon, V. Klaus, Y. Pointin, and M. Mauprivez, A partial 45 MHz sky temperature map obtained from the observations of five ST radars, *Ann. Geophys.*, *19*, 863–871, 2001.

Cherry, N. J., Winds and lee waves over Canterbury, New Zealand, during 1970, *N.Z. J. Sci.*, *15*, 585–600, 1972.

Colwell, R. C., and A. W. Friend, The D region of the ionosphere, *Nature*, *137*, 782, 1936.

Craig, R. A., *The Upper Atmosphere - Meteorology and Physics*, vol. 8 of *International Geophysics Series*. Academic Press, 1965.

Crombie, D. D., Doppler spectrum of sea echo at 13.56 Mc./s., *Nature*, *175*, 681–682, 1955.

Crombie, D. D., Backscatter of HF radio waves from the sea, in *Electromagnetic Probing in Geophysics*, edited by J. R. Wait. The Golem Press, Boulder, Colorado, 1971.

Czechowsky, P., G. Schmidt, and R. Ruster, The mobile SOUSY-doppler radar - technical design and first results, in *Handbook for Middle Atmosphere Program*, edited by S. A. Bowhill, and B. Edwards, vol. 9, pp. 433–446. ICSU, 1983.

DeFant, F., and H. Taba, The threefold structure of the atmosphere and the characteristics of the tropopause, *Tellus*, *9*, 259–274, 1957.

Doviak, R. J., and D. S. Zrnić, Reflection and scatter formula for anisotropically turbulent air, *Rad. Sci.*, *19*, 325–336, 1984.

Doviak, R. J., and D. S. Zrnić, *Doppler Radar and Weather Observations*. Academic Press, San Diego, 2nd edn., 1993.

Dunford, A. J., The Canterbury University ST Atmospheric Radar Development, Ph.D. thesis, University of Canterbury, 1998.

Dunford, A. J., CUSTARD Technical Report - Transmitting Array Design, Tech. rep., University of Canterbury, 1999.

Durran, D. R., Mountain waves and downslope winds, in *Atmosperic Processes over Complex Terrain*, edited by W. Blumen, vol. 23 of *Meteorological Monographs*, chap. 4, pp. 59–81. American Meteorological Society, 1990.

Dwarakanath, K. S., Low-frequency observations of the Vela supernova remnant and their implications, *J. Astrophys. Astr.*, *12*, 199–211, 1991.

Eastwood, E., Aerial investigations using natural noise sources, *Marconi Rev.*, *23*(136), 2–20, 1960.

Ecklund, W. L., K. S. Gage, B. B. Balsley, R. G. Strauch, and J. L. Green, Vertical wind variability observed by VHF radar in the lee of the Colorado Rockies, *Mon. Weath. Rev.*, *110*, 1451–1457, 1982.

Elford, W. G., New radar techniques: precision measurements of meteoroid velocities, decelerations and fragmentation, in *Meteoroids 1998*, edited by W. J. Baggaley, and V. Porubčan, pp. 21–28. Astron. Inst. Slovak Acad. Sci., Britislava, 1999.

Farkas, E., Mountain waves over Banks Peninsula, New Zealand, *N.Z. J. Geol. Geophys.*, *1*, 677–683, 1958.

Fleming, E. L., S. Chandra, J. J. Barnett, and M. Corney, Zonal mean temperature, pressure, zonal wind, and geopotential height as functions of latitude, *Adv. Space Res.*, *10*(12), 11–59, 1990.

Fletcher, J. O., Early developments of weather radar during World War II, in *Radar in Meteorology*, edited by D. Atlas, chap. 1, pp. 3–6. American Meteorological Society, 1990.

Flood, W. A., Revised theory for partial reflection D-region measurements, *J. Geophys. Res. Space Physics*, *73*(17), 5585–5598, 1968.

Frail, D. A., M. F. Bietenholz, C. B. Markwardt, and H. Ögelman, A radio/x-ray comparison of the Vela X region, *Astrophys. J.*, *475*, 224–230, 1997.

Fraser, G. J., The measurement of atmospheric winds at altitudes of 64-120 km using ground-based radio equipment, *J. Atmos. Sci.*, *22*(2), 217–218, 1965.

Fritts, D. C., Gravity wave sources, source variability and lower and middle atmosphere effects, in *Coupling Processes in the Lower and Middle Atmosphere*, edited by E. V. Thrane, T. A. Blix, and D. C. Fritts, NATO ASI Series, pp. 191–208. Kluwer Academic Publishers, 1993.

Fritts, D. C., and G. D. Nastrom, Sources of mesoscale variability of gravity waves. Part II: Frontal, convective and jet stream excitation, *J. Atmos. Sci.*, *49*(2), 111–127, 1992.

Fritts, D. C., and P. K. Rastogi, Convective and dynamical instabilities due to gravity wave motions in the lower and middle atmosphere: Theory and observations, *Rad. Sci.*, *20*(6), 1247–1277, 1985.

Fukao, S., T. Tsuda, T. Sato, S. Kato, K. Wakasugi, and T. Makihira, The MU radar with an active phased array system 1. antenna and power amplifiers, *Rad. Sci.*, *20*, 1155–1168, 1985.

Furumoto, J., and T. Tsuda, Characteristics of energy dissipation rate and effect of humidity on turbulence echo power revealed by MU radar-RASS Measurements, *J. Atmos. Sol. Terr. Phys.*, *63*, 285–294, 2001.

Gage, K. S., Radar observations of the free atmosphere: structure and dynamics, in *Battan Memorial and 40th Anniversary Radar Meteorology Conference*, edited by D. Atlas, pp. 534–565, Boston. American Meteorological Society, 1990.

Gage, K. S., and B. B. Balsley, On the scattering and reflection mechanisms contributing to clear air radar echoes from the troposphere, stratosphere and mesosphere, *Rad. Sci.*, *15*(2), 243–257, 1980.

Gage, K. S., and J. L. Green, Evidence for specular reflection from monostatic VHF radar observations of the stratosphere, *Rad. Sci.*, *13*, 991–1001, 1978.

Gage, K. S., and J. L. Green, Tropopause detection by partial specular reflection with Very-High-Frequncy radar, *Science*, *203*, 1238–1239, 1979.

Gage, K. S., and J. L. Green, A technique for determining the temperature profile from VHF radar observations, *J. Appl. Meteorol.*, *21*, 1146–1149, 1982.

Gage, K. S., J. L. Green, and T. E. VanZandt, Use of Doppler radar for the measurement of atmospheric turbulence parameters from the intensity of clear-air echoes, *Rad. Sci.*, *15*(2), 407–416, 1980.

Gage, K. S., D. A. Carter, and W. L. Ecklund, The effect of gravity waves on specular echoes observed by the Poker Flat MST radar, *Geophys. Res. Let.*, *8*(6), 599–602, 1981a.

Gage, K. S., B. B. Balsley, and J. L. Green, Fresnel scattering model for the specular echoes observed by VHF radar, *Rad. Sci.*, *16*(6), 1447–1453, 1981b.

Gage, K. S., W. L. Ecklund, and B. B. Balsley, A modified Fresnel scattering model for the parameterization of Fresnel returns, *Rad. Sci.*, *20*(6), 1493–1501, 1985.

Gage, K. S., W. L. Ecklund, A. C. Riddle, and B. B. Balsley, Objective tropopause height determination using low-resolution VHF radar observations, *J. Atmos. Ocean. Tech.*, *3*, 248–254, 1986.

Geddes, A. E. M., *Meteorology: An Introductory Treatise.* Blackie and Son Ltd, London, 2nd edn., 1939.

Gossard, E. E., D. E. Wolfe, K. P. Moran, R. A. Paulus, K. D. Anderson, and L. T. Rogers, Measurement of clear-air gradients and turbulence properties with radar wind profilers, *J. Atmos. Ocean. Tech.*, *15*, 321–342, 1998.

Graf, W., R. N. Bracewell, J. H. Deuter, and J. S. Rutherford, The sun as a test source for boresight calibration of microwave antennas, *I.E.E.E. Trans. Antennas. Prop.*, *AP-19*(5), 606–612, 1971.

Green, J. L., J. M. Warnock, R. H. Winkler, and T. E. VanZandt, Studies of winds in the upper troposphere with a sensitive VHF radar, *Geophys. Res. Let.*, *2*, 19–21, 1975.

Green, J. L., K. S. Gage, T. E. VanZandt, W. L. Clark, J. M. Warnook, and G. D. Nastrom, Observations of vertical velocity over Illinois by the Flatland Radar, *Geophys. Res. Let.*, *15*(3), 269–272, 1988.

Greenhow, J. S., Systematic wind measurements at altitudes of 80–100 km using radio echoes from meteor trails, *Phil. Mag.*, *45*, 471–490, 1954.

Hall, G. (ed.), *The ARRL Antenna Handbook*. The American Radio Relay League, Newington, 16th edn., 1991.

Hamming, R. W., *Digital Filters*. Prentice Hall, New Jersey, 3rd edn., 1989.

Hardy, K. R., and K. S. Gage, The history of radar studies of the clear atmosphere, in *Radar in Meteorology*, edited by D. Atlas, chap. 17, pp. 130–142. American Meteorological Society, 1990.

Hildebrand, P. H., and R. S. Sekhon, Objective determination of the noise level in doppler spectra, *J. Appl. Meteorol.*, *13*, 808–811, 1974.

Hines, C. O., Internal atmospheric gravity waves at ionospheric heights, *Canadian J. Phys.*, *38*, 1441–1481, 1960.

Hines, C. O., *The Upper Atmosphere in Motion*, vol. 18 of *Geophysical Monograph*. American Geophysical Union, Washington, 1974.

Hocking, W. K., On the extraction of atmospheric turbulence parameters from radar backscatter Doppler spectra – I. Theory, *J. Atmos. Terr. Phys.*, *45*, 89–102, 1983.

Hocking, W. K., Measurement of turbulent energy dissipation rates in the middle atmosphere by radar techniques: a review, *Rad. Sci.*, *20*(6), 1403–1422, 1985.

Hocking, W. K., Radar studies of small scale structure in the upper middle atmosphere and lower ionosphere, *Adv. Space Res.*, *7*(10), 327–338, 1987.

Hocking, W. K., Recent advances in radar instrumentation and techniques for studies of the mesosphere, stratosphere and troposphere, *Rad. Sci.*, *32*(6), 2241–2270, 1997a.

Hocking, W. K., System design, signal-processing procedures, and preliminary results for the Canadian (London, Ontario) VHF atmospheric radar, *Rad. Sci.*, *32*(2), 687–706, 1997b.

Hocking, W. K., and K. Lawry, Radar measurements of atmospheric turbulence intensities by both C_n^2 and spectral width measurements, in *Handbook for Middle*

Atmosphere Program, edited by B. Edwards, and C. H. Lui, vol. 28, pp. 242–247. ICSU, 1989.

Hocking, W. K., and P. K. L. Mu, Upper and middle tropospheric kinetic energy dissipation rates from measurements of $\overline{C_n^2}$ – review of theories, in-situ investigations, and experimental studies using the Buckland Park atmospheric radar in Australia, *J. Atmos. Sol. Terr. Phys.*, *59*(14), 1779–1803, 1997.

Hocking, W. K., and J. Röttger, Pulse length dependence of radar signal strengths for Fresnel backscatter, *Rad. Sci.*, *18*, 1312–1324, 1983.

Hocking, W. K., R. Ruster, and P. Czechowsky, Absolute reflectivities and aspect sensitivities of VHF radar wave scatterers measured with the SOUSY radar, *J. Atmos. Terr. Phys.*, *48*(2), 131–144, 1986.

Holton, J. R., *An Introduction to Dynamic Meteorology*. Academic Press, London, 3rd edn., 1992.

Holton, J. R., P. H. Haynes, M. E. McIntyre, A. R. Douglass, R. B. Rood, and L. Pfister, Stratosphere-troposphere exchange, *Rev. Geophys.*, *33*, 403–439, 1995.

Holton, J. R., J. A. Curry, and J. A. Pyle (eds.), *Encyclopedia of Atmospheric Sciences*. Academic Press, London, 2003.

Hooper, D. A., Signal and noise level estimation for narrow spectral width returns observed by the Indian MST radar, *Rad. Sci.*, *34*(4), 859–870, 1999.

Hooper, D. A., and J. Arvelius, Monitoring of the Arctic winter tropopause: A comparison of radiosonde, ozondesonde and MST radar observations, in *Proc. MST9-COST76*, edited by B. Edwards, pp. 385–388. SCOSTEP and Meteo France, 2000.

Houghton, J. T., F. W. Taylor, and C. D. Rodgers, *Remote Sounding of Atmospheres*. Cambridge University Press, 1984.

Jones, B. K., *Electronics for Experimentation and Research*. Prentice-Hall, UK, 1986.

Kalnay, E., et al., The NCEP/NCAR 40-year reanalysis project, *Bull. Amer. Meteor. Soc.*, *77*, 437–471, 1996.

Keyser, D., Atmospheric fronts: An observational perspective, in *Mesoscale Meteorology and Forecasting*, edited by S. Ray. American Meteorological Society, 1986.

Kitchen, M., Representative errors for radiosonde observations, *Q. J. R. Meteorol. Soc.*, *115*, 673–700, 1989.

Kraus, J. D., *Radio Astronomy.* McGraw-Hill Book Company, New York, 1966.

Kraus, J. D., *Antennas.* McGraw-Hill Book Company, New York, 2nd edn., 1988.

Kusunoki, K., and H. Eito, Analytical studies of low-level gravity waves over the Kanto Plain associated with a stationary front, *Mon. Weath. Rev.*, *131*, 236–248, 2003.

Lane, T. P., M. J. Reeder, B. R. Morton, and T. L. Clark, Observations and numerical modelling of mountain waves over the Southern Alps of New Zealand, *Q. J. R. Meteorol. Soc.*, *126*, 2765–2788, 2000.

Larsen, M. F., and J. Röttger, Comparison of tropopause height and frontal boundary locations based on radar and radiosonde data, *Geophys. Res. Let.*, *10*(4), 325–328, 1983.

Larsen, M. F., and J. Röttger, Observations of frontal zone and tropopause structures with a VHF Doppler radar and radiosondes, *Rad. Sci.*, *20*(6), 1223–1232, 1985.

Lu, D., T. E. VanZandt, and W. L. Clark, VHF Doppler radar observations of buoyancy waves associated with thunderstorms, *J. Atmos. Sci.*, *44*, 1775–1800, 1984.

Luce, H., M. Crochet, F. Dalaudier, and C. Sidi, Interpretation of VHF ST radar vertical echoes from in situ temperature sheet observations, *Rad. Sci.*, *30*(5), 1003–1025, 1995.

Luce, H., M. Crochet, and F. Dalaudier, Temperature sheets and aspect sensitive radar echoes, *Ann. Geophys.*, *19*, 899–920, 2001.

Marsh, S. H., R. G. T. Bennett, W. J. Baggaley, G. J. Fraser, and G. E. Plank, Measuring meridional mesospheric winds with the AMOR meteor radar, *J. Atmos. Sol. Terr. Phys.*, *62*, 1129–1133, 2000.

Mathews, J. D., D. D. Meisel, D. Janches, V. S. Getman, and Q. H. Zhou, Possible origins of low inclination antapex micrometeors observed using the Arecibo UHF radar, in *Meteoroids 1998*, edited by W. J. Baggaley, and V. Porubčan, pp. 79–82. Astron. Inst. Slovak Acad. Sci., Britislava, 1999.

Mitra, S. N., A radio method of measuring winds in the ionosphere, *Proc. I.E.E.*, *96*(Part IIIA), 441–446, 1949.

Morris, G., and L. Harkness (eds.), *Airbourne Pulsed Doppler Radar*. Artech House, Boston, 2nd edn., 1996.

Muschinski, A., Turbulence and gravity waves in the vicinity of a midtropospheric warm front: A case study using VHF echo-intensity measurements and radiosonde data, *Rad. Sci.*, *32*(3), 1161–1178, 1997.

Nastrom, G. D., Doppler radar spectral width broadening due to beamwidth and wind shear, *Ann. Geophys.*, *15*, 786–796, 1997.

Nastrom, G. D., and T. E. VanZandt, Mean vertical motions seen by radar wind profilers, *J. Appl. Meteorol.*, *33*, 984–995, 1994.

Nastrom, G. D., M. R. Peterson, J. L. Green, K. S. Gage, and T. E. VanZandt, Sources of gravity wave activity seen in the vertical velocities observed by the Flatland VHF radar, *J. Appl. Meteorol.*, *29*, 783–792, 1990.

Nautical Almanac Office, *The Astronomical Almanac for the Year 2002*. Nautical Almanac Office, US Naval Observatory, Washington, and HM Nautical Almanac Office, Rutherford Appleton Laboratory, London, 2001.

NZMS, Summaries of radiosonde data 1956-61, New Zealand Met. Serv. Misc. Pub. 119, 1963.

Ottersten, H., Atmospheric structure and radar backscattering in clear air, *Rad. Sci.*, *4*(12), 1179–1193, 1969.

Palmén, E., and C. W. Newton, A study of the mean wind and temperature distribution in the vicinity of the polar front in winter., *J. Meteor.*, *5*, 220–226, 1948.

Palmén, E., and C. W. Newton, *Atmospheric Circulation Systems: Their Structure and Physical Interpretation*, vol. 13 of *International Geophysics Series*. Academic Press, 1969.

Pfister, W., The wave-like nature of inhomogeneities in the E-region, *J. Atmos. Terr. Phys.*, *33*, 999–1025, 1971.

Press, W. H., S. A. Teukolsky, W. T. Vetterling, and B. P. Flannery, *Numerical Recipes in C*. Cambridge University Press, 2nd edn., 1992.

Price, J. D., and G. Vaughan, The potential for stratosphere-troposphere exchange in cut-off-low systems, *Q. J. R. Meteorol. Soc.*, *119*, 343–365, 1993.

Pritchard, I. T., L. Thomas, and R. M. Worthington, The characteristics of mountain waves observed by radar near the west coast of Wales, *Ann. Geophys.*, *13*, 757–767, 1995.

Probert-Jones, J. R., A history of radar meteorology in the United Kingdom, in *Radar in Meteorology*, edited by D. Atlas, chap. 7, pp. 54–60. American Meteorological Society, 1990.

Rajopadhyaya, D. K., P. T. May, and R. A. Vincent, The retrieval of ice particle size information from VHF wind profiler Doppler spectra, *J. Atmos. Ocean. Tech.*, *11*, 1559–1568, 1994.

Ralph, F. M., M. Crochet, and S. V. Venkateswaran, A study of mountain lee waves using clear-air radar, *Q. J. R. Meteorol. Soc.*, *118*, 597–627, 1992.

Ralph, F. M., P. J. Neiman, and T. L. Keller, Deep tropospheric gravity waves created by leeside cold fronts, *J. Atmos. Sci.*, *56*, 2986–3009, 1999.

Rao, P. B., A. R. Jain, P. Kishore, P. Balamuralidhar, S. H. Damle, and G. Viswanathan, Indian MST radar: 1. System description and sample vector wind measurements in ST mode, *Rad. Sci.*, *30*(4), 1125–1138, 1995.

Rastogi, P. K., A note on the use of coherent integration in periodogram analysis of MST radar signals, in *Handbook for Middle Atmosphere Program*, edited by S. A. Bowhill, and B. Edwards, vol. 9, chap. 8.3B, pp. 509–512. ICSU, 1983.

Rastogi, P. K., An overview of data acquisition, signal coding and data analysis techniques for MST radar, in *Handbook for Middle Atmosphere Program*, edited by S. A. Bowhill, and B. Edwards, vol. 20, pp. 431–438. ICSU, 1986.

Rastogi, P. K., and J. Röttger, VHF radar observations of coherent reflections in the vicinity of the tropopause, *J. Atmos. Terr. Phys.*, *44*, 461–469, 1982.

Revell, C. G., High resolution imagery of the New Zealand area: a view of lee waves, *Weather and Climate*, *2*(1), 23–29, 1982.

Riddle, A. C., Use of the sun to determine pointing of ST radar beams, in *Handbook for Middle Atmosphere Program*, edited by S. A. Bowhill, and B. Edwards, vol. 20, pp. 410–413. ICSU, 1986.

Ridpath, I. (ed.), *Norton's 2000 - Star Atlas and Reference Handbook*. Longman Scientific and Technical, New York, 18th edn., 1989.

Röttger, J., VHF radar observations of a frontal passage, *J. Appl. Meteorol.*, *18*, 85–91, 1979.

Röttger, J., ST radar observations of atmospheric waves over mountainous areas: a review, *Ann. Geophys.*, *18*, 750–765, 2000.

Röttger, J., and M. F. Larsen, UHF/VHF radar techniques for atmospheric research and wind profiler applications, in *Battan Memorial and 40th Anniversary Radar Meteorology Conference*, edited by D. Atlas, pp. 235–281, Boston. American Meteorological Society, 1990.

Röttger, J., and C. H. Liu, Partial reflection and scattering of VHF radar signals from the clear atmosphere, *Geophys. Res. Let.*, *5*, 357–360, 1978.

Röttger, J., C. H. Liu, J. K. Chao, A. J. Chen, C. J. Pan, and I.-J. Fu, Spatial interferometer measurements with the Chung-Li VHF radar, *Rad. Sci.*, *25*(4), 503–515, 1990.

Roy, A. E., and D. C. Clarke, *Astronomy - Principles and Practice*. Institute of Physics Publishing, London, 3rd edn., 1994.

Ruster, R., Winds and waves in the middle atmosphere as observed by ground-based radars, *Adv. Space Res.*, *4*(4), 3–18, 1984.

Ruster, R., Analysis and interpretation of VHF-radar data, *Ann. Geophys.*, *12*, 725–734, 1994.

Ruster, R., G. D. Nastrom, and G. Schmidt, High resolution VHF radar measurements in the troposphere with a vertically pointing beam, *J. Appl. Meteorol.*, *37*, 1522–1529, 1998.

Salby, M. L., *Fundamentals of Atmospheric Physics*. Academic Press, 1996.

Sato, T., Radar principles, in *Handbook for Middle Atmosphere Program*, edited by S. Fukao, vol. 30, chap. 3, pp. 19–53. ICSU, 1989.

Sato, T., and R. F. Woodman, Fine altitude resolution observations of stratospheric turbulent layers by the Arecibo 430 MHz radar, *J. Atmos. Sci.*, *39*, 2546–2552, 1982.

Sato, T., Y. Inooka, S. Fukao, and S. Kato, Multi-beam pattern measurements of the MU radar antenna by satellite OHZORA, *J. Geomag. Geoelectr.*, *41*, 743–751, 1989.

Sato, T., H. Doji, H. Iwai, and I. Kimaru, Computer processing for deriving drop-size distributions and vertical air velocities from VHF Doppler radar spectra, *Rad. Sci.*, *25*(5), 961–973, 1990.

Scorer, R. S., *Environmental Aerodynamics*. Ellis Horwood, Chichester, 1978.

Shain, C. A., The radio emission from Centaurus-A and Fornax-X, *Aust. J. Phys.*, *11*, 517–529, 1958.

Shaw, N., *Meteorology in History*, vol. 1 of *Manual of Meteorology*. Cambridge University Press, London, 1926.

Sheridan, K. V., An investigation of the strong radio sources in Centaurus, Fornax and Puppis, *Aust. J. Phys.*, *11*, 400–408, 1958.

Shutts, G. J., and A. Broad, A case study of lee waves over the Lake District in northern England, *Q. J. R. Meteorol. Soc.*, *119*, 377–408, 1993.

Shutts, G. J., P. Healey, and S. D. Mobbs, A multiple sounding technique for the study of gravity waves, *Q. J. R. Meteorol. Soc.*, *120*, 59–77, 1994.

Skolnik, M. I. (ed.), *Radar Handbook*. McGraw-Hill, New York, 1970.

Strauch, R. G., D. A. Merritt, K. P. Moran, K. B. Earnshaw, and D. van de Kamp, The Colorado wind-profiling network, *J. Atmos. Ocean. Tech.*, *1*, 37–49, 1984.

Sturman, A. P., A case study of lee waves in south-westerly airflow over Bank's Peninsula, New Zealand, *Weather*, *35*, 32–39, 1980.

Swenson, G. W., An amateur radio telescope, *Sky and Telescope*, *55*, 46–61, 1978.

Thuburn, J., and G. C. Craig, GCM tests of theories for the height of the tropopause, *J. Atmos. Sci.*, *54*, 869–882, 1997.

Tsuda, T., W. E. Gordon, and H. Saito, Azimuth angle variations of specular reflection echoes in the lower atmosphere observed with the MU radar, *J. Atmos. Sol. Terr. Phys.*, *59*(7), 777–784, 1997a.

Tsuda, T., T. E. VanZandt, and H. Saito, Zenith-angle dependence of VHF specular reflection echoes in the lower atmosphere, *J. Atmos. Sol. Terr. Phys.*, *59*(7), 761–775, 1997b.

Vanzandt, T. E., A universal spectrum of buoyancy waves in the atmosphere, *Geophys. Res. Let.*, *9*(5), 575–578, 1982.

Vanzandt, T. E., J. L. Green, K. S. Gage, and W. L. Clark, Vertical profiles of refractivity turbulence structure constant: Comparison of observations by the Sunset Radar with a new theoretical model, *Rad. Sci.*, *13*(5), 819–829, 1978.

Vaughan, G., A. Howells, and J. D. Price, Use of MST radars to probe the mesoscale structure of the tropopause, *Tellus*, *47A*, 759–765, 1995.

Vincent, R. A., and I. M. Reid, HF Doppler measurements of mesospheric gravity wave momentum fluxes, *J. Atmos. Sci.*, *40*, 1321–1333, 1983.

Vincent, R. A., P. May, W. K. Hocking, W. G. Elford, B. Candy, and B. H. Briggs, First results with the Adelaide VHF radar: Spaced antenna studies of tropospheric winds, *J. Atmos. Terr. Phys.*, *49*, 353–366, 1987.

Vincent, R. A., S. Dullaway, A. MacKinnon, I. M. Reid, F. Zink, P. T. May, and B. H. Johnson, A VHF boundary layer radar: First results, *Rad. Sci.*, *33*(4), 845–860, 1998.

Wallace, J. M., and P. V. Hobbs, *Atmospheric Science: An Introductory Survey.* Academic Press, New York, 1977.

Waterman, A. T., T. Z. Hu, P. Czechowsky, and J. Röttger, Measurement of anisotropic permittivity structure of upper troposphere with clear-air radar, *Rad. Sci.*, *20*, 1580–1592, 1985.

Watson Watt, R. A., L. H. Bainbridge-Bell, A. F. Wilkins, and E. G. Bowen, Return of radio-waves from the middle atmosphere, *Nature*, *137*, 866, 1936.

WMO, Atmospheric ozone 1985: Global ozone research and monitoring report, Tech. Rep. 16, World Meteorological Organisation, Geneva, 1986.

Wolff, E. A., *Antenna Analysis.* John Wiley & Sons, New York, 1966.

Woodman, R. F., Spectral moment estimation in MST radars, *Rad. Sci.*, *20*(6), 1185–1195, 1985.

Woodman, R. F., and A. Guillen, Radar obsevations of winds and turbulence in the stratosphere and mesosphere, *J. Atmos. Sci.*, *31*, 493–505, 1974.

Worthington, R. M., Tropopausal turbulence caused by the breaking of mountain waves, *J. Atmos. Sol. Terr. Phys.*, *60*, 1543–1547, 1998.

Worthington, R. M., Calculating the azimuth of mountain waves, using the effect of tilted fine-scale stable layers on VHF radar echoes, *Ann. Geophys.*, *17*, 257–272, 1999.

Worthington, R. M., Asymmetry of atmospheric microstructure over synoptic scales, *Ann. Geophys.*, *19*, 921–924, 2001.

Worthington, R. M., and L. Thomas, The measurement of gravity wave momentum flux in the lower atmosphere using VHF radar, *Rad. Sci.*, *31*(6), 1501–1517, 1996a.

Worthington, R. M., and L. Thomas, Radar measurements of critical layer absorption in mountain waves, *Q. J. R. Meteorol. Soc.*, *122*, 1263–1282, 1996b.

Worthington, R. M., and L. Thomas, The frequency spectrum of mountain waves, *Q. J. R. Meteorol. Soc.*, *124*, 687–703, 1998.

Worthington, R. M., R. D. Palmer, and S. Fukao, An investigation of tilted aspect-sensitive scatterers in the lower atmosphere using the MU and Aberystwyth VHF radars, *Rad. Sci.*, *34*(2), 413–426, 1999.

Worthington, R. M., R. D. Palmer, S. Fukao, M. Yamamoto, and I. Astin, Rapid variations in echo power maps of VHF radar backscatter from the lower atmosphere, *J. Atmos. Sol. Terr. Phys.*, *62*, 573–581, 2000.

Worthington, R. M., A. Muschinski, and B. B. Balsley, Bias in mean vertical wind measured by VHF radars: Significance of radar location relative to mountains, *J. Atmos. Sci.*, *58*, 707–723, 2001.

Young, T., *A Course of Lectures on Natural Philosophy and the Mechanical Arts*, vol. 1, p. 464. London, 1807.

Acknowledgements

I would like to offer my sincere thanks to both of my supervisors. Firstly to Jack Baggaley, for his help over the full four years of this project, particularly for the practical advice on antenna construction and ideas for the extension of the radar to measure meteoric ionisation. Thanks also to Adrian McDonald, for his suggestions over the last one and a half years about what to do with the results from the radar and for the numerous readings of this thesis. I am also greatly indebted to Bob Bennett, who has been heavily involved in the design of the antenna and electronic hardware, and to Grahame Fraser for never failing to answer my innumerable questions, no matter how trivial.

A huge thank you must go to Graeme Plank for the countless hours spent constructing the antenna array. I am also very appreciative of the many others (academics, technicians and students) who helped with the construction at Birdlings Flat. I am very grateful to Ross Ritchie, Geoff Graham and Graeme McDonald for the time spent constructing and maintaining the electronic equipment.

I would like to acknowledge those who provided additional data for use in this thesis. Thanks to Hector Alvarez and Jorge May (of the Departamento de Astronomía, Universidad de Chile) for the 45 MHz sky temperature data and to Patricia Reich (of the Max-Planck-Insitut für Radioastronomie, Bonn, Germany) for extracting the data at the correct latitude and resolution. Thanks to Richard Turner (of NIWA, Wellington) for performing a model simulation at the time of the frontal passage examined in this thesis. Thanks also to the MetService for making available their radiosonde data.

My mentors, Geoff Stedman, Roger Reeves and Saskia Besier, also deserve a special mention as they have been a great source of encouragement and (at times much needed) pressure. I am grateful for a teaching assistantship, provided for by the Department of Physics and Astronomy, over the first three years of my graduate studies and also for a Marsden grant (Interstellar Dust Radar Detection – UoC911) which provided funding during my final year.

To numerous members of the department and particularly those who have been

part of the atmospheric group, you have all been very kind and helpful. I would like to thank Bryan Lawrence (for getting me started on this project), Don Grainger, Darlene Heuff and my fellow students, John Grant (for sharing an office for nearly four years), Adam Dunford (for paving the way for this research), Steve Marsh (a Post-Doc who is outstanding in his field), David Galligan, Gareth Thomas, Sarah Wheaton, Daniela Wurl, Mohar Chattopadhyay (for the MetService data and also the delicious recipes), Sam Dean, Scott Osprey, ...

Finally, a big thank you to my family. To Mum and Dad (Carey-Smith), thanks for all your help and prayers over the years and for encouraging me to do what I wanted (and continually reminding me that I might have to work to achieve it). To Mum and Dad (Rendle), thank you for supporting me and providing a home-away-from-home, particularly while I was trying to steal your daughter. Thanks to all my brothers and sisters. And last, but certainly not least, thank you to my wonderful wife, Gwyneth, for your love, encouragement and patience. If not for you these past four years would have been impossible to bear.